Retrospective Theses and Dissertations

Iowa State University Capstones, Theses and Dissertations

1997

Derivatives, dimers, and solutions

Simon Paul Webb
Iowa State University

Follow this and additional works at: https://lib.dr.iastate.edu/rtd

Part of the Physical Chemistry Commons

INFORMATION TO USERS

This manuscript has been reproduced from the microfilm master. UMI films the text directly from the original or copy submitted. Thus, some thesis and dissertation copies are in typewriter face, while others may be from any type of computer printer.

The quality of this reproduction is dependent upon the quality of the copy submitted. Broken or indistinct print, colored or poor quality illustrations and photographs, print bleedthrough, substandard margins, and improper alignment can adversely affect reproduction.

In the unlikely event that the author did not send UMI a complete manuscript and there are missing pages, these will be noted. Also, if unauthorized copyright material had to be removed, a note will indicate the deletion.

Oversize materials (e.g., maps, drawings, charts) are reproduced by sectioning the original, beginning at the upper left-hand corner and continuing from left to right in equal sections with small overlaps. Each original is also photographed in one exposure and is included in reduced form at the back of the book.

Photographs included in the original manuscript have been reproduced xerographically in this copy. Higher quality 6" x 9" black and white photographic prints are available for any photographs or illustrations appearing in this copy for an additional charge. Contact UMI directly to order.

Derivatives, dimers, and solutions

by

Simon Paul Webb

A dissertation submitted to the graduate faculty

in partial fulfillment of the requirements for the degree of

DOCTOR OF PHILOSOPHY

Major: Physical Chemistry

Major Professor: Mark S. Gordon

Iowa State University

Ames, Iowa

1997

UMI Number: 9814705

UMI
300 North Zeeb Road
Ann Arbor, MI 48103

ii

Graduate College

Iowa State University

This is to certify that the Doctoral dissertation of

Simon Paul Webb

has met the dissertation requirements of Iowa State University

Committee Member

Committee Member

Committee Member

Committee Member

Major Professor

For the Major Program

For the Graduate College

To my parents Ray and Jean, my sister Rachel, and my aunt Lilian

TABLE OF CONTENTS

ACKNOWLEDGEMENTS

I want to thank my parents for the support and encouragement they have given to me throughout my education.

I must, of course, thank my advisor Mark Gordon. I thank him for his patience, his guidance, his friendship, and all that I have learnt from him. His science and he have been inspirational to me.

Finally, I thank the members of Mark Gordon's research group, both past and present. I would especially like to thank Mike Schmidt for his invaluable advice and help. His thoughtful discussions of quantum chemistry (and other topics) have been a source of pleasure as well as enlightenment.

ABSTRACT

The research presented in this thesis may be divided into three areas: derivative theory, transition metal chemistry, and solvation effects.

Analytic derivatives. A derivation of the closed shell frozen-core analytic gradient for second order Møller Plesset perturbation (MP2) theory is presented, as well as a derivation of an expression for the localized orbital dipole polarizability. Both methods have been implemented in the electronic structure code GAMESS and are currently in wide use.

Transition metal chemistry. Ab initio electronic structure theory methods have been used to investigate the chemistry of simple titanium compounds. These include the closed shell TiH_4 dimer: Ti_2H_8; the diradical TiH_3 dimer: Ti_2H_6; and the closed shell TiX_4 dimers: Ti_2X_8 ($X = F, Cl, Br$). Both the hydride dimers contain 2 electron, 3 center bonds analogous to those in diborane. Ti_2H_6 is a model compound for more complex di-titanium(III) bridged systems. We have accurately calculated the isotropic singlet-triplet energy gap in Ti_2H_6 (1.43 kcal/mol) and in addition calculated anisotropic effects due to spin-orbit coupling between ground and excited states. Calculations on TiX_4 dimers establish the possibility of halide exchange and thereby explain unexpected NMR line widths observed for $TiCl_4$.

Solvation Studies. The effective fragment potential (EFP) method is used to study the effects of solvating water molecules on the Menshutkin reaction between ammonia and methyl bromide. The effects, relative to the gas phase reaction, of two, four, six, and eight water molecules are examined. The EFP method is found to reproduce all *ab initio* calculations very accurately at a fraction of the cost.

CHAPTER 1. GENERAL INTRODUCTION

I. General Overview

My interests in the field of theoretical chemistry are widespread; however, they may be encompassed by three areas of study: energy derivative theory, transition metal chemistry, and solvation effects. The general motivation behind these areas of study follows, with subsequent description of specific research projects, the results of which are presented in this dissertation.

a) General Motivation. The importance of analytic energy derivatives in theoretical chemistry cannot be overstated. Having found the wavefunction for a particular molecular system (albeit an approximation to the exact wavefunction) and thereby having found the energy, one would almost always like additional information. Energy derivatives can provide a wealth of such information. The first derivative of the energy with respect to a nuclear coordinate perturbation (the energy gradient) helps locate and then identifies stationary points on potential energy surfaces. The first derivative of the energy with respect to an electric field perturbation determines the electric dipole moment. Information from energy second derivatives with respect to these perturbations includes: characterization of stationary points (minimum, transition state, or higher order saddle point), harmonic vibrational frequencies, infrared intensities, and electric polarizabilities.

These energy derivatives can, in principle, be evaluated from the energy by using numeric finite difference methods. However, these methods are very inefficient and often present problems with accuracy and stability. It is absolutely essential, then, to be able to compute energy first derivatives analytically, and it is highly desirable for energy second derivatives.

Transition metal systems are rich with exciting and vital chemistry. From active sites in enzymes to catalysts in countless industrial processes, their importance is only exceeded by their complexity. Much of their chemical behavior is poorly understood; one of the many reasons for this is the difficulty their description presents to theoretical chemistry methodology. This is partly due to their size (> 20 electrons), and partly due to the complex wavefunctions needed to describe the near degenerate energy levels which result from partially filled and non-bonding d-orbitals commonly found in these systems. One approach, which I have taken, is to start with simple transition metal systems, establish the levels of theory needed for a reliable description, examine and learn from their chemical behavior, and then apply the knowledge gained to slightly more complex systems, and so on. This seems an especially important approach given the increasing application of density functional methods to open shell transition metal systems, often without thought to the method's adequacy.

The determination of solvation effects on chemical processes is one of the greatest challenges to computational chemistry. Even though the majority of chemical processes take place in solution the overwhelming majority of *ab initio* calculations carried out so far have been restricted to gas phase systems. This is because the inclusion of more than a handful of solvent molecules in computationally demanding *ab initio* calculations is intractable. A number of methods have been developed in which the solute is treated *ab initio* and solvent molecules are represented by potentials. I have been involved in the development of one such method: the effective fragment potential (EFP) method. This method is an important step in accurate but inexpensive modeling of solvation effects.

While even on their own these three fields are challenging and important, their combination to constitute the study of potential energy surfaces and molecular properties of transition metal systems in solution is a particularly exciting prospect to me.

b) Specific Research Projects.

Analytic Derivatives. As stated above, in order to explore potential energy surfaces and molecular properties efficiently one must be able to compute analytic energy derivatives. Two derivations of such analytic expressions are presented along with test cases: a derivation of the closed shell frozen-core second order Møller-Plesset perturbation theory (MP2) analytic gradient, and a derivation of the analytic expression for localized orbital dipole polarizabilities.

MP2 is the most efficient method of introducing dynamic electron correlation effects into *ab initio* molecular orbital calculations. It is clearly desirable to have the ability to calculate MP2 analytic energy gradients, as the effects of dynamic electron correlation can have a large effect on molecular structure. Inclusion of core electrons in the perturbation treatment, however, has little effect on molecular structure and their exclusion (frozen-core) leads to a saving in computational effort. Therefore, the ability to calculate the closed shell frozen-core MP2 analytic energy gradient is important. There are no derivations of this method available in the literature. A detailed derivation of the closed shell frozen-core MP2 analytic gradient expressions, which was used to implement the method in the electronic structure code GAMESS, is presented.

The dipole polarizability is a measure of how easily the molecular electronic charge distribution can be distorted in an electric field. Calculation of localized orbital dipole polarizabilties corresponds to partitioning the total polarizability into contributions from cores, bonds, and lone pairs. This information is important as one can then easily identify polarizable parts of molecules and also monitor the transferability of bond and lone pair polarizabilities between different molecules. In addition, we use localized orbital dipole polarizabilities to introduce polarization effects into the effective fragment potential (EFP) solvation model. Localized orbital dipole polarizabilities may be calculated by a numeric finite-field difference method; however, this method is cumbersome for molecules containing

more than a few atoms and is difficult to automate. Analytic calculation of these polarizabilities is therefore preferred.

Transition Metal Chemistry. The application of *ab initio* molecular orbital calculations to the chemistry of transition metals has been some what limited until recent years. This is due both to the size and complexity of transition metal systems which have, in the past, rendered accurate calculations impossible. Due to the high performance of modern computers, as well as the development of parallel algorithms, useful and reliable *ab initio* calculations on transition metal systems are becoming more common.

Much of this research focuses on elucidating mechanisms of catalysis. The attraction of knowing in detail how a catalyst works is obvious: if the mechanism is known it is easier to improve efficiency and even tailor functionality of the catalyst to produce, for example, only certain conformations of the product molecule. However, *ab inito* calculations can also furnish information on the fundamental chemistry of transition metals. The papers presented in this dissertation, then, do not deal with specific catalyzed systems but are concerned with simple systems containing titanium; more specifically titanium dimer systems with bridging bonds between the titanium centers. These papers represent part of a systematic study of such systems which will serve to establish adequate levels of theory to describe titanium chemistry and also examine the behavior of titanium centers in various chemical environments. It is clear that observed behavior in such studies will be valuable when addressing specific catalyzed systems and may also lead to predictive rules concerning the chemistry of titanium in general.

Solvation Studies. In 1891 Menshutkin discovered that the nature of a chemical reaction cannot be separated from the medium in which it is carried out. Most chemical reactions occur in solution; therefore another important challenge for computational chemistry is the accurate treatment of solvation effects. A systematic way to understand the effect of solvation on a chemical reaction is to study the gas phase reaction first, then add

solvent molecules a small number at a time (micro-solvation) and monitor the effect on the potential energy surface. However, calculations in which both the solute and surrounding solvent molecules are treated *ab initio* become intractable, due to computational expense, after only a handful of solvent molecules are included. The effective fragment potential (EFP) method has recently been developed to treat the solute *ab initio* and the solvent molecules through inexpensive but accurate potentials added as one-electron terms directly to the *ab inito* Hamiltonian. Work concerning the polarizabilty term in this method is presented, as well as an application of the method to the determination of solvation effects in an interesting test case: the Menshutkin reaction between ammonia and methyl bromide.

II. Dissertation Organization

The formulas for energy first derivatives of SCF wavefunctions are well established and are relatively simple. The formulas for MP2 and CI wavefunctions are more complex, but are known when all electrons are correlated. However, when core (or virtual) orbitals are frozen, this introduces an added complexity to the formulas. Explicit derivations of the formulas are not available for the MP2 frozen-core gradient and those for the CI froze-core gradient lack detail. Chapter 2 in this dissertation shows in detail a derivation of the frozen-core gradient for closed shell MP2 wavefunctions.

Chapters 3, 4, 5, and 6 are application papers on simple titanium dimer systems. Chapter 3 introduces the simplest possible titanium dimer - the closed shell Ti_2H_8. Chapters 4 and 5 address the more complex diradical system Ti_2H_6. In chapter 6 the effect of introducing halides are examined with a study on the dimers of TiX_4 (X = F, Cl, Br).

Chapter 7 examines the methodology to account for polarization effects in the effective fragment potential (EFP) method. Also included in chapter 7 is a derivation of an analytic expression to calculate localized orbital dipole polarizability tensors.

Chapter 8 is an application of the EFP method to the Menshutkin reaction. This is intended as a stringent test of the model as the products are highly charged. Performance in terms of accuracy and computational expense is evaluated by comparison to all *ab initio* calculations.

Chapter 9 contains general conclusions based on Chapters 2-8.

III. Theoretical Background

The non-relativistic time-independent Schrödinger equation[1] may be written as

$$\hat{H}\Psi = E\Psi,$$ (1)

where $\hat{H}$ is the Hamiltonian operator and Ψ is the total wavefunction. It is only possible to solve equation (1) analytically for a two body system, for example the hydrogen atom. Therefore, in order to find solutions we must make a series of well defined approximations.

a) The Born-Oppenheimer Approximation. If we invoke the Born-Oppenheimer approximation;[2] that is we assume that the electrons are moving much faster than the nuclei in a molecule, the nuclear repulsion energy becomes a constant $E_{nuc.}$ at a fixed geometry,

$$E_{nuc.} = \sum_{A>B}^{N} \frac{Z_A Z_B}{R_{AB}},$$ (2)

where N is the number of nuclei, Z_A is the atomic number of nucleus A, and R_{AB} is the distance between nuclei A and B. Then we need only solve equation (1) for the electronic Hamiltonian $\hat{H}_{elec.}$,

$$\hat{H}_{elec.} = -\frac{1}{2}\sum_i^n \nabla_i^2 - \sum_i^n \sum_A^N \frac{Z_A}{r_{iA}} + \sum_{i>j}^n \frac{1}{r_{ij}} \quad , \tag{3}$$

where n is the number of electrons, ∇_i^2 is the Laplacian operator for the ith electron, r_{ia} is the distance between the ith electron and nucleus A, r_{ij} is the distance between the ith and jth electrons. The first term in equation (3) represents the kinetic energy of the electrons, the second term the potential energy due to nuclear-electronic interactions, and the third term the potential energy due electron-electron repulsion.

b) The Hartree-Fock Self-Consistent Field Method. Because of the electron-electron repulsion interaction a three-body term remains in equation (3) and the Schrödinger equation (equation (1)) remains non-solvable. In Hartree-Fock theory[3,4] this n-electron system is separated in to n one-electron systems which can be solved for exactly,

$$\hat{F}\psi_i = \varepsilon_i\psi_i \qquad i = 1, 2, ..., n \quad , \tag{4}$$

where $\hat{F}$ is the Fock operator and ε_i are orbital energies.

The one-electron wavefunctions ψ_i are the Hartree-Fock orbitals and may be conveniently represented by linear combinations of known functions χ_μ centered on the nuclei of the molecule,[5]

$$\psi_i = \sum_\mu C_{\mu i}\chi_\mu \quad . \tag{5}$$

These basis functions χ_μ usually take the form of Gaussian functions,

$$\chi_\mu(r) = Nx^l y^m z^n e^{(-\alpha r^2)},$$ (6)

where N is a normalization constant, and l, m, and n are integers. The variable α is determined by atomic calculations. Equation (5) is then a linear combination of atomic orbitals and is referred to as the LCAO molecular orbital (MO) approximation. When this approximation is introduced into the Hartree-Fock equations (equation (5)) the exact Hartree-Fock wavefunction is found only with a complete or infinite basis set (in practice it is possible to converge to the Hartree-Fock limit with a large well chosen finite basis set).

When deriving the Hartree-Fock equations, the total wavefunction is required to be an antisymmetrized product of spin-orbitals.

$$\Psi(x_1, x_2) = -\Psi(x_2, x_1)$$ (7)

Such an antisymmetrized wavefunction may be described by a Slater determinant. The antisymmetrization requirement ensures that the Pauli exclusion principle is obeyed; that is, no two electrons with the same spin can be found at the same point in space. The Hartree-Fock wavefunction, then, correlates electrons with the same spin.

The Hartree-Fock operator, $\hat{F}$, does *not* account for instantaneous electron-electron repulsion between electrons of opposite spin; each electron feels an average field due to all the other electrons (dependent on the coordinates of only one electron). In order to know the average field felt by a particular electron one must already know the orbitals describing all the other electrons, therefore $\hat{F}$ is dependent on its own eigenfunctions and the Hartree-Fock equations (equation (4)) must be solved iteratively to self-consistency.

The Hartree-Fock wavefunction is the underlying wavefunction used in much of the work presented in this dissertation. Closed-shell calculations in which paired electrons occupy the same spatial orbital are termed restricted Hartree-Fock (RHF) equations. Open-shell calculations in which paired electrons occupy the same spatial orbital and unpaired electrons each have their own α spin orbital are termed restricted open-shell Hartree-Fock (ROHF) calculations.

c) Correlation Energy. As mentioned above, the Hartree-Fock method does not correlate electrons with opposite spin; therefore, it over estimates the electron-electron repulsion potential energy. There are various post-Hartree-Fock methods to include the effects of electron correlation.

Configuration Interaction (CI). The form of the exact wavefunction (for a complete basis set) within the Born-Oppenhiemer approximation is that of a full CI. A full CI is a linear combination of all possible determinants.[4] These determinants may be described by reference to the Hartree-Fock determinant Ψ_0

$$|\Phi\rangle = c_0|\Psi_0\rangle + \sum_{ra} c_a^r|\Psi_a^r\rangle + \sum_{\substack{a>b \\ r<s}} c_{ab}^{rs}|\Psi_{ab}^{rs}\rangle + \sum_{\substack{a<b<c \\ r<s<t}} c_{abc}^{rst}|\Psi_{abc}^{rst}\rangle + \ldots\ldots \tag{8}$$

The energy E_{FCI} obtained from a full CI is the exact energy for the given basis set within the Born-Oppenhiemer approximation. The correlation energy $E_{corr.}$ is defined as the difference between the exact energy and the Hartree-Fock energy, E_0,[6]

$$E_{corr.} = E_{FCI} - E_0. \tag{9}$$

In practice full CI is prohibitively expensive except for very small systems. It is therefore common to truncate equation (8) at single and double excitations.

Multiconfiguration Self Consistent Field (MCSCF) Theory. The Hartree-Fock wavefunction can fail qualitatively if any occupied and unoccupied Hartree-Fock orbitals are quasi-degenerate. This situation arises, for example, during the process of making and breaking bonds or in diradical systems. In an MCSCF calculation this problem is solved by including determinants (configurations) in which these quasi-degenerate orbitals are occupied. The CI coefficients *and* the orbital coefficients are then found variationally so as to minimize the energy,

$$|\Psi_{MCSCF}\rangle = \sum_I c_I |\Psi_I\rangle. \tag{10}$$

The orbitals and electrons which vary among these configurations define an active space (the inactive orbitals are always doubly occupied). If all possible determinants within the active space are included, that is a full CI within the active space, this is called a fully optimized reaction space (FORS) MCSCF.[7] This is the MCSCF method used in some of the work presented in this dissertation.

The correlation energy recovered due to treating the quasi-degeneracy problem is called static or non-dynamic electron correlation energy.

Møller-Plesset Perturbation Theory. Moller-Plesset theory[8] was developed as a Rayleigh-Schrödinger perturbation treatment of interacting particles in atoms and molecules in which the unperturbed wavefunction is that from a Hartree-Fock calculation.

The exact Hamiltonian, $\hat{H}$, is written as zeroth order Hamiltonian, $\hat{H}_0$, which recovers the Hartree-Fock energy, plus a perturbation, V, which is the difference between the exact electron-electron interaction and that described by the zeroth order Hamiltonian,

$$\hat{H} = \hat{H}_0 + V , \tag{11}$$

$$\hat{H}_0 = \sum_{i}^{n} \hat{F}_i - \sum_{i}^{n/2} \sum_{j}^{n/2} \left(2J_{ij} - K_{ij} \right), \tag{12}$$

$$= \sum_{i}^{n} \hat{h}_i + \sum_{i}^{n/2} \sum_{j}^{n/2} \left(2J_{ij} - K_{ij} \right), \tag{13}$$

$$V = \sum_{i>j}^{n} \frac{1}{r_{ij}} - \sum_{i}^{n/2} \sum_{j}^{n/2} \left(2J_{ij} - K_{ij} \right). \tag{14}$$

Where J and K are the coulomb and exchange integrals, respectively, and n is the number of electrons. The exact wavefunction and energy are expanded in a Taylor series and after truncation at the nth order and collection of terms, zeroth to nth order energy terms are recovered. Carrying the expansion to 2nd order gives:

$$E^{MP2} = E_0^{(0)} + E_0^{(1)} + E_0^{(2)}, \tag{15}$$

where $E_0^{(0)}$ is the Hartree-Fock energy, the first order term, $E_0^{(1)}$, is zero and $E_0^{(2)}$ is the first non-zero correction to the Hartree-Fock energy; the MP2 energy correction.[9] The MP2 energy correction recovers up to eighty percent of the correlation energy and the method is widely used due to its computational efficiency relative to CI methods. This kind of electron correlation, which arises due to instantaneous interactions between electrons of opposite spin, is referred to as dynamic electron correlation.

For the above MP2 perturbation treatment to be valid the Hartree-Fock wavefunction must provide a qualitatively correct description of the system. Perturbative methods have been developed in which the zeroth order wavefunction can be multiconfugurational. One such method is multiconfigurational quasidegenerate second order perturbation theory

(MCQDPT).[10] The MP2 and MCQDPT methods are used in work presented in this dissertation.

References

1. (a) Schrödinger, E. *Ann. Physik* **1926,** 79, 361. (b) Schrödinger, E. *Ann. Physik.* **1926.** 79, 489. (b) Schrödinger, E. *Ann. Physik.* **1926,** 79. 734. (d) Schrödinger. E. *Ann. Physik.* **1926,** 80, 437. (e) Schrödinger, E. *Ann. Physik* **1926,** 81, 109.

2. Born, M.; Openheimer, J. R. *Ann. Physik.* **1927,** 84, 457.

3. (a) Hartree, D. R. *Proc. Cambridge Phil Soc.* **1928,** 24, 89. (b) Hartree, D. R. *Proc. Cambridge Phil Soc.* **1928,** 24, 111. (c) Hartree, D. R. *Proc. Cambridge Phil Soc.* **1928,** 24, 426. (d) Fock. V. *Physik* **1930,** 61, 126.

4. Szabo, A.; Ostlund, N. S. in *Modern Quantum Chemistry* , McGraw-Hill, New York. 1989.

5. Roothan, C. C. J. *Rev. Mod. Phys.* **1960,** 32, 179.

6. Löwdin, P. O. *Adv. Chem. Phys.* **1959,** 2, 207.

7. (a) Sunberg, K. R.; Ruedenberg, K. in *Quantum Science,* edited by Calais, J. L.; Goscinski, O.; Linderberg, J.; Ohrn, Y., Plenum, New York, 1976, pp 505. (b) Cheung. L. M.; Sunberg, K. R.; Ruedenberg, K. *Int. J. Quantum Chem.* **1979,** 16. 1103. (d) Roos, B. O.; Taylor, P.; Siegbahn, P. E. M. *Chem. Phys.* 1980, 48, 157.

8. Moller, C.; Plesset, M. S. *Phys. Rev.* **1934,** 46, 618.

9. Binkley, J.S.; Pople, J.A. *Int. J. Quantum Chem.* **1975,** 9. 229.

10. (a) Nakano, H. *J. Chem . Phys.* **1993,** 99, 7983. (b) Nakano, H. *Chem. Phys. Lett.* **1993.** 207, 372.

CHAPTER 2. A DERIVATION OF THE CLOSED SHELL FROZEN-CORE MP2 ANALYTIC GRADIENT

S. P. Webb, G. D. Fletcher, M. S. Gordon.

Abstract

A detailed derivation of the closed shell frozen-core MP2 analytic gradient is presented. The summation ranges and modification of the MP2 gradient terms which are a result of the frozen-core approximation are clearly identified. Timings from full and frozen-core MP2 gradient calculations on the molecule silicocene are also presented.

I. Introduction

The analytic expression for the derivative of the full MP2 energy (all electrons correlated) with respect to nuclear coordinate displacement has long been known.[1] With the development and implementation of more efficient methodology and algorithms[2] has come the widespread use of MP2 gradients to include the effects of dynamic electron correlation in the determination of molecular structure. The recent development of parallel algorithms[3,4] has greatly extended the size of the systems to which the method can be applied.

Usually the effects of including dynamic correlation in the inner shell or core electrons of a molecule are minimal in terms of relative energies and geometry parameters, and therefore core electrons are often not included in the perturbation treatment; this is known as the frozen-core approximation. In addition to an associated reduction in computational effort,[2] the frozen-core approximation can be preferable to full MP2, as the

description of core electrons is of lower quality than the description of valence electrons in many basis sets.

The modification of the MP2 energy expression to exclude core electrons is a trivial matter which requires simply that the summation over occupied orbitals excludes those chosen to be frozen (see equation (28)). The associated reduction in the number of transformed two-electron integrals required results in reduction of the CPU time needed for the calculation. The modification of the MP2 gradient expression, however, is far from trivial.

Handy et al have already addressed the problem of frozen-cores for the CI gradient expression and have *suggested* that the MP2 expression may be found in an analogous fashion.[5] In this paper the analytic frozen-core MP2 gradient expressions for closed shell systems are derived in detail to facilitate serial and parallel implementation of this method in GAMESS.[6] No explicit derivation of the analytic frozen-core MP2 gradient expression is currently available in the literature. Serial algorithm timings on the molecule silicocene are presented to illustrate time savings achieved due to the frozen-core approximation.

II. Theory

(a) **Notation, Definitions, and Techniques.** First we introduce the notation, definitions, and techniques which will be used extensively during the course of the derivation of the MP2 frozen-core gradient. Extensive use is made of the excellent book by Yamaguchi et al.[7]

Notation.

(i) Indices.

f, g	-	frozen-core molecular orbital (MO)
i, j, k, l	-	any occupied MO
a, b, c, d	-	virtual MO
p, q, r, s	-	any MO
$\mu, \nu, \lambda, \sigma$	-	atomic orbital (AO)
superscript x	-	derivative with respect to nuclear displacement x
superscript (x)	-	derivatives of AO integrals only

(ii) Summation ranges.

act.	-	active MOs (usually valence orbitals)
core	-	frozen-core MOs (usually inner shells)
occ.	-	**all** occupied MOs
virt.		virtual MOs
all	-	all MOs

(iii) Symbols.

$(pq\|rs)$	-	electron repulsion integral (ERI) in the MO basis
H_{pq}	-	one-electron Hamiltonian integral
S_{pq}	-	overlap integral
ε_p	-	RHF orbital energy
U_{pq}^x	-	orbital response to nuclear displacement x
$\|p\rangle$	-	MO in bra-ket notation

$$L \qquad\qquad - \qquad\qquad \text{so called MP2 Lagrangian}$$

Definitions.

(i) The MP2 amplitude is defined as:

$$T_{ij}^{ab} = \left[2(ia|jb) - (ib|ja) \right] \big/ D_{ij}^{ab} \tag{1}$$

where

$$D_{ij}^{ab} = \varepsilon_i + \varepsilon_j - \varepsilon_a - \varepsilon_b. \tag{2}$$

(ii) Derivatives with respect to a perturbation x.

The derivative of an MO is given by (reference 7, chapter 3):

$$\frac{\partial |p\rangle}{\partial x} \equiv |p\rangle^x = \left(\sum_\mu^{AO} C_{\mu p} |\mu\rangle \right)^x = \sum_\mu^{AO} C_{\mu p} |\mu\rangle^x + \sum_\mu^{AO} C_{\mu p}^x |\mu\rangle$$

$$= |p\rangle^{(x)} + \sum_\mu^{AO} \sum_q^{all} U_{qp}^x C_{\mu q} |\mu\rangle = |p\rangle^{(x)} + \sum_q^{all} U_{qp}^x |q\rangle. \tag{3}$$

It follows, then, that

$$(pq|rs)^x = (pq|rs)^{(x)} + \sum_t^{all} U_{tp}^x (tq|rs) + \sum_t^{all} U_{tq}^x (pt|rs)$$

$$+ \sum_t^{all} U_{tr}^x (pq|ts) + \sum_t^{all} U_{ts}^x (pq|rt). \tag{4}$$

The derivative of the orthonormality constraint $S_{pq} = \delta_{pq}$ yields:

$$U_{pq}^x + U_{qp}^x + S_{pq}^{(x)} = 0. \tag{5}$$

(iii) Coupled Perturbed Hartree-Fock (CPHF) equations (reference 7, chapter 10). We write

$$U_{pq}^x = \frac{1}{\left(\varepsilon_q - \varepsilon_p\right)} Q_{pq}^x, \tag{6}$$

where

$$Q_{pq}^x \equiv B_{pq}^x + \sum_c^{virt.} \sum_k^{occ.} U_{ck}^x A_{pqck}, \tag{7}$$

$$A_{pqrs} = 4(pq|rs) - (pr|qs) - (ps|qr), \tag{8}$$

$$B_{pq}^x = F_{pq}^{(x)} - S_{pq}^{(x)} \varepsilon_q - \sum_{kl}^{occ.} S_{kl}^{(x)} \left[2(pq|kl) - (pk|ql) \right], \tag{9}$$

$$F_{pq}^{(x)} = H_{pq}^{(x)} + \sum_k^{occ.} \left[2(pq|kk)^{(x)} - (pk|qk)^{(x)} \right]. \tag{10}$$

The CPHF equations are then written as:

$$\mathbf{A}'\mathbf{U}^x = \mathbf{B}^x, \tag{11}$$

where

$$A'_{aibj} = \delta_{ab}\delta_{ij}\left(\varepsilon_i - \varepsilon_a\right) - A_{aibj}. \tag{12}$$

Note that: $\varepsilon_p^x = Q_{pp}^x. \tag{13}$

Techniques.

There are several important tools, some familiar and some less well known, that we summarize here.

(i) Interchange of indices due to equivalence on summation.

e.g. $\displaystyle\sum_{ab} (ia|jb)^x (ib|ja) = \sum_{ab} (ia|jb)(ib|ja)^x \tag{14}$

$$\sum_{ij} \left[(i^x a|jb) + (ia|j^x b) \right] = 2 \sum_{ij} (i^x a|jb) \tag{15}$$

(ii) Splitting summations.

$$\text{e.g.} \quad \sum_k U_{ki}^x = \sum_{k \ne i} U_{ki}^x + U_{ii}^x = \sum_{k > i} U_{ki}^x + \sum_{k < i} U_{ki}^x + U_{ii}^x \tag{16}$$

(iii) The chain rule.

$$\frac{\partial}{\partial x}\left(\frac{1}{D_{ij}^{ab}}\right) = \frac{\partial}{\partial D_{ij}^{ab}}\left(\frac{1}{D_{ij}^{ab}}\right)\frac{\partial D_{ij}^{ab}}{\partial x} = -\left(\frac{1}{D_{ij}^{ab}}\right)^2 \left(D_{ij}^{ab}\right)^x \tag{17}$$

(iv) Cross-multiplication.

$$\text{e.g.} \quad \frac{1}{D_{ij}^{ab}} - \frac{1}{D_{kj}^{ab}} = \frac{D_{kj}^{ab} - D_{ij}^{ab}}{D_{ij}^{ab} D_{kj}^{ab}} = \frac{\varepsilon_k - \varepsilon_i}{D_{ij}^{ab} D_{kj}^{ab}} \tag{18}$$

(v) Z-vector method (reference 7, chapter 18).

$$\sum_{ia} U_{ia}^x L_{ia} \equiv \mathbf{L}^T \mathbf{U}^x \tag{19}$$

$$\mathbf{A'U}^x = \mathbf{B}^x \tag{20}$$

$$\mathbf{U}^x = \mathbf{A'}^{-1}\mathbf{B}^x \tag{21}$$

$$\mathbf{L}^T \mathbf{U}^x = \mathbf{L}^T \mathbf{A'}^{-1}\mathbf{B}^x \tag{22}$$

$$= \mathbf{Z}^T \mathbf{B}^x \tag{23}$$

where

$$\mathbf{Z}^T = \mathbf{L}^T \mathbf{A'}^{-1} \tag{24}$$

$$\mathbf{A'}^T \mathbf{Z} = \mathbf{L} \tag{25}$$

the elements of **Z** are obtained from solution of linear equation (25) and the contribution from equation (19) is evaluated as:

$$\sum_{ia} U_{ia}^x L_{ia} = \sum_{ia} B_{ia}^x Z_{ia} \qquad (26)$$

(b) The General Form of the MP2 Gradient. When written in the AO basis the MP2 energy gradient takes the general form which applies to all analytic first derivatives with respect to a nuclear displacement x.

$$E^x = \sum_{\mu\nu}^{AO} P_{\mu\nu}^{MP2} H_{\mu\nu}^x + \sum_{\mu\nu}^{AO} W_{\mu\nu}^{MP2} S_{\mu\nu}^x + \sum_{\mu\nu\lambda\sigma}^{AO} \Gamma_{\mu\nu\lambda\sigma}^{MP2} (\mu\nu|\lambda\sigma)^x \qquad (27)$$

In practice equation (27) is evaluated by forming the density matrices in the MO basis and back transforming to the AO basis for contraction with AO integral derivatives. The task ahead, then, is to derive the MO counterparts of the density matrices in equation (27); the one-particle density matrix P_{pq}^{MP2}, the energy-weighted density matrix W_{pq}^{MP2}, and the two-particle density matrix Γ_{pqrs}^{MP2} with the appropriate restrictions to introduce the frozen-core approximation.

(c) Expansion in Terms of Orbital Rotations. The first step in the derivation is to take the derivative of the frozen-core MP2 energy expression and expand the resulting derivative MOs in terms of orbital rotations (equations (3) and (4)). The frozen-core closed shell MP2 energy is given by:

$$E^{(2)} = \sum_{ij}^{act.} \sum_{ab}^{virt.} (ia|jb) T_{ij}^{ab}. \qquad (28)$$

Taking the derivative with respect to nuclear displacement x gives:

$$E^{(2)^x} = \sum_{ij}^{act.} \sum_{ab}^{virt.} \left[(ia|jb)^x T_{ij}^{ab} + (ia|jb)(T_{ij}^{ab})^x \right].$$ (29)

The amplitude derivative is

$$\left(T_{ij}^{ab} \right)^x = \left[2(ia|jb)^x - (ib|ja)^x \right] \Big/ D_{ij}^{ab} + \left[2(ia|jb) - (ib|ja) \right] (1/D_{ij}^{ab})^x.$$ (30)

Substituting equation (30) into (29), and recognizing that with the interchange $a \leftrightarrow b$ the first term of (30) yields a term equivalent to the first term (in the square brackets) of (29), gives:

$$E^{(2)^x} = 2\sum_{ij}^{act.} \sum_{ab}^{virt.} (ia|jb)^x T_{ij}^{ab} + \sum_{ij}^{act.} \sum_{ab}^{virt.} (ia|jb) \left[2(ia|jb) - (ib|ja) \right] (1/D_{ij}^{ab})^x.$$ (31)

Applying the chain-rule (equation (17)) to the second term of (31) yields

$$E^{(2)^x} = 2\sum_{ij}^{act.} \sum_{ab}^{virt.} (ia|jb)^x T_{ij}^{ab} - \sum_{ij}^{act.} \sum_{ab}^{virt.} (ia|jb) T_{ij}^{ab} \left(D_{ij}^{ab} \right)^x \Big/ D_{ij}^{ab}.$$ (32)

We now substitute expressions for ERI derivatives (equation (4)), thereby introducing the unknown expansion coefficients or orbital responses U_{pq}^x. $\left(D_{ij}^{ab} \right)^x$ is replaced with specific orbital energy derivatives (equation (2)),

$$E^{(2)^x} = 2\sum_{ij}^{act.} \sum_{ab}^{virt.} T_{ij}^{ab} \left[(ia|jb)^{(x)} + \sum_{p}^{all} U_{pi}^x (pa|jb) + \sum_{p}^{all} U_{pa}^x (ip|jb) + \sum_{p}^{all} U_{pj}^x (ia|pb) \right.$$
$$\left. + \sum_{p}^{all} U_{pb}^x (ia|jp) \right] - \sum_{ij}^{act.} \sum_{ab}^{virt.} \frac{(ia|jb)}{D_{ij}^{ab}} T_{ij}^{ab} \left(\varepsilon_i^x + \varepsilon_j^x - \varepsilon_a^x - \varepsilon_b^x \right).$$ (33)

Since the summation ranges of i and j are identical, as are those for summations over a and b, equation (33) simplifies to:

$$E^{(2)^x} = 2\sum_{ij}^{act.}\sum_{ab}^{virt.} T_{ij}^{ab}\left[(ia|jb)^{(x)} + 2\sum_{p}^{all} U_{pi}^x(pa|jb) + 2\sum_{p}^{all} U_{pa}^x(ip|jb)\right]$$
$$-2\sum_{ij}^{act.}\sum_{ab}^{virt.}\frac{(ia|jb)}{D_{ij}^{ab}}T_{ij}^{ab}\left(\varepsilon_i^x - \varepsilon_a^x\right). \tag{34}$$

Next, we split the MO derivative expansions into core, active, and virtual ranges:

$$E^{(2)^x} = 2\sum_{ij}^{act.}\sum_{ab}^{virt.} T_{ij}^{ab}\left[(ia|jb)^{(x)} + 2\sum_{g}^{core} U_{gi}^x(ga|jb) + 2\sum_{k}^{act.} U_{ki}^x(ka|jb) + 2\sum_{c}^{virt.} U_{ci}^x(ca|jb)\right.$$
$$\left.+ 2\sum_{k}^{occ.} U_{ka}^x(ik|jb) + 2\sum_{c}^{virt.} U_{ca}^x(ic|jb)\right] - 2\sum_{ij}^{act.}\sum_{ab}^{virt.}\frac{(ia|jb)}{D_{ij}^{ab}}T_{ij}^{ab}\left(\varepsilon_i^x - \varepsilon_a^x\right). \tag{35}$$

The occupied MOs are split into core and active orbitals, as some of the techniques used in the next section require that indices run over the same summation ranges, for example k and i both run over active MOs in equation (35).

(d) Removal of Unknown Responses and Singularities. We now proceed to remove the unknown occupied-occupied and virtual-virtual orbital responses in equation (35) by using equation (6). Potential singularities introduced by these substitutions are also addressed.

Starting with the active-active term in equation (35), we split its summations according to equation (16) (note that this can only be done because the summation ranges of k and i are equal in equation (35)),

$$\sum_{k}^{act.} U_{ki}^x(ka|jb) = \sum_{k>i}^{act.} U_{ki}^x(ka|jb) + \sum_{k<i}^{act.} U_{ki}^x(ka|jb) + U_{ii}^x(ia|jb). \tag{36}$$

Substituting (36) back into equation (35 and substituting for U_{ii}^x (equation 5) yields the following active-active expression:

$$4\sum_{ij}^{act.}\sum_{ab}^{virt.}\sum_{k}^{act}T_{ij}^{ab}U_{ki}^x(ka|jb)=4\sum_{ij}^{act.}\sum_{ab}^{virt.}\left[\sum_{k>i}^{act.}U_{ki}^xT_{ij}^{ab}(ka|jb)+\sum_{k<i}^{act.}U_{ki}^xT_{ij}^{ab}(ka|jb)\right]$$
$$-2\sum_{ij}^{act.}\sum_{ab}^{virt.}S_{ii}^{(x)}T_{ij}^{ab}(ia|jb). \tag{37}$$

By interchanging $i \leftrightarrow k$ in the sum over $k < i$ in equation (37) we arrive at

$$4\sum_{ij}^{act.}\sum_{ab}^{virt.}\sum_{k}^{act}T_{ij}^{ab}U_{ki}^x(ka|jb)=4\sum_{ij}^{act.}\sum_{ab}^{virt.}\sum_{k>i}^{act.}\left[U_{ki}^xT_{ij}^{ab}(ka|jb)+U_{ik}^xT_{kj}^{ab}(ia|jb)\right]$$
$$-2\sum_{ij}^{act.}\sum_{ab}^{virt.}S_{ii}^{(x)}T_{ij}^{ab}(ia|jb). \tag{38}$$

Substituting for U_{ik}^x according to equation (5) switches the sign, and i and k, in this response term and introduces an off diagonal overlap term,

$$4\sum_{ij}^{act.}\sum_{ab}^{virt.}\sum_{k}^{act}T_{ij}^{ab}U_{ki}^x(ka|jb)=4\sum_{ij}^{act.}\sum_{ab}^{virt.}\sum_{k>i}^{act.}\left[U_{ki}^xT_{ij}^{ab}(ka|jb)-U_{ki}^xT_{kj}^{ab}(ia|jb)\right]$$
$$-4\sum_{ij}^{act.}\sum_{ab}^{virt.}\sum_{k>i}^{act.}S_{ki}^{(x)}T_{kj}^{ab}(ia|jb)-2\sum_{ij}^{act.}\sum_{ab}^{virt.}S_{ii}^{(x)}T_{ij}^{ab}(ia|jb). \tag{39}$$

By recalling equation (1) and interchange of a and b in the second term in square brackets, the numerators of the terms multiplying the U_{ki}^x responses in equation (39) are equivalent and may be combined. In addition the two overlap terms may be combined,

$$4\sum_{ij}^{act.}\sum_{ab}^{virt.}\sum_{k}^{act}T_{ij}^{ab}U_{ki}^x(ka|jb)=4\sum_{ij}^{act.}\sum_{ab}^{virt.}\sum_{k>i}^{act.}U_{ki}^x(ia|jb)[2(ka|jb)-(kb|ja)]\left\{\frac{1}{D_{ij}^{ab}}-\frac{1}{D_{kj}^{ab}}\right\}$$

$$-2\sum_{ijk}^{act.}\sum_{ab}^{virt.}S_{ik}^{(x)}T_{kj}^{ab}(ia|jb). \tag{40}$$

We now substitute for U_{ki}^x according to equation (6) and cross-multiply (equation (18)) enabling cancellation of the orbital energy terms which result in singularities when MOs k and i are degenerate. The first term in equation (40) is then

$$-4\sum_{ij}^{act.}\sum_{ab}^{virt.}\sum_{k>i}^{act.}\frac{Q_{ki}^x}{(\varepsilon_k-\varepsilon_i)}(ia|jb)[2(ka|jb)-(kb|ja)]\frac{(\varepsilon_k-\varepsilon_i)}{D_{ij}^{ab}D_{kj}^{ab}}$$
$$=-4\sum_{ij}^{act.}\sum_{ab}^{virt.}\sum_{k>i}^{act.}Q_{ki}^xT_{kj}^{ab}(ia|jb)/D_{ij}^{ab}. \tag{41}$$

Now, by substituting Q_{ii}^x for ε_i^x (equation (13)) in the last term of equation (35) and combining with equation (41) we arrive at

$$-4\sum_{ij}^{act.}\sum_{ab}^{virt.}\sum_{k>i}^{act.}Q_{ki}^xT_{kj}^{ab}(ia|jb)/D_{ij}^{ab}-2\sum_{ij}^{act.}\sum_{ab}^{virt.}Q_{ii}^xT_{ij}^{ab}(ia|jb)/D_{ij}^{ab}$$
$$=-2\sum_{ijk}^{act.}\sum_{ab}^{virt.}Q_{ki}^xT_{kj}^{ab}\frac{(ia|jb)}{D_{ij}^{ab}}. \tag{42}$$

where we have expanded the sum over k to include all active orbitals and divided by 2.

The virtual-virtual rotations are dealt with in an exactly analogous manner. As a result of the positive signs of the virtual orbital energies the cross multiplication step (equations (40) - (41)) results in the opposite sign to the active-active case

$$4\sum_{ij}^{act.}\sum_{ab}^{virt.}\sum_{c>a}^{act.}Q_{ca}^xT_{ij}^{bc}(ia|jb)/D_{ij}^{ab}+2\sum_{ij}^{act.}\sum_{ab}^{virt.}Q_{aa}^xT_{ij}^{ab}(ia|jb)/D_{ij}^{ab}$$
$$=2\sum_{ij}^{act.}\sum_{abc}^{virt.}Q_{ca}^xT_{ij}^{bc}\frac{(ia|jb)}{D_{ij}^{ab}}. \tag{43}$$

We now return to the frozen core-active term which was separated from the active-active term in equation (35). Splitting the term into two equal parts and substituting for U_{gi}^x using equation (5) in one of these parts, and then making the appropriate substitutions according to equation (6) gives:

$$4\sum_{ij}^{act.}\sum_{ab}^{virt.}\sum_{g}^{core} U_{gi}^x T_{ij}^{ab}(ga|jb) = 2\sum_{ij}^{act.}\sum_{ab}^{virt.}\sum_{g}^{core}\left[U_{gi}^x T_{ij}^{ab}(ga|jb) + U_{gi}^x T_{ij}^{ab}(ga|jb)\right] \qquad (44)$$

$$= 2\sum_{ij}^{act.}\sum_{ab}^{virt.}\sum_{g}^{core} U_{gi}^x T_{ij}^{ab}(ga|jb) - 2\sum_{ij}^{act.}\sum_{ab}^{virt.}\sum_{g}^{core} U_{ig}^x T_{ij}^{ab}(ga|jb)$$

$$- 2\sum_{ij}^{act.}\sum_{ab}^{virt.}\sum_{g}^{core} S_{ig}^{(x)} T_{ij}^{ab}(ga|jb) \qquad (45)$$

$$= 2\sum_{ij}^{act.}\sum_{ab}^{virt.}\sum_{g}^{core} \frac{Q_{gi}^x}{(\varepsilon_i - \varepsilon_g)} T_{ij}^{ab}(ga|jb)$$

$$+ 2\sum_{ij}^{act.}\sum_{ab}^{virt.}\sum_{g}^{core} \frac{Q_{ig}^x}{(\varepsilon_i - \varepsilon_g)} T_{ij}^{ab}(ga|jb)$$

$$- 2\sum_{ij}^{act.}\sum_{ab}^{virt.}\sum_{g}^{core} S_{ig}^{(x)} T_{ij}^{ab}(ga|jb). \qquad (46)$$

It is not possible to remove the orbital energies which could potentially produce singularities. As mentioned previously this requires indices which run over equal ranges which g and i do not. However, as Handy et al[5] point out for the CI case, if the core and active MOs are chosen sensibly (usually chemical cores and valence orbitals) g and i should never be degenerate and singularities are always avoided.

(e) Identifying Density Matrices. The general form of the energy derivative (equation (27)) enables identification of density matrices. Any term which multiples the one-electron derivative integrals $H_{pq}^{(x)}$ is defined as an MP2 density correction term $P_{pq}^{(2)}$. Likewise any term which multiplies the overlap derivative is an energy-weighted density correction term $W_{pq}^{(2)}$.[8]

By inspection of equation (42) and by recalling that the definition of Q_{pq}^x (equation (7)) contains $H_{pq}^{(x)}$ (equations (9) and (10)) the active-active MP2 density correction $P_{ki}^{(2)}$ is defined as

$$-2\sum_{ijk}^{act.}\sum_{ab}^{virt.} Q_{ki}^x T_{kj}^{ab} \frac{(ia|jb)}{D_{ij}^{ab}} \equiv \sum_{ki}^{act.} Q_{ki}^x P_{ki}^{(2)} ; \qquad (47)$$

the core-active MP2 density correction $P_{gi}^{(2)}$, by inspection of equation (46), is defined by

$$2\sum_{ij}^{act.}\sum_{ab}^{virt.}\sum_{g}^{core} \frac{Q_{gi}^x}{(\varepsilon_i - \varepsilon_g)} T_{ij}^{ab}(ga|jb) \equiv \sum_{i}^{act.}\sum_{g}^{core} Q_{gi}^x P_{gi}^{(2)} . \qquad (48)$$

Note that $P_{ig}^{(2)}$ is identical to $P_{gi}^{(2)}$. An active-active energy-weighted density correction $W_{ki}^{(2)}[I]$ (it is labeled $[I]$ as additional terms, which are labeled $[II]$ and $[III]$, follow) is defined by inspection of the second term in equation (40),

$$-2\sum_{ijk}^{act.}\sum_{ab}^{virt.} S_{ik}^{(x)} T_{kj}^{ab}(ia|jb) \equiv \sum_{ki}^{act.} S_{ki}^{(x)} W_{ki}^{(2)}[I]. \qquad (49)$$

The third term in equation (45) defines $W_{ig}^{(2)}$,

$$-2\sum_{ij}^{act.}\sum_{ab}^{virt.}\sum_{g}^{core} S_{ig}^{(x)} T_{ij}^{ab}(ga|jb) \equiv \sum_{i}^{act.}\sum_{g}^{core} S_{ig}^{(x)} W_{ig}^{(2)}[I]. \qquad (50)$$

Virtual-virtual densities $P_{ca}^{(2)}$ and $W_{ca}^{(2)}$ may be defined in an exactly analogous manner.

(f) The Z-Vector Method, MP2 Lagrangian, and CPHF Equations. If the relevant substitutions into equation (34) are made the derivative of the frozen-core MP2 energy at this point in the derivation is given by:

$$
\begin{aligned}
E^{(2)x} = &\sum_{ij}^{act.} Q_{ij}^x P_{ij}^{(2)} + \sum_{ab}^{virt.} Q_{ab}^x P_{ab}^{(2)} + \sum_{ij}^{act.} S_{ij}^{(x)} W_{ij}^{(2)}[I] + \sum_{ab}^{virt.} S_{ab}^{(x)} W_{ab}^{(2)}[I] \\
&+ 2\sum_{i}^{act.}\sum_{g}^{core} Q_{gi}^x P_{gi}^{(2)} + \sum_{i}^{act.}\sum_{g}^{core} S_{ig}^{(x)} W_{ig}^{(2)}[I] + 4\sum_{ij}^{act.}\sum_{abc}^{virt.} U_{ci}^x (ca|jb) T_{ij}^{ab} \\
&+ 4\sum_{ij}^{act.}\sum_{ab}^{virt.}\sum_{k}^{occ.} U_{ka}^x (ik|jb) T_{ij}^{ab} + 2\sum_{ij}^{act.}\sum_{ab}^{virt.} T_{ij}^{ab} (ia|jb)^{(x)} .
\end{aligned}
\tag{51}
$$

The remaining unknowns are now occupied-virtual orbital responses such as those in the 7th and 8th terms in equation (51) - U_{ci}^x and U_{ka}^x. In addition, the substitutions made above to remove occupied-occupied and virtual-virtual orbital responses (equation(6)) introduced occupied-virtual responses through equation (7) (1st, 2nd, and 5th terms of equation (51)).

The occupied-virtual responses must be solved for using the CPHF equations (equation (11)). The number of unknown response vectors may be reduced from 3N, where N is the number of atoms, to 1 by use of the Z-vector method of Handy[9] (equations (19) - (26)). The procedure is as follows: (i) define the MP2 Lagrangian by collecting terms

$$
\sum_{ia} U_{ia}^x L_{ia} ,
\tag{52}
$$

(ii) solve the following set of simultaneous equations (equation (25)) for **Z**

$$
\mathbf{A}'^T \mathbf{Z} = \mathbf{L} ,
\tag{53}
$$

(iii) evaluate the contribution to the gradient from equation (52) according to equation (26) and, recalling the definition of the one-particle density and the expression for B_{pq}^x (equation (9)), thereby determine $P_{ai}^{(2)}$,

$$\sum_{ai} U_{ai}^x L_{ai} = \sum_{ai} B_{ai}^x Z_{ai} \equiv \sum_{ai} B_{ai}^x P_{ai}^{(2)}. \tag{54}$$

Before carrying out the above procedure on equation (51) we must apply equation (5) to the 8th term in order to switch the response indices. In doing so we also introduce an occupied-virtual energy-weighted density term

$$4\sum_{ij}^{act.}\sum_{ab}^{virt.}\sum_{k}^{occ.} U_{ka}^x(ik|jb)T_{ij}^{ab} = -4\sum_{ij}^{act.}\sum_{ab}^{virt.}\sum_{k}^{occ.} U_{ak}^x(ik|jb)T_{ij}^{ab}$$
$$-4\sum_{ij}^{act.}\sum_{ab}^{virt.}\sum_{k}^{occ.} S_{ak}^{(x)}(ik|jb)T_{ij}^{ab}. \tag{55}$$

Now, we substitute equation (55) into (51) and proceed with step (i) by substituting for C_{pq}^x according to equation (7) and grouping terms,

$$E^{(2)x} = \sum_{ij}^{act.} B_{ij}^x P_{ij}^{(2)} + \sum_{ab}^{virt.} B_{ab}^x P_{ab}^{(2)} + \sum_{ij}^{act.} S_{ij}^{(x)} W_{ij}^{(2)}[I] + \sum_{ab}^{virt.} S_{ab}^{(x)} W_{ab}^{(2)}[I]$$
$$+ 2\sum_{i}^{act.}\sum_{g}^{core} B_{gi}^x P_{gi}^{(2)} + \sum_{i}^{act.}\sum_{g}^{core} S_{ig}^{(x)} W_{ig}^{(2)}[I] - \sum_{a}^{virt.}\sum_{k}^{occ.} S_{ak}^{(x)} W_{ak}^{(2)}[I]$$
$$+ \sum_{c}^{virt.}\sum_{k}^{occ.} U_{ck}^x \left[\sum_{ij}^{occ.} P_{ij}^{(2)} A_{ijck} + \sum_{ab}^{virt.} P_{ab}^{(2)} A_{abck} - 4\sum_{ij}^{act.}\sum_{b}^{virt.} T_{ij}^{cb}(ik|jb) \right.$$
$$\left. + 4N_k \sum_{j}^{act.}\sum_{ab}^{virt.} T_{kj}^{ab}(ca|jb) \right] + 2\sum_{ij}^{act.}\sum_{ab}^{virt.} (ia|jb)^{(x)} T_{ij}^{ab}, \tag{56}$$

where

$$N_k \equiv \begin{cases} 1, & \text{for } k = active \\ 0, & \text{for } k = core \end{cases}.$$

The terms in the square brackets in equation (56), then, define the MP2 Lagrangian (see equation (52)). Moving to steps (ii) and (iii), the following CPHF equations are solved to find the occupied-virtual blocks of the density (indices are re-labeled and signs are changed on both sides of equation (57)),

$$\sum_{b}^{virt.}\sum_{j}^{occ.}\left\{A_{aibj}+\delta_{ab}\delta_{ij}\left(\varepsilon_{b}-\varepsilon_{j}\right)\right\}P_{bj}^{(2)}=L_{ai},\tag{57}$$

where

$$L_{ai}=-\sum_{jk}^{occ.}P_{jk}^{(2)}A_{aijk}-\sum_{bc}^{virt.}P_{bc}^{(2)}A_{aibc}+4\sum_{jk}^{act.}\sum_{b}^{virt.}T_{kj}^{ab}(ij|kb)$$

$$-4N_{i}\sum_{j}^{act.}\sum_{bc}^{virt.}T_{ij}^{bc}(ab|jc),\tag{58}$$

where N_i is defined analogously to N_k in equation (56).

(g) Additional Energy-Weighted Density Terms.

In equations (54) and (56) the MP2 density correction terms $P_{pq}^{(2)}$ are multiplied by B_{pq}^{x} (defined in equation (9)) giving rise to additional energy-weighted density terms which are labeled $[II]$ and $[III]$ (see section h)). Making the appropriate substitutions for B_{pq}^{x} according to equation (9), the MP2 frozen-core gradient expression is now,

$$E^{(2)^{x}}=\sum_{ij}^{occ.}P_{ij}^{(2)}\left[F_{ij}^{(x)}-S_{ij}^{(x)}\varepsilon_{i}-\sum_{kl}^{occ.}S_{kl}^{(x)}\left[2(ij|kl)-(ik|jl)\right]\right]$$

$$+\sum_{i}^{occ.}\sum_{a}^{virt.}P_{ai}^{(2)}\left[F_{ai}^{(x)}-S_{ai}^{(x)}\varepsilon_{i}-\sum_{kl}^{occ.}S_{kl}^{(x)}\left[2(ai|kl)-(ak|il)\right]\right]$$

$$+\sum_{ab}^{virt.}P_{ab}^{(2)}\left[F_{ab}^{(x)}-S_{ab}^{(x)}\varepsilon_{a}-\sum_{kl}^{occ.}S_{kl}^{(x)}\left[2(ab|kl)-(ak|bl)\right]\right]$$

$$+\sum_{ij}^{act.}S_{ij}^{(x)}W_{ij}^{(2)}[I]+\sum_{ab}^{virt.}S_{ab}^{(x)}W_{ab}^{(2)}[I]+\sum_{i}^{act.}\sum_{g}^{core}S_{ig}^{(x)}W_{ig}^{(2)}[I]-\sum_{a}^{virt.}\sum_{k}^{occ.}S_{ak}^{(x)}W_{ak}^{(2)}[I]$$

$$+2\sum_{ij}^{act.}\sum_{ab}^{virt.}(ia|jb)^{(x)}T_{ij}^{ab}.\tag{59}$$

(h) Summary of the One-Particle Gradient. Before addressing the two-particle gradient we summarize the frozen-core MP2 one-particle gradient and its terms.

MP2 density correction terms.

gf = core-core $\qquad P_{gf}^{(2)} = 0$ $\qquad\qquad\qquad\qquad\qquad\qquad$ (60)

gi = core-act. $\qquad P_{gi}^{(2)} = P_{ig}^{(2)} = \dfrac{2}{\left(\varepsilon_i - \varepsilon_g\right)} \sum_j^{act.} \sum_{ab}^{virt.} T_{ij}^{ab}\left(ga|jb\right)$ $\qquad$ (61)

ij = act.-act. $\qquad P_{ij}^{(2)} = -2 \sum_k^{act.} \sum_{ab}^{virt.} T_{ik}^{ab}\left(ka|jb\right)/D_{kj}^{ab}$ $\qquad\quad$ (62)

ab = virt.-virt. $\qquad P_{ab}^{(2)} = 2 \sum_{jk}^{act.} \sum_c^{virt.} T_{jk}^{ab}\left(jb|kc\right)/D_{jk}^{bc}$ $\qquad\quad$ (63)

ai = virt.-core $\qquad P_{ai}^{(2)} = Z_{ai}$ $\qquad\qquad\qquad\qquad\qquad\qquad$ (64)

MP2 energy-weighted density correction terms.

$[I]$ terms:

ij = act.-occ. $\qquad W_{ij}^{(2)}[I] = -2 \sum_k^{act.} \sum_{ab}^{virt.} T_{ik}^{ab}\left(ja|kb\right)$ $\qquad\quad$ (65)

ab = virt.-virt. $\qquad W_{ab}^{(2)}[I] = -2 \sum_{ij}^{act.} \sum_c^{virt.} T_{ij}^{ac}\left(ib|jc\right)$ $\qquad\quad$ (66)

ai = virt.-occ. $\qquad W_{ai}^{(2)}[I] = -4 \sum_{jk}^{act.} \sum_b^{virt.} T_{jk}^{ab}\left(ik|jb\right)$ $\qquad\quad$ (67)

$[II]$ terms:

ij = act.-occ. $\qquad W_{ij}^{(2)}[II] = -\dfrac{1}{2} P_{ij}^{(2)}\left(\varepsilon_i + \varepsilon_j\right)$ $\qquad\qquad$ (68)

ab = virt.-virt. $\qquad W_{ab}^{(2)}[II] = -\dfrac{1}{2} P_{ab}^{(2)}\left(\varepsilon_a + \varepsilon_b\right)$ $\qquad\qquad$ (69)

ai = virt.-occ. $\qquad W_{ai}^{(2)}[II] = -P_{ai}^{(2)}\varepsilon_i$ $\qquad\qquad\qquad\qquad$ (70)

$[III]$ terms:

ij = occ.-occ. $\qquad W_{ij}^{(2)}[III] = -\sum_{pq}^{all} P_{pq}^{(2)}\left[2\left(pq|ij\right) - \left(pi|qj\right)\right]$ $\qquad$ (71)

The total one-particle energy gradient is obtained by first back-transforming the complete MP2 density correction $P_{pq}^{(2)}$ and energy-weighted density correction $W_{pq}^{(2)}$ to the AO-basis. Note that contributions from equation (57) to $P_{pq}^{(2)}$ and contributions from equations (67) and (70) to $W_{pq}^{(2)}$ are for virtual-occupied only. Symmetrization of $P_{pq}^{(2)}$ and $W_{pq}^{(2)}$ is customary prior to the back transformation, and is necessary in the case of $P_{pq}^{(2)}$ to apply equation (71).

$$P_{\mu v}^{(2)} = \sum_{pq}^{all} C_{\mu p} C_{vq} P_{pq}^{(2)}, \tag{72}$$

$$W_{\mu v}^{(2)} = \sum_{pq}^{all} C_{\mu p} C_{vq} W_{pq}^{(2)}, \tag{73}$$

These second order corrections are added to the corresponding SCF densities.

$$P_{\mu v}^{MP2} = P_{\mu v}^{SCF} + P_{\mu v}^{(2)}, \tag{74}$$

$$W_{\mu v}^{MP2} = 2 W_{\mu v}^{SCF} + W_{\mu v}^{(2)}, \tag{75}$$

where

$$P_{\mu v}^{SCF} = 2 \sum_{k}^{occ.} C_{\mu k} C_{vk}, \tag{76}$$

$$W_{\mu v}^{SCF} = \sum_{k}^{occ.} C_{\mu k} C_{vk} \varepsilon_k, \tag{77}$$

and the final MP2 densities $P_{\mu v}^{MP2}$ and $W_{\mu v}^{MP2}$ are contracted with the one-electron Hamiltonian derivatives $H_{\mu v}^{(x)}$ and overlap derivatives $S_{\mu v}^{(x)}$, respectively.

(i) Frozen-Core MP2 Two-Particle Gradient.

The 1st, 2nd, 3rd, and 8th terms of equation (59) contain ERI AO derivatives. The 8th term yields the so-called "non-separable" two-particle density,

$$2\sum_{ij}^{act.}\sum_{ab}^{virt.}T_{ij}^{ab}\sum_{\mu\nu\lambda\sigma}^{AO}C_{\mu i}C_{\nu a}C_{\lambda j}C_{\sigma b}(\mu\nu|\lambda\sigma)^{(x)}$$

$$=\sum_{\mu\nu\lambda\sigma}^{AO}(\mu\nu|\lambda\sigma)^{(x)}\left\{2\sum_{ij}^{act.}\sum_{ab}^{virt.}C_{\mu i}C_{\nu a}C_{\lambda j}C_{\sigma b}T_{ij}^{ab}\right\}. \qquad (78)$$

which corresponds to a back-transformation of the MP2 amplitudes.

Assuming a symmetrized $\mathbf{P}^{(2)}$ the first three terms (in equation (59)) yield the so-called "separable" two-particle density. Substituting for $F_{pq}^{(x)}$ in these terms according to equation (10) gives:

$$\sum_{pq}^{all}P_{pq}^{(2)}F_{pq}^{(x)}=\sum_{pq}^{all}P_{pq}^{(2)}\left[H_{pq}^{(x)}+\sum_{k}^{occ.}\left\{2(pq|kk)^{(x)}-(pk|qk)^{(x)}\right\}\right]. \qquad (79)$$

The core-Hamiltonian term has been dealt with; the two-electron part may be written as follows:

$$\sum_{pq}^{all}P_{pq}^{(2)}\sum_{k}^{occ.}\left\{\sum_{\mu\nu\lambda\sigma}^{AO}(2C_{\mu p}C_{\nu q}C_{\lambda k}C_{\sigma k}-C_{\mu p}C_{\nu k}C_{\lambda q}C_{\sigma k})(\mu\nu|\lambda\sigma)^{(x)}\right\} \qquad (80)$$

$$=\sum_{\mu\nu\lambda\sigma}^{AO}(\mu\nu|\lambda\sigma)^{(x)}\left\{\sum_{pq}^{all}P_{pq}^{(2)}\sum_{k}^{occ.}(2C_{\mu p}C_{\nu q}C_{\lambda k}C_{\sigma k}-C_{\mu p}C_{\lambda q}C_{\nu k}C_{\sigma k})\right\} \qquad (81)$$

$$=\sum_{\mu\nu\lambda\sigma}^{AO}(\mu\nu|\lambda\sigma)^{(x)}\left\{2\left(\sum_{pq}^{all}C_{\mu p}C_{\nu q}P_{pq}^{(2)}\right)\left(\sum_{k}^{occ.}C_{\lambda k}C_{\sigma k}\right)-\left(\sum_{pq}^{all}C_{\mu p}C_{\lambda q}P_{pq}^{(2)}\right)\right.$$
$$\left.\left(\sum_{k}^{occ.}C_{\nu k}C_{\sigma k}\right)\right\}. \qquad (82)$$

$$=\sum_{\mu\nu\lambda\sigma}^{AO}(\mu\nu|\lambda\sigma)^{(x)}\left\{P_{\mu\nu}^{(2)}P_{\lambda\sigma}^{SCF}-\frac{1}{2}P_{\mu\lambda}^{(2)}P_{\nu\sigma}^{SCF}\right\} \qquad (83)$$

In summary, the two-particle density consists of a separable term and a non-separable term.

$$\Gamma^{(2)}_{\mu\nu\lambda\sigma} = \Gamma^S_{\mu\nu\lambda\sigma} + \Gamma^{NS}_{\mu\nu\lambda\sigma},\tag{84}$$

where,

$$\Gamma^S_{\mu\nu\lambda\sigma} = P^{(2)}_{\mu\nu} P^{SCF}_{\lambda\sigma} - \frac{1}{2} P^{(2)}_{\mu\lambda} P^{SCF}_{\nu\sigma}\tag{85}$$

$$\Gamma^{NS}_{\mu\nu\lambda\sigma} = 2\sum_{ij}^{act.} \sum_{ab}^{vir.} C_{\mu i} C_{\nu a} C_{\lambda j} C_{\sigma b} T^{ab}_{ij}.\tag{86}$$

In practice equation (84) must be symmetrized according to the ERI permutational symmetries being exploited in the particular algorithm.

The total frozen-core two-particle gradient is evaluated by adding the SCF two-particle density,

$$\Gamma^{MP2}_{\mu\nu\lambda\sigma} = \Gamma^{(2)}_{\mu\nu\lambda\sigma} + \Gamma^{SCF}_{\mu\nu\lambda\sigma},\tag{87}$$

and then contracting with the two-electron AO derivatives.

We now have all the terms necessary for the evaluation of the closed shell frozen core MP2 gradient (equation (27)).

III. Reduction in Computational Effort

Having identified the summation ranges we now examine the reduction in computational effort required for the frozen-core MP2 gradient computation compared to that required in the full MP2 gradient computation.

(a) **Time Savings in the Two-Electron Transformation.** Inspection of the last two terms in the MP2 Lagrangian (equation (57)), the occupied-occupied blocks of the MP2

density correction (equations (61), (62), and (63)), and all the MP2 energy-weighted density correction [I] terms (equations (65), (66), and (67)), reveals that their formation requires a subset of the transformed integrals required for the corresponding full MP2 terms.

$$\left(\mu\nu|\lambda\sigma\right) \rightarrow \left(jp|qr\right) \qquad \text{full MP2}: j = occ., p = all, q = all, r = all$$

$$\text{frozen core MP2}: j = act, p = act. + virt, q = all, r = all.$$

The above transformation may be carried out by first performing a one-index transformation producing integrals of the type $\left(j\nu|\lambda\sigma\right)$, with the remaining indices transformed step-wise to produce the full set.[10]

If $\lambda\sigma$ is treated as a combined index, the memory required to hold all $\left(j\nu|\lambda\sigma\right)$ integrals is $N^2(N+1)n/2$, where N is the number of basis functions, and n is the number of active orbitals (for full MP2, n is all occupied orbitals). The reduction in memory requirements on going from full MP2 to frozen-core MP2, then, is $N^2(N+1)C/2$ where C is the number of frozen cores. Usually, even with such a reduction, an inadequate amount of memory is available and the transformation is carried out in batches. So, more important than the memory reduction just described is the time savings which are a consequence of a reduction of the number of batches on going from full MP2 to frozen-core MP2.

As many active orbitals j as are allowed by the available memory are transformed at a time. The minimum memory requirement is then $N^2(N+1)/2$ for one orbital to be transformed per batch (this is the same for the full and frozen-core cases). This requires n batches for the full transformation. Clearly, then, by reducing n from all occupied orbitals in the full MP2 to only active occupied orbitals in the frozen-core MP2, the number of batches required is reduced (by C in the minimum memory case) which can result in substantial time savings (see Section V).

(b) Time Savings in the Two-Particle Gradient. The non-separable term of the two-particle gradient (equation (78)) corresponds to a back-transformation of the MP2 amplitudes. As in the two-electron transformation described above, this back-transformation usually requires a batched scheme. As the occupied summation in equation (78) is only over active occupied orbitals the frozen-core scheme again results in fewer batches and therefore substantial time savings.

(c) Terms that Must be Determined in the AO Basis. Inspection of the CPHF equations (equation (57)), the 1st term in the MP2 Lagrangian (equation (58), and the energy-weighted density $[III]$ correction term (equation (71), reveals that MO integrals of the type.

$$(jp|qr) \quad \text{where } j = occ., p = all, q = all, r = all.$$

are required in the frozen-core MP2 as well as the full MP2. If one wishes to take advantage of the savings in computational effort discussed above these terms must be evaluated in the AO basis.

Both Frisch et al[2] and Dupuis[11] have described the formation of the first two terms of the MP2 Lagrangian (equation (58)) in the AO basis. It is done by forming a Fock-like matrix,

$$L_{\mu\nu}^{1,2} = \sum_{\lambda\sigma}^{AO} D_{\lambda\sigma}\left\{2(\mu\nu|\lambda\sigma) - (\mu\lambda|\nu\sigma)\right\} \tag{88}$$

where

$$D_{\lambda\sigma} = -\sum_{jk}^{AO} C_{\lambda j} C_{\sigma k} P_{jk}^{(2)} - \sum_{bc}^{AO} C_{\lambda b} C_{\sigma c} P_{bc}^{(2)}. \tag{89}$$

Frisch et al[2] also describe how to solve the CPHF equations in the AO basis. Equation (57) is re-written as:

$$\sum_b^{virt.} \sum_j^{occ.} A_{aibj} P_{bj}^{(2)} + (\varepsilon_a - \varepsilon_i) P_{ai}^{(2)} = L_{ai}, \qquad (90)$$

and the first term is evaluated with a trial $P_{bj}^{(2)}$ again by forming a Fock-like matrix. The resulting $P_{ai}^{(2)}$ is used as the next trial $P_{bj}^{(2)}$, and the process is repeated until self-consistency. Once the solution is obtained and $P_{pq}^{(2)}$ is completed, the energy-weighted density $[III]$ term (equation (71)) may be formed in the AO basis, again by formation of a Fock-like matrix.

IV. Timings

The molecule silicocene (see Figure 1) was chosen as a test case to demonstrate the reduction in computational effort due to the frozen-core approximation. A 6-31G(d) basis set was employed giving rise to 189 basis functions. Two calculations were carried out: one full MP2 single-point gradient, and one frozen-core MP2 single-point gradient. The number of core orbitals in silicocene is 15; the number of valence orbitals is 27. Therefore, full MP2 calculation involves 42 active occupied orbitals, and the frozen-core MP2 calculation involves 27 active occupied orbitals. The minimum amount of memory required for these calculations is ~ 4 Mwords; 5Mwords were available, therefore only one occupied orbital could be transformed per batch.

Table 1 shows the timings for the two calculations. The transformation steps in which the number of batches required is reduced from 42 in the full MP2 to 27 in the frozen-core MP2 are clearly the origin of the overall speed up by a factor of 1.5.

V. Conclusions

In order to implement the frozen-core MP2 gradient into GAMESS it was necessary to derive the expression from scratch, as no details of summation ranges and other modifications resulting from the approximation are available in the literature. We have presented the derivation here in detail.

Having determined the appropriate expressions and their summation ranges, we have examined the reduction in computational effort resulting from the frozen-core approximation. The main reduction is that in time due to the decrease in the number of batches required in transformation steps. Test calculations on silicocene show that this time reduction can be considerable, especially when the memory available is close to the minimum required.

References

1. Pople, J. A.; Krishnan, R.; Schlegel, H. B.; Binkley, J. S. *Int. J. Quant. Chem.* **1979.** 13. 225.

2. (a) Frisch, M. J.; Head-Gordon, M.; Pople, J. A. *Chem. Phys. Lett.*, **1990,** 166. 275. (b) Frisch, M. J.; Head-Gordon, M.; Pople, J. A. *Chem. Phys. Lett.*, **1990,** 166. 281.

3. Fletcher, G. D.; Rendell, A. P.; Sherwood, P. *Mol. Phys.* **1997,** 91. 431.

4. Nielsen, I. M. B. *Chem. Phys. Lett.*, **1996,** 255, 210.

5. Handy, N. C.; Amos, R. D.; Gaw, J. F.; Rice, J. E.; Simandiras, E. D. *Chem Phys. Lett.* **1985,** 120. 151.

6. Schmidt, M.W.; Baldridge, K.K.; Boatz, J.A.; Jensen, J.H.; koseki, S.; Matsunaga. N.; Gordon, M.S.; Ngugen, K.A. ; Su, S.; Windus, T.L.; Elbert. S.T.; Montgomery. J.; Dupuis, M. *J. Comp. Chem.* **1993,** 14, 1347.

7. Yamaguchi, Y.; Osamura, O.; Goddard, J. D.; Schaefer III, H. F. in *A New Dimension to Quantum Mechanics, Analytic Derivative Methods in Ab Initio Molecular Electronic Structure Theory,* Oxford University Press, 1994.

8. Salter, E. A.; Trucks, G. W.; Fitzgerald, G.; Bartlett, R. J. *Chem. Phys. Lett.* **1987.** 141. 61.

9. Handy, N. C.; Schaefer, H. F. (III) *J. Chem. Phys.* **1984,** 81. 5031.

10. (a) Gordon, M. S. *Chem. Phys. Lett.* **1976,** 44, 507. (b) Del Bene, J. E.; Ditchfield, R.; Pople, J. A. *J. Chem. Phys.* **1971,** 55, 2236.

11. Dupuis, M.; Chin, S.; Marquez, A. in *Relativistic and Electron Correlation Effects in Molecules and Solids,* G. L. Mali editor, Plenum Press, New York. 1994, p315.

Table 1. The total and a breakdown of CPU time in seconds for the full and frozen-core MP2 single-point gradient calculations on silicocene (Si(C₅H₅)₂). The basis set is 6-31G(d), resulting in 189 basis functions. All calculations were carried out on an IBM RS6000/350.

| Step in Algortithm | CPU Time / s | | Speed up |
	Full MP2 Gradient	Frozen-core MP2 Gradient	
2-Electron Transformation[a] + MP2 Energy	6673.9	3993.6	1.67
CPHF	473.1	440.0	1.08
2-Electron Gradient[a]	12595.5	8650.9	1.46
Total	19742.5	13084.5	1.51

[a] step includes batched tranformation with 42 batches required for the full MP2 case and 27 required for the frozen-core case.
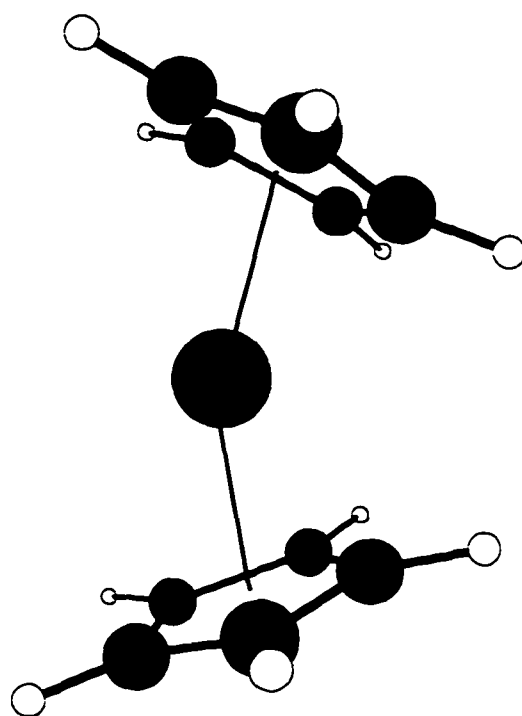
Silicocene $Si(C_5H_5)_2$

Figure 1. The C_{2v} isomer of silicocene.

CHAPTER 3. THE DIMERIZATION OF TiH₄

Simon P. Webb and Mark S. Gordon

Abstract

Ab initio electronic structure calculations using a triple zeta plus polarization basis set, second order perturbation theory, and coupled cluster theory show the dimerization of TiH₄ to be kinetically and thermodynamically very favorable. Six minima have been found on the potential energy surface of Ti₂H₈: two with double hydrogen bridges and four with triple hydrogen bridges. This potential energy surface is very flat suggesting rapid inter-conversion between these isomers is possible. The large thermodynamic driving force for dimerization (up to -46.1 kcal/mol on the classical surface) is attributed to both electrostatic effects and the electron deficiency of titanium.

I. Introduction

During recent years there has been a significant increase in the number of experimental studies of transition metal hydrides.This is indicative of increasingly sophisticated techniques such as low temperature matrix isolation,[1] which facilitate study of these often highly unstable

but important compounds. Theory has a vital role to play both in interpretation of experiment and as a predictive tool; however, adequate *ab initio* calculations on transition metal hydrides have proved challenging. It seems then, that careful systematic theoretical investigation of the simplest transition metal hydrides is necessary as a foundation for work on more complex systems.

This work is highly desirable in view of the fact that molecular species containing Ti-H bonds are rich with exciting chemistry but are often not well characterized or understood.[2] Their role as catalysts in reactions such as hydrosilation,[3] and polymerization of olefins[4] is of particular interest. The ability of some of these compounds to reduce molecular nitrogen has been demonstrated;[4b,5] obviously, successful modification of these species to facilitate a catalytic role in this reaction would be of tremendous importance, but difficult without a solid understanding of basic titanium hydride chemistry.

There have been a number of theoretical studies on TiH_2,[6] and on the titane molecule TiH_4.[7] These studies of simple titanium hydrides have yielded fundamental and pertinent information on the nature of Ti-H bonding. Only two experimental studies of TiH_4 have been found in the literature: the formation of TiH_4 from the decomposition of a $TiCl_4$-H_2 mixture at low pressures in 1963 by Breisacher and Siegel,[8] and a low temperature matrix study of the reaction between naked Ti atoms and H_2.[9] In the latter, the reaction products have been characterized by infrared spectroscopy. The spectra are complex with broad features making interpretation difficult.

A number of titanium hydrides are known to exist as dimers with bridging hydrogens.[2,10] Titanium is also known to form hydrogen bridging bonds with other elements,[2,11] for example in $(\eta 5$ -$C_5H_5)_2TiBH_4$ titanium is bonded to boron through a double hydrogen bridge. A thorough understanding of the simplest titanium hydride dimers will be

useful when considering the many transition metal species containing similar three center. two electron bonding arrangements.

Titanium has valence electron configuration $4s^23d^2$ compared to $2s^22p^2$ and $3s^23p^2$ of its highly studied group IVA analogs carbon and silicon. A recent study[12] has explored the impact of the differences between the s^2d^2 and s^2p^2 electronic configurations of these elements on the structures they form. In this paper we continue this exploration. It is well known that the saturated molecules CH_4 and SiH_4 show no propensity to dimerize: however, this is not the case for TiH_4. We report here results of a detailed *ab initio* analysis of the potential energy surface of the isomers of Ti_2H_8 which show that the dimerization of TiH_4 is thermodynamically and kinetically very favorable. Calculated infrared frequencies are also reported for comparison with experiment.[9]

II. Computational Methods

Preliminary calculations were performed on TiH_4 and Ti_2H_8 using multi-configurational SCF (MCSCF) wave functions and Huzinaga's 21 split valence basis set.[13] For TiH_4 an 8 electron, 8 orbital active space was used for geometry optimization. This includes all valence electrons and allows all Ti-H bonds to be correlated. A natural orbital analysis shows that the maximum occupation of any virtual orbital is 0.07 electrons, with a total of only 3.1% of the 8 valence electrons outside the closed shell configuration. For Ti_2H_8 a full valence 16 electron, 16 orbital MCSCF active space is beyond our capabilities; however, a smaller well chosen active space was thought sufficient to establish the nature of the wavefunction. Therefore, we elected to carry out a single point singles and doubles configuration interaction (CI) calculation at the RHF geometry using the 16 valence electrons (8 RHF orbitals) as a reference, with

excitation into all virtual orbitals. A natural orbital analysis of this CI wavefunction was then used to choose the 12 'most active' natural orbitals. These were then used as a starting point for a 12 electron, 12 orbital MCSCF calculation. A natural orbital analysis of the resulting MCSCF wavefunction revealed the largest occupation of the virtual orbitals to be 0.12 and 0.11; again only 3.1% of the active space electrons are outside the closed shell configuration. It is therefore concluded that the single determinant Hartree-Fock self consistent field (SCF) wavefunction is an adequate reference for the system under investigation.

Then for titanium a triple zeta with polarization (14s11p6d/10s8p3d) basis was employed which consists of Wachter's basis set[14] with two additional p functions[15] and a diffuse d function.[16] For hydrogen, Dunning's basis set[17] (5s1p/3s1p) was used. Collectively this basis set for titanium and hydrogen will be referred to as TZVP. For final single point energies one set of f functions (α_f=0.4)[18] was added to the titanium basis. This basis set will be referred to as TZVP(f).

Geometry optimizations were carried out at the RHF and second order perturbation theory (MP2)[19] levels. Stationary points were characterized as minima or transition states by calculating and diagonalizing the matrix of the energy second derivatives (hessian). Single point energies were calculated at the coupled cluster (CCSD(T))[20] level of theory, with final CCSD(T) calculations employing the TZVP(f) basis set. All RHF and MCSCF calculations were done using GAMESS;[21] the MP2, and CCSD(T) calculations using GAUSSIAN 92.[22]

III. Results and Discussion

TiH₄. Both RHF and MP2 predict TiH$_4$ to be tetrahedral, with a Ti-H bond length of 1.70 Å (Figure 1). These are in good agreement with the results of Schaefer and Thomas.[7] The total energies (given in Table 1) and bond lengths of TiH$_4$ will be used as a baseline against which Ti$_2$H$_8$ isomers can be compared.

Ti₂H₈. The geometries for the double hydrogen bridged (μ-H)$_2$ and triple hydrogen bridged (μ-H)$_3$ minima on the Ti$_2$H$_8$ potential energy surface are shown in Figure 2. Attempts were made to find (μ-H)$_4$ bridged structures; however, no such structures were found. Before considering the (μ-H)$_2$ and (μ-H)$_3$ bridged structures explicitly, we discuss the pathways leading from TiH$_4$ + TiH$_4$ → Ti$_2$H$_8$.

(a) Constrained Optimizations. Continuous 'downhill' paths to dimerization were found via a series of constrained geometry optimizations at the RHF/TZVP level, followed by MP2/TZVP single point energy calculations. These constrained optimizations were carried out by starting from the RHF/TZVP optimized minima of interest, increasing the Ti-Ti separation in small intervals, and at each interval keeping this Ti-Ti separation fixed while minimizing the energy with respect to all other bond lengths and angles.

Plots of the MP2/TZVP single point energies versus the Ti-Ti separation which correspond to dissociating the dimers C$_s$(1) (Figure 2c) and C$_s$(4) (Figure 2f), can be seen in Figure 4a and Figure 4b respectively. The reverse of this separation process is a path to dimerization. Structures along these dimerization paths can be seen in Figures 5a and 5b. In Figure 5a the two TiH$_4$ fragments approach each other in a staggered conformation. A

hydrogen on one TiH_4 (which has a partial negative charge) points directly at the titanium on the other TiH_4 (which has a partial positive charge) and so an attractive interaction occurs. It can be seen from Figure 4a that this initial interaction and the subsequent formation of a second bridging bond continuously lowers the energy until a $(\mu\text{-H})_2$ minimum is reached at Ti-Ti ~3.10 Å. A small barrier to formation of the lower energy $(\mu\text{-H})_3$ structure is then encountered. The situation in Figure 5b is somewhat different. Here the two TiH_4 fragments approach each other in an eclipsed conformation. Again the initial interaction is between a hydrogen from one TiH_4 and the titanium from the other TiH_4. Then two other hydrogens form bridging bonds simultaneously and a $(\mu\text{-H})_3$ structure is formed directly. Figure 4b shows this process lowers the energy continuously.

It is important to note that although these paths to dimerization are probably not the only ones and may not be the lowest energy paths, as the geometries are not optimized at a correlated level of theory, they do establish the fact that dimerization can occur with no barrier.

(b) Minima and Transition States. MP2/TZVP bond lengths and angles are shown in Figure 2 for all minima and Figure 3 for all transition states. Energies are given in Table 2.

Two $(\mu\text{-H})_2$ isomers were discovered: a C_{2v} structure with eclipsed terminal hydrogens (Figure 2a) and a C_{2h} structure with staggered terminal hydrogens (Figure 2b). The Ti-H bond length for the terminal hydrogens in these structures is very similar to that found in the monomeric TiH_4; however, for the bridging hydrogens the Ti-H distance is lengthened considerably (0.15 Å). This is consistent with the findings for other cases of 3 center, 2 electron bonding such as the prototypical B_2H_6.[23a] The two isomers are essentially isoenergetic (Table 2). This may be explained by the large separation of terminal hydrogens on

one titanium center from those on the other, thus avoiding the hydrogen-hydrogen interactions which affect the relative stabilities of (for example) staggered and eclipsed ethane. Interconversion of these (μ-H)$_2$ isomers proceeds via the transition state T.S.(1) (Figure 3a) with effectively no barrier (see Table 2 and Figure 6) suggesting totally free rotation. The internal rotation in (μ-H)$_2$ Ti$_2$H$_8$ may be represented schematically as follows:

C_{2v} T.S.(1) C_{2h}
74.8 i cm^{-1}
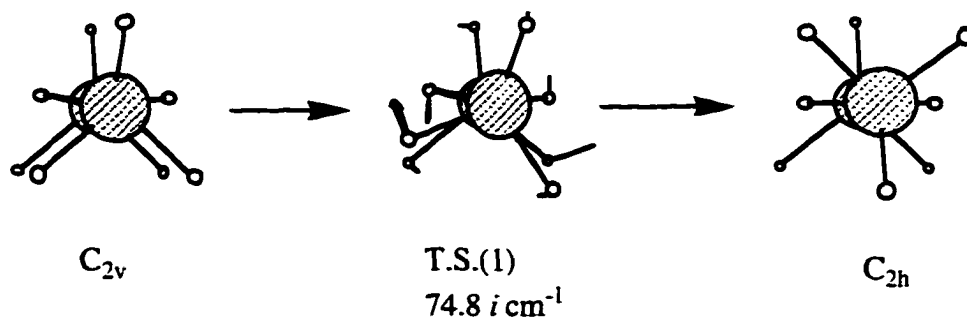
The absence of a barrier to rotation may be explained by the large distances between vicinal hydrogens and by the availability d orbitals which facilitate isoenergetic bonding for any rotational arrangement of the terminal hydrogens. Formation of both these dimers is exothermic relative to the separated monomers by ~37 kcal/mol on the classical potential energy surface (Table 2 and Figure 6a) and by ~34 kcal/mol on the adiabatic ground state surface (zero point vibrational energy included) (Table 2 and Figure 6b) at the CCSD(T)/TZVP(f) level of theory. It may be noted (as it has been previously[23a]) that dynamic electron correlation plays a vital role in the quantitative description of three center, two electron bonding. The dimerization energy of TiH$_4$ is ~14 kcal/mol more exothermic at all correlated levels of theory than at the RHF/TZVP level of theory.
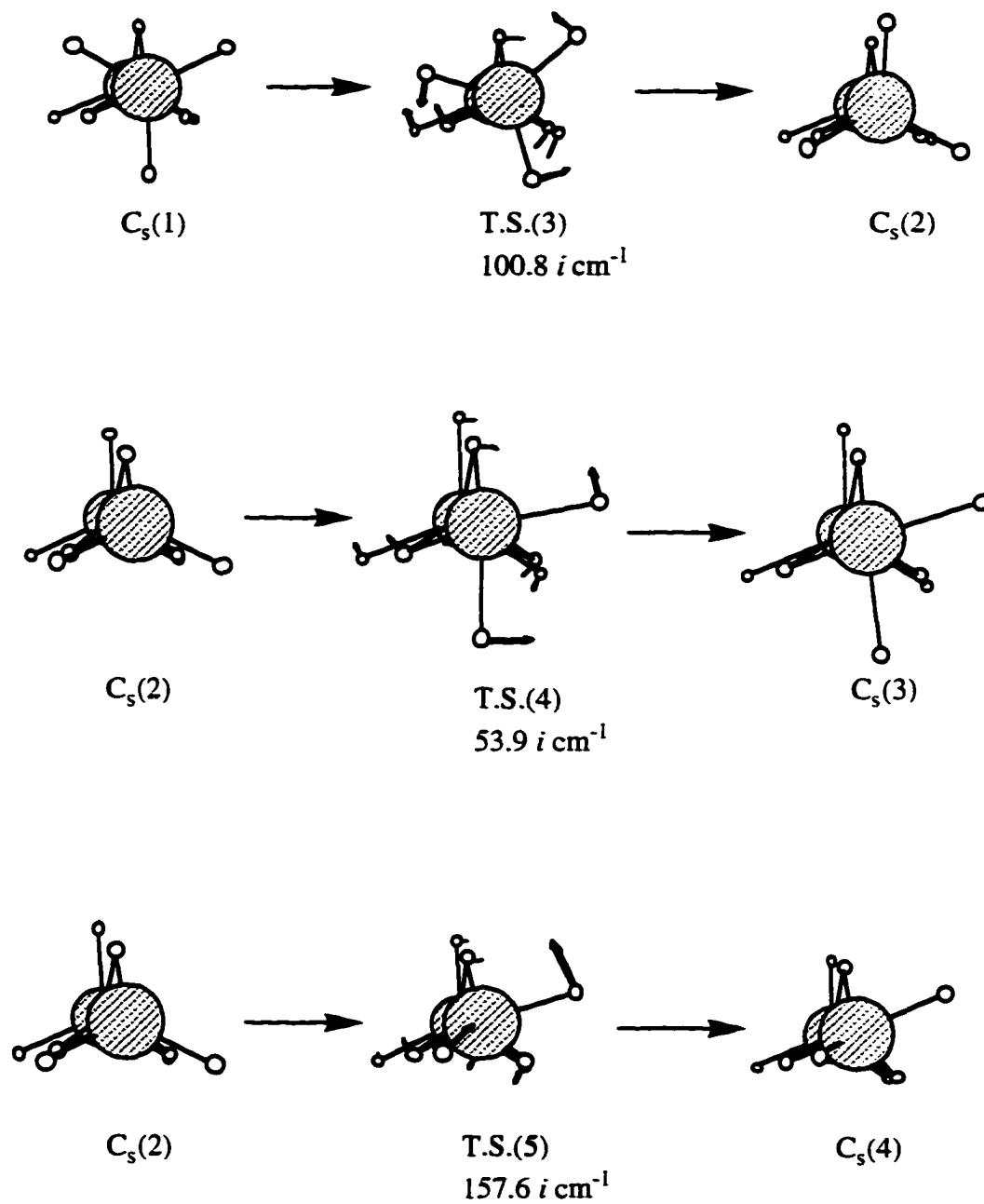
Four (μ-H)$_3$ isomers with C$_s$ symmetry were found: C$_s$(1), C$_s$(2), C$_s$(3), and C$_s$(4)

corresponding to Figures 2c, d, e, and f. These four C_s isomers differ primarily in the orientation of their terminal hydrogens. All four of these structures are several kcal/mol lower in energy than the $(\mu\text{-}H)_2$ isomers, with $C_s(2)$ appearing to be the global minimum. Transition state T.S.(2) (Figure 3b) connects the $(\mu\text{-}H)_2$ C_{2h} isomer (Figure 2b) with the $(\mu\text{-}H)_3$ $C_s(1)$ isomer (Figure 2c), as shown schematically below.

C_{2h} T.S.(2) $C_s(1)$

293.2 i cm^{-1}
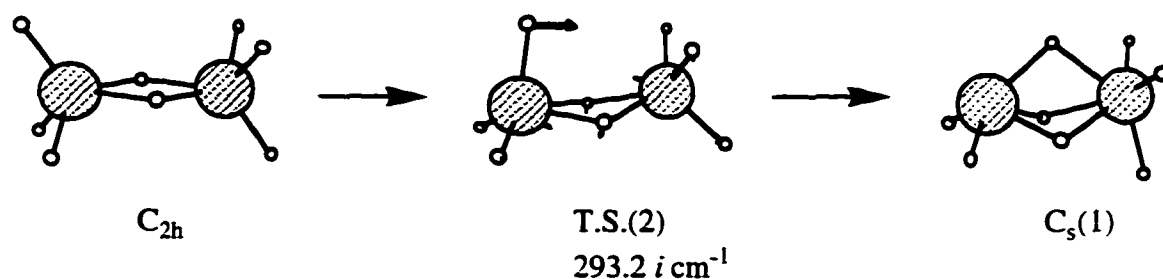
The energy barrier for this process (Table 2 and Figure 6) is 1.9 kcal/mol and 1.8 kcal/mol on the classical and adiabatic ground state potential energy surfaces, respectively. The reverse barriers are 8.3 kcal/mol and 6.0 kcal/mol for the classical and the adiabatic ground state surfaces, respectively.

The $(\mu\text{-}H)_3$ structures are local minima corresponding to different rotational orientations of their terminal hydrogens. It is evident from Figure 6 that the potential energy surface connecting these isomers is quite flat and rapid inter-conversion should be possible via transition states T.S.(3), T.S.(4), and T.S.(5) (Figures 3c, d, and e), as shown below for the MP2 surface.

C_s(1)   T.S.(3)   C_s(2)

$100.8\,i\,\mathrm{cm}^{-1}$

C_s(2)   T.S.(4)   C_s(3)

$53.9\,i\,\mathrm{cm}^{-1}$

C_s(2)   T.S.(5)   C_s(4)

$157.6\,i\,\mathrm{cm}^{-1}$

Again, this flat surface is indicative of the ability of d orbitals to form bonds with similar energy for a range of terminal hydrogen positions.

Figure 6 shows that the $(\mu\text{-}H)_3$ isomers are even more stable relative to the separated

monomers than their $(\mu\text{-H})_2$ counterparts, $C_s(2)$ (the global minimum) being 46.1 kcal/mol more stable than $2TiH_4$ on the classical surface at the CCSD(T)/TZVP(f) level of theory. This can be attributed to the extra stabilizing effect of the third bridging bond, and titanium's desire for high coordination numbers. Dynamic correlation again plays an important role in describing the bridging bonds. At the RHF/TZVP level the $(\mu\text{-H})_3$ isomers are in fact *higher* in energy than the $(\mu\text{-H})_2$ isomers. This reversal in the relative stabilities of the $(\mu\text{-H})_2$ and $(\mu\text{-H})_3$ isomers is due to the effects of dynamic electron correlation. Even using MP2/TZVP single point energies at RHF/TZVP geometries, the $(\mu\text{-H})_3$ $C_s(1)$ isomer is 5.9 kcal/mol more stable than the $(\mu\text{-H})_2$ C_{2h} isomer. The $C_s(1)$ isomer is stabilized by a further 2.2 kcal/mol relative to the C_{2h} isomer with the contraction of its three center bonds on MP2 geometry optimization.

Because the potential energy surface in the $(\mu\text{-H})_3$ region is so flat, single point energy calculations at higher levels of theory and incorporation of vibrational zero point corrections reverses the order of several stationary points. Indeed, at the CCSD(T)/TZVP(f) + ZPE level of theory, T.S.(3) drops 1 kcal/mol below $C_s(2)$. So, very high levels of theory and anharmonic vibrational effects are needed to obtain a highly accurate representation of the $(\mu\text{-H})_3$ bridging region of the surface. Nonetheless, it is clear that in general, the dimerization of $2TiH_4$ to Ti_2H_8 is highly exothermic.

(c) **Bonding in Ti_2H_8** . In order to gain some insight into the nature of the bonding in these Ti_2H_8 isomers, particularly the three center bonds, the RHF/TZVP molecular orbitals of two minima, C_{2h} (Figure 2b) and $C_s(1)$ (Figure 2c) at their MP2/TZVP geometries, were localized using the method of Edmiston and Ruedenberg.[24] In addition, Mulliken populations

and charges were calculated using the MP2 density to give some indication of the degree of polarity in the bonds.

None of the localized molecular orbitals for either of the two structures show any direct sigma titanium-titanium interaction; all LMO's are titanium-terminal hydrogen interactions. or three center, two electron Ti-H-Ti interactions. Figure 7a shows a localized molecular orbital corresponding to one of the three center, two electron bonds in the C_{2h} structure, and Figure 7b shows a plot of the total electron density in this isomer. The total density plot shows ample evidence of a H-Ti-H bridging bond even though, as noted above, the Ti-H distance is considerably longer than is seen in an ordinary bonding situation. Figure 8a shows the localized molecular orbital corresponding to the three center bond in the C_s plane in the structure $C_s(1)$. Plots of the total density can be seen in Figure 8b i) and ii). Three center, two electron bonding is clear here as well. There is some distortion of the three center bonds, due to the unequal numbers of terminal hydrogens on the two titanium centers. There is clearly more electron density between the bridging hydrogens and the titanium with only two terminal hydrogens (the titanium center on the left), producing a short bond/long bond arrangement in the bridges.

Calculated Mulliken charges for the C_{2h} (Figure 2b) and $C_s(1)$ (Figure 2c) isomers are shown in Table 3. Mulliken charges for diborane (B_2H_6) calculated with an equivalent basis set to that used for Ti_2H_8 are also shown for comparison. According to the Mulliken charges diborane has little ionic character (of course this is open to debate: Cioslowski and McKee[23b] use a Bader type analysis and conclude that B_2H_6 is "quite ionic"). The Ti_2H_8 isomers exhibit a higher degree of bond polarization (although the out-of-plane Ti-H-Ti interactions in $C_s(1)$ are much less polar than those for the other bridging bonds seen in Table 3), not surprising considering the difference in the electronegativities of titanium and hydrogen . One may recall that TiH_2 forms a lattice structure in the solid state[25] with a titanium coordination number of 8.

so it may be reasonable to think of Ti_2H_8 as a precursor which, if given the opportunity. would react with other titanium and hydrogen atoms (or indeed other titanium hydride molecules) to form extended polymeric structures.

(d) Calculated I.R. Frequencies. Vibrational frequencies were calculated at the MP2/TZVP level for all minima and transition states found. Those calculated for the C_{2h} (Figure 2b) and $C_s(2)$ (Figure 2d) isomers were chosen for comparison with experiment.

In Margrave's matrix isolation experiment[9] one may expect to observe co-existence of species which would not occur in an unhindered environment. We therefore expect that the presence of Ti_2H_8 dimers should not preclude the presence of TiH_4.

The experimental frequency assigned to a Ti-H stretch in TiH_4 is 1658 cm-1; the calculated Ti-H stretch frequency for TiH_4 is 1788 cm-1. The calculated Ti-H stretch frequency may be scaled to the experimental one by a factor of 0.93. This scaling factor is applied to all calculated frequencies to account for basis set deficiencies and higher order correlation effects.

Vibrational frequencies can be seen in Table 4. The scaled calculated frequencies can be compared to the experimental frequencies observed by Margrave.[9] Although definite assignments are difficult, there are a number of features of the spectra which are *highly consistent* with the presence of hydrogen bridged compounds. Firstly, there is a broad intense feature centered on 1490 cm-1 in the experimental spectrum. This coincides nearly exactly with the most intense calculated frequency (scaled) for the C_{2h} isomer (1487 cm-1). Furthermore a broad intense feature between 1300-1500 cm-1 is considered indicative of a bridge stretch in a double hydrogen bridged compound,[26] and the normal mode of the calculated frequency is in fact a bridge stretch (Figure 9a). Secondly, there is a smaller peak in the spectrum centered at 1140 cm-1 and a corresponding calculated frequency (scaled) at 1081 cm-1.There is a discrepancy here of ~ 60 cm-1 but Kaupp and Schleyer have noted that considerable differences

between calculations and matrix experiments for soft bending modes are expected due to interactions between guest and host molecules.[27] Features in this region are known to be indicative of a bridge deformation in three bridging hydrogen species,[26] and the calculated frequency does correspond to a bridging hydrogen bend in the $C_s(2)$ isomer (Figure 9b).

The most intense calculated frequency for the $C_s(2)$ isomer (at 1539 cm-1) may correspond to a feature seen at 1515 cm-1 in the spectrum (Margrave labels this peak Ti_xH_2), and the presence of a triplet centered at 1658 cm-1 may be explained by the slightly different environments encountered by different terminal hydrogens in the bridging compounds. This is supported by the scaled calculated Ti-H stretch frequencies at 1640, 1660, and 1664 cm-1.

Of course, even though the calculated frequencies are consistent with Margrave's spectrum, to establish the presence of dimers beyond doubt would require a matrix isolation experiment with annealing and monitoring of corresponding changes in peak intensity such as those Andrews and coworkers have performed on magnesium and beryllium hydrides.[28] This is necessary as although there is a large thermodynamic driving force and no barrier to dimerization low mobility in a matrix experiment may inhibit the process.

IV. Summary and Conclusions

TiH_4 is found to dimerize with no barrier and a large thermodynamic driving force (up to 46 kcal mol-1 on the classical potential energy surface) producing both doubly hydrogen bridged and triply hydrogen bridged Ti_2H_8 isomers. The potential energy surface of Ti_2H_8 is very flat suggesting continuous rapid inter-conversion between $(\mu\text{-}H)_2$ and $(\mu\text{-}H)_3$ isomers and also between rotational isomers. It is conceivable that interaction with host molecules in a

matrix isolation experiment could hinder this inter-conversion process.

Inclusion of dynamic electron correlation in calculations is essential to produce both reliable geometries and energetics. The effect of dynamic electron correlation is especially large for the $(\mu\text{-}H)_3$ isomers. Nonetheless, a crucial result is that all bridging structures are found to be quite stable relative to the separated monomers, *even at the Hartree-Fock level of theory*. This is very likely due to the fact that unlike CH_4 and SiH_4, TiH_4 cannot be thought of as a saturated molecule. Thus, the impact of the s^2d^2 electronic configuration of titanium versus the s^2p^2 electronic configuration of carbon and silicon has a spectacular effect on the structure and energetics of the titanium hydrides investigated in this study. The well known ability of titanium to accommodate more than four ligands is obviously essential to the formation of the Ti_2H_8 dimers. The electron deficiency of titanium in TiH_4, that is its desire to fill its available d orbitals is likely the main driving force in the dimerization of TiH_4. In this sense, titanium is a transition metal analog of the electron deficient main group element boron. A desire for higher titanium coordination numbers can also be seen in the energetic preference for triple bridged structures over double bridged structures.

The bonding in the Ti_2H_8 isomers appears to be polar in character with electrostatic attraction between positively charged titanium centers and negatively charged hydrogens. This suggests that the polarized $Ti^{\delta+} - H^{\delta-}$ bonds in TiH_4 have some role to play in the preference for the dimeric Ti_2H_8 species.

Calculated infrared frequencies are consistent with the spectra produced by a matrix isolation experiment on titanium hydrides done by Margrave et al. However, further experimental work is needed to establish without doubt the presence of dimers.

Although different terminal substituents such as chlorine and cyclopentadienyl may have some affect on the system, the large thermodynamic driving force for dimerization with bridging hydrogens seen in this study must have some role to play in systems such as the

titanocene dimer and (η5 -C_5H_5)$_2$TiBH$_4$ which contain bridging hydrogens and one or more titanium centers.

References

1.   Sweeny, R.L. in *Transition Metal Hydrides*, A. Dedieu, Ed. VCH Publishers Inc., 1992; pp 65-101.

2.   Toogood, G.E.; Wallbridge, M.G.H. *Adv. Inorg. Chem. Radiochem.* **1982**, 25, 267.

3.   Barton, T.J.; Boudjouk, P. "Organosilican Chemistry - A Brief Overview", Advances in Chemistry, J. Ziegler, Ed., American Chemical Society, Wash., DC, **1990**.

4.   (a) Pez, G.P. *J. Chem. Soc., Chem. Commun.* **1977**, 560; (b) Pez, G.P.; Kwan, S.C. *J. Am. Chem. Soc.* **1976**, 98, 8079.

5.   Bercaw, J.E.; Marvich, R.H.; Bell, L.G.; Brintzinger, H.H. *J. Am. Chem. Soc.* **1972**, 94, 1219.

6. (a) Kudo, T.; Gordon, M.S. *J. Chem. Phys.*, in press: (b) Demuynk. J.; Schaefer. H.F., *J. Chem. Phys.* **1980**, 72, 311; (c) Tyrrell, J.; Youakim, A. *J. Phys. Chem.* **1980**, 84, 3568; (d) Tyrrell, J.; Youakim, A.*J. Phys. Chem.* **1981** 85, 3614.

7. Thomas, J.R.; Quelch, G.E.; Seidl, E.T.; and Schaefer, H.F. *J. Chem. Phys.* **1992**, 96, 6857, and refs. therein.

8. Breisacher, A; Siegel, B. *J. Am. Chem. Soc.* **1963**, 85, 1705.

9. Xiao, Z.L.; Hauge, R.H.; and Margrave, J.L. *J. Phys. Chem.* **1991**, 95, 2696.

10. (a) Gauvin, F.; Britten, J.; Samuel, E.; and Harrod, J.F. *J. Am. Chem. Soc.* **1992**, 114, 1489. (b) Cristol, S.J.; Ziebarth, T.D.; Turro, N.J.; Stone, P.; and Scribe, P. *J. Am. Chem. Soc.* **1974**, 96, 3017; (c) Britzinger, H.H.; Bercaw, J.E. *J. Am. Chem. Soc.* **1970**, 92, 6182.

11. Marks, T.J.; Jolb, J.R. *Chemical Reviews,* **1977**, 77, 263.

12. Kudo, T.; Gordon, M.S. *J. Phys. Chem.* **1995**, 102, 6806.

13. Huzinaga, S.; Andzelm, J.; Klobukowski, M.; Radzio-Andzelm, E.; Sakai, Y.; Tatewaki, H.; in *Gaussian Basis Sets for Molecular Calculations*, Elsevier, Amsterdam. **1984**.

14. Watchters, A.J.H. *J. Chem. Phys.* **1970**, 52, 1033.

15. Hood, D.M.; Pitzer, R.M.; Schaefer, H.F. *J. Chem . Phys.* **1979**, 71, 705.

16. Rappe, A.K.; Smedley, T.A.; and Goddard, W.A. *J. Phys. Chem.* **1981**, 85, 2607.

17. Dunning, T.H.; Hay, P.J. in *Methods of Electronic Structure Theory*, H.F. Schaefer III, Ed. Plenum Press, N.Y. **1977**, pp 1-27.

18. This choice of exponent is based on energy optimizations for several small Ti-containing compounds and on discussions with Dr. Charles W. Bauschlicher, Jr.

19. (a) Binkley, J.S.; Pople, J.A. *Int. J. Quantum Chem.* **1975**, 9, 229; (b) Krishnan, R; Pople, J.A. *Int. J. Quantum Chem.* **1978**, 14, 91.

20. Pople. J.A.: Head-Gordon M.; and Raghavachari, K. *J. Chem. Phys.*. **1987**. 87. 5968.

21. Schmidt, M.W.; Baldridge, K.K.; Boatz, J.A.; Jenson, J.H.; Koseki, S.; Matsunaga. N.; Gordon, M.S.; Ngugen, K.A. ; Su, S.; Windus, T.L.; Elbert, S.T.; Montgomery. J.; Dupuis, M. *J. Comp. Chem.* **1993**, 14, 1347.

22. Frisch, M.J.; Trucks, G.W.; Head-Gordon, M.; Gill, P.M.W.; Wong, M.W.; Foresman, J.B.; Johnson, B.G.; Schlegel, H.B.; Robb, M.A.; Replogle. E.S.; Gomperts, R.; Andres, J.L.; Raghavachari, K.; Binkley, J.S.; Gonzalez, C.; Martin. R.L.; Fox, D.J.; DeFrees, D.J.; Baker, J.; Stewert, J.J.P.; Pople, J.A.; GAUSSIAN92; GAUSSIAN, INC.; Pittsburgh, PA **1992**.

23. (a) Shen, M.; Schaefer, H.F. *J. Chem. Phys.* **1992**, 96, 2868; (b) Cioslowski. J.; McKee, M.L. *J. Phys. Chem.* **1992**, 96, 9264.

24. Edmiston, C.; Ruedenberg, K. *Rev. Mod. Phys.* **1963**, 35, 457.

25. Greenwood, N.N.; Earnshaw, A. in *Chemsitry of the Elements*, Pergamon Press, pp 73.

26. Marks, T.J.; Jolb, J.R. *Chemical Reviews,* **1977**, 77, 272.

27. Kaupp, M.; Schleyer, P.R. *J. Am. Chem. Soc.* **1993**, 115, 11202.

28. (a) Tague, T.J.; Andrews, L. *J. Phys. Chem.* **1994**, 98, 8611; (b) Tague, T.J.; Andrews, L. *J. Am. Chem. Soc.* **1993**, 115, 12111.

Table 1. Calculated total energies in Hartrees of the titane molecule, and zero point vibrational energy correction at the MP2/TZVP level.

Point Group	TZVP				TZVP(f)	
	$RHF_{(opt)}$	$MP2_{(opt)}$	$CCSD(T)^a$	$Z.P.E._{(MP2)}$	$CCSD(T)^a$	$\Delta H_{(CCSD(T))}^b$
T_d	-850.59992	-850.73823	-850.77402	0.02212	-850.79274	-850.77062

[a] All single point energies calculated at the MP2/TZVP optimized geometry. [b] $\Delta H(CCSD(T))$ value is the single point CCSD(T)/TZVP(f) energy with zero point vibrational energy added.

Table 2. Calculated energies of Ti_2H_8 relative to $2TiH_4$ in kcal mol⁻¹, and zero point energy corrections at the MP2/TZVP level.

	TZVP				TZVP(f)	
	RHF(opt)	MP2(opt)	CCSD(T)[a]	Z.P.E. (MP2)	CCSD(T)[a]	ΔH(CCSD(T))[b]
Minima						
C_{2v}	-23.0	-37.1	-36.8	3.0	-37.2	-34.2
C_{2h}	-23.2	-37.4	-36.9	3.0	-37.4	-34.4
$C_s(1)$	-20.7	-45.5	-41.6	5.2	-43.8	-38.6
$C_s(2)$	-20.7	-46.9	-43.2	5.4	-46.1	-40.7
$C_s(3)$		-43.6	-38.9	5.2	-41.1	-35.9
$C_s(4)$		-43.9	-41.3	4.4	-43.2	-38.8
Transition States						
T.S.(1)		-37.1	-36.7	2.8	-37.2	-34.4
T.S.(2)		-35.5	-34.6	2.9	-35.5	-32.6
T.S.(3)		-45.5	-41.6	2.2	-43.9	-41.7
T.S.(4)		-43.6	-38.9	5.1	-41.2	-36.1
T.S.(5)		-43.9	-41.3	4.3	-43.2	-38.9

[a] All single-point energies calculated at the MP2/TZVP optimized geometry. [b] ΔH(CCSD(T)) values are the single point CCSD(T)/TZVP(f) energies with zero-point vibrational energies added.

Table 3. Mulliken charges calculated using the MP2 density. Comparable basis sets were used; TZVP(f) for Ti_2H_8 and TZVP(d) for B_2H_6.

| Ti_2H_8				B_2H_6	
C_{2h}		$C_s(1)$		D_{2h}	
Ti(1)	0.498	Ti(1)	0.308	B(1)	-0.150
H(3)	-0.143	Ti(2)	0.394	H(3)	0.105
H(5)	-0.111	H(3)	-0.107	H(5)	0.022
H(9)	-0.131	H(4)	-0.133		
		H(5)	-0.106		
		H(6)	-0.141		
		H(7)	0.016		
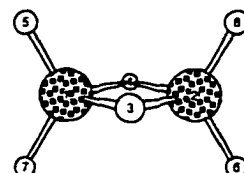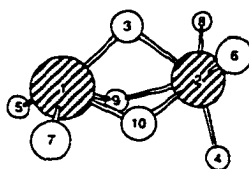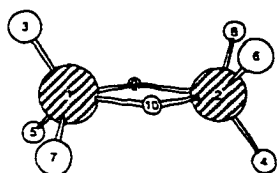
Table 4. Calculated harmonic vibrational frequencies for the Ti_2H_8 isomers C_{2h} and $C_s(2)$.[a]

Symmetry	Vibration	Frequency /cm-1	Scaled Frequency /cm-1	Intensity / km mol-1	Exptl. Frequency[9] /cm-1
		C_{2h}			
B_u	H_t bend	382.5	355.7	128.9	
B_u	H_t bend	489.0	454.8	138.2	
A_u	H_t bend	547.0	508.7	179.7	
B_u	$Ti-H_{br}$ str	1599.0	1487.1	2706.2	1490 broad
B_u	$Ti-H_t$ str	1785.4	1660.4	951.1	1658
A_u	$Ti-H_t$ str	1789.3	1664.0	547.1	1665
		$C_s(2)$			
A'	H_t bend	382.3	355.5	138.6	
A''	$H_{t,br}$ bend	481.4	447.7	138.0	
A'	H_t bend	495.8	461.1	157.7	
A'	H_t bend	526.4	489.5	113.7	
A'	H_t bend	571.4	531.4	297.6	
A'	H_{br} bend	1162.5	1081.1	193.4	1140 broad
A'	H_{br} bend	1340.4	1246.6	100.2	
A'	$Ti-H_{br}$ str	1655.0	1539.1	1405.3	1515
A'	$Ti-H_t$ str	1738.5	1616.8	381.5	1620
A''	$Ti-H_t$ str	1747.7	1625.4	257.9	
A'	$Ti-H_{t,br}$ str	1762.4	1639.0	130.0	
A''	$Ti-H_t$ str	1763.1	1639.7	442.8	1645
A'	$Ti-H_t$ str	1771.0	1647.0	108.6	

[a] Scaling factor of 0.93 used. Only calculated frequencies with an intensity greater than 100 km/mol reported.
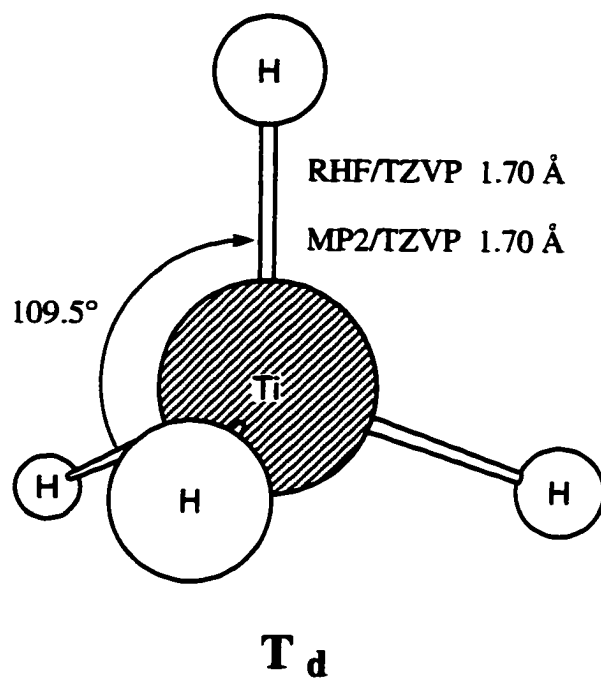
Figure 1. Titane equilbrium geometry.
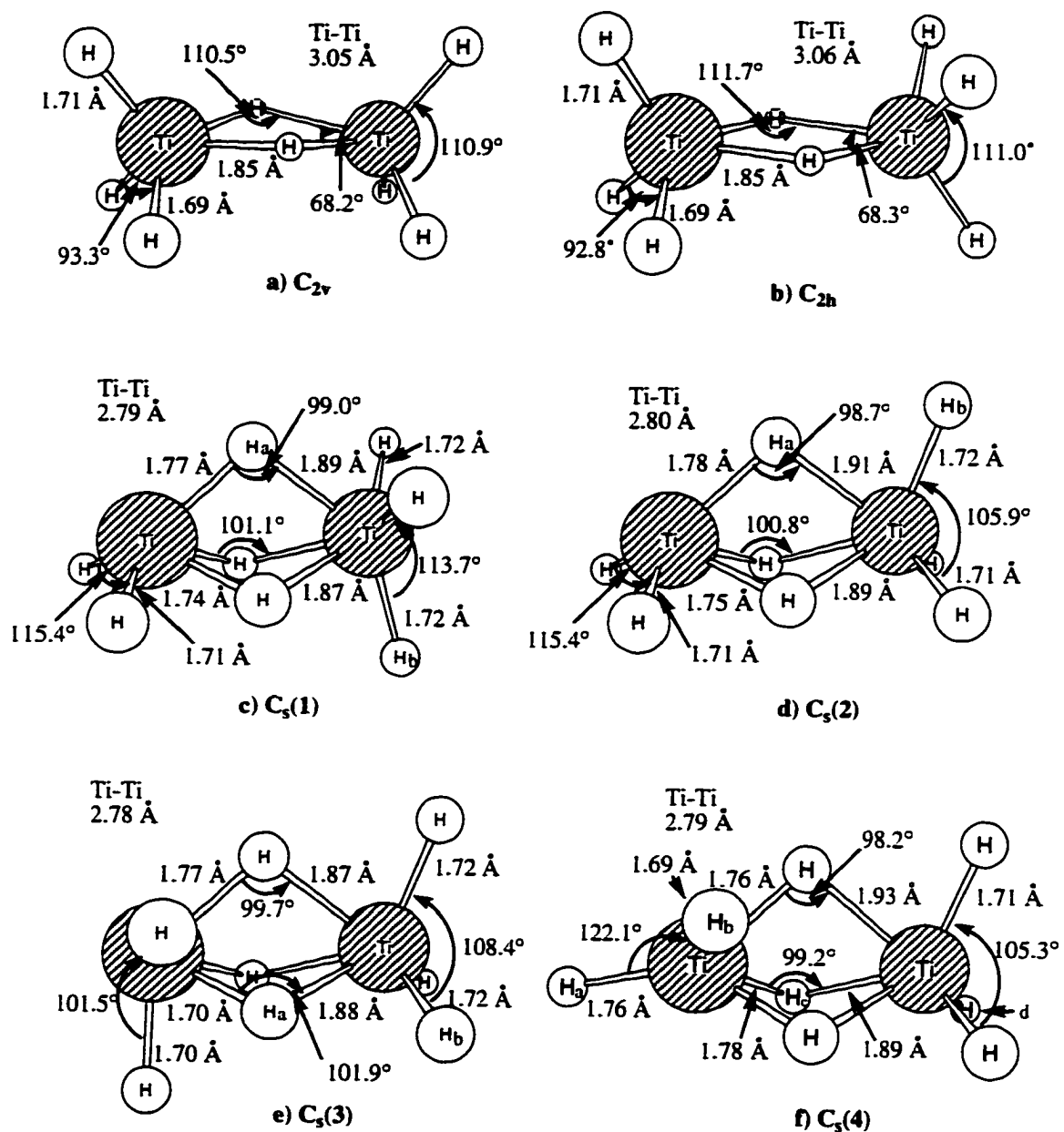
Figure 2. MP2/TZVP optimized structures which are minima on the potential energy surface of Ti_2H_8. In $C_s(1)$, $C_s(2)$ and $C_s(3)$ the two Ti's, H_a and H_b are in the plane. In $C_s(4)$ The two Ti's, H_a, H_b, H_c and H_d are in the plane.
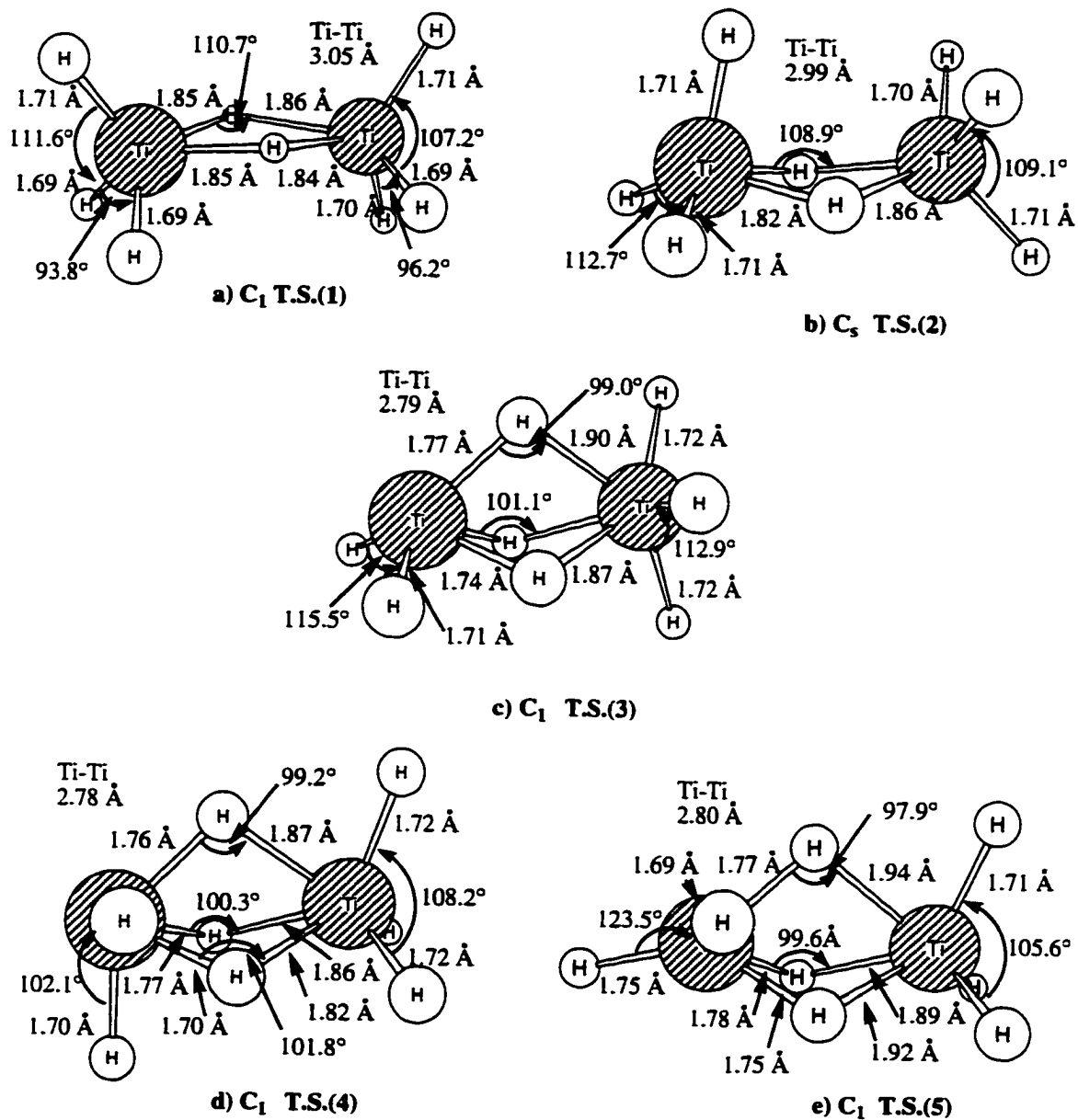
Figure 3. MP2/TZVP optimized structures which are transition states on the potential energy surface of Ti_2H_8.

a)

b)
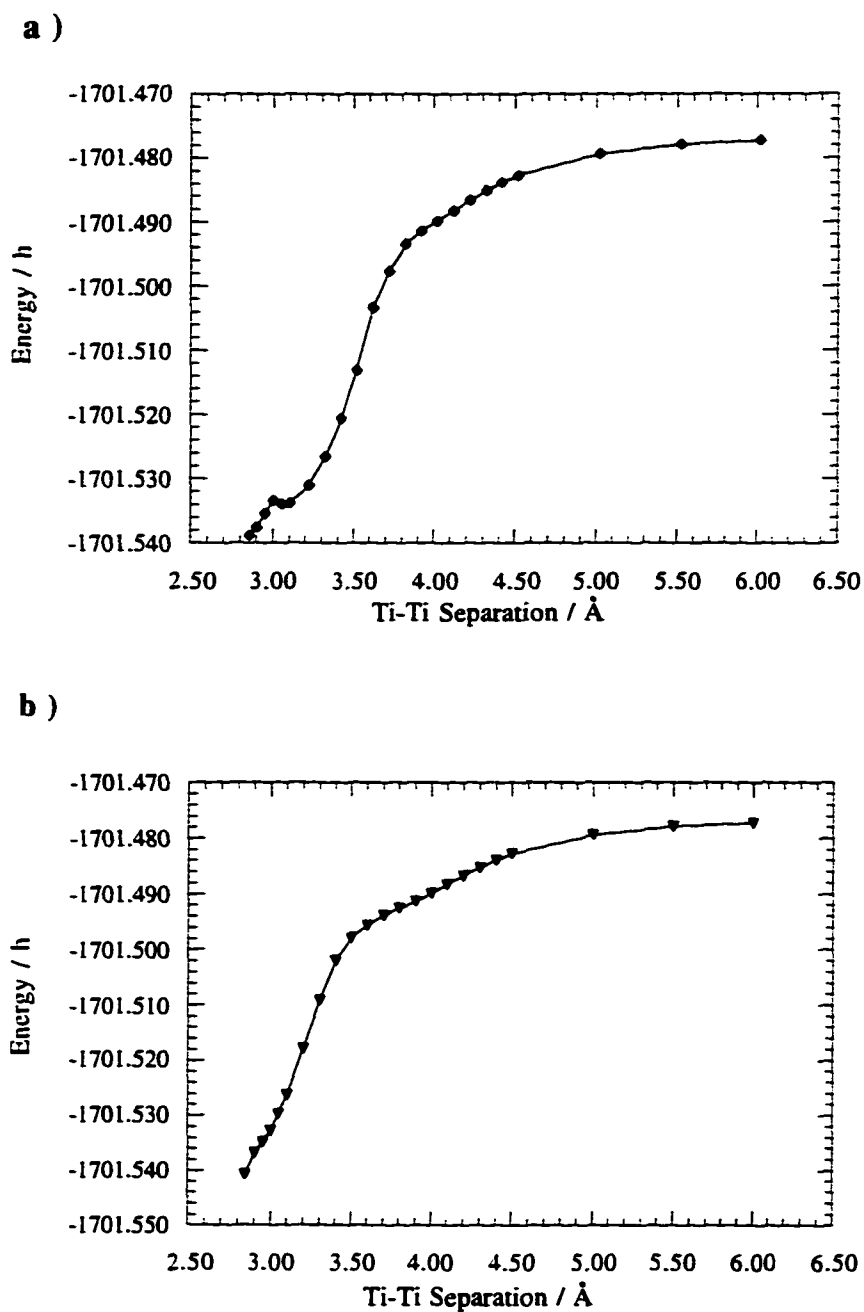
Figure 4. Plots of MP2/TZVP single point energies in Hartrees versus Ti-Ti separation in Å corresponding to a) the dissociation of $C_s(1)$ (Figure 2c) into two TiH_4 fragments and b) the dissociation of $C_s(4)$ (Figure 2f) into two TiH_4 fragments. The single point energies were calculated at the constrained RHF/TZVP optimized geometries (Ti-Ti distance constrained).

a)

4.00 Å 3.90 Å 3.80 Å 3.70 Å 3.50 Å

3.10 Å 3.05 Å 3.00 Å 2.95 Å 2.90 Å 2.85 Å

b)

4.00 Å 3.90 Å 3.80 Å 3.70 Å 3.50 Å

3.10 Å 3.05 Å 3.00 Å 2.95 Å 2.90 Å 2.85 Å
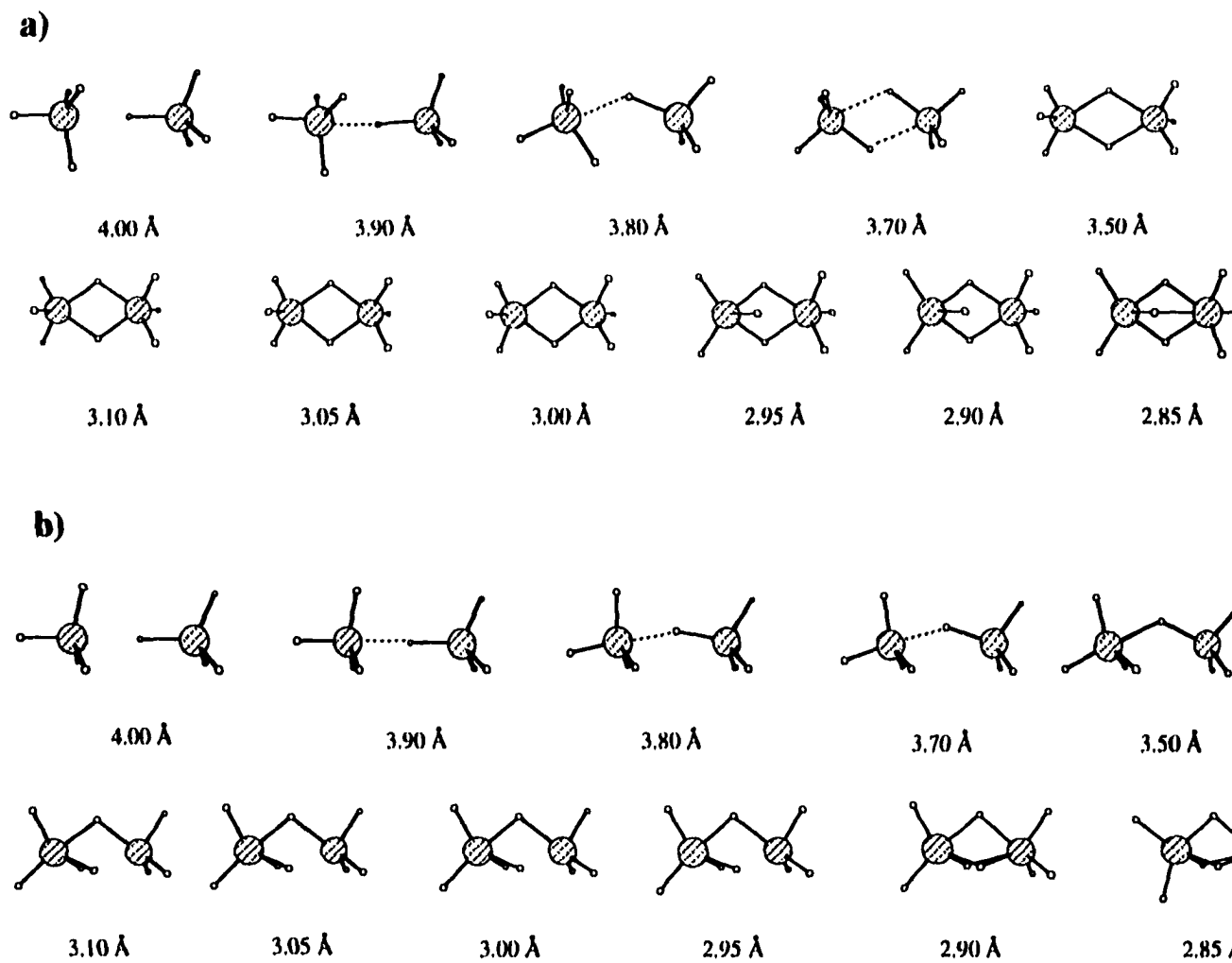
Figure 5. Each structure is the result of a constrained optimization at the RHF/TZVP level in which the Ti-Ti separation was "frozen" at the distance indicated. a) represents a possible dimerization path to Cs(1) (Figure 2c), and b) represents a possible dimerization path to C_s(4) (Figure 2f).
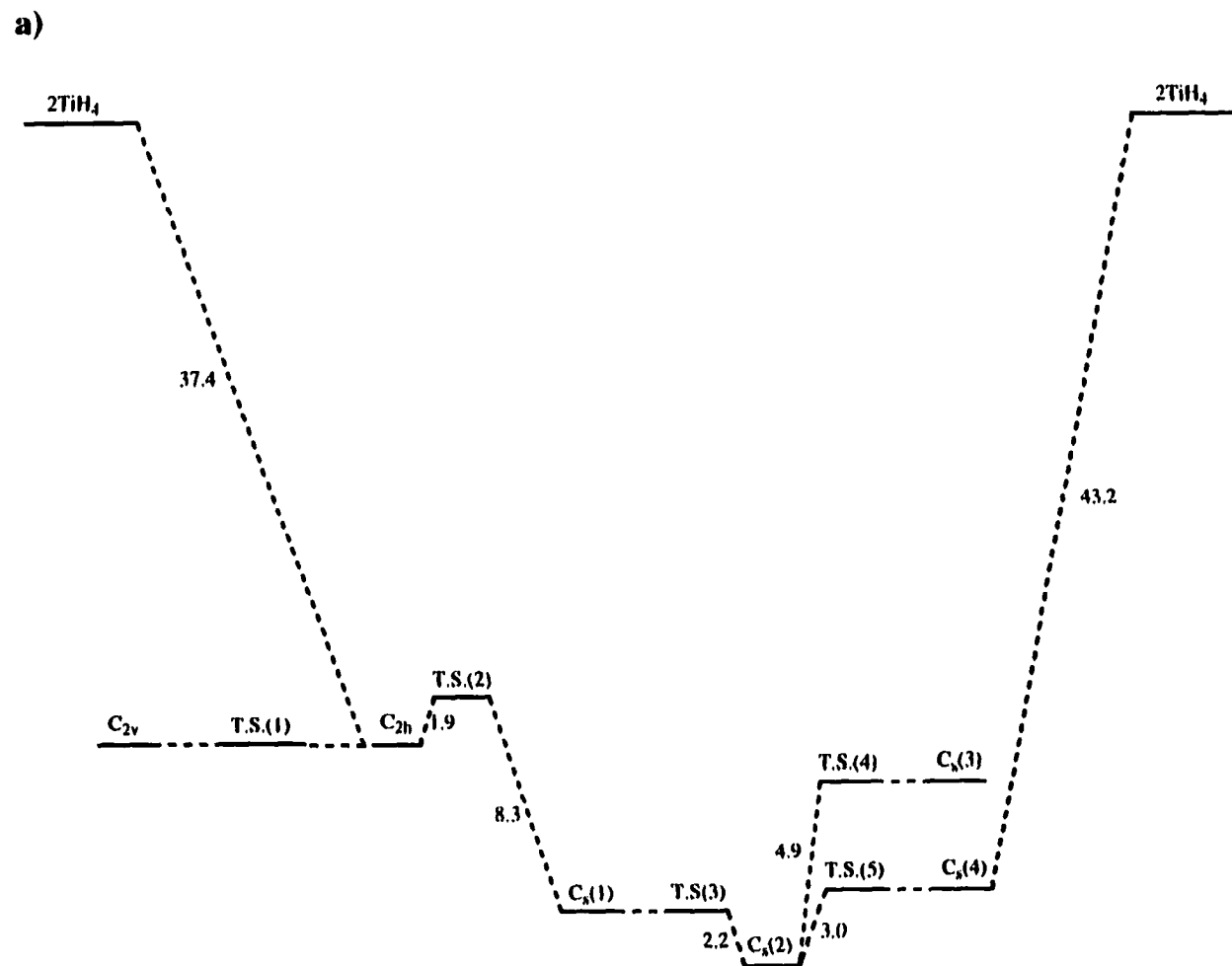
Figure 6. a) CCSD(T)/TZVP(f) potential energy surface for Ti_2H_8. b) CCSD(T)/TZVP(f) potential energy surface for Ti_2H_8 with zero point vibrational energy (calcuated at the MP2/TZVP level) added. All energies in kcal mol^{-1}, diagrams not to scale.
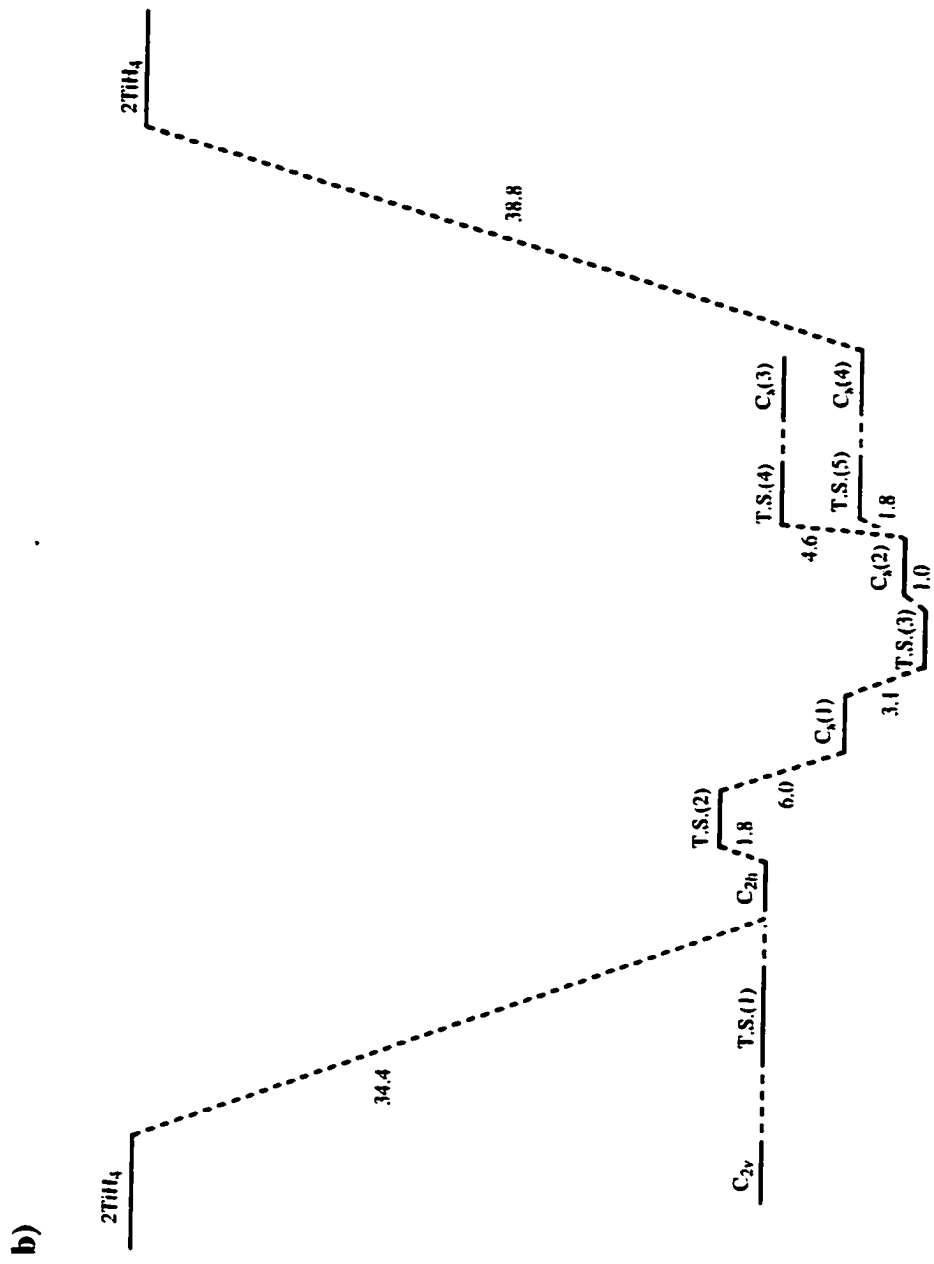
Figure 6. Continuted

a)
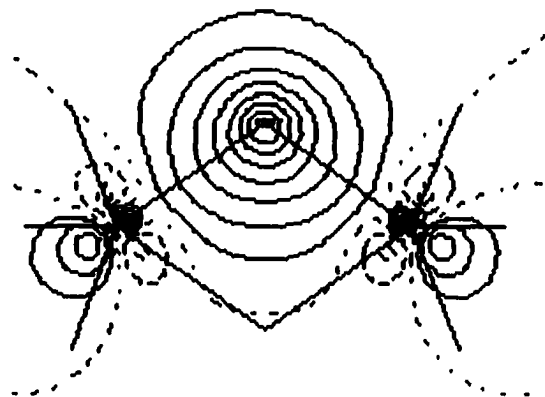
b)
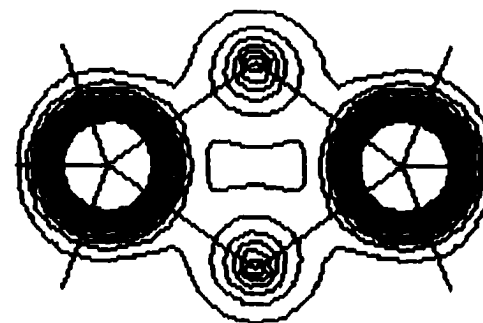
Figure 7. a) Localised molecular orbital corresponding to a three center, two electron hydrogen bridging bond in the C_{2h} isomer. b) Plot of total electron density for the C_{2h} isomer. The contour increments in a) and b) are 0.05 $Bohr^{3/2}$ and $Bohr^3$, respectively.

a)
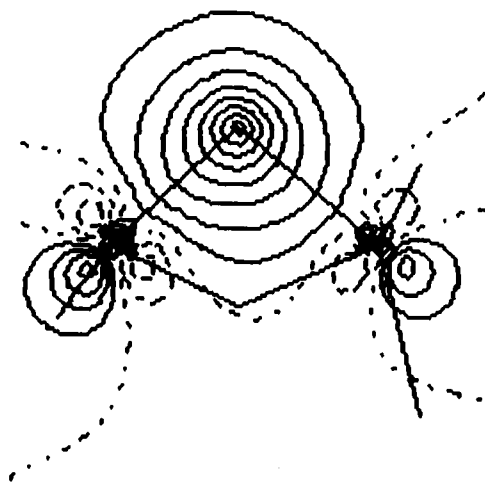
b) i)
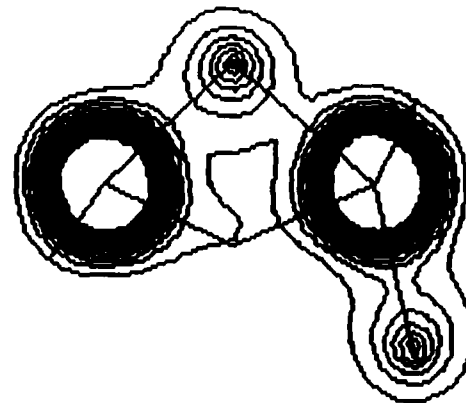
ii)
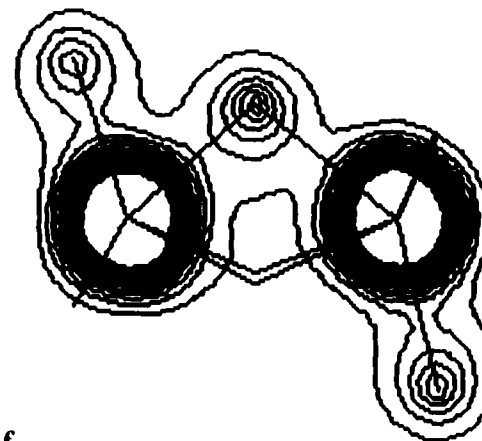
Figure 8. a) Localised molecular orbital corresponding to the in-plane three center, two electron hydrogen bridging bond in the $C_s(1)$ isomer. b) i) Plot of total electron density in the C_s plane of the $C_s(1)$ isomer, ii) Plot of the total density in the plane of one of the remaining bridging hydrogens of the $C_s(1)$ isomer.

Contour increments in a) and b) are 0.05 $Bohr^{3/2}$ and $Bohr^3$, respectively.

a)

C_{2h}
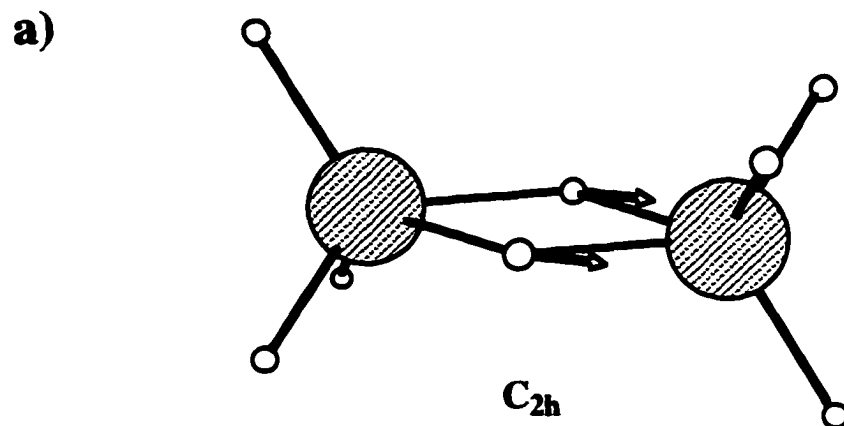
Bridge stretch at 1487 cm^{-1} (scaled).

b)

$C_s(2)$
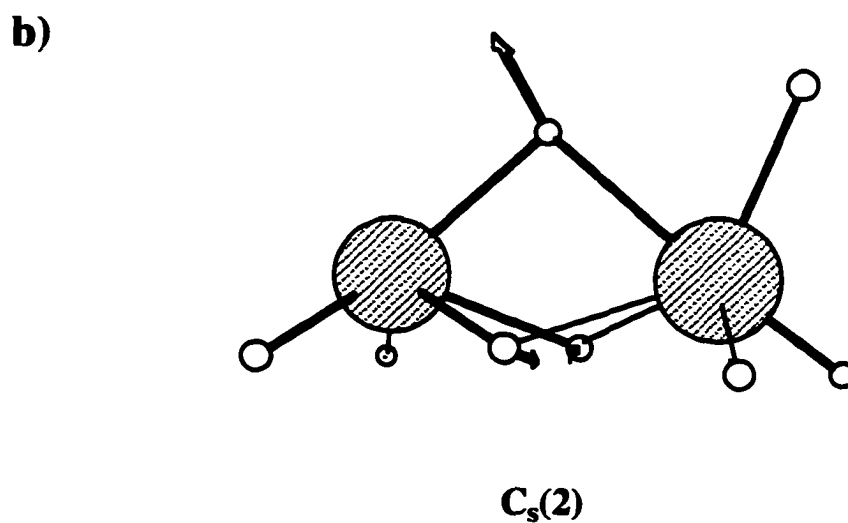
Bridge deformation (bend) at 1081 cm^{-1} (scaled).

Figure 9. a) Normal mode of the calculated frequency (1487 cm^{-1} (scaled)) that corresponds with a broad feature centered at 1490 cm^{-1} in the experimental spectrum.b) Normal mode of calculated frequency at 1081 cm^{-1} (scaled). This may correspond to the experimental peak found at 1140 cm^{-1}.

CHAPTER 4. THE MOLECULAR ELECTRONIC STRUCTURE AND STABILITY OF THE ISOMERS OF Ti_2H_6

Simon P. Webb and Mark S. Gordon

Abstract

Ab Initio calculations have been performed on five singlet and five triplet isomers which are minima on the two lowest potential energy surfaces of Ti_2H_6. We have used single determinant ROHF as well as multiconfigurational methods, employing triple ζ with polarization basis sets. Dynamic correlation effects are accounted for using second order perturbation methods. Staggered and eclipsed C_{3v} triple hydrogen bridged structures, which have been studied previously using single determinant closed shell reference wavefunctions, are shown to require a more sophisticated treatment. The remaining isomers - C_s triple hydrogen bridged, D_{2h} double hydrogen bridged, and D_{4h} quadruple hydrogen bridged - have not previously been considered. The triplets are by definition diradical and the singlets are found to possess largely diradical character. The D_{2h} isomer may be thought of as the simplest model for di-titanium(III) bridged compounds. It is found to be antiferromagnetic with a calculated isotropic exchange interaction of $J = -250$ cm^{-1} (singlet-triplet gap of 1.43 kcal/mol). All isomers are predicted to be stable with respect to $2TiH_3$. The most stable isomer is the triplet C_s structure with an exothermic dimerization energy of 56.4 kcal/mol.

I. Introduction

Titanium hydrides are an important class of compounds. Their catalytic behavior in many reactions, including polymerization of olefins and nitrogen fixation,[1] has ensured continuing interest and research both experimentally and theoretically. In addition to studies of specific systems catalyzed by titanium hyrides,[2,3,4,5] over the last ten years much needed attention has been paid to the fundamental chemistry of simple titanium hydride systems.

Recently Andrews et al carried out low temperature matrix isolation studies on the reaction between laser ablated titanium atoms and hydrogen.[6] Previously to this Margrave, Xiao, and Hauge carried out similar experiments in which they studied the reaction of titanium atoms, produced by the vaporization of a titanium filament, with hydrogen.[7] These two studies between them produced the first reported spectra of the molecules TiH, TiH_2, TiH_3, and TiH_4.

Bauschlicher has carried out a series of *ab initio* calculations on TiH including benchmark full CI calculations.[8] *Ab initio* calculations carried out on TiH_2 have shown its ground state to be a triplet with bent geometry.[9] Studies on H_2---TiH_2 and TiH_4[10] have attempted to clarify peak assignments made in Margrave's experimental work.[7] Also, an *ab initio* study done in this laboratory[11] investigated the dimerization of TiH_4 and concluded that TiH_4 dimers could have been observed in the matrix isolation studies.[6,7] Most recently a study carried out on singlet closed shell Ti_2H_6[12] finds two C_{3v} triple bridged structures: one with an eclipsed conformation; the other staggered. No Ti-Ti bonding interaction was found in these isomers despite short Ti-Ti separations. At their best level of theory Garcia and Ugalde found the structures to be thermodynamically stable with respect to $2TiH_3$ by ~ 20 kcal/mol. However, in this paper we will show that the single determinant reference wavefunction used

in their study provides an inadequate description of the Ti_2H_6 system. Consequently, the Ti_2H_6 potential energy surfaces need to be re-examined.

In this work we have carried out an extensive study of the potential energy surfaces of the lowest singlet and triplet states of Ti_2H_6, in part to investigate the diradical character of this system. We have considered both singlet and triplet states of double, triple, and quadruple hydrogen bridged structures. This study also addresses the stability of Ti_2H_6 with respect to two separated TiH_3 monomers. Obviously this has some bearing on the experimental work of Andrews et al [6] who claim to have observed TiH_3, as dimers could be present in their matrix isolation experiments. Calculation of the infrared frequencies of TiH_3 and Ti_2H_6 are reported for comparison with experiment. We also consider the thermodynamics of the reactions (R1) and (R2).

$$Ti_2H_6 \ + \ 2H \ \rightarrow \ Ti_2H_8 \qquad (R1)$$

$$Ti_2H_6 \ + \ H_2 \ \rightarrow \ Ti_2H_8 \qquad (R2)$$
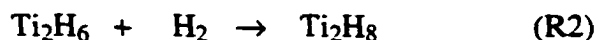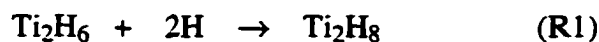
The molecule $H_2Ti(\mu-H)_2TiH_2$ is an important prototype as it can serve as the simplest model for homodinuclear titanium(III) systems. There are numerous examples of such systems in the literature. The compound rac-{$[C_2H_4(\eta^5$-tetrahydroindenyl$)_2]$-Ti(III)$(\mu$-H)$]_2$[13] contains a Ti_2H_2 unit with the two hydrogens bridging to form a flat ring. It is the first structurally characterized titanocene(III) hydride derivative without a supporting organic bridge, and is found to be antiferromagnetic. The titanocene dimer $[(\eta^5$-$C_5H_5)Ti(\mu$-H$)]_2(\mu$-η^5:η^5-$C_{10}H_8)$ has also been shown to have two bridging hydrogens between its two titanium(III) centers, but, in contrast to the compound just discussed, the Ti_2H_2 unit forms a buckled ring with folding

along the H---H axis and there is a carbon-carbon linkage between titanocene units.[14] It is found to be diamagnetic at ambient temperature which suggests either a Ti-Ti bond and/or a substantial singlet-triplet energy gap as the Ti(III) d electrons must be paired or singlet coupled: however, due to lack of detailed magnetic susceptibility measurements as a function of temperature, this has not been established definitively and is the subject of ongoing calculations in this laboratory. The hydroxy derivative of the titanocene dimer[15] was found to be weakly paramagnetic, suggesting diradical character, although the authors were hesitant to rule out Ti-Ti bonding. Other studies include those on $[Cp_2Ti(\mu-X)]_2$ where X=F,Cl,Br, and I.[16,17] They find unpaired electrons exhibiting antiferromagnetic behavior with strengths in the order $Br > Cl \sim I > F$, suggesting dependence on more than just Ti-Ti distance. Two more recent experimental studies[18,19] also demonstrate the sensitivity of the magnetic properties associated with these homodinuclear titanium(III) compounds to the bridging species. Samuel et al find that the compounds $[Cp_2Ti(\mu-OCH_3)]_2$ and $[Cp_2Ti(\mu-OC_2H_5]_2$ are paramagnetic dimers exhibiting *weak* antiferromagnetic behavior suggesting singlet coupling of unpaired electrons. However, Dick et al find the compounds $[Cp_2Ti(\mu-PMe_2)]_2$ and $[Cp_2Ti(\mu-PEt_2)]_2$ to be diamagnetic and *strongly* antiferromagnetic. They suggest either through-ligand coupling of the unpaired Ti electrons or a "super-long" σ type Ti-Ti bond of the type proposed to be present in certain homodinuclear zirconium systems by Rohmer and Benard.[20] The latter appears unlikely considering the Ti-Ti separation of ~3.7 Å. Another example is the complex $[Cp_2Ti(\mu-O)]_2$ which is paramagnetic and weakly ferromagnetic.[21] This is the only ferromagnetic homodinuclear Ti(III) compound known.

It is clear then that the bonding and magnetic properties of these molecules arise from complex interactions between the two metal centers, and between the metal centers and bridging (and possibly terminal) ligands. With the current and constantly increasing scope of *ab initio* calculations it seems reasonable to expect helpful and reliable contributions from "first

principles" theory in this area in the near future. However, establishing adequate levels of theory to describe simple dinuclear titanium(III) systems is vital before approaching the complex systems just described. This is best done by first considering the prototypical $H_2Ti(\mu\text{-}H)_2TiH_2$ system. It is relatively straightforward (relative to experiment) to establish the nature of Ti-Ti interactions using theoretical techniques such as the calculation of natural orbital occupations of MCSCF wavefunctions. In subsequent studies one could then monitor directly the effect of, for example, terminal cyclopentadienyl ligands, and various bridging ligands on the Ti-Ti interaction in homodinuclear titanium(III) systems by comparison to the "baseline" $H_2Ti(\mu\text{-}H)_2TiH_2$ analysis.

The ability to predict magnetic properties of dinuclear complexes is an important goal in the area of molecular materials.[22] The use of *ab initio* calculations in this area has until recently been rather limited. Accurate determination of multiplet splitting energies requires the inclusion of non-dynamic and dynamic correlation effects.[23,24] The relative simplicity of $H_2Ti(\mu\text{-}H)_2TiH_2$ enables us to make a reliable determination of its singlet-triplet splitting energy.

II. Computational Details

(a) **Basis Set.** For titanium we employed a triple ζ with polarization (14s11p6d/10s8p3d) basis set. This consists of Wachter's basis set[25] with two additional sets of p functions[26] and a set of diffuse d functions.[27] For hydrogen Dunning's (5s1p/3s1p) basis set[28] was used. Collectively this basis set is referred to as TZVP and was used in all geometry optimizations. F functions were added to the titanium basis with an exponent of 0.411 for single point energies; this basis set is referred to as TZVP(f). For a final test of basis set

convergence selected single point energies were carried out with the titanium TZVP basis plus one set of f ($\alpha = 0.591$), and g ($\alpha = 0.390$) functions, and a set of diffuse s ($\alpha = 0.035$), p ($\alpha = 0.239$), and d ($\alpha = 0.0207$) functions. Exponents used here are optimized for correlated titanium atoms and are due to Glezakou and Gordon.[29]

(b) Wavefunctions. We now discuss the wavefunctions needed to adequately describe a reference state for the Ti_2H_6 isomers we consider in this paper (see Figure 1). Garcia and Ugalde carried out the only previous calculations on Ti_2H_6.[12] They reported only singlet C_{3v} triple bridged structures and used closed shell single determinant reference wavefunctions. However, careful consideration of the orbitals and electrons reveals the inadequacy of such a single configuration description. These C_{3v} isomers require consideration of three orbitals (a_1, e_x, and e_y) for occupation of the two highest energy electrons, due to the near degeneracy of the orbitals. Several electronic states correspond to the distribution of two electrons in this orbital space: two $^1A_1$ states, four ^1E states, one $^3A_2$ state, and two ^3E states (see Figures 2a and 2b). These group theoretical considerations suggest the need for a multi-configurational (MC) SCF description of those states.

Preliminary Fully Optimized Reaction Space (FORS)-MCSCF[30] (also called CASSCF[31]) calculations illustrate considerable mixing between the $(a_1)^2(e_x)^0(e_y)^0$, and $((a_1)^0(e_x)^2(e_y)^0 + (a_1)^0(e_x)^0(e_y)^2)$ configurations in the $^1A_1$ ground state: a natural orbital analysis of the eclipsed isomer wavefunction shows 1.51 electrons in the a_1 orbital, and 0.24 electrons in each of the degenerate e orbitals. This qualitatively correct description of the $^1A_1$ ground state (taking the eclipsed isomer as an example) is 13.6 kcal more stable than the $^1A_1$ state described with the RHF closed shell wavefunction $(a_1)^2(e_x)^0(e_y)^0$. Therefore, the 2

electron, 3 orbital MCSCF wavefunction is the *simplest qualitatively correct wavefunction* for the $^1A_1$ states. It is the reference wavefuntion used in subsequent perturbation calculations which correct for dynamic electron correlation in the $^1A_1$ states. In order to test for Jahn-Teller effects the geometry of this eclipsed isomer was distorted slightly from C_{3v} to C_s symmetry. Orbital symmetry constraints requiring degenerate e levels were therefore removed and a 2 electron, 3 orbital MCSCF geometry optimization was carried out on this $^1A'$ state with a', a', and a" orbitals active. The resulting optimized geometry returned to essentially C_{3v} symmetry and the energy of this structure was lower by only 0.5 kcal/mol, suggesting negligible Jahn-Teller distortion.

It is formally possible for all four of the ^1E configurations to mix; however, a preliminary FORS-MCSCF calculation suggests that a subset of the ^1E configurations are dominant in each excited ^1E state. The first two degenerate excited ^1E states are dominated by the configurations $(a_1)^1(e_x)^1(e_y)^0$ and $(a_1)^1(e_x)^0(e_y)^1$ (all other CI coefficients are less than 0.025). Therefore, a "state-averaged" restricted open shell Hartree-Fock (ROHF) wavefunction was constructed by assigning equal weights to these two dominant configurations. This single configuration ROHF wavefunction is then used to predict the staggered and eclipsed geometries. It also serves as the reference for perturbation corrections on the averaged ^1E excited state. Note that if the two ^1E configurations are not averaged the result is occupation of only one of a pair of degenerate e orbitals, and this may lead to Jahn-Teller distortions to C_s structures. The question of Jahn-Teller distortion is again addressed by relaxing symmetry constraints to C_s, thereby splitting the degenerate e orbitals into a' and a". The "state-averaged" ^1E excited state is therefore split into a $^1A'$ state (two singly occupied a' orbitals) and a $^1A"$ state (a singly occupied a' and a singly occupied a"). The $^1A'$ state is actually a configuration included in the 2 electron, 3 orbital calculation described in the previous paragraph, and is not

considered further. A singlet ROHF geometry optimization performed on the $^1A''$ state indicated no appreciable geometry change and the resulting structure is almost isoenergetic with the C_{3v} ^1E state, with a decrease in energy of only 0.3 kcal/mol. As in the ground state, Jahn-Teller distortion is therefore considered to be unimportant.

The C_{3v} ^1E state is considerably less stable than the C_{3v} $^1A_1$ state. This is also the case when dynamic electron correlation is accounted for. Since our primary interest is in the nature of the ground state singlet potential energy surface, this higher state is not considered further. The same is true for the third and fourth ^1E excited states, whose dominant configurations are shown in Figure 2a.

The two degenerate ^3E components $((a)^1(e_x)^1(e_y)^0$ and $(a)^1(e_x)^0(e_y)^1)$ are described by a state-averaged wavefunction. This state-averaged ^3E state is lower in energy than the $^3A_2$ state (see Figure 2b). To assess the possibility of Jahn-Teller distortion of the ^3E state, symmetry constraints were relaxed to C_s. Two ROHF/TZVP geometry optimizations were carried out on the eclipsed structure, one with two a' orbitals singly occupied ($^3A'$); one with a'' and a' each singly occupied ($^3A''$). Negligible geometry and energy changes (energy decrease of 0.4 kcal/mol for both $^3A'$ and $^3A''$) occurred, indicating no Jahn-Teller distortion. The ^3E and $^3A_2$ states can both be described qualitatively correctly with a single determinant ROHF wavefunction. With inclusion of dynamic electron correlation, the ^3E state is considerably lower in energy than the $^3A_2$ state. Since ^3E is the lowest energy triplet, the $^3A_2$ state is not considered further.

Test calculations on the *lowest energy* singlet states for other Ti_2H_6 isomers (D_{2h}, C_s, and D_{4h}) show that a correct reference wavefunction requires the inclusion of only two orbitals and the two highest energy electrons in the active space. This is discussed in the next subsection.

(c) Methods. For Ti_2H_6 triplets and the TiH_3 doublet, geometry optimizations were performed at the ROHF level of theory. For singlets, preliminary calculations were carried out at the RHF level. After convergence of the RHF wavefunction, modified virtual orbitals (MVO's) were generated by freezing the occupied orbitals, forming a cation by removal of six electrons and performing one SCF iteration. The resulting orbitals were used as a starting point for two configuration (TCSCF) geometry optimizations, and 2 electrons in 3 orbitals, FORS-MCSCF geometry optimizations where necessary (e.g. C_{3v} $^1A_1$). The $^1A''$ state of the C_s structure was found to be more stable than the $^1A'$ state, so geometries reported for this singlet were obtained from an ROHF calculation. TCSCF wavefunctions frequently over-estimate diradical character. To ensure that the high diradical character found in the Ti_2H_6 isomers in this study is not an artifact of the small active spaces, a FORS-MCSCF/TZVP geometry optimization with 12 electrons in 13 orbitals on the D_{2h} isomer was carried out, using MVO's from an RHF calculation as starting orbitals. This active space is at the limit of our capabilities and includes all but two of the valence electrons in Ti_2H_6. The seven virtual orbitals included in the active space correspond to d-orbital interactions of various orientations. The natural orbital analysis of the resulting wavefunction is virtually identical to that of the TCSCF wavefunction. The occupation numbers of the Ti-Ti σ and σ^* natural orbitals in the $(12,13)$ wavefunction are 1.15 and 0.85 electrons, respectively, compared with 1.11 and 0.89 for the TCSCF calculation. All other occupation numbers are ~ 2.0 or 0.0 in the $(12,13)$ calculation. FORS-MCSCF/TZVP calculations with a $(2,10)$ active space which includes all possible d-orbital orientations also confirm the same diradical character and adequacy of the TCSCF wavfunction.

Stationary points were characterized by calculating and diagonalizing the energy second derivative matrix (hessian). A positive definite hessian (no negative eigenvalues)

indicates a minimum on the potential energy surface.

Dynamic electron correlation effects were included by carrying out RMP2[32] single point energy calculations at ROHF geometries for C_s, D_{2h}, and D_{4h} triplets, and multiconfigurational quasidegenerate second order perturbation theory calculations (MCQDPT)[33] at the ROHF geometries for the C_{3v} ^3E and C_s $^1A''$ states, TCSCF geometries for D_{2h} and D_{4h} singlets, and the 2 electron, 3 orbital FORS-MCSCF geometry for the C_{3v} $^1A_1$ state (note: any future reference to MCSCF will imply FORS-MCSCF). For energetics these single point energy calculations were repeated with the TZVP(f) basis set. For energies relative to 2TiH$_3$ consistent methodology was used, i.e. the dimerization energy was calculated with both energies from RMP2 or both energies from MCQDPT. Additional single point energy calculations on the C_s, D_{2h}, and D_{4h} singlets and triplets were carried out using the largest basis set TZVP(f,g) as a test of basis set convergence.

All calculations were done using the electronic structure code GAMESS.[34]

III. Results and discussion

TiH$_3$. A D_{3h} structure ($^2A'_1$ state) was found to be the lowest energy minimum on the TiH$_3$ potential energy surface and is shown in Figure 3. Total energies are shown in Table 1.

Ti$_2$H$_6$. Multiple minima were found on both the triplet and singlet potential energy surfaces of Ti$_2$H$_6$. Geometries are shown in Figure 1. Energies relative to $^2A'_1$ 2TiH$_3$ are shown in Table 2. Molecular orbital plots along with occupation numbers are shown in Figure 4a and Figure 4b.

(a) Molecular and Electronic Structure, and Energetics. All the structures found in this study of Ti_2H_6 (see Figure 1) involve bridging hydrogens between the two titanium(III) centers. The presence of bridging hydrogens is not particularly surprising and may be attributed to the electron deficiency of the two titaniums and their desire for high coordination numbers.[11] The double hydrogen bridged $(\mu-H)_2$ minima (singlet and triplet) closely resemble the structure of diborane. These D_{2h} structures may be thought of as simple prototypes in which the two titaniums and the bridging ligands are arranged in a fashion similar to that in more complex homodinuclear titanium(III) compounds such as titanocene dimer.[14] From this perspective, the bonding and energetic characteristics of the D_{2h} structure, such as diradical character and singlet-triplet splitting (see sections III c and d), may be thought of as a reference with which to compare these more complex systems. It does not appear that any triple $(\mu-H)_3$ or quadruple $(\mu-H)_4$ hydrogen bridged di-titanium(III) compounds are experimentally known. Homodinuclear transition metal compounds containing Fe and Re with three and four bridging hydrogens, respectively, *are* known experimentally. Examples are $Fe_2(\mu-H)_3(P_3)]^+$[35] and $Re_2(\mu-H)_4 H_4(PEt_2Ph)_4$.[36] So, the remaining $(\mu-H)_3$ and $(\mu-H)_4$ isomers are not yet useful as prototypes, but are highly relevant to the low temperature matrix isolation studies of Margrave[7] and Andrews[6] (see section III b).

The D_{2h}, C_s, and D_{4h} ground state minima either exhibit a high degree of diradical character (D_{2h} and D_{4h} singlets) or are by definition diradicals (triplets and C_s $^1A"$). A natural orbital analysis of the singlet TCSCF/TZVP wavefunctions (see Figure 4a) shows occupancies of 1.11 and 0.89 electrons for the σ and σ^* orbitals, respectively, in the D_{2h} singlet minimum, and 1.09 and 0.91 electrons for π and π^*, respectively, in the D_{4h} singlet minimum. These occupation numbers indicate high diradical character with a *very* small bonding interaction in

these two singlets. Another indication of the D_{2h} and D_{4h} singlet diradical character is the near degeneracy of the TCSCF singlet and the ROHF triplet energies for these structures (Table 2). Of course, if one assumes identical geometries, a pure diradical singlet when excluding dynamic electron correlation will necessarily be less stable than a triplet, due to the intrinsic correlation of the same spin electrons in the triplet. This is in fact the case for the C_s isomer, for which the singlet is purely diradical: the triplet is more stable by 0.5 kcal/mol. The D_{2h} and D_{4h} singlets are 0.5 and 0.6 kcal/mol more stable than their triplet counterparts, respectively. This reinforces what was suggested by the natural orbital analysis (see Figure 4a): there is a very weak bonding interaction in these two singlets. At our best level of theory for these isomers, which includes f and g functions on Ti and dynamic electron correlation through second order perturbation theory (MCQDPT/TZVP(f,g)), we can draw similar conclusions: the C_s singlet and triplet isomers are essentially degenerate with the triplet only 0.3 kcal/mol more stable than the singlet, whereas the D_{2h} and D_{4h} singlets are more stable than their triplet counterparts by 1.3 and 1.4 kcal/mol, respectively, again suggesting weak bonding interactions. The singlet-triplet energy gap for the D_{2h} isomer will be discussed in more detail in section III d) where we consider magnetic properties.

The diradical nature of these isomers cannot be attributed to large Ti-Ti separations. One can clearly see from Figure 1 that the Ti-Ti separations (3.04 Å, 2.81Å, and 2.50Å for the D_{2h}, C_s, and D_{4h} singlets respectively) are close to or well within a separation one might normally associate with a titanium bond based on the titanium atomic radius of 1.47 Å.[37] For the C_s, D_{4h}, and C_{3v} isomers, inspection of the orbitals is sufficient to suggest why there is no Ti-Ti bond formation. Figure 4a shows the relevant d orbitals of the C_s structure. Their orientation presumably reflects a minimization of unfavorable interactions with bridging and terminal hydrogens. The result is d orbital orientations in which no overlap or interaction can be expected and so single occupation of two orthogonal orbitals (one on each titanium) is

energetically favored. For the D_{4h} structure Figure 4a shows the d orbitals to be in a π arrangement. It appears here that even the short Ti-Ti separation of 2.50 Å is too long for effective π orbital overlap. The C_{3v} structures show a coordination number of six on one Ti and only three on the other, making one titanium less saturated than the other. The two electrons prefer to associate with the less saturated Ti in a non-bonding lone pair arrangement (Figure 4b).

For the D_{2h} singlet, mere inspection of the orbitals (Figure 4a) does not make it clear at all why there is no Ti-Ti bond to speak of. Here the orbitals are in an ideal arrangement for the formation of a σ bond yet there is only weak bonding interaction. An explanation of the lack of a strong bonding interaction between the two titaniums in the D_{2h} structure will be suggested in section III c).

The Ti-H bond length behavior (see Figure 1) is similar to that seen in the related Ti_2H_8 isomers.[11] The terminal Ti-H bond lengths are between 1.7 Å and 1.8 Å, within the range of Ti-H bond lengths found in TiH_4 (1.70 Å) and TiH_3 (1.77 Å) at equivalent levels of theory (same basis set, no dynamic correlation). Bridging Ti-H bonds are, as expected, longer than terminal Ti-H bonds by up to ~ 0.2 Å.

At the MCSCF/ROHF levels of theory (see Table 2), the $(\mu$-H$)_2$ D_{2h} isomers are the most stable by a small margin over the $(\mu$-H$)_3$ C_s isomers (1.9 kcal/mol in the singlet and 0.9 kcal/mol in the triplet). The $(\mu$-H$)_4$ D_{4h} isomers are considerably less stable (by ~ 20 kcal/mol). However, all these structures are stable with respect to $2TiH_3$ at this level of theory. The C_{3v} isomers exhibit somewhat different behavior. The triplets are more stable than the singlets by ~ 25 kcal/mol and are themselves more stable than $2TiH_3$ by only ~ 12 kcal/mol. The singlets are *unstable* with respect to $2TiH_3$ by ~ 13 kcal/mol.

Dynamic electron correlation is included through single point energies using second

order perturbation theory. At this level of theory, the $(\mu-H)_3$ C_s structures (singlet and triplet) are clearly the most stable (Table 2). So, as has been shown previously[11], dynamic electron correlation preferentially favors isomers with more than two bridging hydrogens. The D_{4h} isomers with the TZVP basis set are stabilized by 23.0 and 22.2 kcal/mol for the singlet and triplet, respectively, and the C_{3v} isomers are stabilized by 40.4 and 33.1 kcal/mol for the singlet and triplet eclipsed structure. Dynamic electron correlation narrows the spread of isomer stabilities considerably. Another effect of electron correlation is the stabilization of the eclipsed C_{3v} isomers with respect to the staggered isomers by between 4 and 5 kcal/mol. This was also noted by Garcia and Ugalde.[12] With the inclusion of dynamic electron correlation all ground state isomers (including C_{3v} singlets) are stable with respect to 2TiH$_3$. At the best level of theory the TiH$_3$ dimer is thermodynamically favored over the monomer by up to 56.4 kcal/mol (C_s ^{3}A" isomer). Previous work suggests no kinetic barrier to the dimerization of simple titanium hydrides;[11] therefore, one might expect rapid dimerization whenever two TiH$_3$ molecules approach each other.

Inclusion of Ti f functions appears to be necessary for a reliable description of the whole range of Ti$_2$H$_6$ isomers. Their presence has a noticeable effect on the D_{4h} and C_{3v} structures, stabilizing them (relative to 2TiH$_3$) by 5.3, 5.1 (D_{4h} singlet and triplet, respectively), 4.0, and 3.0 kcal/mol (C_{3v} singlet and triplet, respectively) at the correlated level. Increasing the basis set further to TZVP(f,g) makes little difference (0.3 - 1.0 kcal/mol) to the predicted dimerization energies, so the TZVP(f) basis provides a good description of the entire range of isomers.

(b) Calculated I.R. Frequencies. Vibrational frequencies were calculated at the MCSCF/ROHF TZVP level for all minima. The C_s ^{3}A". D_{2h} ^{1}A$_g$, D_{4h} ^{1}A$_g$. and staggered C_{3v}

[3]E minima were chosen for comparison with experimental spectra.

The matrix isolation experiments of Margrave et al [7] and Andrews et al [6] produced the first spectra of simple titanium hydrides. The spectra are very complex: imperfect isolation presumably results in the co-existence of many different titanium hydride species. It has already been shown that the existence of Ti_2H_8 in these experiments is possible.[11] We now examine the likelihood of the presence of Ti_2H_6, having shown this species to be very stable with respect to $2TiH_3$. The assigned experimental Ti-H stretch frequency for TiH_3 is 1580.6 cm-[1]; the calculated ROHF/TZVP stretch frequency is 1668.0 cm-[1]. The calculated stretch frequency, then, may be scaled to the experimental one by a factor of 0.948. All frequencies discussed here are therefore scaled by this factor. Calculated I.R. frequencies, their corresponding intensities, and experimental frequencies are shown in Table 3.

The spectrum produced by Andrews et al has better resolution than that produced by the Margrave group; therefore, comparisons are made mainly with Andrews' data. Broad absorptions corresponding to bridge stretches and bends are characteristic of hydrogen bridged titanium compounds. Two such broad features can be seen in the experimental spectra.[6] The first lies between ~1440 cm-[1] and ~1560 cm-[1] and is fairly well resolved; the second lies between ~1150 cm-[1] and ~1340 cm-[1] with only partial resolution. The most intense calculated frequency for the C_s [1]A" species is 1475.9 cm-[1]; this is a bridge stretch and is close to the resolved experimental peak at 1485.2 cm-[1]. Andrews assigns this peak to the species Ti_xH_y. A number of the calculated frequencies lie within the broad 1150-1340 cm-[1] experimental feature (note that Andrews assigns this broad feature which is centered on 1250 cm-[1] to Ti_xH_y - see spectra for details[6]). The most intense of these calculated frequencies is for the D_{4h} [1]A_g species and appears at 1188.9 cm-[1]; this corresponds to an experimental peak seen at 1200 cm-[1]; a second calculated frequency for D_{4h} [1]A_g with a large intensity occurs at 1223.1 cm-[1] (2

modes), this corresponds to an experimental peak at 1225 cm-1. Both of these calculated

frequencies are bridge stretching modes. The calculated bridge stretching frequency for D_{2h}

^1A_g at 1338.9 cm-1 may correspond to a shoulder seen at 1330 cm-1.

Additional results presented in Table 3 illustrate good agreement between calculated

terminal hydrogen stretching frequencies and the experimental frequencies. However, the

smaller calculated frequencies do not correspond to experimentally reported modes. In

particular, those at 1141.3 cm-1 (C_s $^1A"$) , 1069.4 cm-1 (D_{2h} ^1A_g), and 1079.6 cm-1 (C_{3v} ^3E)

have significant predicted intensities. It has been suggested that discrepancies between

calculations and matrix experiments at the low frequency end of the spectra are common due to

interaction between guest and host molecules.[38] In fact, if one considers the broad feature

centered at 1250 cm-1 in Andrews' argon matrix spectrum[6] and then looks for the

corresponding feature in Margrave's krypton matrix spectrum[7] one can see that it has shifted

~110 cm-1 to 1140 cm-1. This large shift, which must arise from the different interactions

between guest and host in argon versus krypton, is almost zero for higher frequencies.

We conclude that although definite assignment of experimental peaks based on these

calculations is difficult and some of the good agreement may be fortuitous, the results suggest

that Ti_2H_6 could be present. One can make the same conclusion by comparison to Margrave's

spectrum. The fact that Margrave's experiment does not produce TiH_3,[7] makes it appropriate

to consider alternative pathways to the formation of Ti_2H_6. Possibilities include: TiH_2 +

$TiH_4 \rightarrow Ti_2H_6$, and $Ti_2H_4 + H_2 \rightarrow Ti_2H_6$. Andrews et al showed that there is H-atom

participation in their experiment. Since Margrave's experiment did *not* involve H-atoms, it is

relevant to compare the thermodynamics of the following reactions: $Ti_2H_6 + 2H \rightarrow Ti_2H_8$ and

$Ti_2H_6 + H_2 \rightarrow Ti_2H_8$ to assess the likelihood of conversion of Ti_2H_6 to Ti_2H_8 on annealing,

in the two experiments. Calculated energies of formation can be seen in Table 4 for

representative isomers of Ti_2H_6 and Ti_2H_8. At the best level of theory (MP2 and MCQDPT/TZVP(f)), the reactions with H-atoms are highly favorable (- 81.9 kcal/mol and - 85.1 kcal/mol); however, the reactions with H_2 are thermodynamically unfavorable (+18.6 kcal/mol and + 15.5 kcal/mol). This would suggest that on annealing in Andrews' experiment, conversion of Ti_2H_6 to Ti_2H_8 would be probable. Such a conversion would be much less likely in the Margrave experiment.

(c) **Bonding in Ti_2H_6.** We now examine the bonding characteristics of Ti_2H_6 in more detail, paying particular attention to the prototypical D_{2h} $H_2Ti(\mu-H)_2TiH_2$ structure.

Localized Orbitals. The energy localization method of Edmiston and Ruedenberg[39] was used to localize the orbitals for all isomers. The localized orbitals (LMOs) clearly show the presence of titanium-terminal hydrogen σ bonds, and Ti-H-Ti three center, two electron bonds. Representative plots may be seen in Figure 5a. The LMOs also clearly show two non-bonded electrons in each isomer (see Figure 5b for representative plots). The D_{2h} and D_{4h} isomers are clearly diradical in nature, with one electron localized onto on each titanium center for singlets as well as triplets. For the singlet and triplet C_{3v} isomers the non-bonded electrons are found on the three coordinated titanium center, and the three LMOs which represent these electrons are symmetrically equivalent. As the unpaired electrons in the C_s isomers are already localized on each Ti center in the canonical orbital plots (see Figure 4a), one on each titanium center, the LMO plots are not shown.

No strong Ti-Ti bond exists in any of the Ti_2H_6 singlet isomers, even though the Ti-Ti separation is small and two electrons are available. Now, consider the absence of a Ti-Ti bond in the D_{2h} singlet structure, in which the two electrons occupy the bonding σ and antibonding σ * orbitals almost equally with natural orbital occupation numbers of 1.11 and

0.89 electrons, respectively. Recall that the triplet is less stable than the singlet by only ~1 kcal/mol. Intuitively, this reluctance to form a σ bond is somewhat surprising, so the localized charge distribution (LCD) analysis[40] is used in the following paragraphs in an attempt to provide an interpretation.

LCD Energy Analysis. It is possible to force the formation of a Ti-Ti sigma bond by requiring all orbitals in the singlet to contain two electrons; i.e. an RHF singlet with a doubly occupied Ti-Ti σ bond orbital as the HOMO. At the diradical ROHF geometry, this RHF bonded species is destabilized with respect to the diradical by ~125 kcal/mol. If the RHF geometry is allowed to relax, the Ti-Ti bond shortens by ~ 0.5 Å and the destabilization energy is reduced to ~ 98 kcal/mol. Since this is still very large, the energy decomposition, and the density difference plots which require the two species to have identical geometries, are analyzed at the diradical geometry.

The LCD analysis decomposes the total energy into potential and kinetic energies of LMOs and the interactions between them. Using this analysis for both the bonded and diradical system, it is possible to track the origin of the destabilization of the bonded system. As the LCD analysis is only implemented for single determinant wavefunctions we compare the RHF singlet (bonded species) with the ROHF triplet (purely diradical) at the ROHF triplet geometry (see Figure 1).

In the LCD procedure one assigns a local nuclear charge distribution to each LMO. This was done according to the recommendations of Jensen and Gordon[40]: for Ti inner shell LMOs (core electrons) Ti was assigned a nuclear charge of 2, for the terminal Ti-H bond LMOs Ti and H were each assigned a nuclear charge of 1, and for the Ti-H-Ti bridging LMOs H was assigned a nuclear charge of 1 and each Ti was assigned a nuclear charge of 0.5.

An overview of the LCD decomposition strategy is shown in Figure 6. The total energy difference (in Hartrees) between the bonded species and the non-bonded diradical species is

given by $\Delta E = E$(bonded system) - E(non-bonded system). From Figure 6 the total energy difference ΔE(total) is + 0.1952 h, indicating overall destabilization of the molecule on formation of a Ti-Ti bond. This may be decomposed into changes in potential energy (ΔPE = + 0.7237 h) and kinetic energy (ΔKE = - 0.5286 h). So, *overall*, bond formation produces a favorable lowering of the KE, but this is more than offset by an increase in PE. A more detailed decomposition leads to the five contributions to ΔE outlined at the bottom of Figure 6: ΔPE(bond), ΔKE(bond), ΔPE(internal), ΔKE(rest), and ΔPE(interaction). Figure 7 groups these terms according to their physical significance: (a) bond formation; (b) rearrangement of core; terminal Ti-H, and Ti-H-Ti bridge electrons; and (c) interaction of the unpaired electrons/bond electrons with the rest of the molecule.

First consider PE and KE differences between the bond electrons in the Ti-Ti bonded system and the unpaired electrons in the non-bonded system; i.e. the energy difference directly due to bond formation from the two unpaired electrons. The PE term arises from internal energy, except for the very small (- 0.0006 h) unpaired electron-unpaired electron interaction energy. The values for ΔPE(bond) and ΔKE(bond), are + 0.4138 h and - 1.7184 h, respectively, resulting in a net stabilizing effect of - 1.3046 h. The density difference plot in Figure 8a, the RHF bond density minus the density of the unpaired electrons in the non-bonded triplet, clearly shows a build up of electron density between the Ti centers. The depletion of electron density from the atomic centers into the bond region decreases the attractive electron-nuclear interaction (increases PE) and decreases the KE by decreasing the curvature of the electron density. A schematic representation of this is given in Figure 7. So, the changes in the bond region itself favor bond formation due to KE lowering. This is entirely consistent with the Ruedenberg interpretation of covalent bonding[41] and with the origin of hydrogen bond formation suggested by Jensen and Gordon.[40a,b]

Next, consider the PE and KE changes which occur because of electron rearrangement in the rest of the molecule (the core, the terminal Ti-H bonds, and the two Ti-H-Ti bridges)

upon bond formation. The term ΔE(internal) includes self interactions and interactions amongst the core, the terminal Ti-H bonds, and the bridges. ΔPE(internal) and ΔKE(rest) are - 0.6221h and + 1.1898 h, respectively, resulting in a net destabilization of + 0.5677 h. The origin of ΔPE(internal) and ΔKE(rest) may found from density difference plots. Figures 8b and 8c illustrate a build up of electron density around the titanium atoms in the core and Ti-H bonds, respectively. This contraction of the orbitals around the Ti atoms explains the large increase in KE for the core and the Ti-H bonds (+ 0.5549 h and + 0.5474 h, respectively). Figure 8d shows depletion of electron density from directly around the hydrogen in the bridge bond and a corresponding build up closer to the Ti atoms. The KE decrease due to this orbital expansion around the hydrogen and the KE increase due to the corresponding contraction around the titaniums nearly cancel, resulting in the relatively small change in KE of the bridge of + 0.0875 h. We do not decompose ΔPE(internal) for the sake of simplicity; but, it is clear that orbital contractions which are responsible for the increase in KE also produce a corresponding decrease in PE though the KE term dominates. Again, a schematic representation of this can be seen in Figure 7.

Next, consider differences in PE interactions of the bond and the unpaired electrons with the core, Ti-H bond, and the bridges. The LCD analysis shows ΔPE(interaction) to be + 0.9321 h, a large destabilizing effect with all the above interactions making a significant positive contribution. These unfavorable interactions produced by electron-electron repulsion are, in fact, large enough to out weigh the stabilizing effect of the first four terms (ΔPE(bond) + ΔKE(bond) + ΔPE(internal) + ΔPE(rest) = - 0.7369 h) and produce a net destabilization ΔE(total) = + 0.1952 h on bond formation.

In summary, to form a Ti-Ti σ bond in $H_2Ti(\mu\text{-}H)_2TiH_2$ requires the depletion of electronic density from around the Ti's and a build up of charge between them. The potential energy of these two electrons is increased and their kinetic energy is lowered, the kinetic energy term dominating. The remaining electrons contract around the titaniums driving up the

kinetic energy and lowering the potential energy, the kinetic energy term dominating. The net effect of these interactions favor bond formation (ΔPE(bond) + ΔKE(bond) + ΔPE(internal) + ΔPE(rest) = - 0.7369 h); however, the increase in potential energy produced by the unfavorable interaction of the bond with the rest of the molecule (ΔPE(interaction) = + 0.9321 h) is large enough to ultimately ensure net destabilization upon bond formation (by + 0.1952 h). One simple interpretation here is that there is no σ bond in $H_2Ti(\mu$-$H)_2TiH_2$ due to steric repulsions between the bond and the rest of the molecule.

Mulliken populations. MCSCF and ROHF Mulliken populations with the TZVP basis set show positively charged Ti's and negatively charged H's for all isomers (both singlet and triplet). Charges range from ~ + 0.6 to ~ + 0.8 on the Ti's, and ~ - 0.1 to ~ - 0.3 on the hydrogens. These charges indicate considerable bond polarization in Ti_2H_6.

(d) Magnetic Properties of D_{2h} $H_2Ti(\mu$-$H)_2TiH_2$. Magnetic properties of molecular systems comprising dinuclear complexes which have a single unpaired electron on each metal center depend strongly on the intramolecular interaction of the metal centers with each other. This interaction itself can be affected by perturbations due to bridging and terminal ligands. If the singlet state is lowest in energy the interaction is antiferromagnetic: if the triplet state is lowest in energy the interaction is ferromagnetic.[22] Here we focus on the D_{2h} Ti_2H_6 structures, since they are the most closely related to experimentally known compounds.

The isotropic interaction between metal centers in these dinuclear complexes is reflected by the calculated singlet-triplet energy gap, where effects of spin-orbit coupling and magnetic dipole-dipole interactions are neglected. The isotropic effect has been found to be highly dominant in determining the magnetic interactions in di-titanium molecules studied experimentally,[17,18] and is the only effect considered here. Results of a study on the much smaller spin-orbit coupling effects[22] will be presented elsewhere.[42] To be consistent with

most of the experimental work referenced, we define the isotropic interaction parameter J by $-2J = E(\text{triplet}) - E(\text{singlet})$. Inclusion of dynamic as well as non-dynamic correlation effects is known to be essential to obtain reliable calculated singlet-triplet energy gaps in paramagnetic dinuclear complexes. A method which has achieved some success is "dedicated-difference configuration interaction" (DDCI2).[43] This CISD method (which is applicable to any multiplet splitting) calculates the singlet-triplet energy gap directly at one geometry, using the same reference orbitals for singlet and triplet (usually ROHF triplet geometry and orbitals). This reduces the number of configurations in the variational CISD, as many of these configurations make exactly the same contribution to the energy of both multiplicities. This method is a relatively inexpensive way of including dynamic correlation, and has been effective in predicting singlet-triplet energy gaps in compounds such as $[Cu_2Cl_6]^{2-}$ and $[Ni(NH_3)_4Cl]_2^{2+}$ in qualitative, and to some degree, quantitative agreement with experiment.[44]

We determine the singlet-triplet energy gap in D_{2h} $H_2Ti(\mu\text{-H})_2TiH_2$ by calculation of the singlet and triplet energies separately. These are single point MCQDPT energies at the geometries and reference wavefunctions of the TCSCF singlet and the ROHF triplet. Therefore, orbital and geometry relaxation effects are included. Table 5 shows the calculated values of the singlet-triplet energy gap in D_{2h} $H_2Ti(\mu\text{-H})_2TiH_2$. It is clear from Table 5 that basis set convergence is very rapid, suggesting large cancellation of error. At the MCSCF/TZVP(f,g) and ROHF/TZVP(f,g) levels the singlet ^1A_g state is predicted to be more stable than the triplet $^3B_{3u}$ state by 0.56 kcal/mol ($J = -98$ cm^{-1}), due to the small Ti-Ti bonding interaction discussed earlier. As expected, the inclusion of dynamic correlation stabilizes the singlet preferentially to the triplet as the ROHF wavefunction already contains like spin electron correlation. MCQDPT/TZVP(f,g) predicts that singlet ^1A_g is lower in energy than triplet $^3B_{3u}$ by 1.43 kcal/mol ($J = -250$ cm^{-1}). The intramolecular metal-metal interaction in D_{2h} $H_2Ti(\mu\text{-}$H$)_2TiH_2$ is therefore predicted to be antiferromagnetic. As neglect of dynamic correlation

(MCSCF) already results in a more stable singlet state, it is unlikely that a more sophisticated treatment of dynamic correlation than MCQDPT will change the sign of J. Review of the literature supports this, given that MCSCF generally underestimates the stability of the singlet with respect to the triplet in these types of systems.[23,45]

To asseses the effect of neglecting geometry and orbital relaxation, calculations were repeated with both singlet and triplet at the triplet geometry; first allowing orbital relaxation in the singlet calculation and then using the "frozen" ROHF orbitals for the singlet calculation. Constraining both geometries to that of the triplet lowered the singlet-triplet energy gap by 0.05 kcal/mol and 0.30 kcal/mol without and with dynamic correlation, respectively. The additional effect of neglecting orbital relaxation lowered the gap by a further 0.15 kcal/mol and 0.04 kcal/mol without and with dynamic correlation, respectively. These effects are not negligible in terms of wavenumbers (0.34 kcal/mol corresponds to $J = 60$ cm^{-1}).

The singlet-triplet splitting energy in D_{2h} $H_2Ti(\mu$-$H)_2TiH_2$ is for the homodinuclear titanium(III) system in which interactions of the Ti centers with bridging and terminal ligands is *minimal* and the Ti-Ti σ-σ ground state isotropic interaction is the least perturbed by its environment. The most closely related experimentally characterized compound is *rac*-{[$C_2H_4(\eta^5$-tetrahydroindenyl)$_2$]-Ti(III)(μ-H)]$_2$[13] which also has bridging hydrogens. It exhibits antiferromagntic behavior (no value for J is reported; only the sign) in line with our prediction for D_{2h} $H_2Ti(\mu$-$H)_2TiH_2$. The experimentally measured antiferromagnetic singlet-triplet splitting in [$Cp_2Ti(\mu$-$OCH_3)$]$_2$ is 1.53 ± 0.02 kcal/mol ($J = -268 \pm 4$ cm^{-1})[18] very close to the calculated value of 1.43 kcal/mol for D_{2h} $H_2Ti(\mu$-$H)_2TiH_2$. Superficially this may indicate that effects due to bridging ligands, terminal ligands, and Ti-Ti separation, which is 3.35 Å in [$Cp_2Ti(\mu$-$OCH_3)$]$_2$ and 3.04 Å in D_{2h} $H_2Ti(\mu$-$H)_2TiH_2$, are small. However, even if one is to trust that the calculated value is accurate enough for such a comparison, it may

indicate opposing effects which cancel each other in this case, considering that replacement of the (μ-OCH$_3$) bridging ligands with (μ-Cl) ligands[18,17] results in a experimentally determined value of $J = -111$ cm^{-1} (S-T gap of 0.63 kcal/mol), and replacement with (μ-O) will even change the sign of the interaction ($J = + 8$ cm^{-1}). Thus, future work will focus on the effect of systematic replacement of bridging and terminal hydrogens with other species on the fundamental electronic structure of this system, in order to establish trends allowing prediction and therefore modification of the magnetic properties of molecules. This seems a reasonable goal given that prediction of trends is easier than prediction of absolute J values.

IV. Conclusions

Five singlet and five triplet minima were found on the two lowest potential energy surfaces of Ti$_2$H$_6$, all with bridging hydrogens. The (μ-H)$_3$ C$_{3v}$ staggered and eclipsed structures, which have been described in the past by a closed shell RHF reference wavefunction, actually require a 2 electron, 3 orbital FORS-MCSCF reference wavefunction; the triplet structures require an ROHF reference wavefunction in which two degenerate states are averaged. The remaining minima are adequately described with TCSCF or ROHF reference wavefunctions.

No Ti-Ti bonding is possible in the triplet minima. More surprising is the prediction there is little or no Ti-Ti bonding in the singlet minima as well. In the (μ-H)$_3$ C$_{3v}$ minima both of the non-bonded electrons are found on the least saturated Ti. The (μ-H)$_3$ C$_s$ minima (^{1}A" and ^{3}A") are both purely diradical. Natural orbital analysis of the wavefunctions of the (μ-H)$_2$

D_{2h} singlet and the (μ-H)$_4$ D_{4h} singlet show a large amount of diradical character. although a slight bonding interaction is predicted in the D_{2h} and D_{4h} singlets. This is supported by calculated singlet-triplet splittings of 1.3 and 1.4 kcal/mol for the D_{2h} and D_{4h} structures. respectively. All minima are predicted to be stable with respect to $2TiH_3$. The C_s structure is the most stable with an exothermic dimerization energy of ~ 56 kcal/mol. Inclusion of dynamic correlation is found to be important, its effects being especially large for the (μ-H)$_3$ and (μ-H)$_4$ structures.

Comparison of calculated frequencies of representative Ti_2H_6 isomers with the experimental spectra of Andrews et al suggests that the presence of Ti_2H_6 in the matrix is entirely possible. The same conclusion may reached by comparison of calculated frequencies to the spectra of Margrave et al. In Margrave's experiment TiH_3 is not observed, suggesting a route to Ti_2H_6 other than the dimerization of TiH_3. $TiH_2 + TiH_4 \rightarrow Ti_2H_6$, and $Ti_2H_4 + H_2 \rightarrow Ti_2H_6$ are suggested as possibilities. The absence of H atoms in the Margrave experiment will reduce the likelihood of the hydrogenation reaction $Ti_2H_6 \rightarrow Ti_2H_8$ on annealing, due to unfavorable thermodynamics when the reaction occurs with H_2.

Localized orbital plots of the terminal Ti-H and bridging Ti-H-Ti bonds are much the same as those seen in Ti_2H_8. The lack of Ti-Ti bonding in C_s, D_{4h}, and C_{3v} singlets may be rationalized in terms of location of electrons, symmetry and orientation of d-orbitals. This is not the case for the D_{2h} singlet which appears ideally suited to Ti-Ti σ bond formation. An LCD energy analysis suggests that the lack of Ti-Ti bonding in the D_{2h} isomer arises due to steric crowding; i.e. unfavorable interactions of the bond with the surrounding molecule.

The D_{2h} $H_2Ti(\mu$-H)$_2TiH_2$ structure is an excellent prototype for the many homodinuclear titanium (III) compounds known experimentally. A good example is titanocene

dimer $[(\eta^5-C_5H_5)Ti(\mu-H)]_2(\mu-\eta^5:\eta^5-C_{10}H_8)$. Experimental evidence suggests either a Ti-Ti

bond or a large singlet-triplet energy gap in this compound. Since we find no such bond in

$H_2Ti(\mu-H)_2TiH_2$ and a very small singlet-triplet energy gap, it appears that the presence of the

cyclopentadienyl rings and/or the distortion of the bridge out of the plane must modify the

electronic structure in such a way that bond formation is facilitated or the singlet is stabilized

significantly, preferentially to the triplet. This is the subject of an ongoing study.

Paramagnetic homodinuclear titanium (III) compounds for which the singlet is more

stable than the triplet are antiferromagnetic. If the triplet is more stable than the singlet, the

compound is ferromagnetic. By this criterion we find $H_2Ti(\mu-H)_2TiH_2$ to be antiferromagnetic,

and conclude that this is due to a small bonding interaction between Ti's in the singlet (isotropic

interaction).

References

1. Toogood, G. E. ; Wallbridge, M. G. H. *Adv. Inorg. Chem. Radiochem.* **1982** 25, 267.

2. Bode, B.; Gordon, M. S., The Catalyzed Hydrosilation Reaction, *J. Am. Chem. Soc.*.

Submitted.

3. Kawamura-Kuribayahi, H.; Koga, N.; Morokuma, K. *J. Am. Chem. Soc.* **1992.** 114. 2359.

4. Gauvin, F.; Britten, J.; Samuel, E.; Harrod, J. F. *J. Am. Chem. Soc.* **1992,** 114. 1489.

5. Jolly, C. A.; Marynick, D. S. *J. Am. Chem. Soc.* **1989,** 111. 7968.

6. Chertihin, G. V.; Andrews, L. *J. Am. Chem. Soc.* **1994,** 116, 8322.

7. Xiao, Z. L.; Hauge, R. H.; Margrave, J. L. *Phys. Chem.* **1991,** 95, 2696.

8. Baushlicher, C. W. *J. Phys. Chem.* **1988,** 92, 3020.

9. a) Fujii, T. S.; Iwata, S. *Chem. Phys. Lett.* **1996,** 251, 150. b) Kudo, T.; Gordon, M. S. *J. Chem . Phys.* **1995,** 102, 6806.

10. a) Ma, B.; Collins, C. L.; Schaefer, H. F. *J. Am. Chem. Soc.* **1996,** 118, 870. b) Schaefer, H. F. *J. Chem . Phys.* **1992,** 96, 6857.

11. Webb, S. P.; Gordon, M. S. *J. Am. Chem. Soc.* **1995,** 117, 7197.

12. Garcia, A.; Ugalde, J. M. *J. Phys. Chem.* **1996,** 100, 12277.

13. Xin, S.; Harrod, J. F.; Samuel, E. *J. Am. Chem. Soc.* **1994,** 116, 11562.

14. a) Troyanov, S. I.; Antropiusová, H.; Mach, K. *J. Organometal. Chem.* **1992,** 427, 49. b) Davidson, A.; Wreford, S. S. *J. Am. Chem. Soc.* **1974,** 96, 3017. c) Brintzinger, H. H.; Bercaw, J. E. *J. Am. Chem. Soc.* **1970,** 92, 6182.

15. Guggenberger, L. J.; Tebbe, F. N. *J. Am. Chem. Soc.* **1975,** 98, 4137.

16. Coutts, R. S. P.; Wailes, P. C.; Martin, R. L. *J. Organometal. Chem.* **1973,** 47, 375.

17. Jungst, R.; Sekutowski, D.; Davis, J.; Luly, M.; Stucky, G. *Inorg. Chem.* **1977,** 16, 1645.

18. Samuel, E.; Harrod, J. F.; Gourier, D.; Dromzee, Y.; Robert, F.; Jeannin, Y. *Inorg. Chem.* **1992,** 31, 3252.

19. Dick, D. G.; Stephan, D. W. *Can. J. Chem.* **69,** 1146.

20. Rohmer, M.; Bénard, M. *Organometallics.* **1991,** 10, 157.

21. Lukens, W. W.; Andersén, R. A. *Inorg. Chem.* **1995**, 34, 3440.

22. a) Kahn, O. *Angew. Chem. Int. Ed. Engl.* **1985**, 24, 834. b) Kahn, O. *Molecular Magnetism* ; VCH; New York, 1993; Chapters 6-9.

23. Mödl, M.; Povill, A.; Rubio, J.; Illas, F. *J. Phys. Chem. A* **1997**, 101, 1526.

24. Castell, O.; Caballol, R.; García, V.M.; Handrick, K. *Inorg. Chem.* **1996**, 35, 1609.

25. Watchers, A. J. H. *J. Chem. Phys.* **1970**, 52, 1033.

26. Hood, D. M.; Pitzer, R. M.; Schaefer, H. F. *J. Chem . Phys.* **1979**, 71, 705.

27. Rappe, A. K.; Smedley, T. A.; Goddard, W. A. *J. Phys. Chem.* **1981**, 85, 2607.

28. Dunning, T. H.; Hay, P.J. In *Methods of Electronic Structure Theory*; Schaefer, H. F., III. Ed.; Plenum Press: New York. 1977; pp 1-27.

29. Glezakou, V-A.; Gordon, M. S. *J. Phys. Chem. A* **1997**, 101, 8714.

30. (a) Sunberg, K. R.; Ruedenberg, K. in *Quantum Science,* edited by Calais, J. L.; Goscinski, O.; Linderberg, J.; Ohrn, Y., Plenum, New York, 1976, pp 505. (b) Cheung, L. M.; Sunberg, K. R.; Ruedenberg, K. *Int. J. Quantum Chem.* **1979**, 16, 1103. (c) Ruedenberg, K.; Schmidt, M.; Gilbert, M. M.; Elbert, S. T. *Chem. Phys.* **1982**, 71,41.

31. Roos, B. O.; Taylor, P.; Siegbahn, P. E. M. *Chem. Phys.* **1980**, 48, 157.

32. (a) Knowles, P. J.; Andrews, J. S.; Amos, R. D.; Handy, N. C.; Pople, J. A. *Chem. Phys. Lett.* **1991**, 186, 130. (b) Lauderdale, W. J.; Stanton, J. F.; Gauss, J.; Watts, J. D.; Bartlett, R. J. **1991**, 187, 21.

33. (a) Nakano, H. *J. Chem . Phys.* **1993**, 99, 7983. (b) Nakano, H. *Chem. Phys. Lett.* **1993**, 207, 372.

34. Schmidt, M.W.; Baldridge, K.K.; Boatz, J.A.; Jensen, J.H.; koseki, S.; Matsunaga, N.; Gordon, M.S.; Ngugen, K.A. ; Su, S.; Windus, T.L.; Elbert, S.T.; Montgomery, J.; Dupuis, M. *J. Comp. Chem.* **1993**, 14, 1347.

35. Dapporto, P.; Fallani, G.; Midollini, L.; Sacconi, L. *J. Am. Chem. Soc.* **1972**, 95, 2023.

36. Bau, R.; Carroll, W. E.; Teller, R. G.; Koetzle, T. F. *J. Am. Chem. Soc.* **1977**, 99, 3872.

37. Clark, R. J. H.*The Chemistry of Titanium and Vanadium* ; Elsevier; Amsterdam, 1968; pp 6.

38. Kaupp, M.; Schleyer, P.R. *J. Am. Chem. Soc.* **1993**, 115, 11202.

39. Edmiston, C.; Ruedenberg, K. *Rev. Mod. Phys.* **1963**, 35, 457.

40. a) Jensen, J. H.; Gordon, M.S. *Acc. Chem. Res.* **1996**, 29, 536. b) Jensen, J. H.; Gordon, M. S. *J. Am. Chem. Soc.* **1995**, 99, 8091. c) England, W.; Gordon, M. S. *J. Am. Chem. Soc.* **1971**, 93, 4649.

41. Ruedenberg, K. *Rev. Mod. Phys.* **1962**, 34, 326.

42. Webb, S. P.; Gordon, M. S. To be submitted.

43. Handrick, K.; Malrieu, J. P.; Castell, O. *J. Chem . Phys.* **1994**, 101, 2205.

44. a) Castell, O.; Miralles, J.; Caballol, R. *Chem . Phys.* **1994**, 179, 377. b) Castell, O.; Caballol, R.; García, V. M.; Handrick, K. *Inorg. Chem.* **1996**, 35, 1609.

45. Fink, K.; Fink., R.; Staemmler, V. *Inorg. Chem.* **1994**, 33, 6219.

Table 1. Calculated total energies (in Hartrees) of TiH$_3$ ^{2}A'$_1$ state.

Point Group	State	TZVP			TZVP(f)		TZVP(f,g)	
		ROHF(opt)	MCQDPT[a]	RMP2[a]	MCQDPT[a]	RMP2[a]	MCQDPT[a]	RMP2[a]
D$_{3h}$	^{2}A'$_1$	-850.07580	-850.16532	-850.16293	-850.17907	-850.17635	-850.18219	-850.17944

[a] All single-point energies calculated at the ROHF/TZVP optimized geometry.

Table 2. All energies relative to $2 \times TiH_3$ D_{3h} $^2A'_1$ monomer energy in kcal/mol ($E = E(Ti_2H_6) - E(2 \times TiH_3)$).

Point Group	MCSCF Active Space	State	TZVP MCSCF	TZVP MCQDPT	TZVP(f) MCQDPT	TZVP(f,g) MCQDPT	State	TZVP ROHF	TZVP RMP2	TZVP(f) RMP2	TZVP(f,g) RMP2
			Singlet					**Triplet**			
C_s	not applicable ROHF used	$^1A''$	-41.0	-55.0	-55.2	-56.1	$^3A''$	-41.5	-53.2	-55.5	-56.4
D_{2h}	(2,2)	^1A_g	-42.9	-49.6	-51.2	-51.6	$^3B_{1u}$	-42.4	-48.5	-50.0	-50.3
D_{4h}	(2,2)	^1A_g	-22.2	-45.2	-50.5	-51.5	$^3A_{2u}$	-21.8	-44.0	-49.1	-50.1
C_{3v} eclipsed	(2,3)	$^1A_1$	13.3	-27.1	-31.2	-	^3E	-11.9	-45.0[a]	-48.3[a]	-
staggered		$^1A_1$	13.3	-22.4	-26.3	-	^3E	-11.8	-40.2[a]	-43.2[a]	-
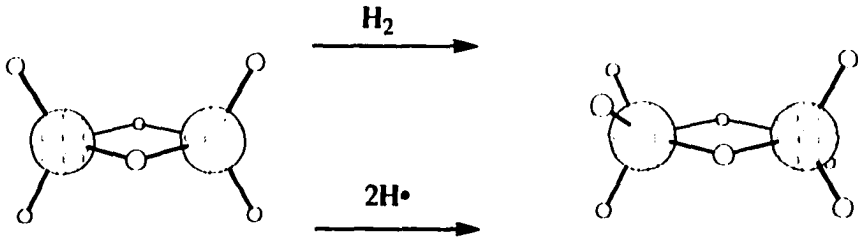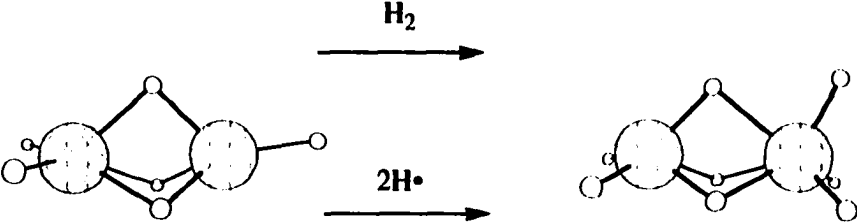
[a] Dynamic correlation effects in the C_{3v} ^3E structures were calculated using the MCQDPT method.

Table 3. Calculated Harmonic Vibrational Frequencies for selected Ti_2H_6 isomers.

Vibration[a]	Intensity / km mol^{-1}	Frequency[b] / cm[-1]	Scaled Frequency[c] /cm[-1]	Exptl. Frequency[d] /cm[-1]	Exptl. Assignment
$C_s(^1A'')$					
H_t bend	296.2	625.7	593.0	500 (broad)	Ti_xH_y
H_{br} bend	402.3	744.2	705.2		
H_{br} bend	376.1	831.0	787.5		
H_{br} bend	751.7	1204.3	1141.3		
$Ti-H_{br}$ str	398.0	1375.7	1303.7	1305	
$Ti-H_{br}$ str	1829.6	1557.4	1475.9	1485.2	Ti_xH_y
$Ti-H_t$ str	921.2	1656.8	1570.1	1570	
$Ti-H_t$ str	356.6	1706.6	1617.2	1632	Ti_xH_y
$D_{2h}(^1A_g)$					
H_t bend	376.6	574.8	544.7	500 (broad)	Ti_xH_y
H_{br} bend	175.4	744.6	705.6		
$Ti-H_{br}$ str	663.8	1128.5	1069.4		
$Ti-H_{br}$ str	2249.7	1412.9	1338.9	1330	
$Ti-H_t$ str	2040.1	1679.5	1591.5	1590	
$Ti-H_t$ str	328.7	1749.2	1657.6	1656.7	TiH_4
$D_{4h}(^1A_g)$					
H_{br} bend	213.8 (x2)	943.9	894.4		
$Ti-H_{br}$ str	2360.8	1254.6	1188.9	1200	Ti_xH_y
$Ti-H_{br}$ str	898.8 (x2)	1290.7	1223.1	1225	Ti_xH_y
$Ti-H_t$ str	1437.5	1685.0	1596.8	1590	
$C_{3v}(^3E)$					
H_{br} bend	136.9 (x2)	808.3	766.0		
H_{br} bend	411.1	892.5	845.7		
$Ti-H_{br}$ str	1659.4	1139.3	1079.6		
$Ti-H_{br}$ str	313.1	1485.2	1407.4	1422.7	$TiH(H_2)$
$Ti-H_t$ str	711.6 (x2)	1742.3	1651.0	1640.5	Ti_xH_y

[a] H_t = terminal hydrogen; H_b = bridging hydrogen. [b] Only calculated frequencies with an intensity greater than 100 km/mol are reported. [c] Scaling factor of 0.948 used. [d] Reference 6.

Table 4. Thermodynamics of the reactions $Ti_2H_6 + H_2 \rightarrow Ti_2H_8$ and $Ti_2H_6 + 2H \rightarrow Ti_2H_8$ for selected isomers of Ti_2H_6 and Ti_2H_8. The MCSCF and MCQDPT methods are used for Ti_2H_6; the RHF and MP2 methods for Ti_2H_8. Energies are in kcal/mol.

	MCSCF/RHF		MCQDPT/MP2	
	TZVP	TZVP(f)	TZVP	TZVP(f)
H_2	+73.6	+71.0	+19.9	+15.5
2H•	-10.8	-13.5	-78.0	-81.9
H_2	+72.7	+70.0	+22.5	+18.6
2H•	-9.8	-12.5	-80.6	-85.1

D_{2h} (^1A_g) C_{2h}

C_s ($^1A''$) C_s

Table 5. Calculated singlet-triplet energy gap (E(triplet) - E(singlet)) for D_{2h} $H_2Ti(\mu-H)_2TiH_2$ in kcal/mol.

Basis Set	Method of Singlet/Triplet Calculation	
	MCSCF/ROHF	MCQDPT2/MCQDPT2
TZVP	0.56	1.33
TZVP(f)	0.56	1.40
TZVP(f,g)	0.56	1.43
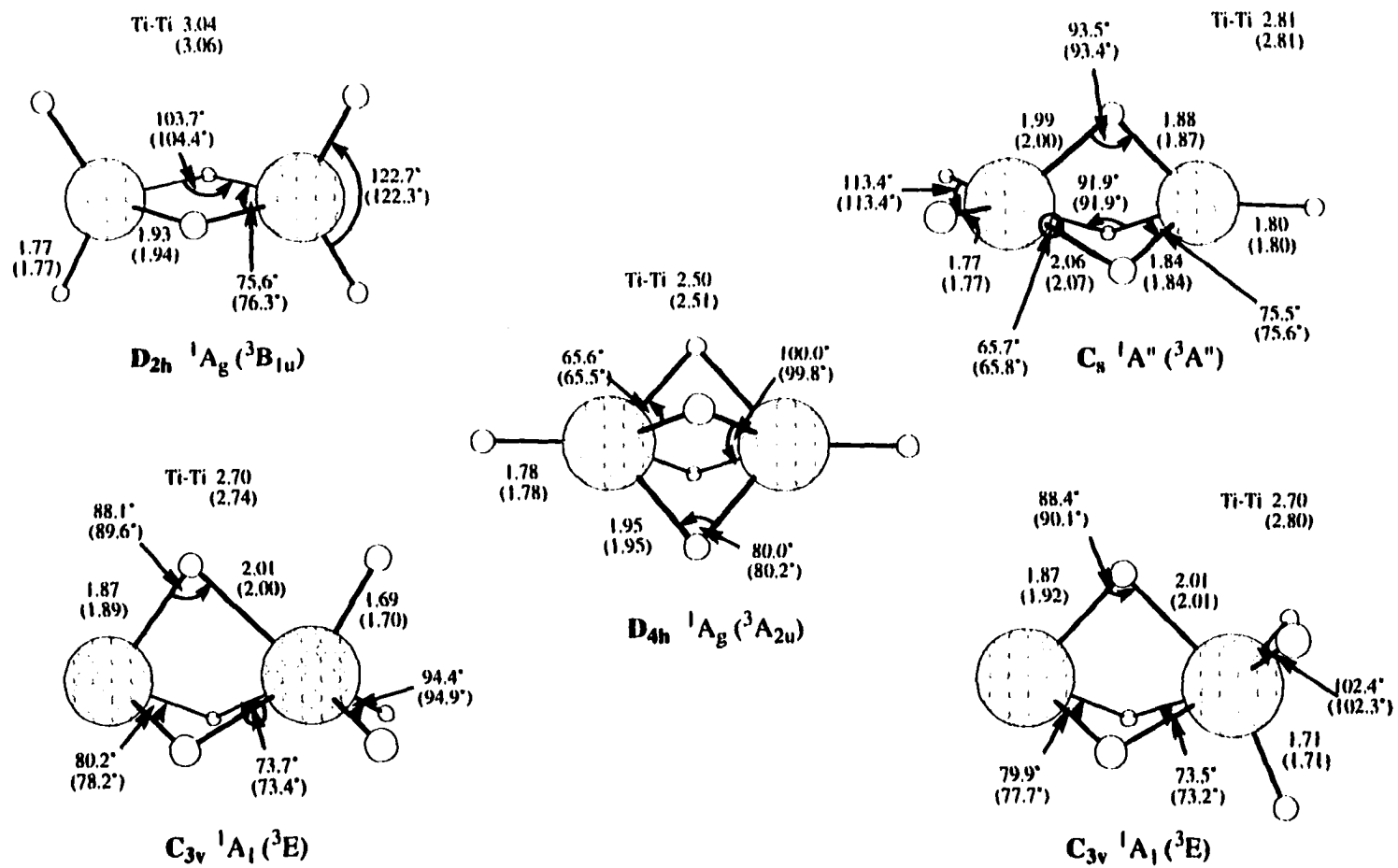
Figure 1. MCSCF/TZVP singlet and ROHF/TZVP triplet local minima on the two lowest potential energy surfaces of Ti_2H_6. Bond lengths are in Angstroms. Brackets signify triplet geometry.

2a)

^1E $\begin{matrix} e \\ a_1 \end{matrix}$

^1E C $\begin{matrix} e \\ a_1 \end{matrix}$ - C

^1E $\begin{matrix} e \\ a_1 \end{matrix}$

^1E $\begin{matrix} e \\ a_1 \end{matrix}$
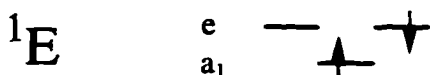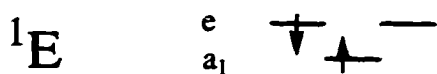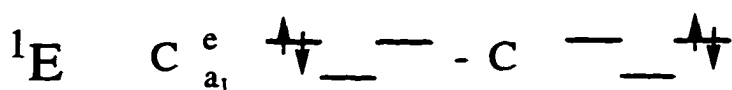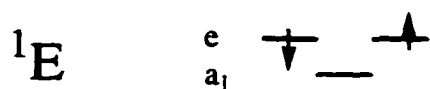
average of 2 states

E = -6.9 kcal/mol

$^1A_1$ $\begin{matrix} e \\ a_1 \end{matrix}$
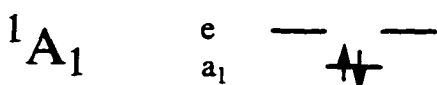
(2,3) MCSCF

E = -13.6 kcal/mol

$^1A_1$ C $\begin{matrix} e \\ a_1 \end{matrix}$ + C
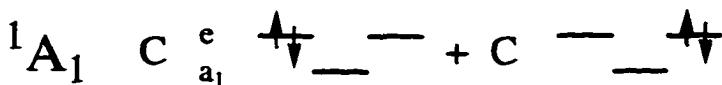
Figure 2. a) Possible singlet states for C_{3v} isomers. Energies given are for the eclipsed isomer and are relative to the closed shell RHF energy with double occupation of the a_1 orbital. b) Possible triplet states for C_{3v} isomers. Energies given are for the eclipsed isomer and are relative to the closed shell RHF energy with double occupation of the a_1 orbital.

2b)

$^3A_2$ — E = -32.9 kcal/mol

^3E

^3E

average of 2 states

E = -38.9 kcal/mol
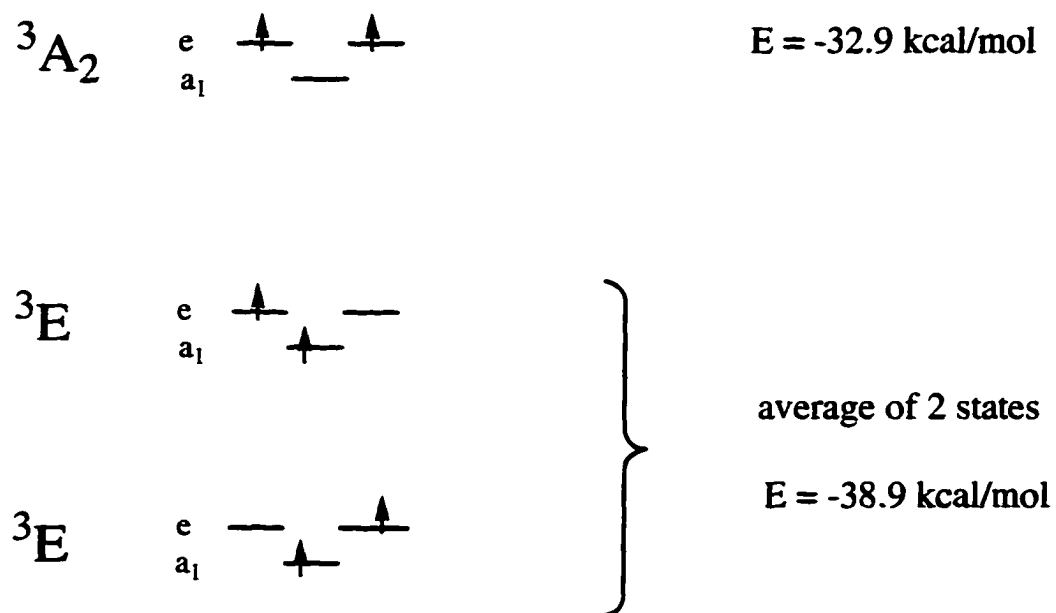
Figure 2. Continued.

D_{3h} $^2A'_1$
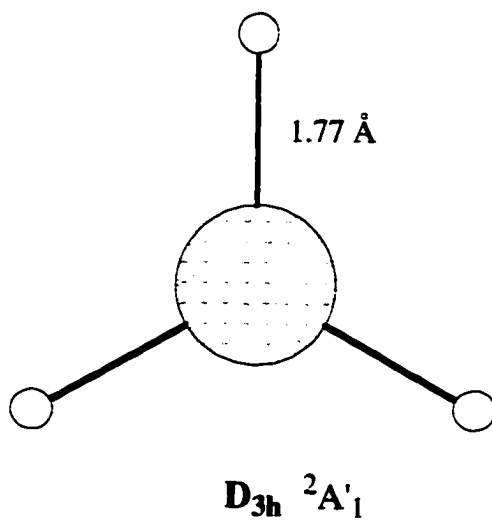
Figure 3. ROHF/TZVP optimized minimum energy structure of TiH_3.

a) C_s

a"   a'

states	occ. #		occ. #
$^1A''$	1.0		1.0
$^3A''$	1.0		1.0
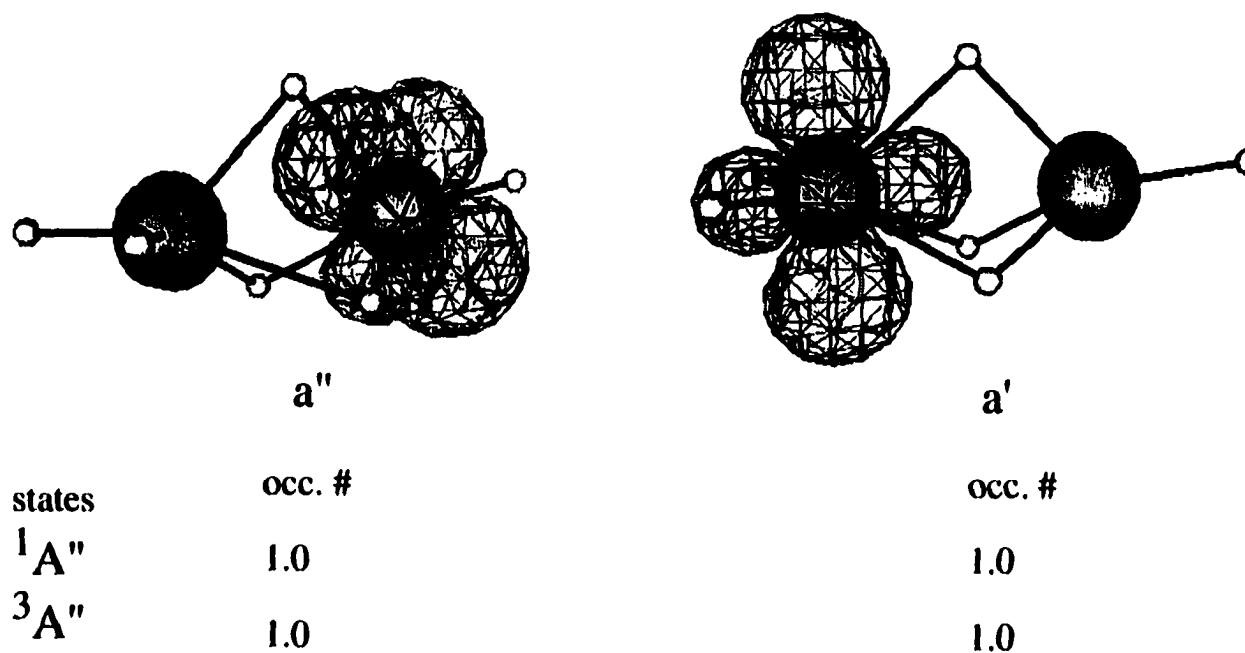
Figure 4. a) Three dimensional plots of the 2 HOMO's in the C_s, D_{2h}, and D_{4h} Ti_2H_6 isomers. For the D_{2h} and D_{4h} singlets these orbitals constitute the active orbitals used in the TCSCF calculations. Occupation numbers shown for the D_{2h} and D_{4h} isomers are from a natural orbital analysis. Singlet and triplet state orbitals are qualitatively the same; therefore only one set is shown. The orbital contour value used in the plots is 0.04 Bohr3/2. b) Three dimensional plots of the three active molecular orbitals in the $^1A_1$ and ^3E C_{3v} eclipsed isomers. Singlet occupation numbers are from a natural orbital analysis. Singlet and triplet state orbitals are qualitatively the same; therefore only one set is shown. The orbital contour value used is 0.04 $Bohr^{3/2}$.

D$_{2h}$

a$_g$

b$_{1u}$
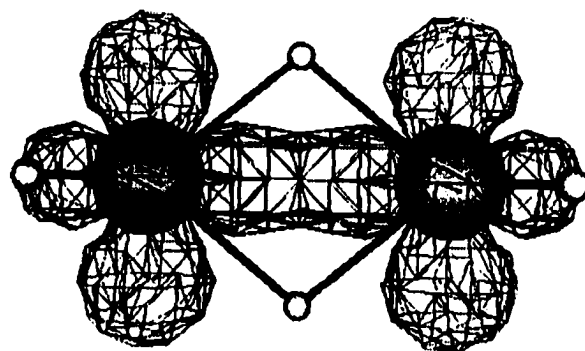
states	occ. #		occ. #
^1A_g	1.11		0.89
$^3B_{1u}$	1.0		1.0
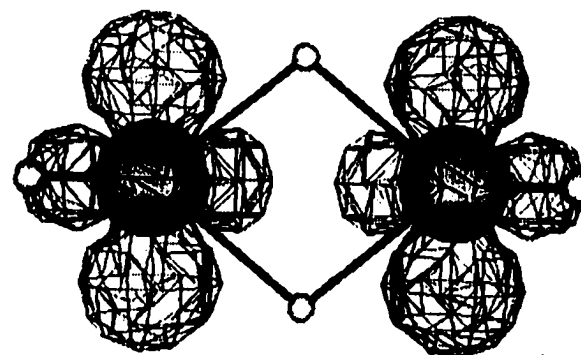
Figure 4. a) Continued.

D$_{4h}$
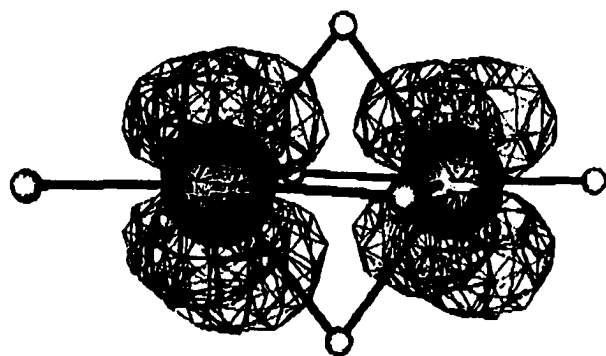
b$_{1g}$

states	occ. #
^1A_g	1.09
$^3A_{2u}$	1.0
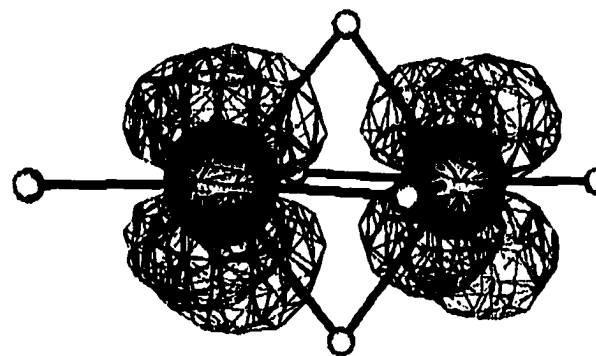
b$_{2u}$

	occ. #
	0.91
	1.0

Figure 4. a) Continued.

b) C$_{3v}$

e

states	occ. #		occ. #
$^1A_1$	0.25		0.25
^3E	0.50		0.50

a$_1$
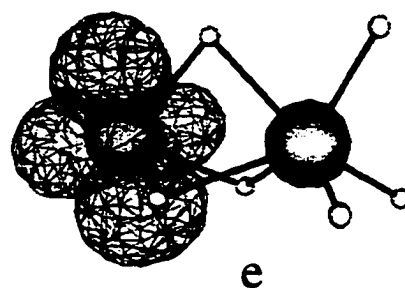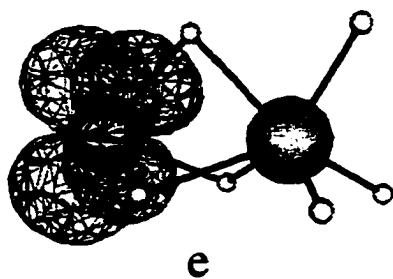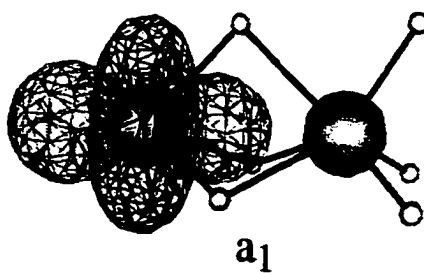
states	occ. #
$^1A_1$	1.51
^3E	1.00

Figure 4. Continued.

a)
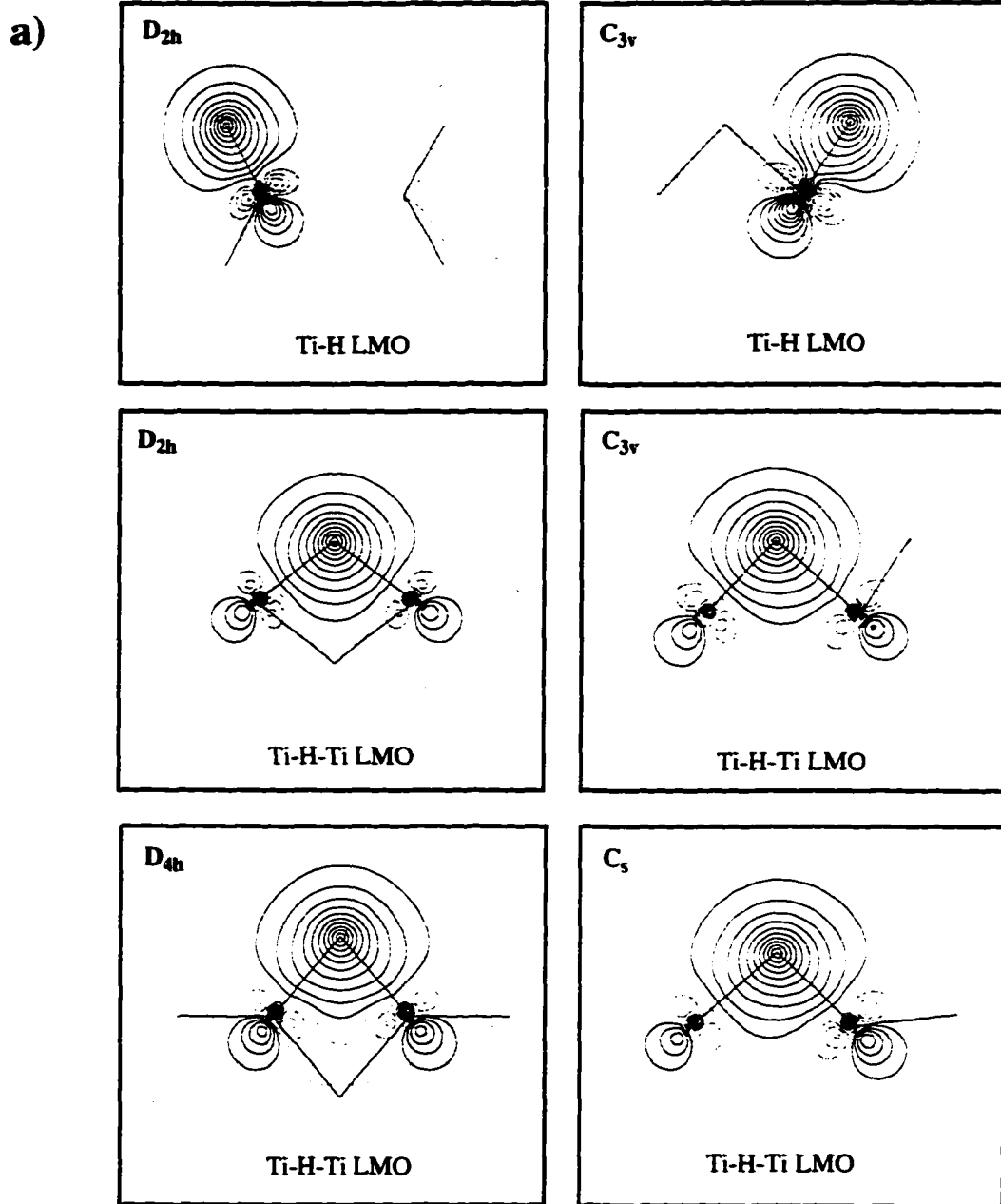
Figure 5. a) Localized orbital plots showing representative titanium-terminal hydrogen bonds and titanium-hydrogen-titanium bridging bonds in the isomers of Ti_2H_6. Contour increments are 0.05 $Bohr^{3/2}$. b) Localized orbital plots showing unpaired/non-bonded electrons for D_{2h}, D_{4h}, and C_{3v} Ti_2H_6 isomers. Singlet and triplet plots are qualitatively the same so only one set for each structure is shown. For D_{4h} the two d-orbital lobes with opposite phase are in the plane perpendicular to the page. Only one of three equivalent plots shown for the C_{3v} isomer. Contour increments are 0.05 $Bohr^{3/2}$.

b)

Figure 5. Continued.

$$\Delta E(\text{total}) = E(\text{bonded} - E(\text{non-bonded}$$
$$\text{system}) \quad \text{system})$$

| $\Delta PE(\text{total})$ | $+ 0.7237$ h |
| $\Delta KE(\text{total})$ | $- 0.5286$ h |

| $\Delta E(\text{total})$ | $+ 0.1952$ h |
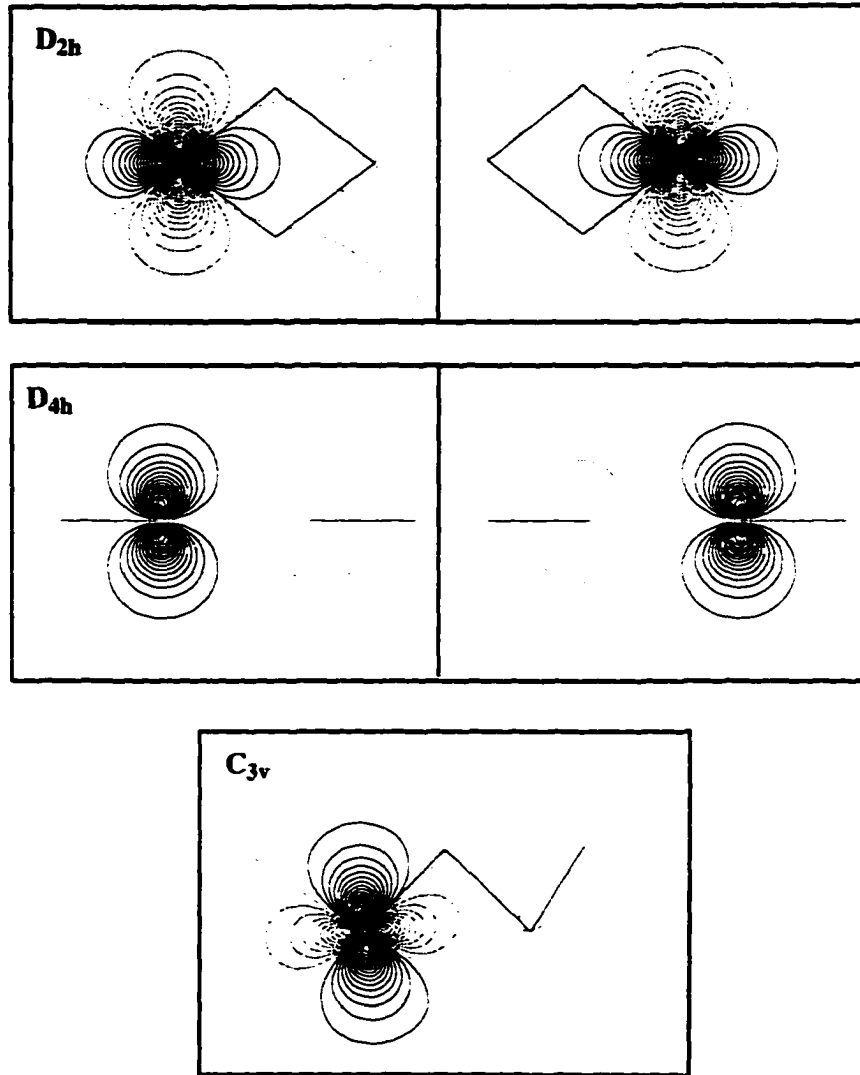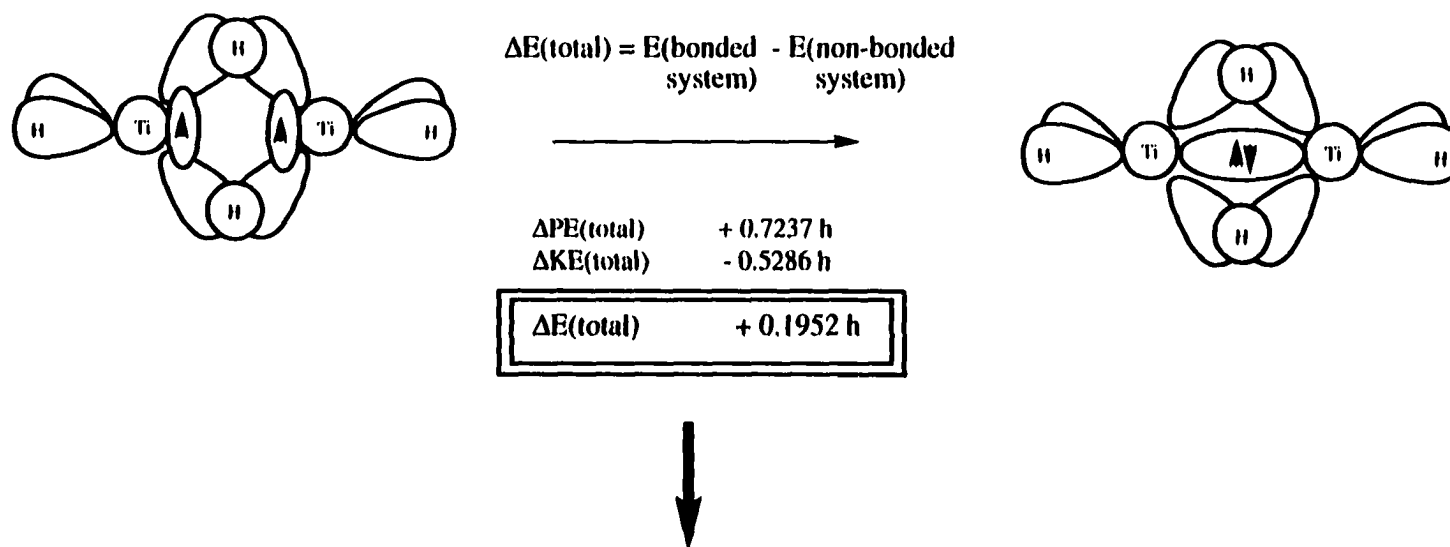
LCD analysis used to decompose this energy difference $\Delta E(\text{total})$ into contributions from:

1) bond formation ($\Delta PE(\text{bond})$ and $\Delta KE(\text{bond})$)
2) rearrangement of remaining electrons in the rest of the molecule ($\Delta PE(\text{internal})$ and $\Delta KE(\text{rest})$)
3) bond/unpaired electrons interacting with the rest of the molecule ($\Delta PE(\text{interaction})$)

Figure 6. LCD energy analysis strategy for $H_2Ti(\mu\text{-}H)_2TiH_2$. $\Delta E(\text{total})$ is energy difference (in Hartrees) between the system constrained to have a Ti-Ti bond and the non-bonded diradical triplet system.
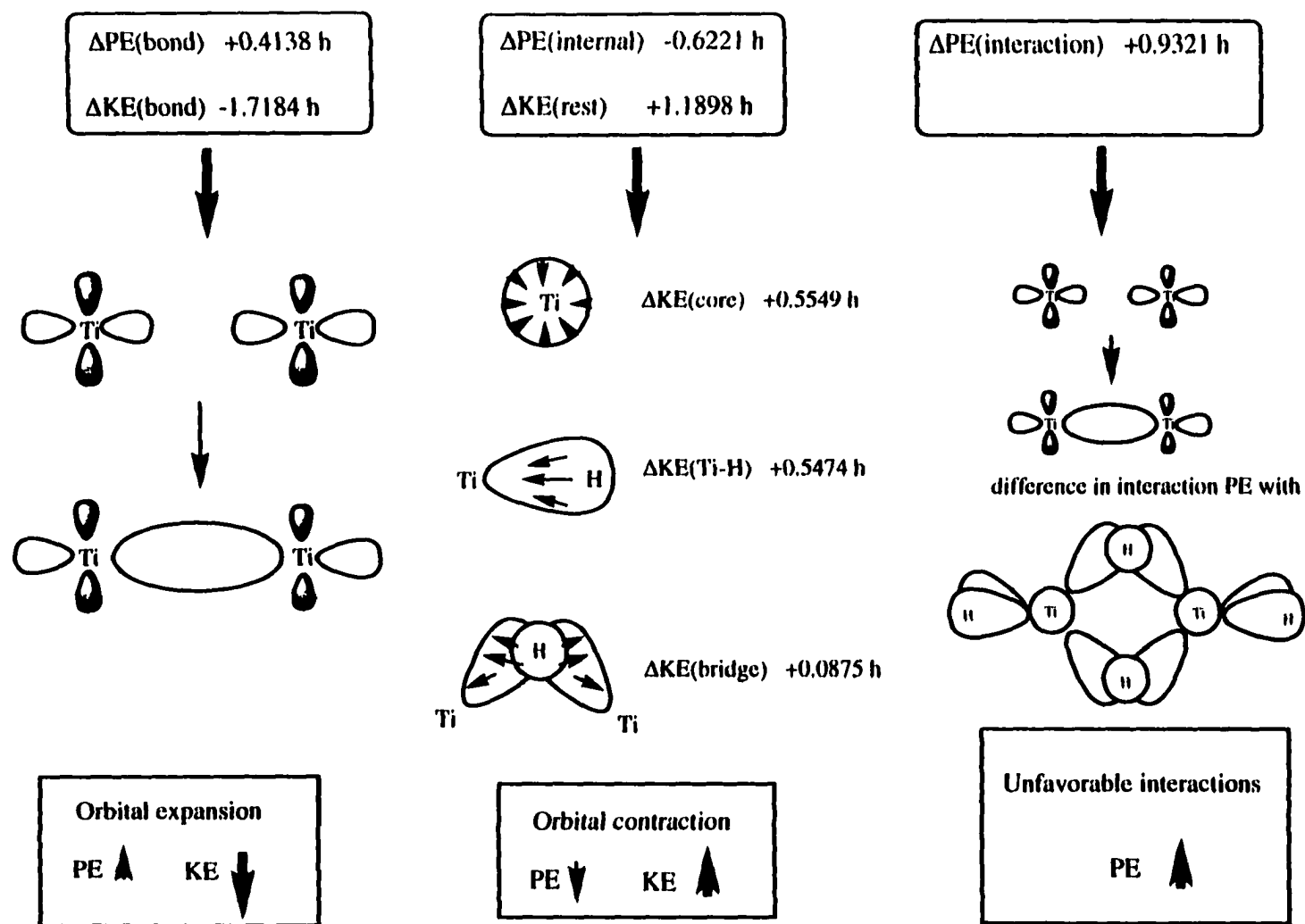
Figure 7. LCD analysis breakdown of ΔE(total) and schematic explanations of energy increases and decreases. Small arrows within orbitals indicate movement of electrons when a Ti-Ti bond is formed.

a)   b)

c)   d)
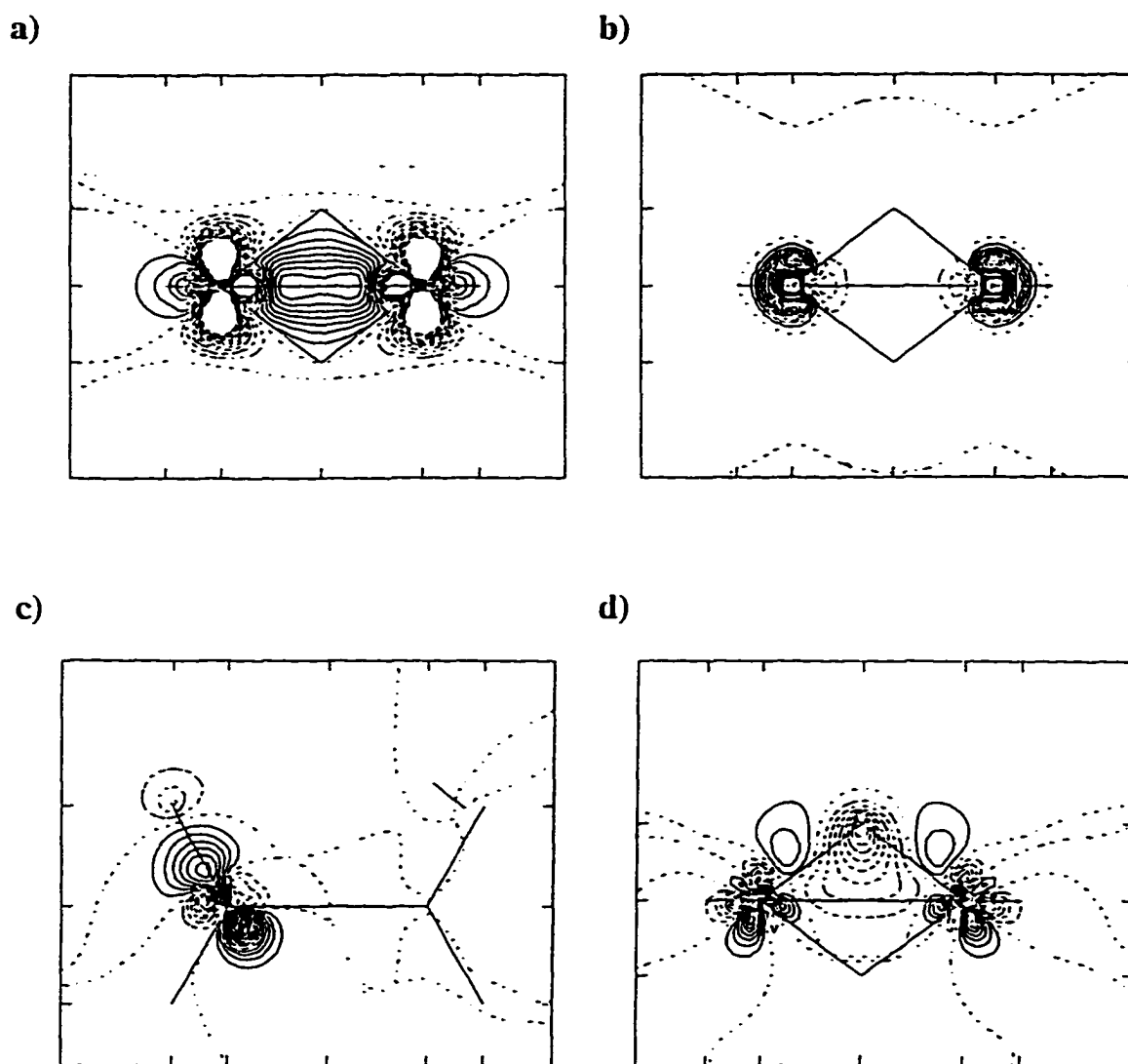
Figure 8. Density difference plots for a) the Ti-Ti bond; b) the Ti core electrons; c) a terminal Ti-H bond; and d) a Ti-H-Ti bridging bond. These plots represent the RHF Ti-Ti bonded system's density minus the ROHF triplet's density. For a) and b) contour increments are 0.002 bohr^3; for c) and d) contour increments are 0.001 bohr^3.

CHAPTER 5. THE EFFECT OF SPIN-ORBIT COUPLING ON THE MAGNETIC PROPERTIES OF $H_2Ti(\mu-H)_2TiH_2$

A paper submitted to the Journal of Chemical Physics

Simon P. Webb and Mark S. Gordon

Abstract

Excited states of singlet and triplet $H_2Ti(\mu-H)_2TiH_2$ have been calculated using FORS-MCSCF wavefunctions. The effects of orbital relaxation are determined by optimizing orbitals for all states separately and comparing to state-averaged calculations, and are found to be small. Dynamic electron correlation included through second-order perturbation is found to have a considerable effect on excited state relative energies, but not on the ordering of states. Spin-orbit coupling effects are introduced by a one-electron operator which uses an effective nuclear charge to replace two-electron effects. The resulting splitting of 0.182 cm^{-1} between the triplet $M_s = 0$ and $M_s = \pm 1$ components is due almost entirely to the angular momentum operator perpendicular to the plane of the Ti-H-Ti bridge. An overall ferromagnetic effect of 0.645 cm^{-1} on the ground state singlet-first excited triplet energy gap is predicted. Orbital interactions responsible for spin-orbit coupling effects are identified.

I. Introduction

Often the magnetic properties of molecular systems are highly dependent on intramolecular interactions. In dinuclear complexes comprising two metal centers each with an

unpaired electron, if singlet coupling of the electrons is energetically favored over triplet coupling, the interaction is antiferromagnetic; if triplet coupling is favored over singlet coupling, the interaction is ferromagnetic.[1] There are a number of effects which can contribute to the intramolecular interaction. The magnitude and sign of the singlet-triplet energy gap, where the singlet and triplet are the two lowest energy states, and where effects due to spin-orbit coupling and magnetic dipole-dipole interactions are neglected, is a measure of the isotropic exchange interaction. In a previous study on the isomers of Ti_2H_6[2] we calculated the isotropic exchange interaction of D_{2h} $H_2Ti(\mu-H)_2TiH_2$ to be antiferromagnetic with $J = -250$ cm^{-1}, where J is defined by $-2J = E(triplet) - E(singlet)$.

The isotropic exchange interaction usually dominates spin-orbit coupling and magnetic dipole-dipole interaction effects in determining the magnetic properties of dinuclear complexes. However, when the singlet-triplet splitting itself is very small and ferromagnetic, these normally subtle effects can be important, influencing the magnetic properties of the system in the low temperature range. What is more, electron paramagnetic resonance (EPR) experiments are generally able to detect these much smaller effects as they result in the zero-field splitting (ZFS) of the triplet state M_s components.[1]

In EPR experiments there are two allowed transitions within the triplet manifold, corresponding to $\Delta M_s = \pm 1$, and a forbidden transition $\Delta M_s = 2$ (between $M_s = +1$ and $M_s = -1$) at half field. The transitions are only observable when the principle axes of the molecule (see Figure 1) are parallel or nearly parallel to the x, y, z components of the applied magnetic field; otherwise they produce only continuous background.[3] A $\Delta M_s = \pm 1$ spectrum, then, consists of three sets of doublet peaks corresponding to applied magnetic fields in x, y, and z directions. Analysis of the spectrum is carried out by use of an effective spin Hamiltonian H associated with the triplet spin quantum number $S = 1$.[4,1]

$$\mathbf{H} = \beta\mathbf{H}\cdot\mathbf{g}\cdot\mathbf{S} + \mathbf{S}\cdot\mathbf{D}\cdot\mathbf{S} \qquad (1)$$

The first term in equation (1) accounts for the Zeeman perturbation due to the applied magnetic field H; **g** is the gyromagnetic tensor and β is the electronic Bohr magneton. The second term accounts for dipolar and spin-orbit coupling effects and involves the zero-field splitting (ZFS) tensor **D**. The principal values (diagonal elements) and orientations of **g** and **D** are deduced from a fit to the experimental data; that is a fit to the measured resonance fields of the allowed transitions. The zero-field splitting parameters D and E are then calculated from the principal values of **D** according to equations (2) and (3).[4] The z axis is usually defined by the largest principal value of **D**.

$$D = 3D_z/2 \qquad (2)$$

$$E = (D_x - D_y)/2 \qquad (3)$$

D is known as the axial zero-field splitting parameter; E is the rhombic zero-field splitting parameter. A recent application of EPR spectroscopy and analysis of the resulting spectrum using the method just outlined can be found in a study of rac-{$[C_2H_4(\eta^5$-tetrahydroindenyl$)_2]$-Ti(III)$(\mu$-H)$]_2$.[6] As mentioned above, the origin of the splitting of the triplet M_s components lies in two types of interactions; the interaction between magnetic dipoles and the interactions due to spin-orbit coupling. The spin-orbit coupling interactions are often referred to as anisotropic exchange interactions or psuedodipolar interactions.[1,5]

The anisotropic exchange interaction tensor **D$_e$** is found in the analysis of experimental data by subtraction of the magnetic dipole-dipole interaction tensor **D$_d$** from the total ZFS

tensor **D**. The dipole-dipole interaction tensor **D$_d$** is calculated according to an expression dependent on **g** and $1/r^3$, where r is the metal-metal separation: axial and rhombic terms D_d and E_d are calculated by application of equations (2) and (3) to this tensor.[1] The axial and rhombic exchange interaction parameters **D$_e$** and **E$_e$** are found in practice by simply applying equations (4) and (5).[5]

$$D_e = D - D_d \qquad (4)$$

$$E_e = E - E_d \qquad (5)$$

The axis of the largest principal values in **D$_d$** and **D$_e$** may or may not coincide depending on the system under study. If they do not coincide then the dominant effect determines the definition of axial and rhombic; i.e. the largest principal value in **D** defines the z axis. Experiment has shown that **D** in di-titanium systems is dominated by **D$_d$** with the largest element along the metal inter-nuclear axis.[5] Therefore we have defined the Ti-Ti axis in D_{2h} $H_2Ti(\mu-H)_2TiH_2$ as the z axis (see Figure 1).

The approach just outlined is a purely phenomenological one which extracts the triplet splitting energies due to certain phenomena from experiment. It does not reveal any information on the mechanisms by which these phenomena occur. To this end the parameters D_e and E_e have been used in expressions based on perturbation theory to calculate singlet-triplet splitting energies of *excited states*.[1] Two examples are: the study of $[Cp_2Ti(\mu-OR]_2$ by Samuel et al[5], and the study of $[Cu_2(t-Bupy)_4(N_3)_2](ClO_4)_2$ by Gatteschi et al.[4] The aim is not only to characterize the excited states, but also to also to establish how the singlet versus triplet stability of the excited states affects the spin-orbit coupling related terms D_e and E_e. *A priori* prediction of the sign and magnitude of these anisotropic exchange effects is cited as the ultimate goal.[4]

However, the expressions used are highly dependent on approximations, such as the determination and use of orbital energy differences from only the singly occupied orbitals (the "active orbital approach"). Also, assumptions are made as to which excited state orbitals are included in the spin-orbit coupling scheme. In addition these expressions can only be used when the EPR spectrum is highly resolved, producing reliable values for D and E. This is not always the case. To our knowledge *ab initio* methods have not, until now, been applied directly to this spin-orbit coupling problem. Through *ab initio* calculations on $H_2Ti(\mu-H)_2TiH_2$ using multiconfigurational wavefunctions, our aim is two-fold: to predict excited state energies, and to calculate spin-orbit effects at a level which enables clear identification of the orbital or state interactions which cause the exchange effects represented by D_e and E_e.

The relative simplicity of $H_2Ti(\mu-H)_2TiH_2$ makes it an ideal first candidate due both to manageability of calculations and its status as *the* simplest model for di-titanium(III) systems. Any modification of D_e and E_e by the presence of more complex ligands may then be identified readily in any future calculations by direct comparison.

II. Computational Details

A triple ζ with polarization (14s11p6d/10s8p3d) basis set is used for titanium. This consists of Wachter's basis set[7] with two additional sets of p functions[8] and a set of diffuse d functions.[9] For hydrogen Dunning's (5s1p/3s1p) basis set[10] was used. Collectively this basis set is referred to as TZVP.

Preliminary calculations on singlet D_{2h} $H_2Ti(\mu-H)_2TiH_2$ were carried out at the RHF level. After convergence of this single determinant wavefunction, modified virtual orbitals

(MVO's) were generated by freezing the occupied orbitals. forming a cation by removal of six electrons and performing one SCF iteration. The resulting orbitals were used as a starting point for a two configuration (TCSCF) geometry optimization. For the triplet state a geometry optimization at the ROHF level of theory was performed.

For the ground state and lowest energy triplet, TCSCF and ROHF wavefunctions have been shown to be qualitatively correct.[2] Excited state calculations require fully optimized reaction space (FORS) MCSCF calculations[11] with an active space that consists of 2 electrons in up to 10 orbitals depending on symmetry.

Dynamic electron correlation effects, when required, are included through single point multiconfigurational quasidegenerate second order perturbation theory calculations (MCQDPT).[12]

Spin-orbit coupling effects (SOC) are treated using a one-electron spin-orbit coupling operator.[13] The operator uses an effective nuclear charge Z_{eff} to replace two-electron effects. The Z_{eff} of 9.873 used for titanium was chosen to reproduce the first zero-field splitting energy in neutral atomic ^3F Ti, $J(2 \rightarrow 3) = 170.132$ cm^{-1}.[14] A similar Z_{eff} is obtained if one chooses to reproduce the doublet splitting in ^2D Ti(III).

All calculations were done using the electronic structure code GAMESS.[15]

III. Results and discussion

Calculated geometries for the lowest energy singlet and triplet states of D_{2h} $H_2Ti(\mu$-$H)_2TiH_2$ at the TCSCF/TZVP and ROHF/TZVP levels, respectively, are shown in Figure 1. We first consider the excited states of D_{2h} $H_2Ti(\mu$-$H)_2TiH_2$, and then examine SOC effects.

a) Excited States. It is necessary to consider 2 electrons in 10 orbitals in order to arrive at correct descriptions of the excited states of $H_2Ti(\mu-H)_2TiH_2$. These orbitals include Ti-Ti bonding and antibonding interactions of the type $\sigma\,\sigma^*$, $\pi\,\pi^*$, and $\delta\,\delta^*$ with some participation of bridging and terminal hydrogen atomic orbitals (see Figure 2). Tables 1 and 2 show the electronic structures and energies of the first twenty singlet and twenty triplet states of D_{2h} $H_2Ti(\mu-H)_2TiH_2$.

The singlet energies in Table 1 are from a state-averaged 2 electron, 10 orbital MCSCF calculation at the TCSCF/TZVP ^1A_g ground state geometry (see Figure 1). Starting orbitals were symmetrized (D_{2h}) and resemble those shown in Figure 2. The calculation was carried out with no symmetry constraints, with each of the first 20 states weighted equally. Using this wavefunction as a starting point and freezing the non-active orbitals, a 2 electron, 10 orbital MCSCF triplet calculation was carried out at the same geometry using the same procedure to obtain the first 20 triplet states that are detailed in Table 1. These are the orbitals used in the SOC calculations described below.

To assess the effects of orbital and geometry relaxation, as well as dynamic electron correlation, a subset of the states shown in Table 1 was analyzed (see Table 2). The singlet energies were calculated at the TCSCF/TZVP ^1A_g ground state geometry; the triplet energies at the ROHF/TZVP $^3B_{1u}$ geometry (see Figure 1). Initially, all orbitals allowed by symmetry were included in each MCSCF calculation on each state. Then, any orbitals with negligible occupation were discarded and the reduced space used for reoptimization of the wavefunction and subsequent perturbation corrections for dynamic electron correlation. When more than one state of a given symmetry was considered (five ^1A_g and five $^3B_{1u}$ states), the orbital coefficients for each of the roots were optimized separately.

From Tables 1 and 2 one can see the effects of orbital and geometry relaxation by

comparing the columns headed MCSCF. For the first six states the difference is less than ~ 0.6 kcal/mol and for the remaining states it is no greater than ~ 1.0 kcal/mol. The MCQDPT results in Table 2 show that the effects of dynamic correlation are greater, with differences in the range ~ 0.3 kcal/mol to ~ 5.7 kcal/mol between the MCSCF and MCQDPT methods. However, except for two cases (S_8,S_9 and T_9, T_{10}), the MCSCF wavefunction does order the states correctly.

b) Spin-Orbit Coupling. The effects of SOC on the ground state singlet S_0 and first excited triplet T_1 were determined using a one-electron SOC operator.[13] Since current codes do not include the effects of dynamic electron correlation as obtained by MCQDPT in the SOC calculation, one does not anticipate quantitatively accurate values for the SOC related exchange parameters D_e and E_e. However, one hopes to obtain qualitatively useful information. By systematically increasing the number of states included in the SOC calculation, ferromagnetic or antiferromagnetic effects can be assigned to mixing of specific states induced by SOC. Figure 3 is a schematic representation of the effect of SOC when all 20 singlet and triplet states are included in the calculation. Figure 4 shows the effect of systematically adding states to the wavefunction; in effect, a decomposition of the total. For the purposes of the following discussion, both S_0 and T_1 will be referred to as ground states; S_1 - S_{19} and T_2 - T_{20} will be referred to as excited states.

The effect of SOC on the ground state singlet-triplet gap in this case is predicted to be a ferromagnetic one. This effect, however, is very small compared to the much larger isotropic effect (+ 0.6 cm-1 compared to - 205 cm-1). The calculated SOC splitting parameters of D_e = 0.018 cm-1 and E_e = 0.182 cm-1 lie within the range of experimentally determined values for related systems. Gatteschi et al found D_e = 0.376 cm-1 and E_e = 0.070 cm-1 in their di-copper system;[4] Samuel et al found D_e = 0.0012 cm-1 and E_e = - 0.0065 cm-1 for their di-titanium

system.[5] In the copper system SOC effects dominate; therefore, the axial component is defined by the largest element of the exchange interaction tensor $\mathbf{D_e}$ and is perpendicular to the Cu-Cu axis; in the titanium system, however, dipole effects dominate and the axial component is along the Ti-Ti axis as defined by the dipole interaction tensor $\mathbf{D_d}$. The lack of dynamic correlation in the present calculations means that qualitative information, such as identifying which SOC interactions are important, is more reliable than the absolute values of D_e and E_e. Nevertheless, the agreement with available experimental data is encouraging.

Figure 4 demonstrates how SOC affects S_0 and T_1 if the number of states included in the SOC is built up from three (S_0-S_2, T_1-T_3), to six (S_0-S_5, T_1-T_6), to twelve (S_0-S_{11}, T_1-T_{12}). Figure 5 identifies which states are coupled in these calculations and shows cartoon representations of the d-orbital interactions deemed responsible for ferromagnetic and antiferromagnetic contributions which make up the total effect when all states are included. For ease of visualization the cartoons do not represent molecular orbitals; in fact each d-orbital represents an unpaired electron localized on a Ti center.

When only the first three states (S_0-S_2, T_1-T_3) are included, T_1 is stabilized preferentially to S_0; there is a ferromagnetic effect of 1.160 cm^{-1}. Inspection of the SOC matrix elements (see Figure 5) reveals the interactions responsible are purely between states with σ and π interactions, with no participation of the bridging hydrogens. This is consistent with the findings of Kahn who predicts ferromagnetic interaction when there is no bridging ligand mediation between two d-orbitals in an orthogonal orientation.[1] Due to symmetry constraints, the angular momentum operator which gives rise to *all* of these interactions is L_z which acts along the inter-nuclear axis (see Figure 1). From Figure 5 it can be seen that there is no excited state-excited state coupling; this is also due to the symmetry constraints imposed by the angular momentum operators. The SOC calculation also shows that the $M_s = +1$ and $M_s = -1$

components of T_1, which themselves have mixed with other states due to SOC, now mix with each other forming two spin states via plus-plus and plus-minus linear combinations. One of these is degenerate with the $M_s = 0$ spin state; the other is not. This D_e splitting is calculated to be only 0.020 cm^{-1}.

The addition of three more states (S_0-S_5, T_1-T_6) results in an antiferromagntic effect of - 0.495 cm^{-1}. The ground state-excited state coupling responsible for this effect (see Figure 5) is between states with σ and δ_1 interactions (see Figure 2 and Table 1) which do include contributions from the bridging hydrogens. Again, this is consistent with the findings of Kahn.[1] Introduction of these states also results in a small but significant coupling between excited states that results in indirect coupling of more excited states with the ground states. E_e is calculated to be 0.181 cm^{-1}, suggesting that the splitting of the $M_s = 0$ and the $M_s = \pm1$ T_1 levels is due almost entirely to the effects of the introduction of these three states and the resulting SOC interactions. The angular momentum operator that is responsible for the coupling between states with σ and δ_1 interactions is L_x, where the x axis is perpendicular to the plane of the bridge in the molecular orientation for these calculations (see Figure 1). Based on this result, an experimentally determined exchange tensor $\mathbf{D_e}$ in this case would have its major component on the x diagonal element.

The inclusion of the next six states (S_0-S_{11}, T_1-T_{12}) has a small effect that brings the energy levels essentially to the same values as those in the full twenty singlet and triplet state SOC. The very small antiferromagnetic effect of - 0.019 cm^{-1} appears to arise from a number of SOC matrix elements of similar magnitude describing both ground state-excited state, and excited state-excited state interactions. Figure 5 shows a cartoon representation of the former. No additional splitting within T_1 results from the inclusion of these states.

In summary, spin-orbit coupling in D_{2h} $H_2Ti(\mu-H)_2TiH_2$ obtained with the first twenty

singlet and twenty triplet states produces a very small ferromagnetic effect that arises from competing ferromagnetic and antiferromagnetic interactions between ground and excited state orbitals, as well as interactions between excited states. Splitting of the $M_s = 0$ and $M_s = \pm 1$ T_1 levels ($E_e = 0.182$ cm^{-1}) is caused almost entirely by the introduction of S_3-S_4, and T_4-T_5 and the resulting interactions. The angular momentum operator L_x along the axis perpendicular to the bridge plane (see Figure 1) is responsible for most of these interactions. In contrast, magnetic dipole-dipole interactions are almost always largest along the inter-nuclear axis (z axis). If this is assumed to be so for D_{2h} $H_2Ti(\mu\text{-}H)_2TiH_2$, the two effects which result in splitting of the triplet state have their largest components along perpendicular axes. This has been observed experimentally both in a di-copper system[4] and a di-titanium system,[5] and supports the contention of Samuel et al that they can estimate the Ti-Ti separation accurately in their system using the dipolar component of the zero-field splitting tensor, because SOC related exchange effects are minimal along the Ti-Ti axis.

IV. Conclusions

Excited state energies of singlet and triplet $H_2Ti(\mu\text{-}H)_2TiH_2$ have been calculated. The effect of orbital relaxation (optimizing the orbitals for each state) is found to be small. Dynamic correlation makes a considerable difference in terms of energetics, but has little effect on the ordering of the states.

In dinuclear complexes spin-orbit coupling effects can contribute to the splitting of the triplet state as measured by EPR spectroscopy. Through *ab initio* calculations which include spin-orbit coupling we have identified which states couple in D_{2h} $H_2Ti(\mu\text{-}H)_2TiH_2$ to produce

these contributions. The calculated anisotropic exchange parameter $E_e = 0.182$ cm^{-1}, which corresponds to the splitting of $M_s = 0$ and $M_s = \pm 1$, is due almost entirely to coupling brought about by the angular momentum operator perpendicular to the plane of the Ti-H-Ti bridge (L_x). The effect of the operator along the Ti-Ti axis (L_z) was found to be much smaller. This is similar to what was found to be the case experimentally in $[Cp_2Ti(\mu\text{-}OR]_2$, allowing the Ti-Ti separation to be accurately estimated using the point dipole approximation. The ferromagnetic effect of spin-orbit coupling on the ground state singlet-first excited triplet energy gap is found to be *very* small relative to the isotropic antiferromagnetic interaction in $H_2Ti(\mu\text{-}H)_2TiH_2$, and therefore plays no role in determination of overall magnetic properties of the system.

Given the importance of dynamic correlation both in determining the isotropic interaction energy and in the effect it has on excited state energies, a first step toward achieving reliable absolute values of D_e and E_e can be made with its inclusion in the spin-orbit coupling calculations.

The calculations presented here should be viewed as a first step in using *ab initio* computational chemistry techniques to determine how the SOC induced exchange contribution to zero-field splittings is modified by bridging and terminal ligands in paramagnetic dinuclear titanium(III) compounds.

References

1. a) Kahn, O. *Angew. Chem. Int. Ed. Engl.* **1985**, 24, 834. b) Kahn, O. *Molecular Magnetism* ; VCH; New York, 1993; Chapters 6-9.

2. Webb, S. P.; Gordon, M. S. To be submitted.

3. Gatteschi, D.; Bencini, A. in "Magneto-Structural Correlations in Exchange Coupled Systems," Willett, R. D.; Gatteschi, D.; Kahn, O., eds., NATO ASI Series, Ser. C. Vol. 140, p. 241. Reidel, Dordrecht, (1985).

4. Boillot, M.; Journaux, Y.; Bencini, A.; Gatteschi, D.; Kahn, O. *Inorg. Chem.* **1985**, 24, 263.

5. Samuel, E.; Harrod, J. F.; Gourier, D.; Dromzee, Y.; Robert, F.; Jeannin, Y. *Inorg. Chem.* **1992**, 31, 3252.

6. Xin, S.; Harrod, J. F.; Samuel, E. *J. Am. Chem. Soc.* **1994**, 116. 11562.

7. Watchers, A. J. H. *J. Chem. Phys.* **1970**, 52, 1033.

8. Hood, D. M.; Pitzer, R. M.; Schaefer, H. F. *J. Chem . Phys.* **1979**, 71, 705.

9. Rappe, A. K.; Smedley, T. A.; Goddard, W. A. *J. Phys. Chem.* **1981**, 85, 2607.

10. Dunning, T. H.; Hay, P.J. In *Methods of Electronic Structure Theory*; Schaefer, H. F., III. Ed.; Plenum Press: New York. 1977; pp 1-27.

11. (a) Sunberg, K. R.; Ruedenberg, K. in *Quantum Science*, edited by Calais, J. L.; Goscinski, O.; Linderberg, J.; Ohrn, Y., Plenum, New York, 1976, pp 505. (b) Cheung, L. M.; Sunberg, K. R.; Ruedenberg, K. *Int. J. Quantum Chem.* **1979**, 16, 1103. (c) Ruedenberg, K.; Schmidt, M.; Gilbert, M. M.; Elbert, S. T. *Chem. Phys.* **1982**, 71,41. (d) Roos, B. O.; Taylor, P.; Siegbahn, P. E. M. *Chem. Phys.* **1980**, 48, 157.

12. (a) Nakano, H. *J. Chem . Phys.* **1993**, 99, 7983. (b) Nakano, H. *Chem. Phys. Lett.*

1993, 207, 372.

13. Koseki, S.; Gordon, M. S.; Schmidt, M. W.; Matsunaga, N. *J. Phys. Chem.* **1995**, 99. 12764.

14. *NIST Atomic Spectroscopic Database,* http://aeldata.nist.gov/archive/data.html

15. Schmidt, M.W.; Baldridge, K.K.; Boatz, J.A.; Jensen, J.H.; koseki, S.; Matsunaga. N.; Gordon, M.S.; Ngugen, K.A. ; Su, S.; Windus, T.L.; Elbert, S.T.; Montgomery, J.; Dupuis, M. *J. Comp. Chem.* **1993**, 14, 1347.

Table 1. Electronic structure and MCSCF/TZVP energetics for the first 20 singlet and triplet states of D_{2h} $H_2Ti(\mu\text{-}H)_2TiH_2$. Energies (kcal/mol) are relative to the ground state ^1A_g.

Singlets[a]				Triplets[b]		
State		Configurations	MCSCF (2,10)	State		Configurations	MCSCF (2,10)

State		Configurations	MCSCF (2,10)	State		Configurations	MCSCF (2,10)
S_0	^1A_g	$(\sigma)^2 (\sigma^*)^2$	0.00	T_1	$^3B_{1u}$	$(\sigma\sigma^*)^{1,1}$	0.59
S_1	$^1B_{1g}$	$(\sigma\pi)^{1,1} (\sigma^*\pi^*)^{1,1}$	4.29	T_2	$^3B_{1g}$	$(\sigma\pi)^{1,1} (\sigma^*\pi^*)^{1,1}$	4.18
S_2	^1A_u	$(\sigma\pi^*)^{1,1} (\sigma^*\pi)^{1,1}$	4.41	T_3	^3A_u	$(\sigma\pi^*)^{1,1} (\sigma^*\pi)^{1,1}$	4.47
S_3	^1A_g	$(\pi)^2 (\pi^*)^2$	8.78	T_4	$^3B_{1u}$	$(\pi\pi^*)^{1,1}$	8.83
S_4	$^1B_{3g}$	$(\sigma\delta_1^*)^{1,1} (\sigma^*\delta_1)^{1,1}$	18.00	T_5	$^3B_{3g}$	$(\sigma\delta_1^*)^{1,1} (\sigma^*\delta_1)^{1,1}$	17.25
S_5	$^1B_{2u}$	$(\sigma\delta_1)^{1,1} (\sigma^*\delta_1^*)^{1,1}$	20.69	T_6	$^3B_{2u}$	$(\sigma\delta_1)^{1,1} (\sigma^*\delta_1^*)^{1,1}$	19.78
S_6	$^1B_{2g}$	$(\pi\delta_1^*)^{1,1} (\pi^*\delta_1)^{1,1}$	22.89	T_7	$^3B_{2g}$	$(\pi\delta_1^*)^{1,1} (\pi^*\delta_1)^{1,1}$	22.25
S_7	$^1B_{3u}$	$(\pi\delta_1)^{1,1} (\pi^*\delta_1^*)^{1,1}$	23.66	T_8	$^3B_{3u}$	$(\pi\delta_1)^{1,1} (\pi^*\delta_1^*)^{1,1}$	22.97
S_8	$^1B_{1u}$	$(\sigma_1\sigma_1^*)^{1,1} (\sigma_2\sigma_2^*)^{1,1}$	27.40	T_9	$^3B_{3u}$	$(\sigma\delta_2)^{1,1} (\sigma^*\delta_2^*)^{1,1}$	27.44
S_9	$^1B_{3u}$	$(\sigma\delta_2)^{1,1} (\sigma^*\delta_2^*)^{1,1}$	28.04	T_{10}	$^3B_{1u}$	$(\sigma_1\sigma_1^*)^{1,1} (\sigma_2\sigma_2^*)^{1,1}$	27.58
S_{10}	^1A_g	$(\sigma_1\sigma_1^*)^{2,2}(\sigma_2\sigma_2^*)^{2,2}$	28.60	T_{11}	^3A_g	$(\sigma_1\sigma_2)^{1,1} (\sigma_1^*\sigma_2^*)^{1,1}$	28.58
S_{11}	$^1B_{2g}$	$(\sigma\delta_2^*)^{1,1} (\sigma^*\delta_2)^{1,1}$	29.31	T_{12}	$^3B_{2g}$	$(\sigma\delta_2^*)^{1,1} (\sigma^*\delta_2)^{1,1}$	29.57
S_{12}	^1A_u	$(\sigma\pi^*)^{1,1} (\sigma^*\pi)^{1,1}$	32.37	T_{13}	^3A_u	$(\sigma\pi^*)^{1,1} (\sigma^*\pi)^{1,1}$	32.26
S_{13}	$^1B_{1g}$	$(\sigma\pi)^{1,1} (\sigma^*\pi^*)^{1,1}$	32.71	T_{14}	$^3B_{2u}$	$(\pi\delta_2)^{1,1} (\pi^*\delta_2^*)^{1,1}$	32.42
S_{14}	$^1B_{3g}$	$(\pi\delta_2^*)^{1,1} (\pi^*\delta_2)^{1,1}$	32.96	T_{15}	$^3B_{1g}$	$(\sigma\pi)^{1,1} (\sigma^*\pi^*)^{1,1}$	32.54
S_{15}	$^1B_{2u}$	$(\pi\delta_2)^{1,1} (\pi^*\delta_2^*)^{1,1}$	33.11	T_{16}	$^3B_{3g}$	$(\pi\delta_2^*)^{1,1} (\pi^*\delta_2)^{1,1}$	33.44
S_{16}	^1A_g	$(\delta_1)^2 (\delta_1^*)^2$	34.56	T_{17}	$^3B_{1u}$	$(\delta_1\delta_1^*)^{1,1}$	40.10
S_{17}	^1A_u	$(\delta_1\delta_2^*)^{1,1} (\delta_1^*\delta_2)^{1,1}$	43.45	T_{18}	^3A_u	$(\delta_1\delta_2^*)^{1,1} (\delta_1^*\delta_2)^{1,1}$	42.34
S_{18}	$^1B_{2u}$	$(\sigma\delta_1)^{1,1} (\sigma^*\delta_1^*)^{1,1}$	45.47	T_{19}	$^3B_{2u}$	$(\sigma\delta_1)^{1,1} (\sigma^*\delta_1^*)^{1,1}$	43.62
S_{19}	$^1B_{3g}$	$(\sigma\delta_1^*)^{1,1} (\sigma^*\delta_1)^{1,1}$	47.05	T_{20}	$^3B_{3g}$	$(\sigma\delta_1^*)^{1,1} (\sigma^*\delta_1)^{1,1}$	47.48

[a] Singlet states are from a single 2 electron, 10 orbital MCSCF/TZVP calculation at the ^1A_g ground state geometry and are weighted equally. [b] Triplet states are from a single 2 electron, 10 orbital MCSCF/TZVP calculation at the ^1A_g ground state geometry.

$(\sigma\pi)^{1,1} (\sigma^*\pi^*)^{1,1}$ represents the following configurations:

Config. #	σ	σ^*	π	π^*
1	1	0	1	0
2	0	1	0	1

Table 2. Excited state energies (kcal/mol) of D_{2h} $H_2Ti(\mu\text{-}H)_2TiH_2$. Energies are relative to the ground state ^1A_g.

Singlet[a]					Triplet[b]				
State		Natural Orbital Occupation	MCSCF	MCQDPT	State		Natural Orbital Occupation	MCSCF	MCQDPT
S_0	^1A_g	$(\sigma_1)^{1.11}(\sigma_1^*)^{0.89}$	0.00	0.00	T_1	$^3B_{1u}$	$(\sigma_1)^{1.00}(\sigma_1^*)^{1.00}$	0.56	1.33
S_1	$^1B_{1g}$	$(\sigma_1)^{0.53}(\pi)^{0.53}(\sigma_1^*)^{0.47}(\pi^*)^{0.47}$	4.80	4.08	T_2	$^3B_{1g}$	$(\sigma_1)^{0.54}(\pi)^{0.54}(\sigma_1^*)^{0.46}(\pi^*)^{0.46}$	4.49	3.99
S_2	^1A_u	$(\sigma_1)^{0.52}(\pi^*)^{0.52}(\sigma_1^*)^{0.48}(\pi)^{0.48}$	4.91	4.43	T_3	^3A_u	$(\sigma_1)^{0.52}(\pi^*)^{0.52}(\sigma_1^*)^{0.48}(\pi)^{0.4}$	4.74	4.43
S_3	^1A_g	$(\pi)^{1.03}(\pi^*)^{0.97}$	8.24	11.24	T_4	$^3B_{1u}$	$(\pi)^{1.00}(\pi^*)^{1.00}$	7.85	9.90
S_4	$^1B_{3g}$	$(\sigma_1)^{0.61}(\delta_1^*)^{0.61}(\sigma_1^*)^{0.39}(\delta_1)^{0.39}$	17.78	15.44	T_5	$^3B_{3g}$	$(\sigma_1)^{0.61}(\delta_1^*)^{0.61}(\sigma_1^*)^{0.39}(\delta_1)^{0.39}$	16.88	13.94
S_5	$^1B_{2u}$	$(\sigma_1)^{0.45}(\delta_1)^{0.45}(\sigma_1^*)^{0.55}(\delta_1^*)^{0.55}$	20.36	19.62	T_6	$^3B_{2u}$	$(\sigma_1)^{0.45}(\delta_1)^{0.45}(\sigma_1^*)^{0.55}(\delta_1^*)^{0.55}$	19.31	18.00
S_6	$^1B_{2g}$	$(\pi)^{0.59}(\delta_1^*)^{0.59}(\pi^*)^{0.41}(\delta_1)^{0.41}$	23.47	22.02	T_7	$^3B_{2g}$	$(\pi)^{0.60}(\delta_1^*)^{0.60}(\pi^*)^{0.41}(\delta_1)^{0.41}$	22.35	20.11
S_7	$^1B_{3u}$	$(\pi)^{0.43}(\delta_1)^{0.43}(\pi^*)^{0.57}(\delta_1^*)^{0.57}$	24.22	23.38	T_8	$^3B_{3u}$	$(\pi)^{0.42}(\delta_1)^{0.42}(\pi^*)^{0.58}(\delta_1^*)^{0.58}$	23.03	21.72
S_8	$^1B_{1u}$	$(\sigma_1)^{0.57}(\sigma_1^*)^{0.43}(\sigma_2)^{0.57}(\sigma_2^*)^{0.43}$	28.11	24.15	T_9	$^3B_{3u}$	$(\sigma_1)^{0.61}(\delta_2)^{0.61}(\sigma_1^*)^{0.39}(\delta_2^*)^{0.39}$	27.94	22.20
S_9	$^1B_{3u}$	$(\sigma_1)^{0.60}(\delta_2)^{0.60}(\sigma_1^*)^{0.40}(\delta_2^*)^{0.40}$	28.25	22.63	T_{10}	$^3B_{1u}$	$(\sigma_1)^{0.52}(\sigma_1^*)^{0.56}(\sigma_2)^{0.48}(\sigma_2^*)^{0.44}$	27.87	23.81
S_{10}	^1A_g	$(\sigma_1)^{0.52}(\sigma_1^*)^{0.56}(\sigma_2)^{0.48}(\sigma_2^*)^{0.44}$	29.30	25.60	T_{11}	^3A_g	$(\sigma_1)^{0.49}(\sigma_1^*)^{0.51}(\sigma_2)^{0.49}(\sigma_2^*)^{0.51}$	28.82	24.80
S_{11}	$^1B_{2g}$	$(\sigma_1)^{0.46}(\delta_2^*)^{0.46}(\sigma_1^*)^{0.54}(\delta_2)^{0.54}$	29.63	25.76	T_{12}	$^3B_{2g}$	$(\sigma_1)^{0.46}(\delta_2^*)^{0.46}(\sigma_1^*)^{0.54}(\delta_2)^{0.54}$	30.04	26.29
S_{16}	^1A_g	$(\delta_1)^{0.69}(\delta_1^*)^{1.31}$	34.09	33.74	T_{17}	$^3B_{1u}$	$(\delta_1)^{1.00}(\delta_1^*)^{1.00}$	38.39	39.97
-	^1A_g	$(\delta_2)^{1.30}(\delta_2^*)^{0.70}$	52.76	47.95	-	$^3B_{1u}$	$(\delta_2)^{1.00}(\delta_2^*)^{1.00}$	57.33	57.69

[a] Singlet energy calculations were obtained at the ground state ^1A_g geometry. [b] Triplet energy calculations were obtained at the lowest energy $^3B_{3u}$ geometry.

A separate MCSCF/TZVP calculation was done for every excited state allowing the orbitals to be optimized specifically for the state in question. The natural orbitals are those defined in Figure 2.
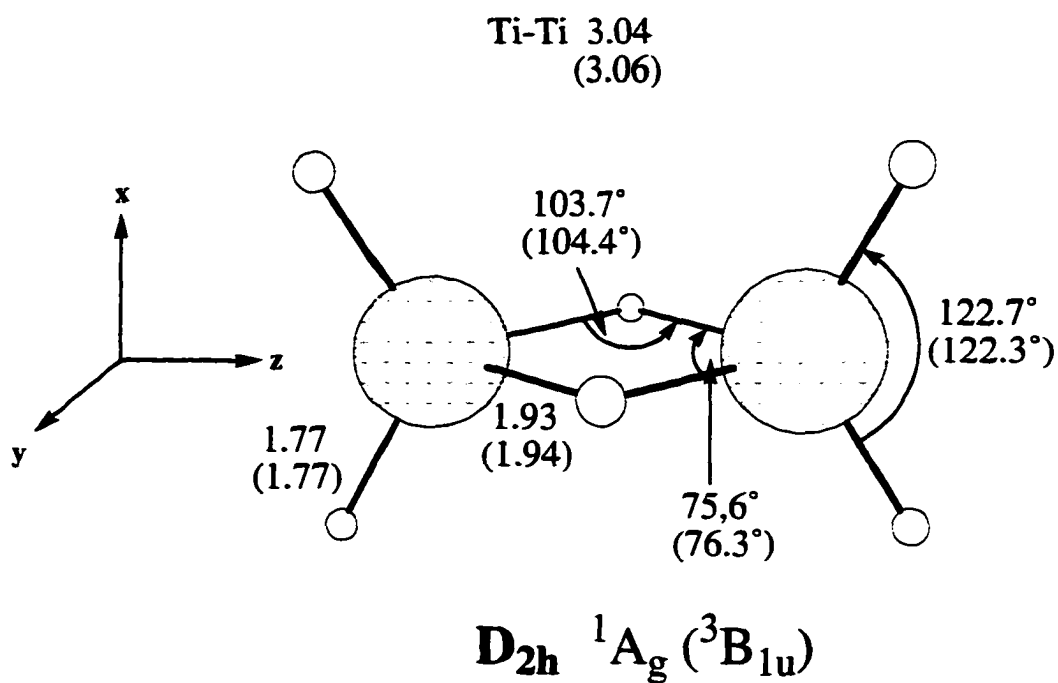
Figure 1. MCSCF/TZVP singlet and ROHF/TZVP triplet geometries of D_{2h} $H_2Ti(\mu$-H$)_2TiH_2$. Bond lengths are in Angstroms. Brackets signify triplet geometry.

a$_g$ σ_1

b$_{1u}$ σ_1^*

a$_g$ σ_2

b$_{1u}$ σ_2^*

b$_{1g}$ π

a$_u$ π^*

b$_{2u}$ δ_1

b$_{3g}$ δ_1^*

b$_{3u}$ δ_2

b$_{2g}$ δ_2^*
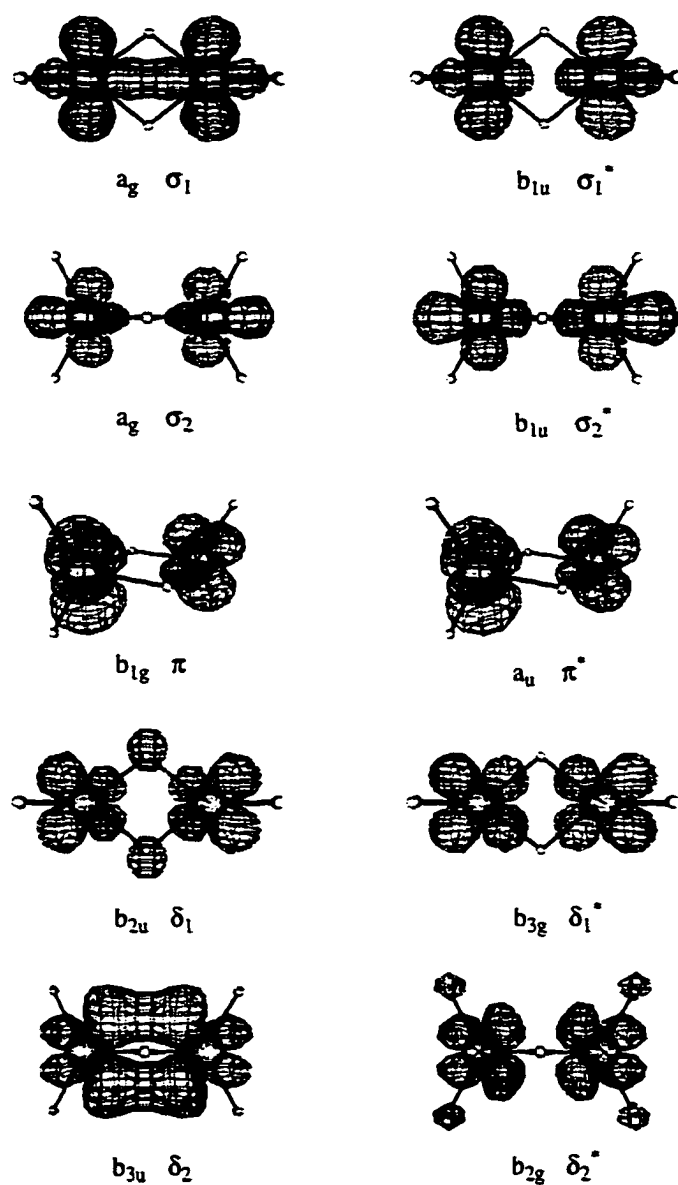
Figure 2. Three dimensional plots of the natural orbitals from a 2 electron, 10 orbital MCSCF/TZVP calculation, optimized for the ^1A_g ground state of D$_{2h}$ H$_2$Ti(μ-H)$_2$TiH$_2$. For the ground state, occupation numbers for these active space natural orbitals is zero except for σ_1 and σ_1^*. The shapes of these orbitals remain qualitatively the same in excited state calculations. The orbital contour value for the plots is 0.04 Bohr$^{-3/2}$. The z axis is defined by the Ti-Ti axis, the Ti-H-Ti bridge is in the yz plane, and the Ti-H terminal bonds are in the xz plane.

T_1

12.632 cm^{-1}

Ms

0

±1

204.877 cm^{-1}

$E_e = 0.182$ cm^{-1}

$D_e = 0.019$ cm^{-1}

204.232 cm^{-1}

S_0

12.188 cm^{-1}
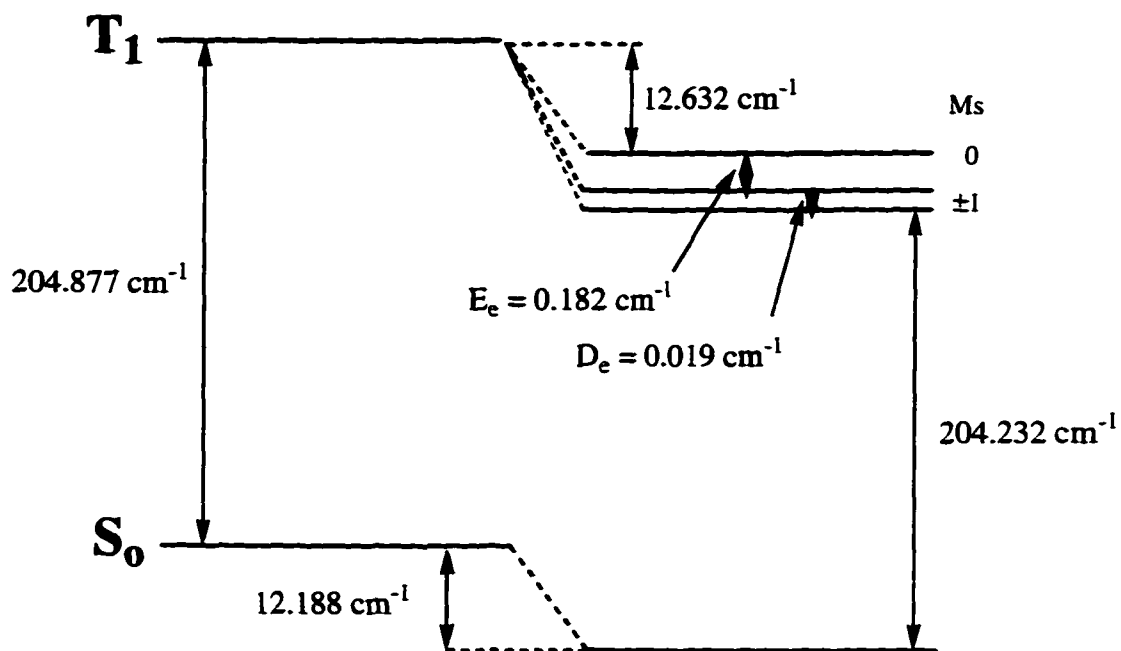
Total ferromagnetic effect (triplet stabilized preferentially to the singlet) of 0.645 cm^{-1}.

Figure 3. Schematic representation of the effects of a spin-orbit coupling calculation on S_0 and T_1 which includes the first 20 singlet (S_0 - S_{19}) and triplet (T_1 - T_{20}) states of D_{2h} $H_2Ti(\mu-H)_2TiH_2$. D_e and E_e are the axial and rhombic exchange parameters, respectively.
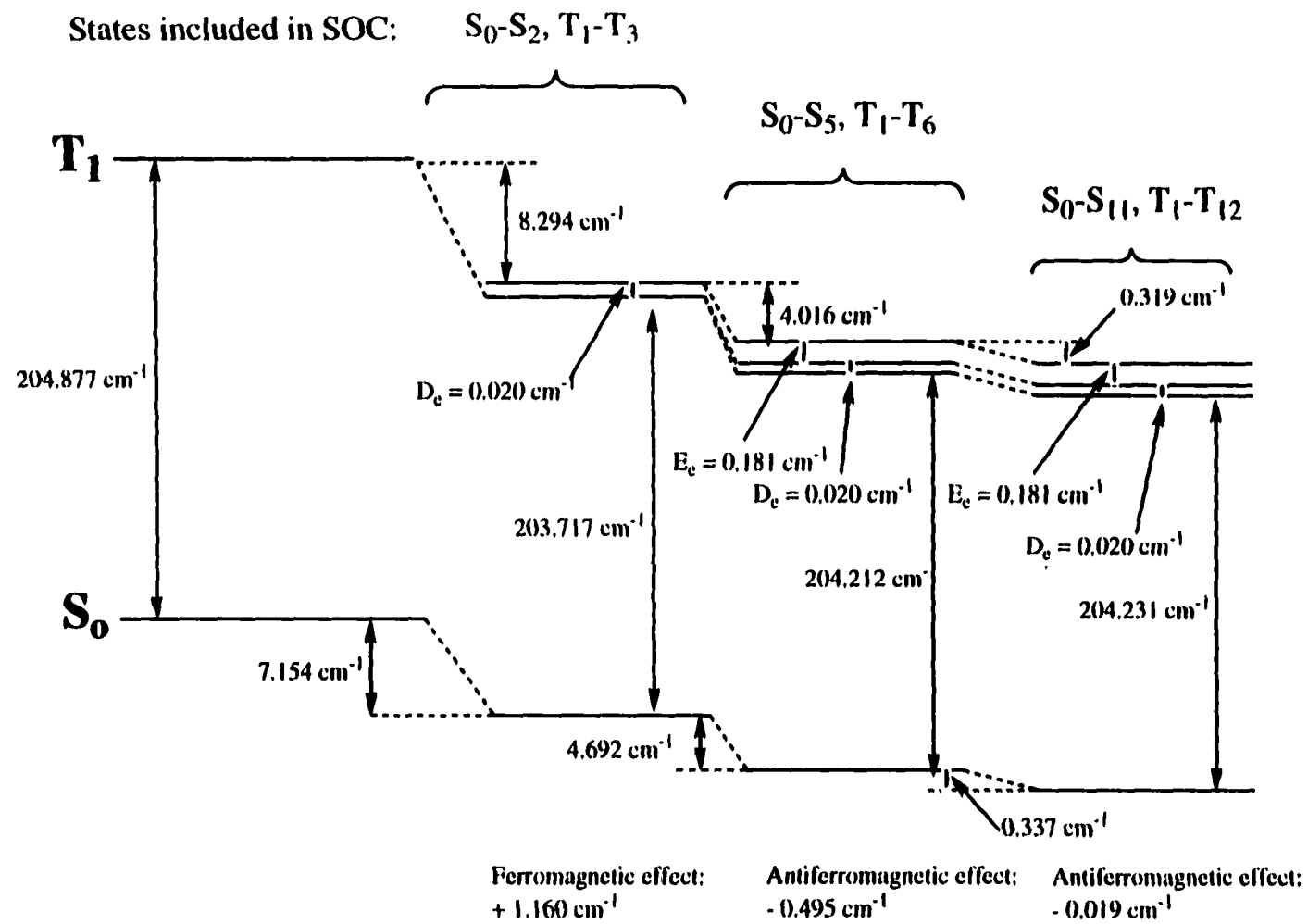
Figure 4. Decomposition of the total effect of spin-orbit coupling on S_0 and T_1 by adding the states included in the calculation a few at a time.

S_0-S_2, T_1-T_3 $\qquad$ S_0-S_5, T_1-T_6 $\qquad$ S_0-S_{11}, T_1-T_{12}

Ferromagnetic effect:	Antiferromagnetic effect:	Antiferromagnetic effect:
+ 1.160 cm^{-1}	- 0.495 cm^{-1}	- 0.019 cm^{-1}
$D_e = 0.020$ cm^{-1}, $E_e = 0.000$ cm^{-1}	$D_e = 0.020$ cm^{-1}, $E_e = 0.181$ cm^{-1}	$D_e = 0.020$ cm^{-1}, $E_e = 0.181$ cm^{-1}
All states which are coupled by SOC matrix elements.	Additional states coupled by significant SOC matrix elements.	Additional States coupled by significant SOC matrix elements.

		Ground state-excited state elements:		Ground state-excited state elements:	
S_0-T_2	^1A_g - $^3B_{1g}$	S_0-T_5	^1A_g - $^3B_{3g}$	S_0-T_{12}	^1A_g - $^3B_{2g}$
		T_1-T_6	$^3B_{1u}$ - $^3B_{2u}$	T_1-T_9	$^3B_{1u}$ - $^3B_{3u}$
T_1-T_3	$^3B_{1u}$ - ^3A_u	T_1-S_5	$^3B_{1u}$ - $^1B_{2u}$	T_1-S_9	$^3B_{1u}$ - $^1B_{3u}$
T_1-S_2	$^3B_{1u}$ - ^1A_u	Selected excited state-excited state elements:		Selected excited state-excited state elements:	
		T_3-T_4	^3A_u - $^3B_{1u}$	T_3-T_4	^3A_u - $^3B_{1u}$
		T_3-T_6	^3A_u - $^3B_{2u}$	T_3-T_6	^3A_u - $^3B_{2u}$
		S_2-T_4	^1A_u - $^3B_{1u}$	S_2-T_4	^1A_u - $^3B_{1u}$

Only Interaction $\qquad$ Dominant New Interaction $\qquad$ Dominant New Interaction

Ground state-excited state $\qquad$ Ground state-excited state

Note: this is the largest ground state-excited state interaction. Several excited state-excited state interactions have similar matrix elements.

Figure 5. States which are coupled via spin-orbit coupling (with non-negligble matrix elements). With addition of more states in each calculation (e.g. going from S_0-S_2, T_1-T_3 to S_0-S_5, T_1-T_6) only the new couplings are identified (the couplings identified in the previous column (e.g. S_0-S_2, T_1-T_3) are still present. Only selected excited state-excited state couplings are explicitly identified as they are numerous.

CHAPTER 6. INTERMOLECULAR SELF-INTERACTIONS OF THE TITANIUM TETRAHALIDES TiX₄ (X = F,Cl,Br)

Simon P. Webb and Mark S. Gordon

Abstract

Ab Initio calculations have been performed on the closed shell molecules TiX_4 and Ti_2X_8 (X = F, Cl, Br) in order to determine the magnitude and the nature of the intermolecular self-interactions of the titanium tetrahalides. Geometry optimizations have been carried out using an effective core potential basis set with polarization, including the effects of dynamic electron correlation through MP2. The importance of higher order correlation effects is examined through CCSD(T) single-point energy calculations. Basis set effects are investigated using MP2 single-point energy calculations with large all electron basis sets. Ti_2F_8 is predicted to be a bound dimer with bridging bonds, stable by - 9.6 kcal/mol relative to separated monomers. Ti_2Cl_8 and Ti_2Br_8 are predicted to be weakly bound dimers whose structures are that of associated monomers. Ti_2Cl_8 is exothermic by 4.5 kcal/mol relative to separated monomers. Transition states have been found which represent paths to halide exchange between monomers confirming the contention that unexpected NMR line widths found by Pratt for $TiCl_4$ are due to dimerization and Cl exchange.

I. Introduction

The titanium tetrahalides are considered to be among the most important titanium compounds as they are used as starting materials for the preparation of many organo-titanium systems.[1] This is especially true of $TiCl_4$ which is the precursor for a number of Ziegler-Natta catalysts.[1,2a,3] Due to the importance of this class of compounds, an understanding of their basic fundamental chemistry through experiment and *ab initio* calculations is an appropriate goal which has received considerable attention.

Gas phase TiF_4 has been made by the reaction between $TiCl_4$ and NaF, and its infra-red spectrum has been measured.[4] Confusion over peak assignments due to the possible range of products (TiF_nCl_{4-n}, n = 0-4) was eliminated by *ab initio* calculation of the vibrational frequencies of all these products.[5] Another theoretical study investigated the complexes between H_2CO and $TiCl_4$.[6] RHF calculations using a double ξ quality basis set found that within the $(H_2CO-TiCl_4)_2$ dimer, H_2CO was found to interact with $TiCl_4$ more strongly than in the monomer, illustrating the modification of the reactivity of the titanium tetrahalides due to their intermolecular interactions.

Experiment has shown TiF_4 to be molecular with a coordination number of four in the gas phase and a polymer chain with a Ti coordination number of six in the solid state[7] (the exact structure is unknown). In contrast gas phase *and* solid state $TiCl_4$ and $TiBr_4$ are found to be molecular with Ti coordination numbers of four.[7a] These observations are indicative of considerable attractive intermolecular (dimer) interactions in the tetraflouride and little or no attraction in the other tetrahalides. The lack of monotonic behavior of the melting and boiling points of the titanium tetrahalides[8] (see Table 1) provides further evidence of this.

Consideration of additional experimental evidence suggests there *is* attractive

intermolecular interaction in $TiCl_4$. NMR studies by Pratt suggest that liquid $TiCl_4$ exhibits some "local order" which involves chlorine exchange between monomers.[9] Pratt based his conclusions on measurements made on both mixed $TiCl_4/VCl_4$ solutions and pure $TiCl_4$ solutions. The $TiCl_4/VCl_4$ mixture produced only one [35]Cl NMR signal, and the shift of this signal was dependent on the $TiCl_4/VCl_4$ ratio. This led to the conclusion that there must be rapid exchange of chlorines in $TiCl_4/VCl_4$. Furthermore, the line width was greater than expected, which Pratt explained as "arising from an exchange not quite rapid enough to produce a complete collapse of the two signals". In pure $TiCl_4$ the [35]Cl NMR line width was found to be larger than expected and temperature dependent, becoming narrower on heating over a small temperature range (23°C - 67°C). Again it was concluded that there is rapid exchange of chlorines between monomers, and that the increased line width is due to two superimposed lines resulting from two different chlorine environments, possibly those in the monomer and in the dimer.

A more recent study discovered the presence of $TiCl_4$ dimers at cryogenic temperatures.[10] The abundance of the dimer was found to be dependent on the deposition rate, and the authors suggested that kinetics are important in the dimerization process. The existence of such dimers establishes that an attractive interaction exists between $TiCl_4$ monomers and offers a reasonable mechanism for the chlorine exchange observed in the earlier work of Pratt.[9] No experimental data is available on possible intermolecular interactions between $TiBr_4$ monomers.

Ab initio studies of the dimerization energies of other halide systems such as magnesium dihalide clusters,[11] zinc, cadmium, and mercury dihalide dimers,[12] and chlorogallane dimers[13] have proved useful in establishing and explaining trends in their intermolecular interactions and general reactivity. A study of titanium tetrahydride TiH_4 revealed a large attractive intermolecular interaction resulting in the formation of strongly bound

Ti_2H_8 dimers with hydrogen bridges.[14] This may be explained by the electron deficiency of titanium and its desire for large coordination numbers due to its unfilled d-shell. The introduction of lone pairs in the titanium tetrahalides results in more complicated species than the tetrahydride. Reliable determination of the magnitude and nature of the intermolecular self-interactions exhibited by the titanium tetrahalides and explanation of their differences is clearly desirable. In this paper we will present results of an *ab initio* study in which we calculate dimerization energies of TiX_4, with X=F,Cl, and Br.

Presumably, the magnitude of any attractive or repulsive interactions between titanium tetrahalide monomers is dependent in part on effects due to the nature of the titanium-halide bond. This could include effects due to bond polarity, and to titanium's electron deficiency. Steric effects may also play a role in the observed trends due to the increase in size of the halides down the group. We use the results of our study on the dimerization of titanium tetrahydride[14] as a reference and monitor directly the effect of halide replacement on monomer interaction.

Our aim is three-fold: to provide reliable quantitative information on the intermolecular self-interactions of TiX_4 (X = F, Cl, Br), assess the effect of substituents of varying size and electronegativity on intermolecular interaction and the dimerization process, and explore the potential energy surface by which halide exchange can occur between two monomers via dimers.[9]

We use various methods, including population analysis, orbital localization, and energy decomposition to analyze *ab initio* wave functions in order to investigate this system.

II. Computational Methods

Initially, geometry optimizations of the titanium tetrahalides TiX_4 (X = F, Cl, Br) and their dimers Ti_2X_8 were carried out at the RHF level of theory using the Stevens-Basch-Krauss-Jasien-Cundari effective core potential[15] (SBK) basis set with d polarization functions (F α = 0.800, Cl α = 0.750, Br α = 0.389) added to halide atoms. This double ζ quality basis set will be referred to as SBKP. For transition metals SBK does not include the $3s^23p^6$ electrons as part of the effective core, as their explicit treatment using a one-electron basis set has been found to be required for an adequate description of their electronic structure. Geometry optimizations were then done with the SBKP basis set using second-order perturbation theory (MP2)[16] to account for dynamic electron correlation.

All stationary points were characterized by calculating and diagonalizing the matrix of the second derivative of the energy (hessian): no imaginary frequencies indicates a minimum on the potential energy surface; one imaginary frequency indicates a transition state.

Single point energies using the coupled cluster method, CCSD(T),[17] with the SBKP basis set were carried out on selected structures to assess the effects of higher order dynamic electron correlation. In addition, for the fluorine and chlorine systems single point MP2 energy calculations were carried out with all electron basis sets to asses the adequacy of the effective core potential. For titanium a triple ζ (14s11p6d/10s8p3d) basis set was used. This consists of Wachter's basis set[18] with two additional sets of p functions[19] and a set of diffuse d functions.[20] For fluorine we employed the triple ζ (10s6p/5s3p) basis set of Dunning;[21] for chlorine the triple ζ (14s9p/8s4p) basis set of McLean and Chandler[22] was used. Polarization functions were added to this triple ζ basis: f functions on the titanium (α = 0.40),[14] two sets of

d polarization functions on the halides, and diffuse s and p functions on the halides also. The 2d polarization function exponents and the diffuse sp function exponents are the defaults in GAMESS.[23] This basis set is referred to as TZVP. To test for convergence of this TZVP all electron basis set, selected single point MP2 energies were carried out retaining the above halide basis sets but with an expanded titanium basis set, denoted TZVP(g). This consists of the titanium triple ζ basis described above plus one set of f ($\alpha = 0.591$), and g ($\alpha = 0.390$) functions, and a set of diffuse s ($\alpha = 0.035$), p ($\alpha = 0.239$), and d ($\alpha = 0.0207$) functions. Exponents used here are optimized for correlated titanium atoms and are due to Glezakou and Gordon.[24] The semi-core electrons as well as the valence electrons in Ti ($3s^2 3p^6 4s^2 3d^2$) were correlated in all post Hartree-Fock calculations. Single point energies determined at one level of theory (A) using geometries obtained at another level of theory (B) are denoted A//B.

The RHF and MP2 calculations were carried out using the electronic structure code GAMESS;[23] the CCSD(T) single point energies were done using Gaussian 92.[25]

III. Results and Discussion

TiX₄. The titanium tetrahalides TiX_4 (X = F, Cl, Br) were found to be tetrahedral at both the RHF and MP2 levels of theory. This is consistent with previous *ab initio* calaculations[26] and gas phase experiments.[27] Calculated and experimentally determined bond lengths and total energies are given in Tables 2 and 3 respectively.

Ti₂X₈. The Ti_2X_8 dimers which were found to be minima and transition states at the MP2/SBKP level of theory all possess C_{2h} symmetry and are shown in Figure 1. Energies of the dimers relative to the monomers can be seen in Table 4.

(a) Molecular Structure and Energetics. First we consider the molecular structures of the titanium tetrahalides and their dimers. Calculated Ti-X bond lengths in TiX_4 at the MP2/SBK level are in excellent agreement with available experimental data (see Table 2). It appears that for the TiX_4 monomers introduction of dynamic electron correlation has only a minimal effect on the calculated bond lengths. For TiF_4 the Ti-F bond length is increased by only ~ 0.02 Å; for $TiCl_4$ and $TiBr_4$ the Ti-X bond lengths are both shortened by only ~ 0.01 Å.

The Ti_2X_8 structures found (see Figure 1) indicate large substituent effects due to the halide ligands. Only double halide bridged $(\mu-X)_2$ Ti_2X_8 dimers were found; while Ti_2H_8 isomers[14] with a $(\mu-H)_3$ bridging arrangement have been shown to be more stable than those with a $(\mu-H)_2$ bridging arrangement no analogous structures have been found for the halides. Other structural effects can be seen by comparing a $(\mu-H)_2$ Ti_2H_8 minimum energy structure (see Figure 2) with the tetrahalide dimer structures. The analogous di-bridged halide structures are actually transition states for exchanging the bridging atoms (see Figures 1 and 3). As expected, the halide bond lengths are longer than in the hydride (MP2/SBKP optimized geometries). This increase is modest for the fluoride, with the Ti-Ti separation increasing by ~0.3 Å, the bridging bond lengths increasing by ~ 0.2 Å, and the terminal bond lengths increasing by 0.07 Å or less. This is indicative of the small size and large electronegativity of fluorine, which results in short bonds. There is then a more substantial increase in these same parameters on going from the fluoride to the chloride (~ 0.5 Å, ~ 0.4 Å, and ~ 0.4 Å), followed by a modest increase on going from chloride to bromide (~ 0.25 Å, ~ 0.15 Å, and ~ 0.15 Å). The large differences between the fluoride and chloride is clearly a result of both the increased size and lower electronegativity of Cl. The electronegativities of Cl and Br are very similar; the changes on going from chloride to bromide, then, are due entirely to the larger size

of Br. Dynamic electron correlation effects on the transition state halide dimer *geometries* are found to be minimal (see Figure 1).

In the halide dimer minima the substituent effect is even more apparent. The fluoride dimer retains its bridging bonds, though now the bridge is no longer symmetric with Ti-F-Ti bridging bond lengths of 1.91 Å and 2.13 Å (MP2/SBKP optimized geometries). This effect is exaggerated greatly in the chloride and bromide where covalent bridging bonds no longer exist. Instead, these structures resemble weakly bound Van der Waals complexes. In fact, within the dimer the geometries of the TiX_4 moieties are hardly distorted from those of the separated monomers, with little change from a purely tetrahedral arrangement (see Table 2 and Figure 1). For the fluoride minimum dynamic electron correlation has only a minor effect on the structure; however, for the chloride and bromide the effect is large. Dynamic electron correlation allows the tetrahalide moieties in these dimers to approach much more closely. The Ti-Ti separation is reduced by 1.61 Å and 1.83 Å in the chloride and bromide, respectively, on going from RHF to MP2 optimized structures.

We now consider energetics (see Table 4). Comparison with the Ti_2H_8 dimer reveals that the introduction of halides makes the dimerization process much less favorable. At the RHF/SBKP level of theory the fluoride dimer minimum and transition state are stable with respect to separated monomers by 8.6 kcal/mol and 6.1 kcal/mol, respectively. For the chloride and bromide the transition states are highly unstable with respect to separated monomers; their formation is endothermic by 23.5 and 26.0 kcal/mol, respectively. The chloride and bromide minima are essentially isoenergetic with their separated monomers (dimerization energies of - 0.3 and - 0.1 kcal/mol, respectively). This is consistent with the notion that these are weakly bound Van der Waals species, since dispersion effects are not accounted for at the Hartree-Fock level of theory.

Table 4 shows that inclusion of dynamic electron correlation through MP2 using the SBKP basis set stabilizes all of the dimers with respect to the monomers. The fluoride dimer

minimum and transition state are now predicted to be more stable than two separated monomers by 14.3 and 12.4 kcal/mol, a stabilization of 5.7 and 6.3 kcal/mol, respectively. The chloride and bromide minima are predicted to be weakly bound dimers with exothermic dimerization energies of 5.2 and 6.3 kcal/mol, respectively. However, the correlation effect is clearly largest for the chloride and bromide transition states which are stabilized by 18.3 and 19.4 kcal/mol respectively at the MP2/SBKP level. This suggests that electron-electron repulsion is large in these bound dimer conformations and therefore steric effects are playing a role in their instability.

To assess the effect of including dynamic electron correlation in the geometry optimizations on the energetics, single point MP2/SBKP energies were calculated at RHF/SBKP optimized geometries. For both fluoride dimers and for the chloride and bromide transition states, MP2//RHF reproduce the MP2//MP2 energies very well, giving values of - 14.1, - 12.2, + 6.2, and + 7.3 kcal/mol. For the chloride and bromide minima, where dynamic electron correlation has a large structural effect, this is not the case. MP2/SBKP single point energies give dimerization energies of -1.8 and -1.5 kcal/mol for the chloride and bromide, respectively, compared with - 5.0 kcal/mol and - 6.4 kcal/mol for the MP2//MP2 energies. Inclusion of dynamic electron correlation in the geometry optimization, then, is essential to properly describe the weakly bound dimers.

Higher order correlation effects introduced through CCSD(T)//MP2 calculations with the SBKP basis set (see Table 4a) are small. The difference between the MP2 and CCSD(T) dimer energies relative to separated monomers is only - 2.5 kcal/mol and + 0.6 kcal/mol for the Ti_2F_8 minimum and Ti_2Cl_8 minimum, respectively.

It is clear from MP2/TZVP and MP2/TZVP(g) energies at the MP2/SBKP optimized geometries that the SBKP basis set over estimates the exothermicity of the fluoride dimer but appears to do very well for the chloride (see Tables 4a and b). We expect that the SBKP basis set is also reliable for the bromide calculation. The largest basis set, TZVP(g), demonstrates

convergence of dimerization energies to ~ 1 kcal/mol or less.

(b) Melting and Boiling Point Trends, and Halide Exchange. The

calculated dimerization energies are entirely consistent with the melting and boiling point trends

of the titanium tetrahalides. TiF_4 has a higher boiling point than $TiCl_4$ even though it has lower

molecular mass (see Table 1). This suggests larger intermolecular interactions in TiF_4 than in

$TiCl_4$. Other experimental evidence[7] indicates that TiF_4 forms polymeric chains in the solid

phase while $TiCl_4$ remains in discrete molecular units, again suggesting larger intermolecular

interactions in TiF_4. The dimerization energies calculated during this study (see Table 4b) show

the intermolecular dimerization energy of TiF_4 (- 9.6 kcal/mol) to be more than twice that of

$TiCl_4$ (- 4.5 kcal/mol). So, Ti_2F_8 is a bound dimer with bridging bonds, which is consistent

with the formation of polymer chains, while the Ti_2Cl_8 minimum is a weakly bound Van der

Waals dimer. As $TiCl_4$ and $TiBr_4$ exhibit almost equal attractive intermolecular self-interactions

their boiling/melting points resume the trend expected based only on molecular mass.

Pratt has suggested that chlorine exchange between titanium tetrachloride monomers

may be a possible explanation for unexpected results in his NMR experiments.[9] The transition

states shown in Figure 1 represent possible paths to halide exchange. First we consider halide

exchange in TiF_4 and $TiCl_4$ dimers, as data from the full range of basis sets is available. Figure

3 shows a possible mechanism for halide exchange in the fluoride and chloride.

For the fluoride the entire process is exothermic with respect to separated monomers. If

the separated monomers are energetic enough not to be trapped in the dimer wells (possible in

the gas phase) halide exchange and separation of monomers is a barrierless process. The result

is a monomeric system with very rapid halide exchange between monomers. If the monomers

have less kinetic energy, come together and are trapped in one of the wells (for example,

during a phase transition from gas to solid) the small barrier between minima, which is 1.9

kcal/mol at the MP2/TZVP level, represents a path to the exchange of bridging fluorines. This scenario results in a bound dimer with constant and rapid exchange of bridging fluorines.

The transition state leading to chlorine exchange is endothermic with respect to separated monomers by 5.0 kcal/mol at the MP2/TZVP level. This value represents the effective barrier that approaching monomers must overcome to achieve halide exchange. Monomers which come together and are trapped in the minima wells are only weakly bound by 4.2 kcal/mol. These modest barriers to dimerization, chloride exchange, and separation of monomers provide a possible explanation of the temperature dependent NMR line widths observed by Pratt.[9] At high temperatures, dimerization, exchange of chlorines, and the separation process would be expected to occur very rapidly. Therefore on the NMR time scale only one Cl environment is detected and a narrow line width is observed. At lower temperatures approaching monomers are more likely to "see" a barrier to dimerization; consequently exchange is slower and both monomer and dimers co-exist on the NMR time scale. This produces different Cl environments and an increased line width.

Inspection of Figure 3 reiterates the fact that MP2/SBKP energies are reliable for the chloride system. This suggests that energies calculated at the MP2/SBKP level for the bromide system may also be trusted. We therefore conclude that a similar halide exchange process is possible in the bromide system, which would result in comparable effects to those seen by Pratt in the chloride experiment.

(c) Bonding. The method of Edmiston and Ruedenburg[28] was used to localize the molecular orbitals and thereby examine the nature of the bonding in the titanium halide systems. Plots of the localized molecular orbitals (LMOs) resulting from RHF/SBKP localization calculations at the MP2/SBKP geometries are shown in Figures 4 - 7. Mulliken populations of these localized orbitals are highly basis set dependent and inadequate for a truly meaningful assignment of electrons to Ti and X (X = F, Cl, Br). However, the method is

useful in determining trends in a series of molecules where an equivalent basis set is used throughout; therefore, Mulliken populations of the LMOs are also presented.

Figure 4 shows the LMOs of TiX_4 ($X = F$, Cl, Br). Inspection of these plots clearly reveals the presence of Ti-X σ bonds and also suggests that lone-pair back-bonding is occurring. Mulliken populations of the σ bonds confirm the expected trend in this series of molecules, revealing a highly polarized Ti-F bond, and Ti-Cl and Ti-Br bonds which are still polarized but much less so. Populations of the lone-pair LMOs are indicative of the trend in the degree of back-bonding. Ti LMO populations are 0.06, 0.11, and 0.11 electrons for the fluoride, chloride, and bromide respectively. This suggests the degree of back-bonding to follow the trend F<Cl=Br, though the differences are clearly very small.

Figures 5, 6, and 7 show selected LMOs of Ti_2X_8 ($X = F$, Cl, Br). Both the Ti_2F_8 minimum and transition state orbitals are presented as they are both bound dimers with bridging bonds (see Figures 5a and b). As the Ti_2Cl_8 and Ti_2Br_8 minima are weakly bound dimers with no bridging bonds, the perturbation of the monomer LMOs is not visually apparent; therefore, their LMOs plots are not shown. The Ti_2Cl_8 and Ti_2Br_8 transition states do have bridging bonds, so their plots are shown (see Figures 6 and 7).

For the transition states only one of four equivalent bridge LMOs is shown. The bridging arrangement is not a 3 center, 2 electron bond like that found in Ti_2H_8;[14] the LMOs clearly show participation of "lone-pair" electrons in the bridges resulting in a Ti-X-Ti bridge made up of two 2 center, 2 electron bonds. In total, the two halides in this arrangement donate 6 electrons and the titaniums donate 2 electrons to the bridges. Each of the bridging halides therefore has 2 remaining non-bonding lone-pairs (one is shown). The fluoride minimum does not have four equivalent bridging bonds; it possesses a long bond, short bond Ti—F-Ti arrangement. These two non-equivalent bonds are shown in Figure 5 b.

The LMO plots involving terminal halides show titanium-halide σ bonds and also the

same kind of lone-pair back bonding character seen in the monomers (see Figure 4).

(d) The Dimerization Process. In a study on the dimerization of BF_3, Nxumalo and Ford[29] discounted several dimer structures which they predicted to be exothermically stable with respect to monomers. Their reason was an energy barrier which, they claim, resulted from large unfavorable distortion energies of the monomers. In fact, their approach which separates the energetics of dimerization process into two distinct stages: a) distortion of the monomers, and b) reaction of the distorted monomers to form a dimer, produces an artificial barrier. Such a barrier will *always* appear if the monomer geometries are significantly distorted in the dimer. In reality the energetics of the process of dimerization are determined by a *continuous* competition between endothermic effects due to structural distortion and exothermic effects due to monomer-monomer interaction, during the approach of the monomers as well as at the end point.

A more physical, computational approach, then, to determine whether a barrier exists is to carry out a number of constrained geometry optimizations where only the distance between monomers is constrained (for example constrain the Ti-Ti distance only), thereby creating a reaction path to dimerization. This method was used to establish that there is no energy barrier to the dimerization of TiH_4,[14] and is applied here to TiF_4 and $TiCl_4$.

These constrained optimizations were carried out on the $2TiF_4$ and $2TiCl_4$ systems at the MP2/SBKP level; RHF/SBKP energies at these points are also plotted (see Figures 8a and b). As point group symmetry was constrained to be C_{2h} the paths shown are not necessarily the minimum energy paths; nonetheless, they establish that the dimerization of TiF_4 and $TiCl_4$ are barrierless processes.

LCD analysis. In order to demonstrate the validity of our argument that the energetics of the process of dimerization are governed by a continuous competition between endothermic

monomer distortion and exothermic monomer interaction. we have carried out an energy

decomposition. The LCD analysis has proved a useful tool in understanding intermolecular

interactions.[30] It decomposes the total energy of the system into potential and kinetic energies

of LMOs and the interactions between them. We have carried out the analysis at the RHF level

at points on the energy paths plotted in Figures 8a and b.

The analysis requires that a local nuclear charge distribution is assigned to each LMO.

For semi-core LMOs, Ti was assigned a nuclear charge of 2; for the Ti-X bond LMOs Ti and

X were each assigned a nuclear charge of 1; and for the X lone-pair LMOs, X was assigned a

nuclear charge of 2. Note that these assignments were defined in the separated monomers and

were applied consistently as the monomers approached each other. The LCD analysis allows us

to determine the total internal energies of the monomers and the total interaction energy between

them along the reaction path. This is done by summing the relevant individual LMO

contributions.The resulting plots are shown in Figures 9 and 10.

In these plots the bold curve is the total energy and is the sum of the remaining two

curves which are the total internal energy of the monomers ($\Delta E(2TiX_4)$) and the total

interaction energy of the monomers ($\Delta E(TiX_4(1)|TiX_4(2))$). Clearly one can make a general

observation that the internal energy goes up and the interaction energy goes down during these

dimerization processes and the total energy along the path is the result of the competition

between these two effects. In the fluoride system (Figure 9) at the RHF/SBKP level of theory

the dimerization process is barrierless and the resulting dimer is exothermic by 8 kcal/mol

relative to separated monomers. In this case the favorable monomer interaction dominates the

unfavorable structural deformations. In the chloride system (Figure 10) at the RHF/SBKP level

of theory the total energy remains the same as that of the separated monomers (MP2 is required

to observe the weakly bound minimum - see Figure 8b) until a Ti-Ti separation of less than 6 Å

then the total energy relative to the monomers increases rapidly as the transition state Ti-Ti

separation is approached. So, in this case the interaction and structural deformation effects

cancel each other out until a Ti-Ti separation of ~ 6 Å and then the endothermic structural deformation effects begin to dominate. This is suggestive of steric effects.

We intend to carry out a more detailed LCD analysis of these two systems in order to explain their radically different behaviors.

IV. Conclusions

The titanium tetrahalides TiX_4 ($X = F$, Cl, Br) are all found to have attractive intermolecular interactions. TiF_4 possesses the largest attractive interaction, forming a bound dimer. Smaller interactions were found for $TiCl_4$ and $TiBr_4$; in these cases only weakly interacting Van der Waals dimers are predicted. This is consistent with known experimental data which suggests that solid state TiF_4 is a bridged polymer chain, and solid state $TiCl_4$ and $TiBr_4$ remain molecular in structure. The predicted interactions are also consistent with the non-monotonic behavior of the titanium tetrahalide melting points.

Transition states with symmetrically equivalent bridging halides were found. These represent possible routes to halide exchange between monomers. Such a mechanism readily explains the unexpected results of NMR experiments on $TiCl_4$.

Dynamic correlation, introduced through MP2, was found to be very important for energetics for all the dimer structures studied. It was found to be less important for determining structures of the fluoride minimum and transition state, and the chloride and bromide transition states. However, inclusion of dynamic correlation was found to be essential for geometry optimizations of the chloride and bromide minima. Higher order correlation effects introduced through CCSD(T) were found to have little effect.

The effective core potential basis set SBKP was found to overestimate the dimerization

energy of TiF_4, with an exothermic dimerization energy of 14.3 kcal/mol compared to 9.6 kcal/mol predicted by the all electron basis set TZVP. SBKP was found to be a reliable basis set for $TiCl_4$, agreeing well with the all electron result (5.2 kcal/mol compared to 4.5 kcal/mol). It is concluded that SBKP is also a reliable basis for $TiBr_4$.

References

1. Wailes, P. C.; Coutts, R. S. P.; Weigold, H. in *Organometallic Chemistry of Titanium, Zirconium, and Hafnium,* Academic Press; New york, 1974; Chapters 1-3.

2. Greenwood, N.N.; Earnshaw, A. in *Chemistry of the Elements,* Pergamon Press, new York, 1984, (a) Chapter 21 pp 1134. (b) Chapter 6 pp 222.

3. Sakai, S. *J. Phys. Chem.* **1994**, 98, 12053.

4. · (a) Beattie, I. R.; Jones, P. J. *J. Chem. Phys.* **1989**, 90, 5209. (b) DeVore, T.C.; Gallaher, T. N. *J. Chem. Phys.* **1985**, 82, 2512.

5. Bauschlicher Jr., C. W.; Taylor, P.; Komornicki, A. *J. Chem. Phys.* **1990**, 92, 3982.

6. Branchadell, V.; Oliva, A. *J. Am. Chem. Soc.* **1992**, 114, 4357.

7. (a) Mousty-Desbuquoit, C.; Riga, J.; Verbist, J. J. *Inorg. Chem.* **1987**, 26, 1212. (b)

Euler, R. D.; Westrum, E. F. *J. Phys. Chem.* **1961**. 65. 132.

8. Clark, R. J. H. in *The Chemistry of Titanium and Vanadium* ; Elsevier: Amsterdam, 1968; pp 25.

9. Pratt, D. W. *Thesis.* **1967**, University of California, Berkeley.

10. Rytter, E.; Kvisle, S. *Inorg. Chem.* **1985**, 24. 639.

11. Axten, J.; Mendel, T.; Bock, C. W. *J. Phys. Chem.* **1994**, 98. 7823.

12. (a) Kaupp, M.; von Schnering, H. G. *Inorg. Chem.* **1994**. 33. 4718. (b) Kaupp, M.; von Schnering, H. G. *Inorg. Chem.* **1994**, 33, 2555.

13. Duke, B. J.; Hamilton, T. P.; Schaefer III, H. F. *Inorg. Chem.* **1991**, 30, 4225.

14. Webb, S. P.; Gordon, M. S. *J. Am. Chem. Soc.* **1995**, 117, 7197.

15. (a) Cundari, T. R.; Stevens, W. J. *J. Chem. Phys.* **1993**, 98, 5555. (b) Stevens, W. J.; Basch, H.; Krauss, M.; Jaisen, P. *Can. J. Chem.* **1992**, 70, 612. (c) Stevens, W. J.; Basch, H.; Krauss *J. Chem. Phys.* **1984**, 81, 6026.

16. (a) Binkley, J.S.; Pople, J.A. *Int. J. Quantum Chem.* **1975**, 9, 229; (b) Krishnan, R; Pople, J.A. *Int. J. Quantum Chem.* **1978**, 14, 91. (d) Frisch, M. J.; Head-Gordon, M.; Pople, J. A. Chem. Phys. Lett., 1990, 166, 275.

17. Pople, J.A.; Head-Gordon M.; and Raghavachari, k. *J. Chem. Phys.*, **1987**, 87, 5968.

18. Watchers, A. J. H. *J. Chem. Phys.* **1970**, 55, 716.

19. Hood, D. M.; Pitzer, R. M.; Schaefer, H. F. *J. Chem . Phys.* **1979**, 71, 705.

20. Rappe, A. K.; Smedley, T. A.; Goddard, W. A. *J. Phys. Chem.* **1981**, 85, 2607.

21. Dunning, T. H. *J. Chem. Phys.* **1971**, 72, 5639.

22. McLean, A. D.; Chandler, G. S. *J . Chem. Phys.* **1980**, 72, 5639.

23. Schmidt, M.W.; Baldridge, K.K.; Boatz, J.A.; Jensen, J.H.; koseki, S.; Matsunaga, N.; Gordon, M.S.; Ngugen, K.A. ; Su, S.; Windus, T.L.; Elbert, S.T.; Montgomery, J.; Dupuis, M. *J. Comp. Chem.* **1993**, 14, 1347.

24. Glezakou, V-A.; Gordon, M. S. *J. Phys. Chem.* **1997**, 101, 8714.

25. Frisch, M.J.; Trucks, G.W.; Head-Gordon, M.; Gill, P.M.W.; Wong, M.W.; Foresman, J.B.; Johnson, B.G.; Schlegel, H.B.; Robb, M.A.; Replogle, E.S.; Gomperts, R.; Andres, J.L.; Raghavachari, K.; Binkley, J.S.; Gonzalez, C.; Martin, R.L.; Fox, D.J.; DeFrees, D.J.; Baker, J.; Stewert, J.J.P.; Pople, J.A.; GAUSSIAN92; GAUSSIAN, INC.; Pittsburgh, PA **1992**.

26. (a) Russo, T. V.; Martin, R. L.; Hay, P. J. *J. Chem. Phys.* **1995**, 102, 8023. (b) Russo, T. V.; Martin, R. L.; Hay, P. J.; Rappé, A. K. *J. Chem. Phys.* **1995**, 102, 9315.

27. (a) Moore, E. A.; Healy, A. *J. Chem. Soc. Faraday Trans.* **1995**, 91, 1735. (b) Dobbs, K. D.; Hehre, W. J. *J. Comp. Chem.* **1987**, 8, 880. (c) Morito, Y.; Vehara, H. *J. Chem. Phys.* **1966**, 45, 4543.

28. Edmiston, C.; Ruedenberg, K. *Rev. Mod. Phys.* **1963**, 35, 457.

29. Nxumalo, L. M.; Ford, T. A. *J. Mol. Struc. (Theochem)*, **1995**, 357, 59.

30. a) Jensen, J. H.; Gordon, M.S. *Acc. Chem. Res.* **1996**, 29, 536. b) Jensen, J. H.; Gordon, M. S. *J. Am. Chem. Soc.* **1995**, 99, 8091. c) England, W.; Gordon, M. S. *J. Am. Chem. Soc.* **1971**, 93, 4649.

Table 1. The melting and boiling points of the titanium tetrahalides.[a]

	Melting Point/°C	Boiling Point/°C
TiF_4	-	284.0
$TiCl_4$	-24.0	136.4
$TiBr_4$	39.0	233.0
TiI_4	150.0	377.0

[a] Reference 8.

Table 2. Calculated and experimental Ti-X bond lengths in Angstroms for the tetrahedral TiX$_4$ molecules (X = F, Cl, Br).

	RHF/SBKP /Å	MP2/SBKP /Å	Experiment[a] /Å
TiF$_4$	1.746	1.765	1.754
TiCl$_4$	2.183	2.171	2.170
TiBr$_4$	2.337	2.328	2.339

a Reference 27.

Table 3. a) Total energies (in Hartrees) of TiX_4 (X = F, Cl, Br) calculated using the SBKP basis set. b) Total energies (in Hartrees) of TiX_4 (X = F, Cl, Br) calculated using the all electron basis sets TZVP and TZVP(g).

a)

	SBKP		
	RHF[a]	MP2[a]	CCSD(T)[b]
TiF_4	-153.19990	-154.20671	-154.23138
$TiCl_4$	-116.45762	-117.33226	-117.39495
$TiBr_4$	-110.29105	-111.14418	-111.18487

[a] Geometry optimized at this level of theory. [b] Single-point energy calculated at the MP2/SBKP geometry.

b)

	MP2	
	TZVP[a]	TZVP(g)[a]
TiF_4	-1247.93521	-1247.96689
$TiCl_4$	-2687.76258	-2687.79513

[a] Single-point energy calculated at the MP2/SBKP geometry.

Table 4. a) Calculated energies (in kcal/mol) of Ti_2X_8 relative to TiX_4 (X = F,Cl,Br) and MP2 zero-point energy corrections all using the SBKP basis set. b) Calculated MP2 single point energies (in kcal/mol) of Ti_2X_8 relative to TiX_4 (X = F,Cl,Br) with the all electron basis sets TZVP and TZVP(g).

a)

		SBKP			
		RHF[a]	MP2[a]	Z.P.E.	CCSD(T)[b]
Ti_2F_8	min	- 8.6	- 14.3	+ 1.1	- 16.8
Ti_2F_8	T.S.	- 6.1	- 12.4	+ 1.0	
Ti_2Cl_8	min	- 0.3	- 5.2	+ 0.3	- 4.6
Ti_2Cl_8	T.S.	+ 23.5	+ 5.2	+ 0.6	
Ti_2Br_8	min	- 0.1	- 6.4	+ 0.2	
Ti_2Br_8	T.S.	+ 21.5	+ 6.6	+ 0.3	

[a] Geometry optimized at this level of theory. [b] Single-point energy calculated at the MP2/SBKP geometry.

b)

		MP2	
		TZVP[a]	TZVP(g)[a]
Ti_2F_8	min	- 9.6	- 10.5
Ti_2F_8	T.S.	- 7.6	- 8.7
Ti_2Cl_8	min	- 4.5	
Ti_2Cl_8	T.S.	+ 5.0	

[a] Single-point energy calculated at the MP2/SBKP geometry.
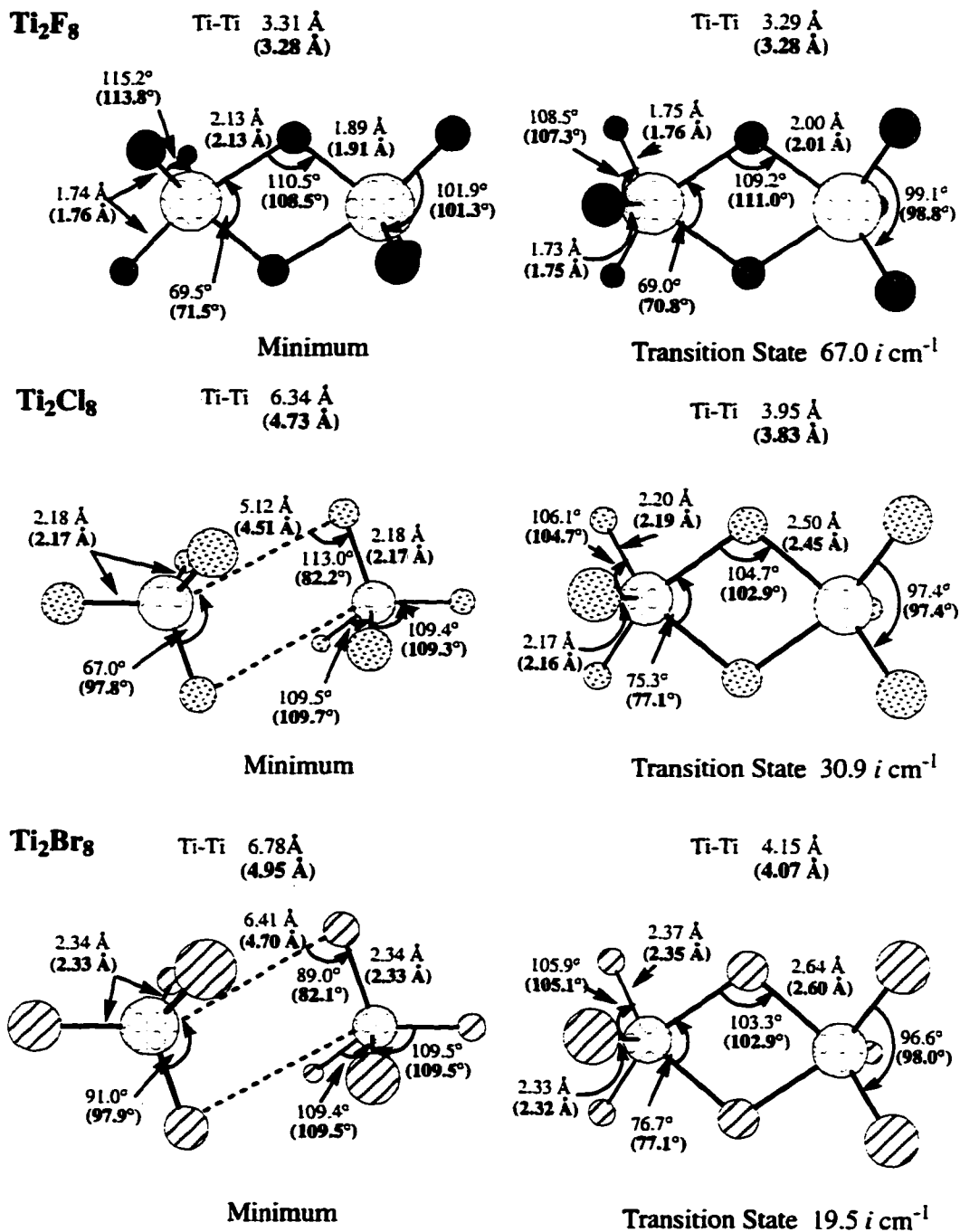
Figure 1. RHF and MP2/SBKP optimized structures for minima and transition states on the potential energy surface of Ti_2X_8 (X = F, Cl, Br). MP2 geometries are given in parentheses.
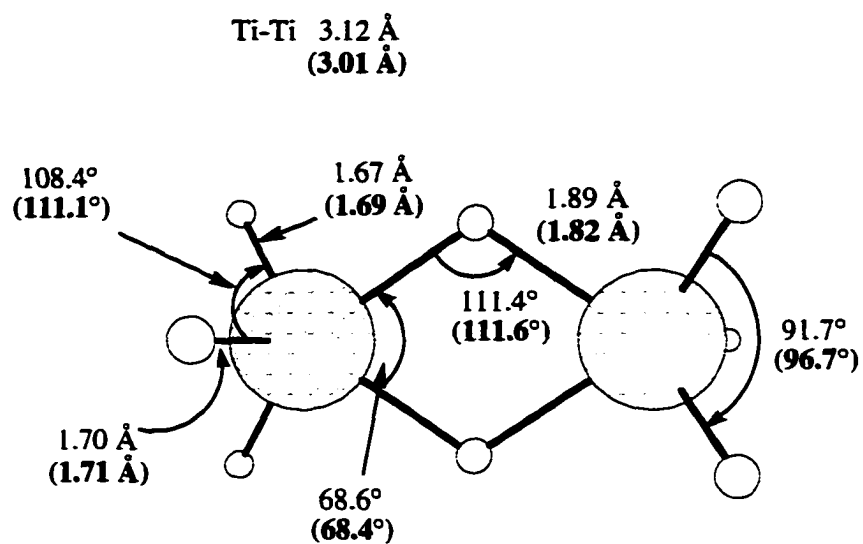
Figure 2. Calculated energies (in kcal/mol) of C_{2h} Ti_2H_8 relative to $2TiH_4$. (opt) indicates that the geometry has been optimized at that level of theory.
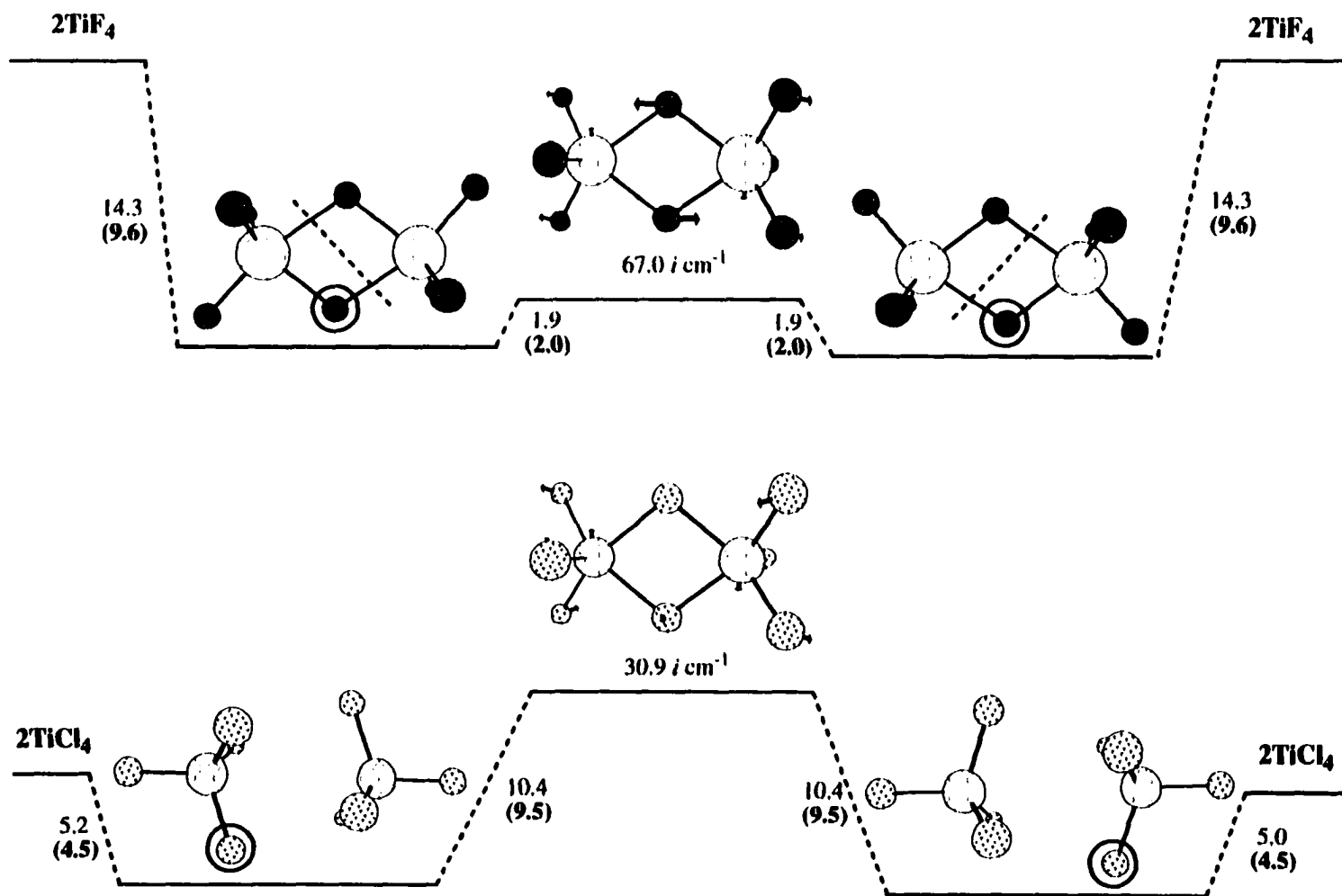
Figure 3. Possible mechanisms for halide exchange in T2iF$_4$ and 2TiCl$_4$. Energies are in kcal/mol.MP2/SBKP energies (optimized structures) are in normal typface; MP2/TZVP single point energies are in bold. Circles indicate halides which are exchanged.
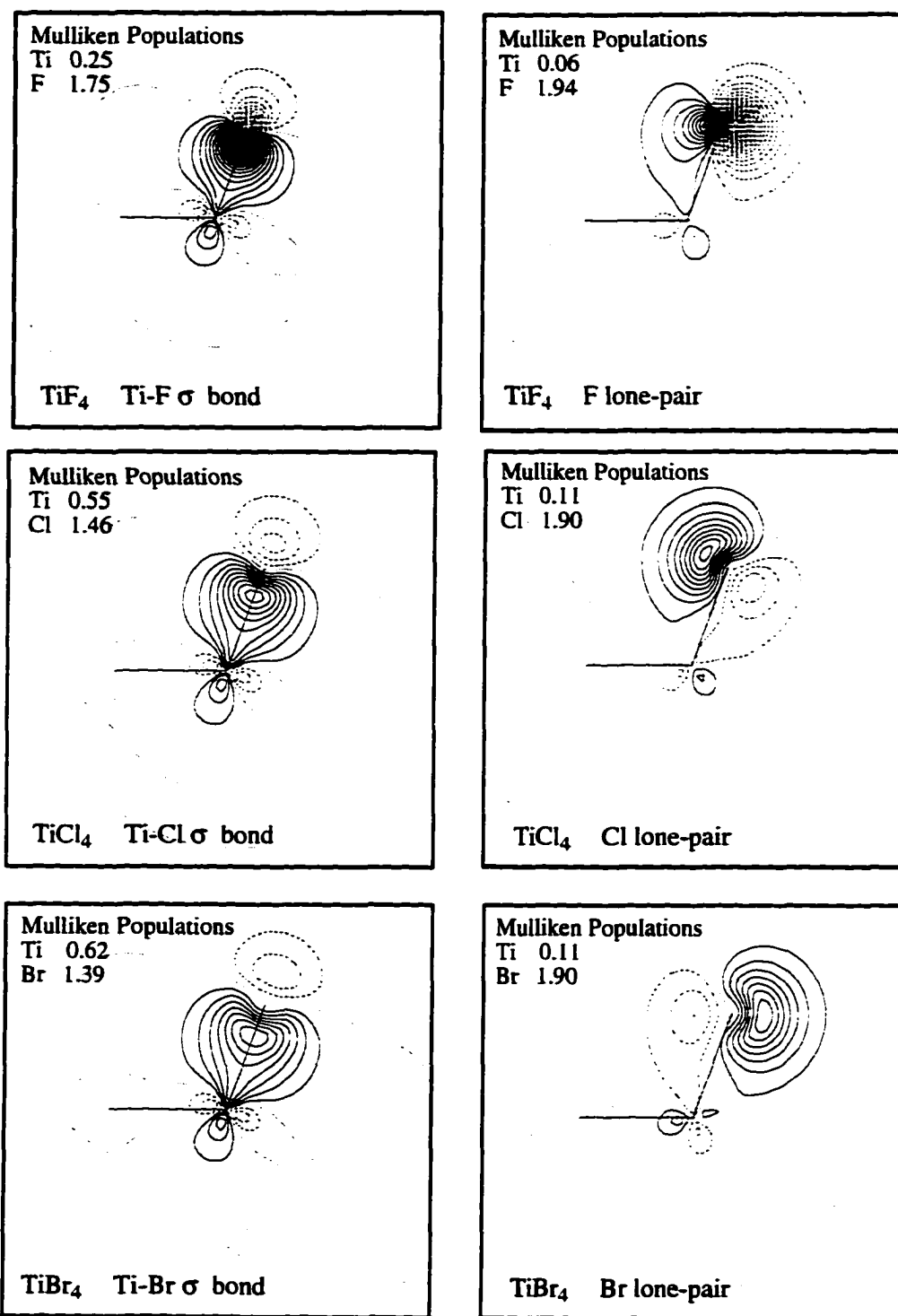
Figure 4. LMO plots of Ti-X σ-bonds and X lone-pairs in TiX$_4$ (X=F,Br,Cl). The contour increments are 0.05 Bohr$^{3/2}$.
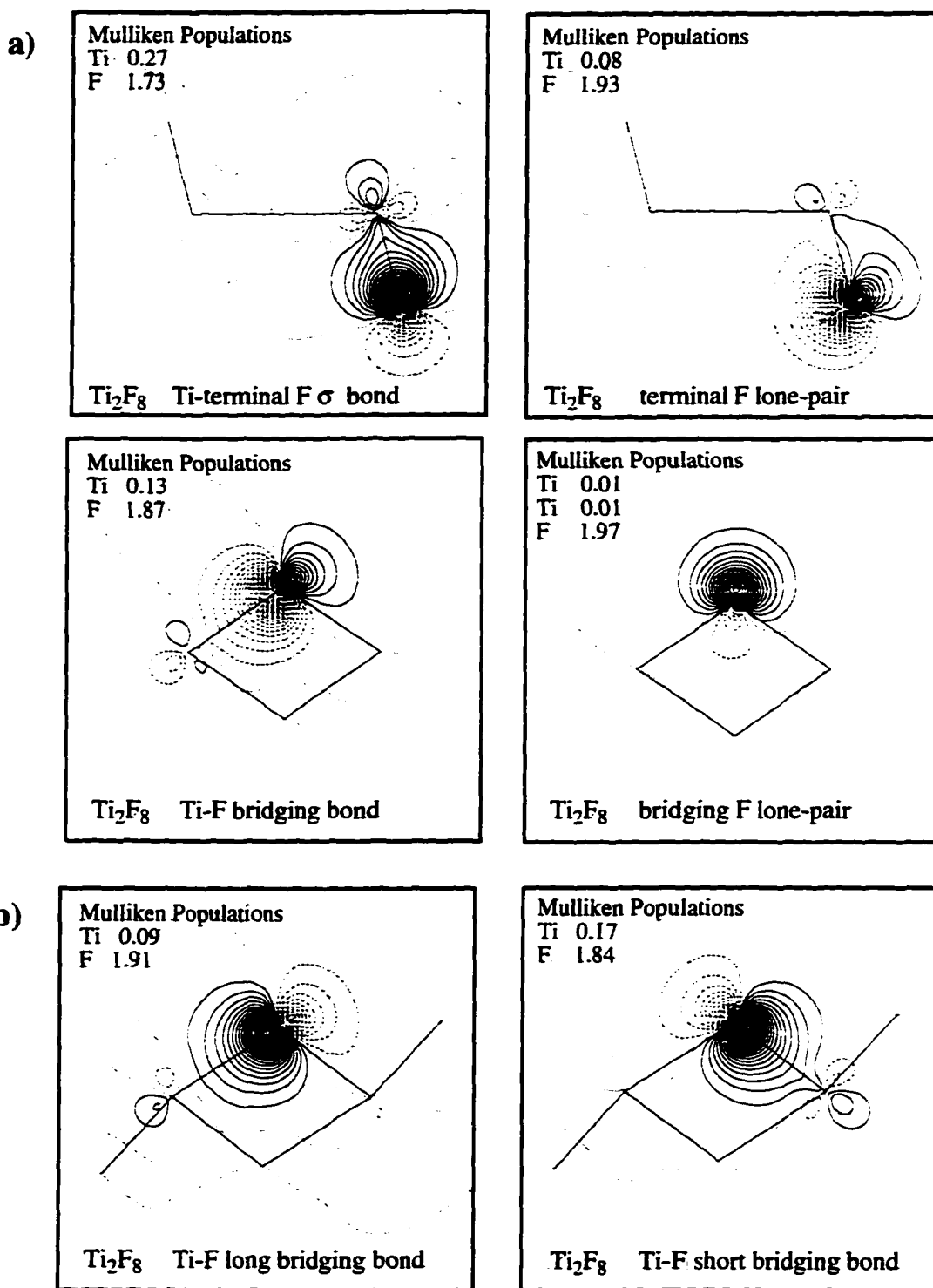
Figure 5. a) LMO plots of a Ti-F σ-bond, F lone-pairs, and a Ti-F bridging bond in the Ti_2F_8 transition state. b) LMO plots of Ti-F bridging bonds in the Ti_2F_8 minimum. The contour increments are 0.05 $Bohr^{3/2}$.
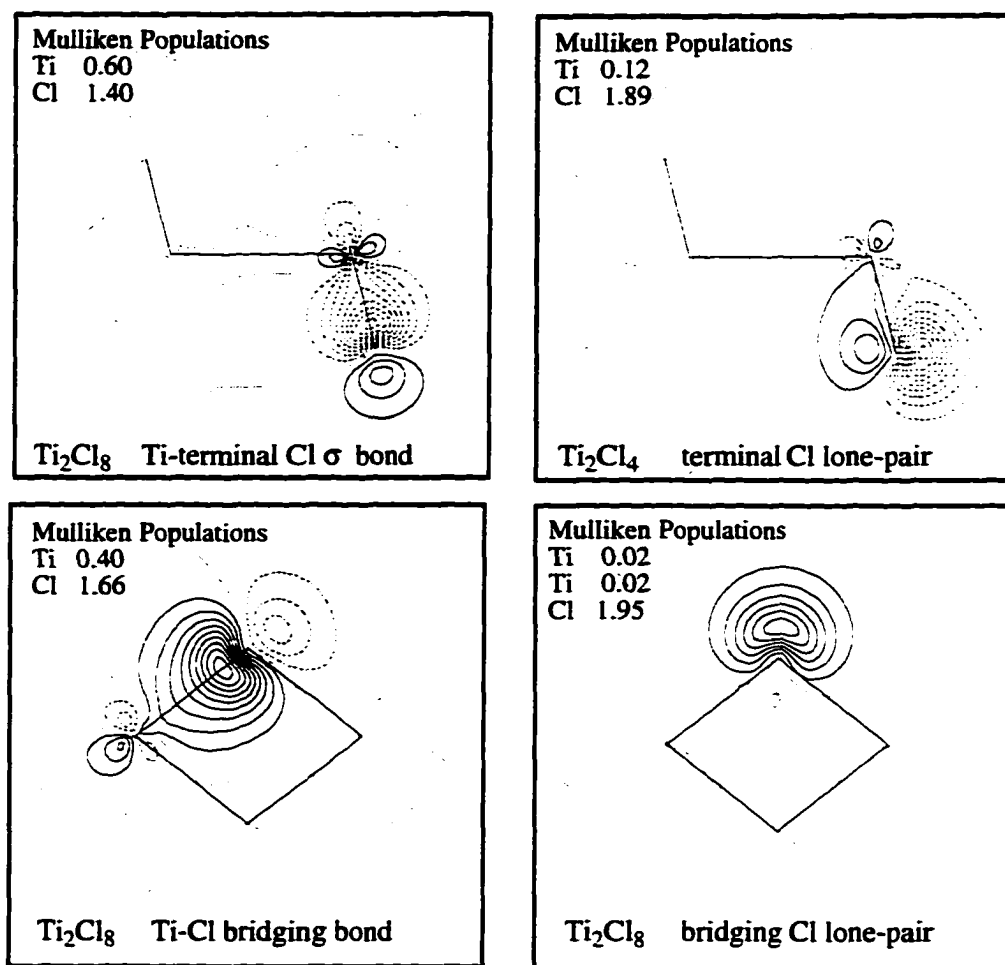
Figure 6. LMO plots of a Ti-Cl σ-bond, Cl lone-pairs, and a Ti-Cl bridging bond in the Ti_2Cl_8 transition state. The contour increments are 0.05 $Bohr^{3/2}$.
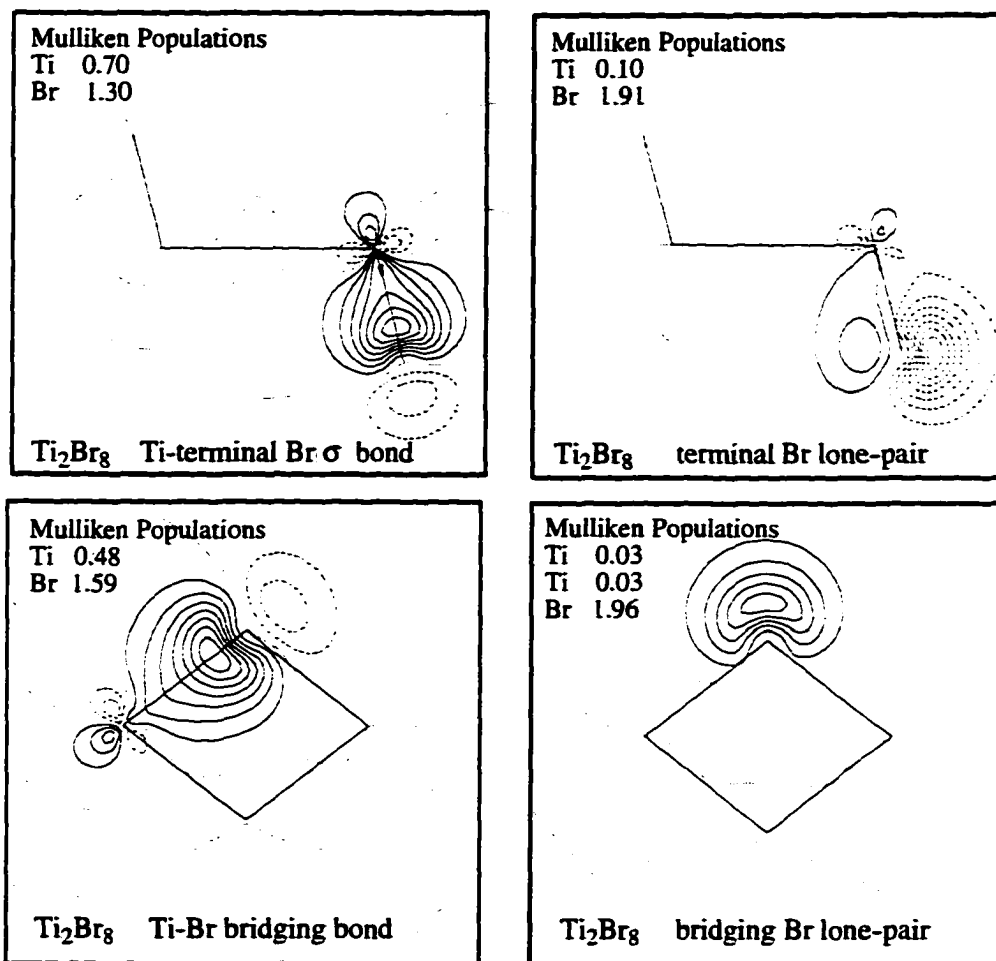
Figure 7. LMO plots of a Ti-Br σ-bond, Br lone-pairs, and a Ti-Br bridging bond in the Ti_2Br_8 transition state. The contour increments are 0.05 $Bohr^{3/2}$.
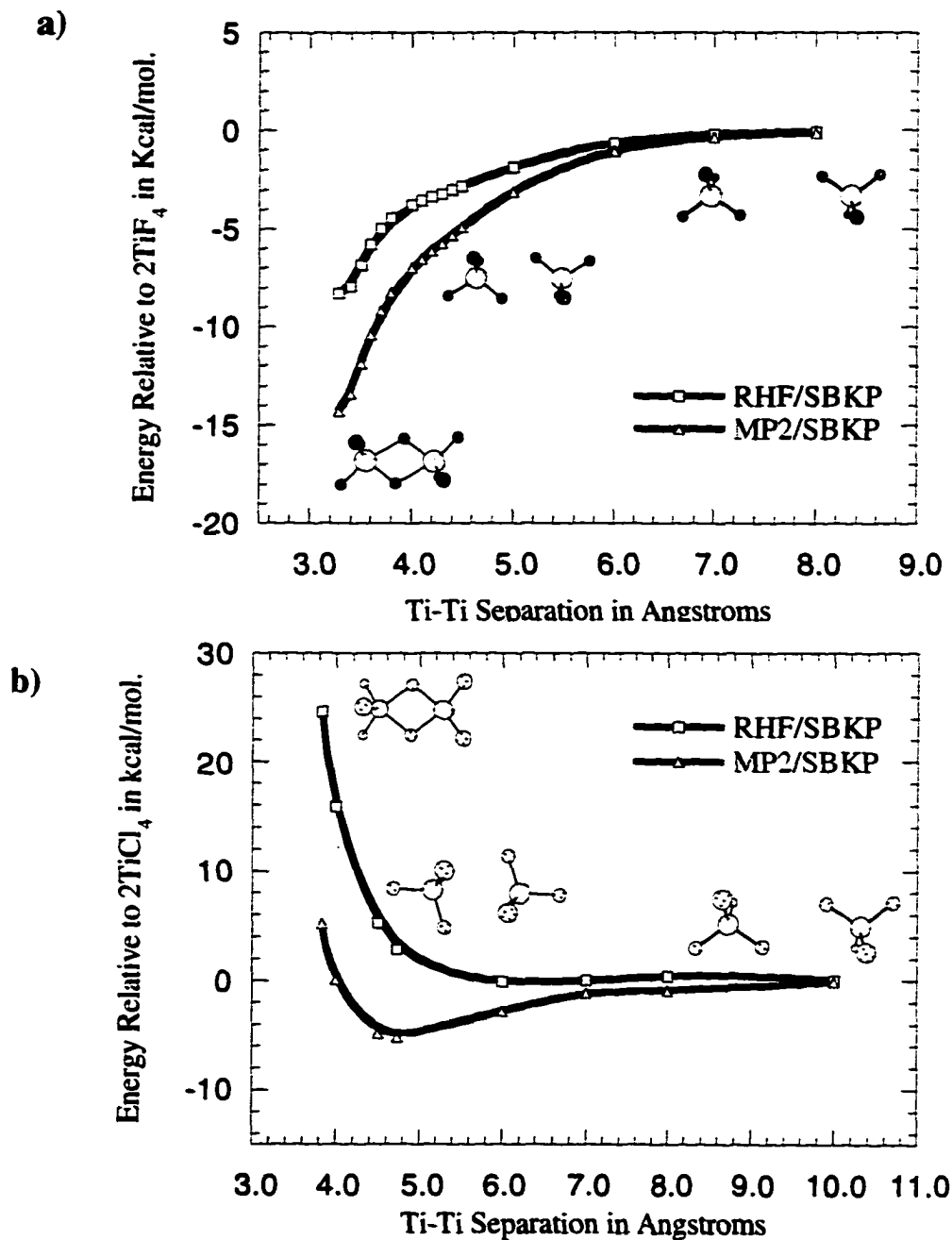
Figure 8. Plots of (a) Ti_2F_8 energy and (b) Ti_2Cl_8 energy (kcal/mol) relative to $2TiF_4$ and $2TiCl_4$, respectively, versus Ti-Ti separation. The plots labled MP2/SBKP are of energies from MP2/SBKP constrained optimizations; the plots labled RHF/SBKP are of RHF/SBKP single point energies at MP2/SBKP constrained geometries.
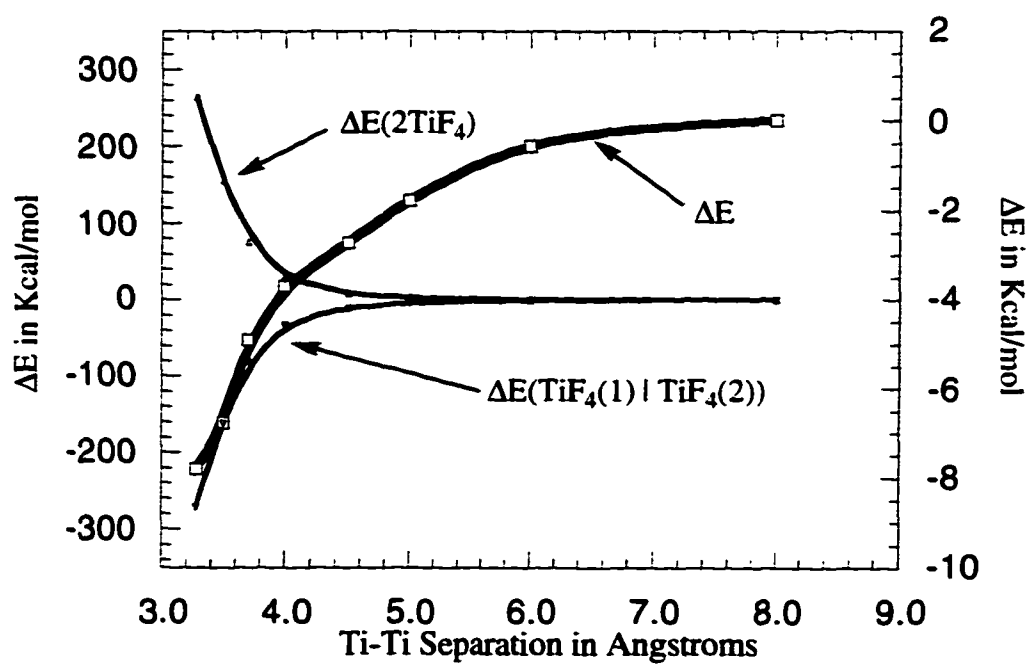
Figure 9. Plot of the change in total energy (bold curve labled ΔE, right y-axis) and plots of internal ΔE(2TiF$_4$) and interaction ΔE(TiF$_4$(1) I TiF$_4$(2)) energies (left y-axis). Energies are relative to those at a Ti-Ti separation of 8 Å.
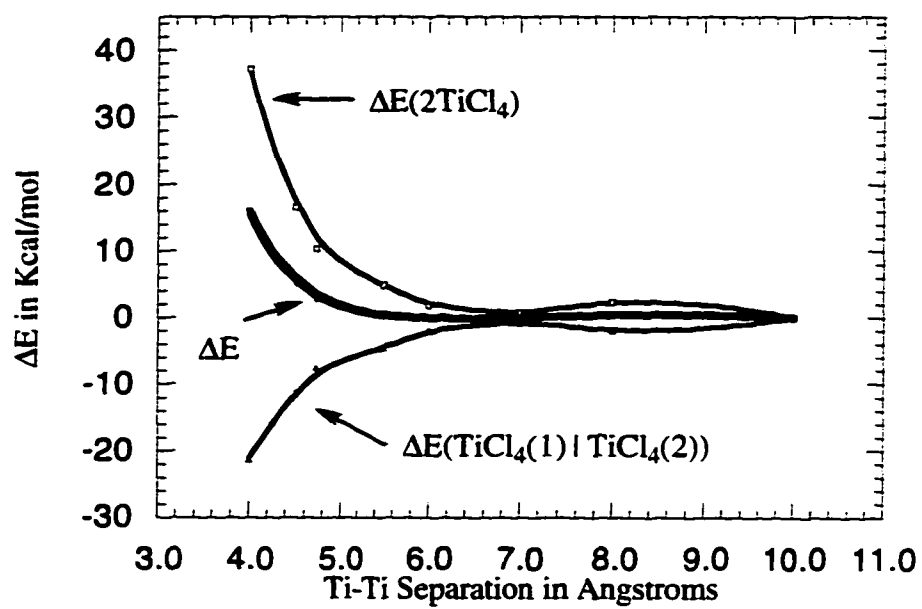
Figure 10. Plot of the change in total RHF energy (bold curve labled ΔE) and plots of internal ΔE(2TiCl$_4$) and interaction ΔE(TiCl$_4$(1) I TiCl$_4$(2)) energies. Energies are relative to those at a Ti-Ti separation of 10 Å.

CHAPTER 7. POLARIZATION IN THE EFFECTIVE FRAGMENT METHOD FOR MODELING SOLVATION EFFECTS

Simon P. Webb and Mark S. Gordon

Abstract

The effective fragment method models solvent effects accurately and cheaply by treating the solute fully *ab initio* and introducing the effects of solvent molecules through potentials added directly to the *ab initio* one-electron Hamiltonian. One of these potentials allows for the polarization of the solvent by the *ab initio* solute. As the solvent can repolarize the solute the effects of polarization must be treated in a self-consistent manner. This was originally achieved by convergence of the *ab initio* wavefunction, polarization of solvent, introducing the effects of the polarized solvent into the *ab initio* Hamiltonian, reconverging the wavefunction, and so on until self-consistency. A method is presented where the effects of polarization are added at each SCF iteration, thereby simultaneously converging polarization effects and the *ab initio* wavefunction. This results in a time saving of a factor of two over the original method. The solvent molecules are polarized via bond and lone pair localized orbital dipole polarizability tensors. Originally these were calculated numerically. An analytic method for their calculation is presented.

I. Introduction

The effective fragment method[1,2] has been developed to accurately and cheaply model the effects of discrete solvent molecules on a solute which is treated with *ab initio* quantum mechanics. The effects of the solvent molecules are introduced by adding

perturbative one-electron terms to the *ab initio* Hamiltonian of the solute, producing an effective Hamiltonian for the solvated system. Presently these one-electron terms account for the effects found at the Hartree-Fock level of theory; which are: electrostatic, polarization, and exchange repulsion.

The dominant electrostatic term is represented by distributed multipoles which are determined from a distributed multipole analysis[3] of the wavefunction from a single *ab initio* calculation on the solvent molecule. The effects of the polarization of solvent molecules by the solute and the resulting induced dipoles, which act back on the solute, are treated in a self-consistent manner and are introduced via bond and lone pair localized orbital dipole polarizabiltity tensors.[4] The exchange repulsion term is determined by a fitting procedure for each particular solvent molecule[5] and also includes charge-transfer effects. Ongoing extensions of the model include replacement of the fitted exchange potential with a generalized exchange potential term, which will remove the need for any fitting and will apply to any solvent molecule,[6] and the addition of a term to represent dispersion effects.[7]

Originally the polarization term, mentioned above, was calculated by converging the self-consistent field (SCF) wavefunction, polarizing the solvent fragment(s), allowing the polarized solvent to act back on the solute, reconverging the SCF wavefunction and so on, until overall self-consistency. This is, of course, costly as convergence of the SCF *ab initio* wavefunction has to be achieved many times. In this paper we will present a method which adds the polarization effects at each SCF iteration, thereby converging the SCF wavefunction and the polarization effects simultaneously. This method will be shown to achieve overall self-consistency in the same number of iterations needed for an unpolarized SCF calculation, and reduce the number of iterations needed for self-consistency in the polarized system by half compared to the old method.

Localized orbital dipole polarizabilities used to allow polarization of the solvent may be calculated numerically by a finite-field difference method.[4] In this paper we present a

derivation of an analytic expression for localized orbital dipole polarizabilities., which is based on the earlier work of Moccia et al.[8] The analytic calculation of these localized polarizability tensors has several advantages over the numeric calculation.

(II) Theory and Methods

a) The Effective Fragment Method. As outlined above, the effective fragment model treats discrete solvent molecules by introducing one-electron terms into the *ab initio* Hamiltonian (equation (1)). The part of the system which is treated *ab initio* is referred to as the action region (AR). This is the region where chemistry occurs and may be simply the solute, or the solute plus some number of solvent molecules if, for example, proton transfer between solvent and solute is occurring. Alternatively it could be the active site of an enzyme. The solvent molecules represented by effective fragments, then, are spectator molecules which perturb the active region;

$$\mathbf{H} = \mathbf{H}_{AR} + \mathbf{V}.$$ (1)

$\mathbf{V}$ represents the potential due to the solvent molecules (or fragments). In the present Hartree-Fock (HF) implementation of the method there are three terms in $\mathbf{V}$: electrostatic, polarization, and exchange repulsion/charge transfer. The effective fragment interaction Hamiltonian describing the interaction between the nth solvent molecule and an AR electron is then[5]

$$V_{el}(n,s) = \sum_{k=1}^{K} V_k^{Elec}(n,s) + \sum_{l=1}^{L} V_l^{Pol}(n,s) + \sum_{m=1}^{M} V_m^{Re\,p}(n,s),$$ (2)

where s represents the electronic coordinates, k is the number of multipolar expansion points. L is the number of valence localized orbitals, and M is the number of terms in the repulsive potential. Interactions between solvent molecules and AR nuclei, and also solvent-solvent interactions are described by similar terms. In this paper we are concerned with the second term in equation (2) which accounts for the effects of polarization.

b) Calculation of Polarization Energy E^{Pol}. Polarization of the solvent fragments is described by a perturbation model which employs bond and lone pair localized orbital dipole polarizabilities α'_{fg}

$$V_l^{Pol}(\mu) = -\frac{1}{2} \sum_{f,g}^{x,y,z} F_f(\mathbf{r_1}) \alpha'_{fg}(\mu) \langle F_g(\mathbf{r_1}) \rangle. \tag{3}$$

The elements of these tensors α'_{fg} may be obtained from finite-field perturbed Hartree-Fock calculations on the isolated solvent molecule (see section II c), and are centered at the centroids of charge of the solvent's L localized valence orbitals. The result, for example, in water is four polarizable points: one on each O-H bond and one on each oxygen lone-pair. Dipoles which are induced at these polarizable points are assumed to be a linear function of the applied field;

$$\vec{\mu}_i = \tilde{\alpha}_i \vec{F}_i. \tag{4}$$

The energy of polarization E_{pol} is the sum of two terms; the energy due to interaction of the induced dipoles on the solvent molecules with the field E_{int} and the energy required to induce dipoles in the solvent molecule E_{sol}.[2,9] The specific expression for E_{pol} determines the variational operator whose general form is shown in equation (3). To demonstrate the origin of the factor of 1/2 in equation (3) we show the single fragment case where E_{pol} is simply:

$$E_{pol} = E_{int} + E_{sol} = -\sum_i \bar{\mu}_i \cdot \bar{F}_i^{ai} + \frac{1}{2}\sum_i \bar{\mu}_i \cdot \bar{F}_i^{ai}$$
$$= -\frac{1}{2}\sum_i \left(\tilde{\alpha}_i \bar{F}_i^{ai}\right) \cdot \bar{F}_i^{ai} . \tag{5}$$

Here $\bar{F}_i^{ai}$ is the total field felt at polarizable point i on the single fragment, due to the *ab initio* AR wavefunction. This field contains an electronic contribution and a nuclear contribution:

$$\bar{F}_i^{ai} = \left\langle \psi \left| \hat{\bar{F}}_i \right| \psi \right\rangle + \bar{F}_i^{nuc} . \tag{6}$$

The derivation for the *multiple* fragment case is complicated;[2] therefore, for the purposes of this paper we include only the final result. For the multi-fragment case E_{pol} and the expression used in the variational operator included in the quantum mechanical self-consistent calculations is given by:

$$E_{pol} = -\frac{1}{2}\sum_i \left(\tilde{\alpha}_i \bar{F}_i^{tot}\right) \cdot \bar{F}_i^{tot} + \frac{1}{2}\sum_i \left(\tilde{\alpha}_i \bar{F}_i^{tot}\right) \cdot \bar{F}_i^{\mu} ; \tag{7}$$

$\bar{F}_i^{tot}$ is the total field felt at polarizable point i; $\bar{F}_i^{\mu}$ is the field felt at polarizable point i due to induced dipoles on other fragments. We now discuss the origin of these fields.

A schematic of the problem for an *ab initio* solute + two fragment case is shown in Figure 1. Consider the polarizable point $i=1$ located on fragment 1 in Figure 1. It feels a total field $\bar{F}_1^{tot}$ given by:

$$\bar{F}_1^{tot} = \bar{F}_1^{ai} + \bar{F}_1^{EFP} + \bar{F}_1^{\mu} , \tag{8}$$

where F_1^{ai} is the field due to the *ab initio* AR wavefunction felt at polarizable point 1. F_1^{EFP} is the static field, due to the distributed multipole expansion on fragment 2, felt at polarizable point 1, and F_1^{μ} is the field due to the induced dipole at polarizable point 2 felt at polarizable point 1. This field F_1^{tot} induces a dipole μ_1 at the polarizable point 1.

$$\vec{\mu}_1 = \tilde{\alpha}_1 \vec{F}_1^{tot} \tag{9}$$

Simultaneously, an exactly analogous process occurs at polarizable point 2.

$$\vec{F}_2^{tot} = \vec{F}_2^{ai} + F_2^{EFP} + \vec{F}_2^{\mu} \tag{10}$$

$$\vec{\mu}_2 = \tilde{\alpha}_2 \vec{F}_2^{tot} \tag{11}$$

These induced dipoles $\vec{\mu}_1$ and $\vec{\mu}_2$, which themselves are interdependent and must be made self consistent, act back on the *ab initio* wavefunction through the operator given by equation (3). The newly perturbed wavefunction produces a new field which then acts back on the fragment polarizable points. The induced dipoles, then, must be made self-consistent with the AR *ab initio* field as well as with each other.

Methods to achieve self-consistency. The scheme to achieve self-consistency in the original EFP implementation is represented by the flow chart in Figure 2. The procedure starts with a complete SCF calculation (step 1), where the one-electron EFP terms describing electrostatic effects and exchange repulsion/charge transfer are included and polarization is not. The wavefunction is fully converged and the resulting electron density (step 2) is then used to calculate the fields $\vec{F}_i^{ai}$ due to the AR (step 3). The static fields due to the EFPs $\vec{F}_i^{EFP}$ are added (step 4) and the total fields induce dipoles μ_i at the fragment polarizable points (step 5). These induced dipoles are then iterated to self-consistency among the fragment polarizable points (steps 6-8). The resulting fields and induced dipoles are then used

to calculate the perturbation operator (equation (3)), and it is added to the one-electron Hamiltonian (step 9). The SCF is then reconverged (steps 1-2) and the whole process is repeated until self-consistency is achieved, indicated by constant (within a prescribed tolerance) electron density and induced dipoles between macro-iterations of the SCF wavefunction. This procedure is costly as the number of SCF cycles required is very large.

Figure 3 shows a flow chart representing the first alternative method - method 2. Here, on the first cycle the initial guess electron density is used to calculate the fields $\bar{F}_i^{ai}$ due to the AR (step 2). The static EFP fields $\bar{F}_i^{EFP}$ are added (step 3a) and dipoles μ_i are induced at the polarizable points (step 4). Note that on the first SCF cycle $\bar{F}_i^{\mu}$ is zero. As in the first method, the induced dipoles are micro-iterated to self-consistency (step 5-7). Then the effect of the converged induced dipoles are added through the perturbation operator (step 8), and the next SCF cycle is started. In this scheme the converged fields due to induced dipoles $\bar{F}_i^{\mu}$ are saved from each SCF iteration and are added as an initial guess in the next iteration (step 3b). This procedure provides a better guess at the converged $\bar{F}_i^{\mu}$ on each successive SCF iteration and therefore results in fewer micro-iterations on the induced dipoles. The whole procedure is repeated until the wavefunction converges indicating overall self-consistency. This procedure, then, adds the polarization effect into each SCF iteration, thereby converging the density and the induced dipoles simultaneously.

Figure 4 shows a flow chart representing method 3 which contains a further refinement to method 2. Initially method 3 proceeds as in method 2 (steps 1-3). Again, on the first cycle the total field which produces the induced dipoles (step 4) has only contributions from F^{ai} and F^{EFP}. No micro-iterations are carried out on the induced dipoles, and the field due to induced dipole is saved (step 5). The effect of the induced dipoles is then introduced into the AR *ab initio* wavefunction (step 6). On the next SCF cycle, the fields due to the induced dipoles $\bar{F}_i^{\mu}$ saved from the previous iteration are added to the new $\bar{F}_i^{ai}$ and $\bar{F}_i^{EFP}$, and new induced dipoles calculated. This process is repeated until the wavefunction converges

indicating overall self-consistency. In this method the induced dipole iterations amongst the fragments are also folded into the SCF iterations.

All three methods were tested on a water trimer system where one water was treated *ab initio* and the other two waters were replaced by effective fragments. Figure 5 represents the number and type of iterations (SCF or dipole/field) and their nesting for methods 1 to 3. Table 1 shows the totals for each type of iteration, and also the final energy at convergence.

Consider method 1 in Figure 5: the number of SCF iterations required for convergence in an unpolarized environment is 10. The induced dipoles/field require 4 micro-iterations for self consistency. The perturbation to the one-electron Hamiltonian resulting from the converged induced dipole requires 6 more SCF iterations for wavefuction convergence. This process continues and Table 1 shows that a total of 19 SCF cycles and 12 dipole/field micro-iterations are required for complete self-consistency.

For method 2 (see Figure 5b) after the initial guess 4 induced dipole/field micro-iterations are required; the resulting perturbation is added to the one-electron Hamiltonian and an SCF cycle is completed. On the next cycle only 3 induced dipole/field micro-iterations are required, and on the next only 2. This demonstrates the value of saving the previous induced dipole as an initial guess for the next SCF iteration. By the fourth SCF iteration the induced dipole is no longer changing, indicating that it converges faster than the electron density. Table 1 shows that total self-consistency is achieved in 10 SCF cycles and 17 induced dipole/field micro-iterations. As the induced dipole/field micro-iterations are extremely inexpensive compared to the SCF iterations, this represents a time saving of just under a factor of two compared to method 1.

Figure 5c demonstrates the simultaneous convergence of the induced dipole/field and the AR density. It requires (see Table 1) 10 induced dipole/field and SCF iterations for complete convergence. This method is clearly cheaper than method 2; however, numerical

stability with larger numbers of fragments needs to investigated. For this reason method 2 is the method of choice as it is guaranteed to converge.

The final energies obtained for all three methods are the same (see Table 1), so at convergence all three methods are equivalent.

d) Localized Polarizability Tensors. As previously stated, the bond and lone pair localized orbital dipole polarizabilities α_{fg}^{l} required for the above procedure may be obtained from numeric finite-field perturbed Hartree-Fock calculations on the isolated solvent molecule.[2, 4] In this subsection we present an alternative analytic method for calculating α_{fg}^{l}; but, first we briefly outline finite-field method.

Numerical calculation of α_{fg}^{l}. Stevens and Garmer developed the numerical method[4] used to calculate α_{fg}^{l} in the original implementation of the EFP method,[2] where the superscript l refers to the localized orbital (LMO) ϕ_l. The method entails numerically taking the derivative of each localized orbital dipole μ_f^l with respect to an applied field F_g:

$$\alpha_{fg}^{l} = \lim_{F_g \to 0} \frac{\left(\mu_f^l\right)_g}{F_g} = \lim_{F_g \to 0} \frac{\mu_f^l(F_g) - \mu_f^l(0)}{F_g} \tag{12}$$

$$= \frac{-2\left[\langle \phi_l | \hat{\mu}_f | \phi_l' \rangle - \langle \phi_l^0 | \hat{\mu}_f | \phi_l^0 \rangle \right]}{F_g}, \tag{13}$$

where ϕ_l' and ϕ_l^0 are perturbed and unperturbed LMOs, respectively.

This finite field method requires four SCF calculations: one with no external field and the remaining three with fields in x, y, and z directions, respectively. With the correct choice of field strengths and wavefunction convergence tolerances, accuracy of 10^{-3} Bohr^3 can be achieved.[4] For generation of EF potentials for many different solvents[6] an automated

procedure is obviously highly desirable, as manual application of equation (13) for a molecule containing more than a few LMOs is clearly very tedious. Stevens et al report the development of a driver for automation; however, they also report problems such as alignment of perturbed LMOs with their corresponding unperturbed LMOs because of inconsistent ordering. We have therefore derived and implemented an analytic method of calculating α_{fg}^l based on the earlier work of Maestro and Moccia[8] which generates all $\tilde{\alpha}^l$ tensors for a given molecule in a single calculation.

Analytic calculation of α_{fg}^l. The derivation of the analytic expression for elements of the *total* RHF polarizability tensor $\tilde{\alpha}$ is as follows; where E_{elec} is the electronic energy, F and G are components of the electric field along the f and g axes, and μ_f is the component of the electronic dipole in the f direction:[10]

$$\alpha_{fg} = -\frac{\partial^2 E_{elec}}{\partial F \partial G} \quad . \tag{14}$$

$$= -\frac{\partial \mu_f}{\partial G} = -2\sum_i^{d.o.}\left(\frac{\partial h_{ii}^f}{\partial G}\right) \tag{15}$$

$$= -2\sum_i^{d.o.}\sum_m^{all}\left(U_{mi}^g h_{mi}^f + U_{mi}^g h_{im}^f\right) \tag{16}$$

$$= -4\sum_i^{all}\sum_j^{d.o.}U_{ij}^g h_{ij}^f \tag{17}$$

$$= -4\sum_i^{virt}\sum_j^{d.o.}U_{ij}^g h_{ij}^f - 4\sum_i^{d.o.}\sum_j^{d.o.}U_{ij}^g h_{ij}^f \tag{18}$$

$$= -4\sum_i^{virt}\sum_j^{d.o.}U_{ij}^g h_{ij}^f - 2\sum_{ij}^{d.o.}\left(U_{ij}^g + U_{ji}^g\right)h_{ij}^f \tag{19}$$

$$= -4\sum_i^{virt}\sum_j^{d.o.}U_{ij}^g h_{ij}^f \tag{20}$$

The upper limits on the summations indicate sums over virtual (virt), all (all) and doubly occupied (d.o.) orbitals. The solution of the coupled perturbed Hartree-Fock (CPHF)

equations[10] is required to give the orbital responses U_{ij}^g to a perturbing field G, where i and j are canonical MO indices. The matrix elements h_{ij}^f are dipole integrals $\langle i|\hat{\mu}_f|j\rangle$: f and g are Cartesian coordinate axes along which the perturbing fields lie.

We wish to decompose the total α polarizability tensor into localized orbital contributions; that is, contributions from lone pairs and bonds. By means of a unitary transformation one may transform canonical orbitals ϕ to localized orbitals ψ^l:

$$\psi_l = \sum_j^{d.o.} \phi_j T_{lj} \ , \tag{21}$$

where $\mathbf{T}$ is determined during the course of an orbital localization procedure.[11,12] Similarly, one may transform equation (15) into a localized basis,

$$\alpha_{fg}^l = -\frac{\partial \mu_f^l}{\partial G} = -2\frac{\partial h_{ll}^f}{\partial G} = -2\frac{\partial}{\partial G}\left[\sum_j^{d.o.}\sum_k^{d.o.} T_{lj} T_{lk} h_{jk}^f\right] \tag{22}$$

$$= -2\sum_j^{d.o.}\sum_k^{d.o.} T_{lj} T_{lk}\left(\frac{\partial h_{jk}^f}{\partial G}\right) - 2\sum_j^{d.o.}\sum_k^{d.o.} h_{jk}^f\left(\frac{\partial T_{lj}}{\partial G} + \frac{\partial T_{lk}}{\partial G}\right) \tag{23}$$

Equation (23) shows that the analytic expression for localized dipole polarizabilities consists of two terms. The second term allows the localization to "relax" in the presence of the electric field; that is, the response of each localized dipole μ_f^l to the field is coupled to the response of every other localized dipole μ_f^l. The first term in equation (23), then, represents the decoupled localized dipole polarizabilties. Stevens and Garmer decoupled the localized orbital polarizability tensors $\tilde{\alpha}^l$ in their numeric method by zeroing off-diagonal Fock matrix elements during the SCF cycles for all localized orbitals except the one which they were calculating $\tilde{\alpha}^l$. They found that the uncoupled polarizabilities were less anisotropic, with the elements of $\tilde{\alpha}^l$ perpendicular to the bond (z) axis (α_{xx}^l and α_{yy}^l), for σ-bond LMOs, in closer agreement with each other. They also found that the decoupled localized orbital

polarizabilities are more transferable from molecule to molecule. The localized orbital polarizability tensors used in the EFP analytic gradient derivations are assumed to be symmetric. In fact these tensors are symmetrized before use. Since we find that decoupled localized orbital polarizability tensors are generally more symmetric than coupled ones (see results), decoupled localized polarizability tensors are the logical choice in the EFP implementation. Therefore, for the remainder of this paper the second term in equation (23) is not considered further.

One may arrive at a final analytic expression (equation (26)) for the lth decoupled localized orbital polarizability by applying the steps in the total $\bar{\alpha}$ derivation (equations (15) - (20)) to the first term in equation (23).

$$\alpha_{fg}^{l} = -2\sum_{j}^{d.o.}\sum_{k}^{d.o.} T_{lj}T_{lk}\left(\frac{\partial h_{jk}^{f}}{\partial G}\right) \tag{24}$$

$$= -2\sum_{jk}^{d.o.} T_{lj}T_{lk}\sum_{i}^{all}\left(U_{ij}^{g}h_{ik}^{f} + U_{ik}^{g}h_{ji}^{f}\right) \tag{25}$$

$$= -4\sum_{jk}^{d.o.}\sum_{i}^{all} T_{lj}T_{lk}U_{ij}^{g}h_{ik}^{f} \tag{26}$$

$$= -4\sum_{jk}^{d.o.}\sum_{i}^{virt} T_{lj}T_{lk}U_{ij}^{g}h_{ik}^{f} - 2\sum_{jki}^{d.o.}\left(U_{ij}^{g} + U_{ji}^{g}\right)h_{ik}^{f} \tag{27}$$

$$= -4\sum_{jk}^{d.o.}\sum_{i}^{virt} T_{lj}T_{lk}U_{ij}^{g}h_{ik}^{f}. \tag{28}$$

Equation (28) can be written in terms of transformed orbital responses U_{il}^{g} and dipole integrals h_{il}^{f}:

$$U_{il}^{g} = \sum_{j}^{d.o.} U_{ij}^{g}T_{lj} \tag{29}$$

$$h_{il}^{f} = \sum_{k}^{d.o.} h_{ik}^{f}T_{lk} \tag{30}$$

$$\alpha_{fg}^{l} = -4\sum_{i}^{virt} U_{il}^{g}h_{il}^{f}. \tag{31}$$

The result is L $\tilde{\alpha}^l$ tensors where L is the number of localized orbitals. The decomposition represented by equation (31) should recover the total dipole polarizability $\bar{\alpha}$ if all occupied orbitals are localized and their contributions are summed. The following proof demonstrates that this is the case:

$$-4\sum_{i}^{virt}\sum_{l}^{d.o.}U_{il}^{g}h_{il}^{f} = -4\sum_{i}^{virt}\sum_{l}^{d.o.}\left(\sum_{j}^{d.o.}U_{ij}^{g}T_{lj}\right)\left(\sum_{k}^{d.o.}h_{ik}^{f}T_{lk}\right) \tag{32}$$

$$= -4\sum_{i}^{virt}\sum_{j}^{d.o.}\left\{\sum_{k}^{d.o.}\left[\underbrace{\sum_{l}^{d.o.}T_{lj}T_{kl}^{\dagger}}_{\delta_{jk}}\right]U_{ij}^{g}h_{ik}^{f}\right\} \tag{33}$$

$$= -4\sum_{i}^{virt}\sum_{j}^{d.o.}U_{ij}^{g}h_{ij}^{f} \tag{34}$$

Often, when canonical orbitals are localized the chemical core orbitals are excluded from the localization scheme. The reason for this is that the core orbitals do not usually participate directly in the chemical activity of the molecule in question. The scheme for calculating analytically localized dipole polarizability tensors out lined above may easily be modified to accommodate this procedure.

The total core polarizability tensor α^c may be calculated using equation (20), but limiting the second summation to just the core MOs.

$$\alpha^c = -4\sum_{i}^{virt}\sum_{j}^{core}U_{ij}^{g}h_{ij}^{f} \tag{35}$$

The localized orbital polarizability tensors for the valence orbitals may be calculated by applying the sums in equations (29) and (30) to the number of localized orbitals L only and then applying equation (31) as before.

Application to CH_4 and H_2O. The analytic method to calculate localized orbital dipole polarizabilities has been implemented in the electronic structure package GAMESS[13] for RHF and ROHF high spin wavefunctions, and for both the Boys localization scheme,[11] and the Edmiston-Ruednberg energy localization procedure.[12]

The first test case considered is that of methane. In the standard orientation of CH_4 (see Figure 6) an applied field in, for example, the x direction will effect the x components of all four LMO dipoles equally. The same is true for applied fields in the y and z directions and their effects on y and z dipoles, respectively. Consequently, when $f=g$ the applied field will have no effect on the localization transformation matrix T and therefore the coupling term in equation (23) will be zero for the diagonal elements of each localized orbital polarizability tensor α'_{ff}. For CH_4 in the standard orientation, then, the approximate analytic method, arrived at by neglecting the second term in equation (23), and the numeric method should agree for diagonal elements α'_{ff}. Figures 6 and 7 show this to be the case with agreement to the third decimal place in the analytic and numeric calculation of α'_{ff} for CH_4 . It is clear that when the dipole component and the applied field do not lie in the same direction, the coupling term in equation (23) is no longer zero, and the off diagonal elements calculated by the two methods do not agree. The analytic method predicts larger off diagonal elements than the numeric method. The analytic core polarizability tensors are presented in Figures 6 and 7 to demonstrate the inertness of the cores to a polarizing field. Basis set effects can be seen by comparison of Figures 6 and 7. The larger more flexible basis set results in larger diagonal elements (and therefore a larger mean), but smaller off diagonal elements.

Figures 8 and 9 show the results of the application of the numeric and analytic methods to water. There are two pairs of equivalent LMOs in H_2O; two oxygen lone-pairs and two O-H bonds, so, only two tensors are presented in each water calculation.

The analytic core polarizability tensor is again presented to demonstrate how

unpolarizable the core orbitals are. Individual elements of the oxygen lone-pair tensors and O-H bond tensors clearly show an effect associated with the decoupling in the analytic scheme. There is a higher degree of symmetry in the analytic O-H bond LMO polarizability than in the numeric counterpart; that is, the elements xz and zx agree more closely in the analytic calculation than in the numeric calculation. The analytic and numeric lone-pair tensors have comparable small asymmetries; but, the analytic tensors have considerably larger off-diagonal elements. Inspection of Figure 8 shows that for the TZV(p,d) basis set the mean analytic and numeric localized polarizabilities are similar but are not identical. When the size of the basis set is increased to TZV(3d,3p) (see Figure 9), the two methods are essentially in agreement. This suggests that the added flexibility of the larger basis set accounts for the approximation made when discarding the coupling term in equation (18) to the extent that the trace is exactly correct, but the redistribution amongst the diagonal terms due to decoupling remains.

Stevens and Garmer carried out a survey of a number of molecules and examined the transferability of the localized orbital polarizabilities of certain bonds.[4] In order to do this the bond polarizabilities had to be calculated with the bond direction the same in each case. The analytic bond polarizability tensors calculated above may be rotated by a unitary transformation in order to project bond directions and lone-pairs onto the z-axis. This facilitates studies such as that by Stevens and Garmer.

Figure 10 shows localized orbital polarizability tensors for CH_4, where the C-H bond tensor has been rotated so as to project the bond direction onto the z-axis. For both TZV(p,d) and TZV(3d,3p) the zz element is largest indicating the C-H bond is most easily polarized along the bond axis. The xx and yy elements are exactly equal which is indicative of the high symmetry of CH_4. There is clearly a large basis set effect with a significant increase in the mean polarizability on going from TZV(p,d) to TZV(3d,3p). Interestingly, most of this increase is due to the larger elements perpendicular to the bond axis (xx and yy). This

indicates that the smaller basis set provides an adequate description of the polarizability along the bond, as the same basis functions that describe the bond (TZV valence) can effectively describe distortion of electron density along the bond axis (in the direction of overlap). However, distortion of electron density in directions perpendicular to the bond axis clearly will not be described well by the TZV valence basis functions and requires more flexibility.

(III) Conclusions

The effects of polarization when added to the EFP method need to be made self-consistent. Self consistency may be achieved by adding the polarization effects each SCF iteration instead of after every converged SCF calculation of the wavefunction. This technique, which amounts to simultaneously converging the orbitals and the induced dipoles in the whole system, is therefore able to reduce the number of SCF iterations required for complete self-consistency by half.

Localized dipole polarizability tensors centered at the centroids of charge of the solvent (fragment) LMOs are used to introduce polarization into the EFP method. These may be calculated by a numeric finite-field method. However, this method is not easily automated and quickly becomes cumbersome as the number of LMOs in the solvent increases. We have presented an analytic expression for the calculation of these tensors. The expression used decouples each localized orbital polarizability tensor from the others. In the equivalent numeric calculation where elements of the Fock matrix were zeroed out, this was found to improve transferability amongst different molecules. We plan to utilize the superior transferability of the decoupled tensors in a future study which will survey analytic localized polarizabilities for a large sample of compounds. We have found that for H_2O it also

increases the symmetry of the tensors. This is advantageous for the EFP method where the tensors are required to be symmetric in the derivation of analytic energy gradients with respect to nuclear displacements.

References

1. Jensen, J. H.; Day, P. N.; Gordon, M. S.; Basch, H.; Cohen, D.; Garmer, D. R.; Krauss, M.; Stevens, W. J. in *Modeling the Hydrogen Bond*, edited by Douglas A. Smith, ACS Symposium Series 569, 1994, p. 139.

2. Day, P. N.; Jensen, J. H.; Gordon, M. S.; Webb, S. P.; Stevens, W. J.; Krauss, M.; Garmer, D. R.; Basch, H.; Cohen, D. *J. Chem . Phys.* **1996**, 105, 1969.

3. a) Stone, A. J. *Chem. Phys. Lett.* **1981**, 83, 233. b) Stone, A. J.; Alderton, M. *Mol. Phys.* **1985**, 56, 1047.

4. Garmer, D. R.; Stevens, W. J. *J. Phys. Chem.* **1989**, 93, 8263.

5. Chen, W.; Gordon, M. S. *J. Chem . Phys.* **1996**, 105, 11081.

6. Jensen, J. H.; Gordon, M. S. *J . Chem. Phys.* submitted.

7. Rauhut, G.; Boughton, J. W.; Pulay, P. *J. Chem. Phys.* **1995**, 103, 5662.

8. Maestro, M.; Moccia, R. *Mol. Phys.* **1975**, 29, 82.

9.   Debye, P. in *Polar Molecules*, Dover, Mineola, NY, 1945, p. 30.

10.   Yamaguchi, Y.; Osamura, O.; Goddard, J. D.; Schaefer III, H. F. in *A New Dimension to Quantum Mechanics, Analytic Derivative Methods in Ab Initio Molecular Electronic Structure Theory*, Oxford University Press, 1994, Chapters 17 and 10.

11.   Boys, F. S. in *The Quantum Theory of Atoms, Molecules and Solids*, edited by P.O. Löwdin, Acedemic Press, 1966.

12.   Edmiston, C.; Ruedenberg, K. *Rev. Mod. Phys.* **1963**, 35, 457.

13.   Schmidt, M.W.; Baldridge, K.K.; Boatz, J.A.; Jensen, J.H.; koseki, S.; Matsunaga, N.; Gordon, M.S.; Ngugen, K.A.; Su, S.; Windus, T.L.; Elbert, S.T.; Montgomery, J.; Dupuis, M. *J. Comp. Chem.* **1993**, 14, 1347.

Table 1. Total number of each type of iteration needed for total self-consistency in the water trimer system (one *ab initio* water; two fragment waters), and the final energies in Hartrees at convergence.

	Method 1	Method 2	Method 3
Total # SCF Iterations	19	10	10
Total # Diple/Field Iterations	12	17	10
Final Energy/ Hartree	-75.94711015	-75.94711016	-75.94711016
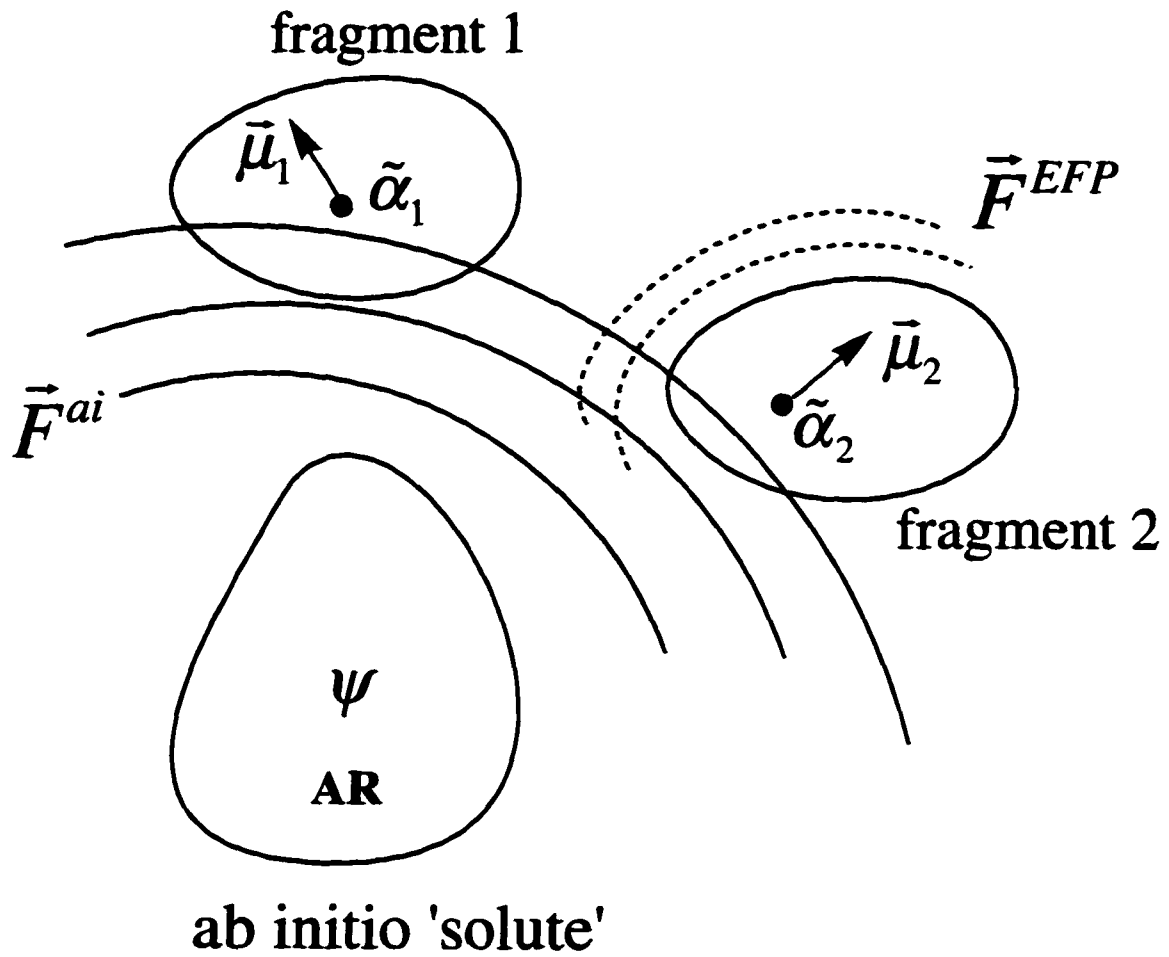
fragment 1

$$\vec{F}_i^{\,tot} = \vec{F}_i^{\,ai} + \vec{F}_i^{\,EFP} + \vec{F}_i^{\,\mu} \qquad i = 1,2$$

Figure 1. A schematic of the self-consistency problem for an *ab initio* solute and two fragment solvent molecules.

Step #.

1   SCF calculation

2   converged SCF $\longrightarrow$ **P**

3      $\vec{F}_i^{ai} = \left\langle \mathbf{P}\vec{D}_i \right\rangle + \vec{F}_i^{nuc}$

4      $\vec{F}_i^{tot} = \vec{F}_i^{ai} + \vec{F}_i^{EFP}$

5      $\vec{\mu}_i = \tilde{\alpha}_i \vec{F}_i^{tot}$

6      $\vec{F}_i^{\mu}$

7      $\vec{F}_i^{tot+\mu} = \vec{F}_i^{tot} + \vec{F}_i^{\mu}$ $\vec{\mu}_i' - \vec{\mu}_i > tol$

8      $\vec{\mu}_i = \tilde{\alpha}_i \vec{F}_i^{tot+\mu}$

           $\vec{\mu}_i' - \vec{\mu}_i < tol$

9      $\hat{\mathbf{F}} = \hat{\mathbf{F}} + \hat{\mathbf{V}}^{pol}$
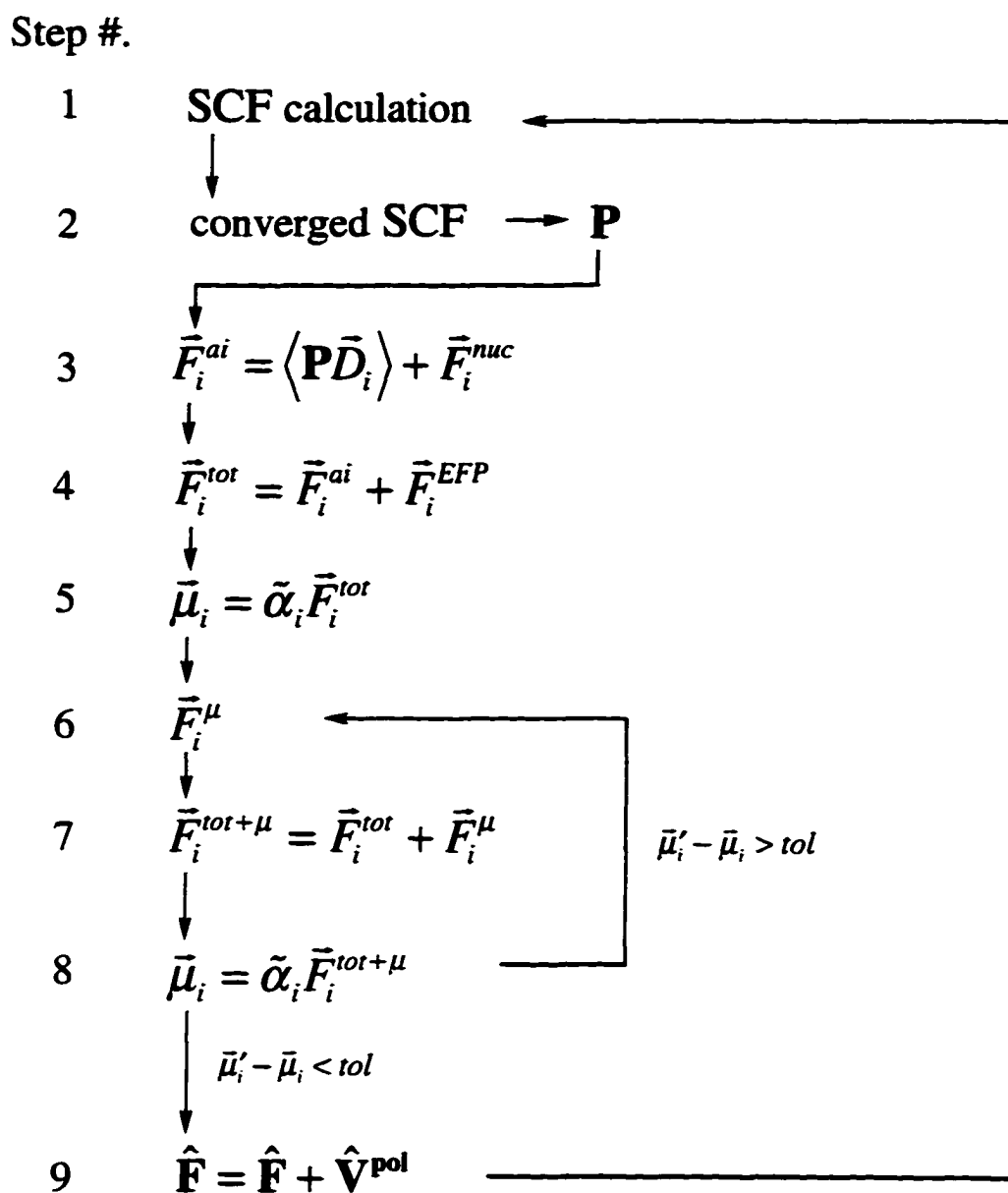
Figure 2. Flow chart of the original method to reach polarized self-consistency in the EFP method.

$\mathbf{P}$ = electron density; $\hat{\mathbf{F}}$ = Fock matrix; $\hat{\mathbf{V}}^{pol}$ = perturbation due to polarization; $\vec{D}_i$ = field integrals at i; $\vec{F}_i^{ai}$ = *ab initio* field felt at i; $\vec{F}_i^{EFP}$ = static field felt at i due to other fragment(s); $\vec{F}_i^{nuc}$ = field due to nuclei; $\vec{\mu}_i$ = induced dipole at i; $\vec{F}_i^{\mu}$ = field at i due to induced dipoles on other fragment(s).

Step #.

1   guess ⟶ **P**

2    $\vec{F}_i^{ai} = \left\langle \mathbf{P}\vec{D}_i \right\rangle + \vec{F}_i^{nuc}$

3a $\vec{F}_i^{tot} = \vec{F}_i^{ai} + \vec{F}_i^{EFP}$

3b $\vec{F}_i^{tot(+\mu)} = \vec{F}_i^{tai} + \vec{F}_i^{EFP} + \left(\vec{F}_i^{\mu} \right)$

4    $\vec{\mu}_i = \tilde{\alpha}_i \vec{F}_i^{tot(+\mu)}$ $\mathbf{P'} - \mathbf{P} < tol$

5    $\vec{F}_i^{\mu}$

6    $\vec{F}_i^{tot+\mu} = \vec{F}_i^{tot} + \vec{F}_i^{\mu}$ $\vec{\mu}_i' - \vec{\mu}_i > tol$

7    $\vec{\mu}_i = \tilde{\alpha}_i \vec{F}_i^{tot+\mu}$

     $\vec{\mu}_i' - \vec{\mu}_i < tol$

8    $\hat{\mathbf{F}} = \hat{\mathbf{F}} + \hat{\mathbf{V}}^{pol}$
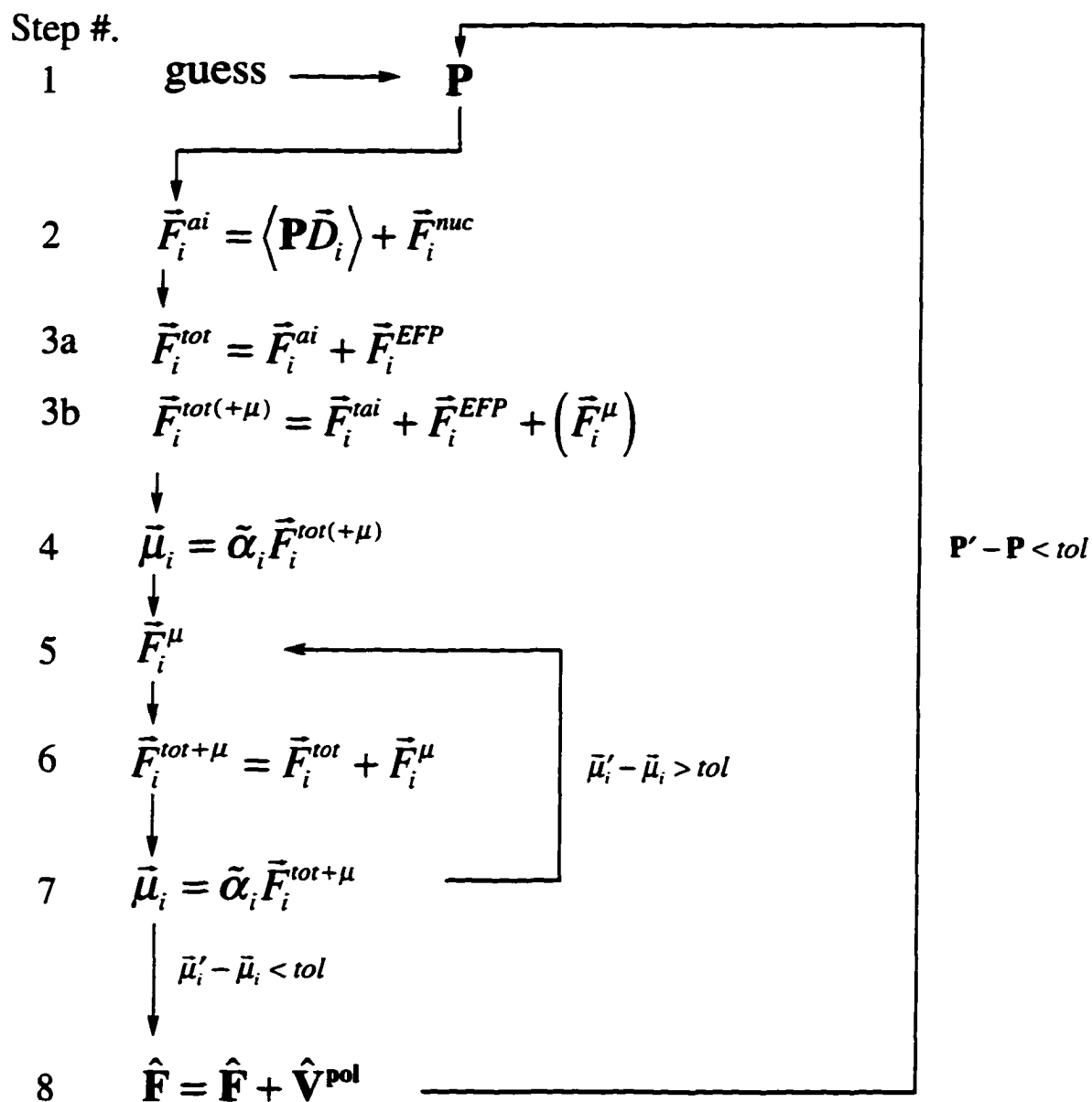
Figure 3. Flow chart of method 2 to reach polarized self-consistency in the EFP method.

$\mathbf{P}$ = electron density; $\hat{\mathbf{F}}$ = Fock matrix; $\hat{\mathbf{V}}^{pol}$ = perturbation due to polarization; $\vec{D}_i$ = field integrals at i; $\vec{F}_i^{ai}$ = *ab initio* field felt at i; $\vec{F}_i^{EFP}$ = static field felt at i due to other fragment(s); $\vec{F}_i^{nuc}$ = field due to nuclei; $\vec{\mu}_i$ = induced dipole at i; $\vec{F}_i^{\mu}$ = field at i due to induced dipoles on other fragment(s).

Step #.

1   **guess** $\longrightarrow$ **P**

2    $\vec{F}_i^{ai} = \left\langle \mathbf{P}\vec{D}_i \right\rangle + \vec{F}_i^{nuc}$

3    $\vec{F}_i^{tot+\mu} = \vec{F}_i^{tai} + \vec{F}_i^{EFP} + \left(\vec{F}_i^{\mu} \right)$ $\mathbf{P'} - \mathbf{P} < tol$

4    $\vec{\mu}_i = \tilde{\alpha}_i \vec{F}_i^{tot(+\mu)}$

5    $\vec{F}_i^{\mu}$

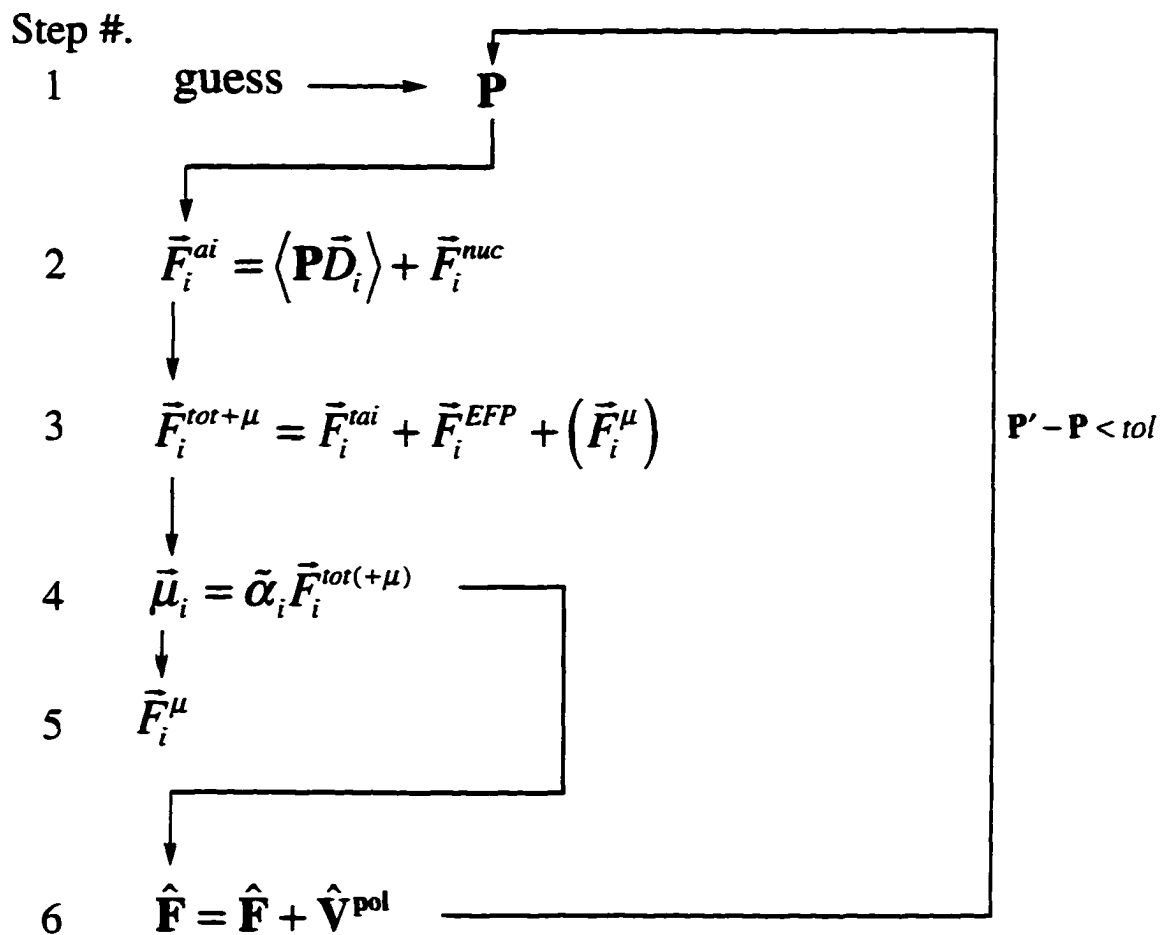6 $\hat{\mathbf{F}} = \hat{\mathbf{F}} + \hat{\mathbf{V}}^{pol}$

Figure 4. Flow chart of method 3 to reach polarized self-consistency in the EFP method.

$\mathbf{P}$ = electron density; $\hat{\mathbf{F}}$ = Fock matrix; $\hat{\mathbf{V}}^{pol}$ = perturbation due to polarization; $\vec{D}_i$ = field integrals at i; $\vec{F}_i^{ai}$ = *ab initio* field felt at i; $\vec{F}_i^{EFP}$ = static field felt at i due to other fragment(s); $\vec{F}_i^{nuc}$ = field due to nuclei; $\vec{\mu}_i$ = induced dipole at i; $\vec{F}_i^{\mu}$ = field at i due to induced dipoles on other fragment(s).
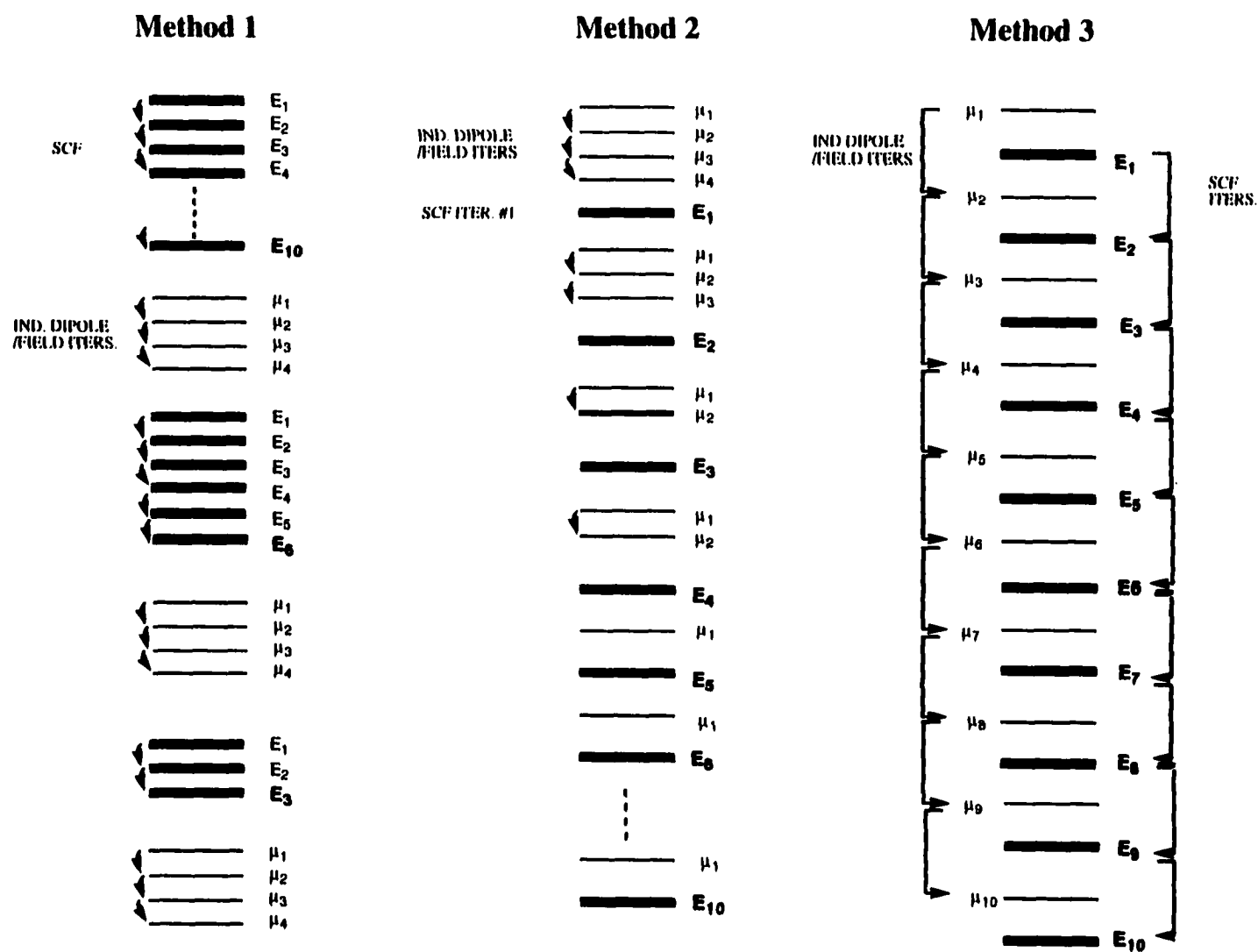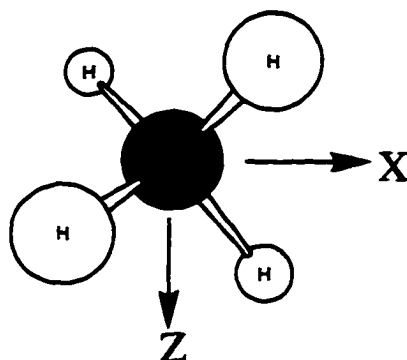
Figure 5. Nesting of SCF and induced dipole/field cycles in the water trimer test case (1 *ab initio* water; 2 EFP waters) for methods 1 to 3. The diagrams represent complete convergence in each case.

Basis Set: TZV(p,d)

analytic core polarizability tensor

	X	Y	Z
X	0.00491	0.00000	0.00000
Y	0.00000	0.00491	0.00000
Z	0.00000	0.00000	0.00491

mean α = 0.00491

analytic   **numeric**

C-H bond

	X	Y	Z
X	3.36162	1.73790	1.73790
Y	1.73790	3.36162	1.73790
Z	1.73790	1.73970	3.36162

mean α = 3.36162

	X	Y	Z
X	3.36107	1.43351	1.43351
Y	1.43351	3.36107	1.43351
Z	1.43351	1.43351	3.36107

mean α = 3.36107

Figure 6. Localized dipole polarizability tensors calculated analytically and numerically for CH_4 in Bohrs^3 using a TZV(d,p) basis set. The mean is the trace/3.

Basis Set: TZV(3p,3d)
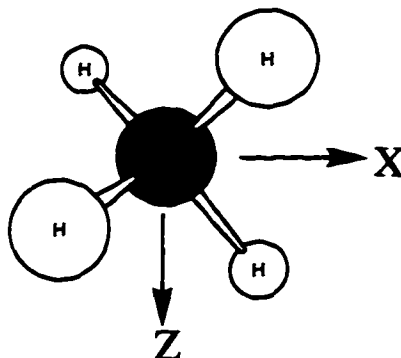
analytic core polarizability tensor

	X	Y	Z
X	0.00452	0.00000	0.00000
Y	0.00000	0.00452	0.00000
Z	0.00000	0.00000	0.00452

mean α = 0.00452

analytic   **numeric**

C-H bond

	X	Y	Z
X	3.85106	1.34155	1.34155
Y	1.34155	3.85106	1.34155
Z	1.34155	1.34155	3.85105

mean α = 3.85106

	X	Y	Z
X	3.85240	1.00115	1.00115
Y	1.00115	3.85240	1.00115
Z	1.00115	1.00115	3.85240

mean α = 3.85240

Figure 7. Localized dipole polarizability tensors calculated analytically and numerically for CH_4 in Bohrs^3 using a TZV(3d,3p) basis set. The mean is the trace/3.

Basis Set: TZV(p,d)

analytic core polarizability tensor

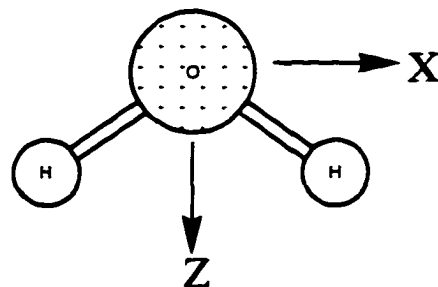|	X	Y	Z
X	0.00127	0.00000	0.00000
Y	0.00000	0.00149	0.00000
Z	0.00000	0.00000	0.00156

mean α = 0.00144

analytic

numeric

lone pair on oxygen

	X	Y	Z
X	0.96352	0.00000	0.00000
Y	0.00000	1.72996	0.84955
Z	0.00000	0.74910	1.07411

mean α = 1.25586

	X	Y	Z
X	1.40802	0.00013	0.00108
Y	0.00000	1.76912	0.34297
Z	0.00000	0.22904	1.02953

mean α = 1.39230

O-H bond

	X	Y	Z
X	2.55700	0.00000	1.48268
Y	0.00000	0.31110	0.00000
Z	1.41728	0.00000	1.59679

mean α = 1.48830

	X	Y	Z
X	2.11504	0.00000	1.38404
Y	0.00101	0.27096	0.00093
Z	1.02763	0.00000	1.63891

mean α = 1.34164

Figure 8. Localized dipole polarizability tensors calculated analytically and numerically for H_2O in Bohrs^3 using a TZV(d,p) basis set. The mean is the trace/3.

Basis Set: TZV(3p,3d)

analytic core polarizability tensor

	X	Y	Z
X	0.00115	0.00000	0.00000
Y	0.00000	0.00125	0.00000
Z	0.00000	0.00000	0.00130

mean α = 0.00124

analytic   **numeric**

lone pair on oxygen

	X	Y	Z
X	1.47825	0.00000	0.00000
Y	0.00000	2.35103	1.04967
Z	0.00000	0.95519	1.92883

mean α = 1.91937

	X	Y	Z
X	1.94896	0.00016	0.00112
Y	0.00000	1.94318	0.38858
Z	0.00000	0.35164	1.86674

mean α = 1.91962

O-H bond

	X	Y	Z
X	2.63907	0.00000	1.20894
Y	0.00000	0.87139	0.00000
Z	1.05472	0.00000	1.76245

mean α = 1.75764

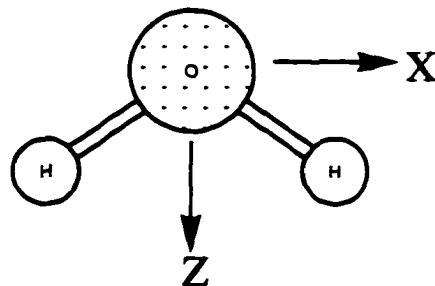|	X	Y	Z
X	2.16550	0.00000	1.05054
Y	0.00066	1.27836	0.00062
Z	0.58518	0.00000	1.82228

mean α = 1.75538

Figure 9. Localized dipole polarizability tensors calculated analytically and numerically for H_2O in Bohrs^3 using a TZV(3d,3p) basis set. The mean is the trace/3.
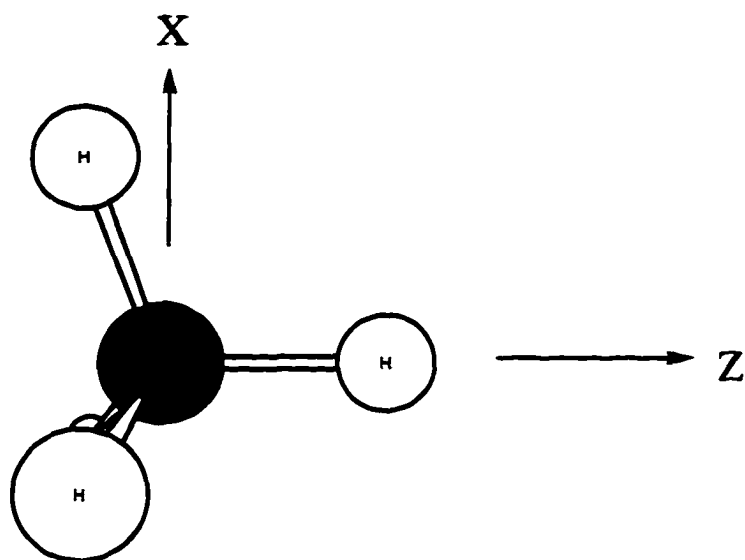
C-H bond

Basis Set: TZV(p,d)				Basis Set: TZV(3p,3d)		
	X	Y	Z		X	Y	Z
X	1.62372	0.00000	0.00000	X	2.50953	0.00000	0.00000
Y	0.00000	1.62372	0.00001	Y	0.00000	2.50951	0.00002
Z	0.00000	0.00000	6.83742	Z	0.00000	0.00002	6.53412

mean α = 3.36162   mean α = 3.85106

Figure 10. Analytic localized dipole polarizability tensors for a C-H bond in CH_4 projected onto the z-axis. Units are Bohrs^3. The mean is the trace/3.

CHAPTER 8. SOLVATION OF THE MENSHUTKIN REACTION: A RIGOROUS TEST OF THE EFFECTIVE FRAGMENT MODEL

Simon P. Webb and M. S. Gordon

Abstract

The recently developed effective fragment potential (EFP) method is used to study the effect of two, four, six, and eight solvating water molecules on the Menshutkin reaction between ammonia and methyl bromide. The EFP method reproduces all *ab initio* geometries and energetics for the two water case very accurately. Energetics from all *ab initio* single point energies at the EFP geometries for the four, six, and eight water cases are in good agreement with corresponding EFP energetics. In the gas phase the above Menshutkin reaction is kinetically highly unstable with a barrier of 34.0 kcal/mol at the RHF level with a double ξ basis set with polarization and diffuse functions. An ion-pair product is found, in agreement with previous work, which is exothermic by 4.7 kcal/mol. The addition of solvating water molecules has the effect of lowering the barrier and increasing the exothermicity of the ion-pair product. For eight solvating EFP water molecules, the barrier is 20.3 kcal/mol and the ion-pair product is exothermic by - 31.4 kcal/mol.

I. Introduction

Modeling of solvation effects is one of the great challenges in computational chemistry. Continuum based methods[1] are widely used and are becoming increasingly sophisticated. Some of these methods now employ variable cavity shapes produced by a union of spheres centered on each atom of the solute, and account for effects such as cavitation energy, dispersion, and repulsion.[2] The continuum approach has proved to be very important. Even the simplest single sphere self-consistent reaction field method has provided useful information concerning solvent effects on suitable systems.[3] The more sophisticated methods are able to handle a wide range of molecules and reactions.[4] However, continuum methods are unable to identify the role of individual solvent molecules in the solvation process, thereby precluding detailed analysis of the mechanism of solvation in the systems under study.

Another approach to the solvation problem has been to characterize the *ab initio* gas phase potential energy surface and then introduce discrete *ab initio* waters one at a time forming a supermolecule. While this approach has yielded fundamental information on the solvation process[5] it quickly becomes prohibitively expensive if more than a handful of solvent molecules are included. The importance of the discrete solvent molecule approach is reflected in the development and increasing popularity of hybrid QM/MM methods which treat the solute with *ab initio* or semi-empirical techniques and the solvent molecules with cheaper molecular mechanics force fields.[6]

The effective fragment potential (EFP) method[7] has recently been developed. It accounts for solvent effects on chemical reactions by treating solute molecules fully *ab initio* and introducing discrete solvent molecules through potentials added as one-electron terms directly to the *ab initio* Hamiltonian. The potentials are derived directly from separate *ab initio* calculations on water and water dimer. This method has already shown that it can reproduce all

ab initio RHF relative energies and geometries in a study on the internal rotation in ground state formamide with up to five waters.[9] It has also successfully reproduced the results of all *ab initio* MCSCF calculations on excited state formamide with two water molecules.[10] Recently, Day and Pachter[11] have reported results of a study on aqueous glutamic acid, using the EFP method to model the effects of up to ten water molecules. In this paper we further test the EFP method by its application to the Menshutkin reaction.[12] This reaction in which neutral reactants lead to separated ion products, is the most stringent test of the method to date.

In 1890 Menshutkin studied the reaction between the alkyl nitrides and alkyl halides (R1).

$$R_3N \;+\; RX \;\rightarrow\; R_4N^+ \; X^- \qquad\qquad (R1)$$
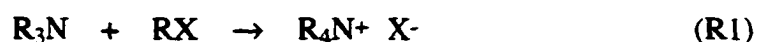
He found that the reaction rate increases dramatically when the polarity of the solvent is increased.[12] This increase in reaction rate with solvent polarity is attributed to the stabilization of the reaction path to ion separation, by the solvent. The reaction (R2) between ammonia and alkyl halide

$$NH_3 \;+\; RX \;\rightarrow\; RNH_3^+ \; X^- \qquad\qquad (R2)$$
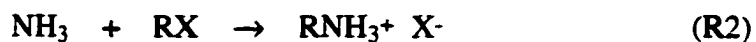
is an example of a Menshutkin reaction and is an intermediate step in the formation of primary amines,[13] an important industrial process. Investigating the effect of solvation on the Menshutkin reaction, then, is important in terms of understanding the fundamental process of solvation and in terms of industrial applications. Consequently, there have been a number of theoretical investigations of the solvent effect on this reaction.

Sola et al have studied the reaction between ammonia and methyl bromide.[14] In the

gas phase the reactants were found to form an "ion-pair reactant" which lies in a shallow well (-2.8 kcal/mol relative to separated reactants). The transition state is found to be high in energy (23.3 kcal/mol relative to separated reactants) leading to an "ion-pair product" which lies in a shallow well (20.7 kcal/mol relative to separated reactants), and finally highly unstable separated products are predicted (103.8 kcal/mol relative to separated reactants). They introduced discrete solvent molecule effects by addition of two *ab initio* waters and in separate calculations modeled the bulk effects of water, methanol, and hexane using a continuum method.[2] The addition of two discrete waters; one associated with the NH_3 group the other with the Br, resulted in an earlier and lower energy transition state (10.8 kcal/mol relative to separated reactants), and stabilized the ion-pair product (- 0.2 kcal/mol relative to separated reactants) and the separated ions (59.2 kcal/mol relative to separated reactants), with the overall process remaining endothermic. The continuum model gives the free energy of activation of the hydrated reaction as 8.3 kcal/mol and predicts the separated products to be stable with respect to reactants by 44.0 kcal/mol. With hexane as the solvent, formation of ion-pair reactants and products are predicted, along with a high energy transition state and endothermic final product ions, illustrating the effect of solvent polarity.

Gao and Xia used a QM/MM approach in statistical mechanical Monte Carlo simulations to study the ammonia - methyl chloride Menshutkin reaction in water solution.[15] The solute is modeled using the semi-empirical AM1 method; the 256 solvent water molecules by the TIP3P potential.[16] The predicted free energy of activation is 26.3 ± 0.3 kcal/mol which compares favorably with the experimental value of 23.5 kcal/mol for the related iodide system. Gao et al contend that the large discrepancy with the predicted value of Solà et al suggests that the description of discrete solute-solvent interactions is necessary in this system. For the reaction free energy Gao et al predict - 36 kcal/mol; indicating an exothermic reaction in water solution.

Maran, Pakkanen, and Karelson[17] have studied the reaction between ammonia and the

alkyl halides - methyl chloride, methyl bromide, and methyl iodide. using the semi-empirical method AM1 and describing solvent effects (water and hexane) through a multi-cavity self-consistent reaction field method. Their calculated barrier (no entropy effects included) for the chloride, bromide, and iodide systems are 21 kcal/mol. 25 kcal/mol. and 37 kcal/mol. respectively. More recently, the same authors have carried out *ab initio* calculations to examine in detail just the gas phase reactions.[18]

In this paper we report results of a study in which we apply the EFP method to micro-solvation of the reaction between ammonia and methyl bromide.

$$NH_3 \quad + \quad CH_3 \quad \rightarrow \quad CH_3NH_3{}^+ \quad Br^- \qquad (R3)$$
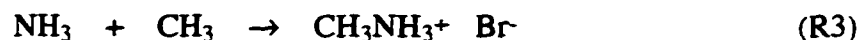
We examine the EFP method's accuracy by comparison to all *ab initio* calculations and also explore the effects of 0-8 water molecules on the reaction profile.

II. Computational Details

The gas phase potential energy surface of the reaction between ammonia and methyl bromide was explored using restricted Hartree-Fock (RHF) and second-order perturbation theory (MP2)[19] geometry optimization methods. For solvated systems only RHF calculations were carried out. Characterization of all stationary points was achieved by calculating and diagonalizing the energy second derivative matrix (hessian). A positive definite hessian (no negative eigenvalues) indicates a minimum on the potential energy surface; one negative eigenvalue indicates a transition state.

For hydrogen, carbon, nitrogen, and oxygen, the double ξ basis set of Dunning and Hay[20] was used; for bromine the double ξ basis of Binning and Curtiss was employed.[21] P polarization functions were added to hydrogens, and d polarization functions were added to all heavy atoms. A diffuse sp shell was also added to bromine. Exponents used are the defaults in GAMESS.[22] Collectively this basis set is referred to as DZVP.

Water molecules were added to the system through use of the effective fragment potential (EFP) method.[7,8] The method is described in detail in a previous paper,[8] and a summary is given in an application to the solvated internal rotation of formamide.[9] Also summarized in the latter paper are the geometry search procedure, and the intrinsic reaction coordinate (IRC) procedure which follows the minimum energy path from transition states to minima. Both techniques are utilized in this study. Numeric calculation of the hessian is carried out through double displacements of the stationary point geometries using analytic calculation of the energy gradients.

For comparison, *ab initio* waters were added in a supermolecule approach. For the two water system all *ab initio* geometry optimizations and hessians were done to test the accuracy of the EFP geometries, relative energies, and calculated frequencies. For larger numbers of waters (4 - 8) all *ab initio* single point energy calculations were performed to test relative energies.

III. Results and Discussion

(a) **Gas Phase Surface.** In order to establish a point of reference, we first explore and characterize the gas phase potential energy surface of the reaction between ammonia and methyl bromide. Results of RHF/DZVP and MP2/DZVP geometry searches are presented in Figures 1 and 2, and Table 1. The minimum energy path, found by an IRC procedure,[9] linking

the ion-pair reactant with transition states and ion-pair products is shown in Figure 3.

The first part of the surface; that is the ion-pair reactant, transition state (1), and ion-pair product (1), is qualitatively the same as that predicted by Solà et al.[14] However, Table 1 shows some quantitative discrepancies. The ion-pair reactant to transition state barrier is found to be ~ 10 kcal/mol higher than that in the earlier study. The relative RHF/DZVP energy of the transition state and ion-pair product agrees closely with the earlier work (8.4 kcal/mol compared to 8.9 kcal/mol). Consequently, the ion-pair product itself is predicted to be ~ 10 kcal/mol less stable (relative to separated reactants) than predicted by Solà et al. Tests done during the course of this study show that the small size of the underlying 3-21G basis set used by Solà is the main source of these energy discrepancies. This is confirmed below via comparison with results from calculations[18] with basis sets more comparable in quality to those used in the present study. Inclusion of polarization and diffuse functions is found to make a considerable difference to predicted geometries, but the effect on relative energies is found to be relatively small.

Dynamic correlation introduced through MP2 does result in some contraction in bond lengths, but makes little difference to the energetics. Therefore, RHF is considered adequate for study of the solvated system. Mulliken populations (see Table 2), while not meaningful in an absolute sense, do show that the Br accumulates charge as the reaction proceeds through the first transition state. It has acquired a charge of ~ - 0.9 in the ion-pair product (1).

Normally, from the ion-pair product the potential energy surface is assumed to proceed directly to the highly unstable separated products: $NH_3CH_3^+$ + Br^-; however, Maran et al[18] recently discovered a second ion-pair product, at the RHF, CISD, MP2, and MP3 levels using a 6-31G* basis set, with the Br directly interacting with an NH_3 hydrogen via a hydrogen bond. This latter species is predicted to be thermodynamically stable with respect to separated reactants. We also consider this species in which the bromine is weakly bound to an

NH_3 hydrogen. Figure 2 and Table 1 show that there is a very small barrier of 0.3 kcal/mol at the RHF/DZVP level of theory leading from the C_{3v} ion-pair reactant to a C_s transition state (Figure 3 indicates that this is little more than a shoulder on the PES) in which the Br has moved in toward a hydrogen. This transition state leads to a C_s minimum, described above, which is stable with respect to separated reactants by 6.5 kcal/mol at the RHF/DZVP level of theory. The separated products lie 105.9 kcal/mol above this minimum. Dynamic correlation effects on relative energies are more pronounced in this region of the surface with destabilization of the C_s transition state by ~ 3 kcal/mol and stabilization of the C_s ion-pair product by ~ 5 kcal/mol due to the MP2 correction. However, RHF still provides a reasonable description of the process. Mulliken populations (see Table 2) indicate that the charge on the Br is lowered considerably on formation of the second ion-pair product due to the formation of the strong Br---H-N hydrogen bond.

The RHF and MP2 energetics calculated in this study (Table 1) and those from Maran, Karelson, and Pakkanen[18] are in reasonable agreement. They predict a first transition state 30.8 and 30.3 kcal/mol relative to the ion-pair reactant at RHF/6-31G* and MP2/6-31G*, respectively. For the second ion-pair product they predict - 6.5 and - 8.8 kcal/mol relative to the ion-pair reactant at RHF/6-31G* and MP2/6-31G*, respectively. Our results for this particular Menshutkin reaction (R3), then, confirm their conclusion that the gas phase reaction to form the ion-pair product (2) (see Figure 2) is thermodynamically favorable (i.e. exothermic) but kinetically highly unfavorable, due to the high (> 30 kcal/mol) initial barrier.

(b) Two Waters. Next, two *ab initio* waters were introduced. No symmetry constraints were placed on the system during the geometry optimizations. Figure 4 and Table 3 show the structures and relative energies of what were found to be lowest energy species on the potential energy surface. The structures were found by first identifying the lowest energy transition state with two water molecules and then performing IRC calculations by first

stepping out forward and backward from the transition state along the imaginary mode leading to reactant and product minima. Also shown in Figure 4 and Table 3 are the corresponding structures and energetics from calculations with the two *ab initio* waters replaced by two EFP waters. The EFP method is found to do an excellent job of reproducing the all *ab initio* results. All EFP bond lengths are within 0.06 Å of those predicted *ab initio* and most agree much more closely than this upper bound. EFP relative energies are found to agree with the all *ab initio* relative energies to within 0.5 kcal/mol. The EFP and *ab initio* imaginary frequency at the transition state are also in excellent agreement.

The effect of two water molecules is found to be dramatic (see Table 3). The barrier from ion-pair reactant to transition state is lowered by 11.8 kcal/mol to a value of 22.2 kcal/mol and the ion-pair product is now stable with respect to the ion-pair reactant by 19.2 kcal/mol. The transition state geometry (see Figure 4) shows that it is occurring earlier in the reaction, an effect also observed by previous studies[14] and predicted by the Hammond postulate.

Figure 5 shows the all *ab initio* and the two EFP water minimum energy paths (MEPs). Both curves are relative to the respective ion-pair reactant minimum. Note that the EFP MEPS does not go to zero at its end point indicating that it is in a shallow well above the true minimum. The two MEPs map onto each other very closely up through the transition state but diverge by up to ~ 5 kcal/mol on the part of the surface representing the migration of the bromine anion.

The MEPs for the two water molecule case (see Figure 5) show that two waters are sufficient to produce an exothermic ion-pair product complex directly. Inspection of the ion-pair product structure (see Figure 4) reveals that the MEP from the transition state leads directly to the arrangement seen in the gas phase (the migration mentioned above), with the bromine hydrogen bonded to an amine hydrogen. The presence of the two waters has removed the small barrier to this process seen in the gas phase. The stability of the ion-pair product solvated with two waters (exothermic by ~ 19 kcal/mol relative to the ion-pair reactants), then, is partly due

to the same effect seen in the gas phase and partly due to the waters which hydrogen-bond to the charged bromine and amine hydrogen.

(c) Four and Six Waters. Having shown that the EFP method reproduces all *ab initio* geometries to a high degree of accuracy geometry optimizations and IRC calculations with additional water molecules have been performed only with the EFP method.

As the number of water molecules increases, the number of stationary points on the potential energy surface will increase rapidly. One advantage of the Menshutkin reaction is that the solute molecules must be co-linear in the transition state. The approach is therefore the same as with two waters: attempt to find the lowest energy transition state and follow MEPs to determine reactants and products.

In an attempt at systematic addition of waters, the starting points for the four and six water systems were obtained by addition of water molecules to the transition state found previously for the two water system. This was done in a symmetric fashion, resulting in a transition state for the four water system which is essentially C_s, and a six water transition state which possesses a nearly C_3 axis of rotation (see Figures 6 and 7).

To check the accuracy of the EFP method for these four and six water cases all *ab initio* RHF/DZVP single point energies were calculated at the EFP geometries. Again agreement is found to be excellent. For the four water case relative energies are found to agree to within 0.6 kcal/mol and for the six water case to within 3.0 kcal/mol.

The effect of the presence of four EFP waters is a reduction of the ion-pair reactant – transition state barrier by 7.9 kcal/mol compared to that in the two EFP water case (see Table 3). The resulting barrier is only 13.7 kcal/mol. Figure 6 shows that the four water transition state occurs earlier than the two water transition state as expected. The exothermicity of the ion-pair product is increased by 13.5 kcal/mol, compared to the two water case; with four waters it is exothermic by 33.9 kcal/mol relative to the ion-pair reactant. Again the waters enable the

barrierless migration of the Br to the amine group where it is hydrogen bonded to an amine hydrogen and two water hydrogens.

The six water system based on the approximately C_3 transition state does not follow the predicted trend based on the two and four water results. The ion-pair reactant - transition state barrier has increased by 8.4 kcal/mol compared to the four water case, and the exothermicity of the ion-pair product has decreased by 13.5 kcal/mol. This can be explained using the structures in Figure 7. The transition state appears earlier in the reaction than in the two and four water cases, as one would expect. The larger barrier, then, must be explained by preferential stabilization by the water molecules of the ion-pair reactant relative to the transition state. It appears that six waters allow more flexibility in the ion-pair reactant which no longer has a co-linear arrangement of NH_3 and CH_3Br as it did in the two and four water cases. Presumably this added flexibility made possible by the solvent is the reason for preferential stabilization of the ion-pair reactant over the transition state. For the ion-pair product the opposite is true; the symmetric arrangement of waters has constrained $NH_3CH_3^+$ and Br^- to a co-linear arrangement, no longer allowing the barrierless migration of Br to the amine hydrogen. The result is a less exothermic reaction (see Table 3).

To determine if there are more energetically favorable arrangements of the water molecules, alternative non-symmetric arrangements of solvent molecules were explored. Figure 8 shows a non-symmetric four water transition state geometry and the ion-pair reactant and product found by following the MEPs from this transition state. This results (Table 3) in an increase in the barrier to the transition state from the ion-pair reactant, by 4.2 kcal/mol, to 18.0 kcal/mol and a decrease in the exothermicity of the reaction, by 7.7 kcal/mol, to - 26.2 kcal/mol. In order to make a meaningful comparison, we must compare not only the barrier heights and exothermicities but also the relative energies of the symmetric and non-symmetric cases. Figure 9 shows the two MEPs for these four water systems. Both curves are plotted relative to the energy of the ion-pair reactant obtained from the non-symmetric transition state

(Figure 8). The plots show that the ion-pair reactant obtained from the non-symmetric transition state is ~ 4 kcal/mol more stable than that obtained from the symmetric transition state, the transition states themselves are nearly isoenergetic, and the ion-pair product obtained from the symmetric transition state is ~ 4 kcal/mol more stable than that obtained form the non-symmetric transition state. Taking the lowest energy structures to determine the energetics, gives a barrier of 17.5 kcal/mol and an ion-pair product exothermic by 30.1 kcal/mol.

The six water non-symmetric system (see Figure 10) has a transition state with a ring, or crown, of five hydrogen-bonded waters, with two of the waters also hydrogen-bonded to bromine. The sixth water is outside the ring but is hydrogen bonded to it and also to one of the amine hydrogens. Table 3 shows that in this non-symmetric six water system the barrier from ion-pair reactant to transition state is 16.2 kcal/mol, a reduction of 6.0 kcal/mol compared to the symmetric system. The ion-pair product is exothermic by - 28.9 kcal/mol, a stabilization of 8.5 kcal/mol relative to the symmetric system. The MEPs shown in Figure 11 are plotted relative to the ion-pair reactant obtained from the non-symmetric transition state. The two ion-pair reactants are almost isoenergetic (there is a difference of only 1.0 kcal/mol). The non-symmetric transition state, however, is considerably more stable than its symmetric counterpart (by 7.0 kcal/mol) and the corresponding ion-pair product is 9.5 kcal/mol more stable than the symmetric analog. The non-symmetric surface is therefore clearly more favorable.

Returning to Table 3 and Figures 9 and 11, one may compare the most favorable four and six water systems to see that the four water case is still slightly favored. This may mean that the increase in stabilization is not monotonic with number of water molecules, or that more arrangements of solvent molecules must be considered.

(d) Eight Waters. The eight water transition state was found to have five waters in a crown arrangement like that seen in the non-symmetric six water case, with the three remaining waters forming a chain along the underside of the co-linear solute (see Figure 12). The ion-pair

reactant - transition state barrier is calculated to be 20.3 kcal/mol, and the ion-pair product is exothermic by 31.4 kcal/mol (see Table 3). The transition state occurs earlier than that in the non-symmetric six water structure (see Figure 10); however, any resulting stabilization of the transition state appears to be (judging by the increased barrier height) offset by the more effective hydrogen-bonding in the eight water cases between the amine hydrogens and water oxygens (compare the ion-pair reactants in Figure 12 and 10). The ion-pair product retains the amine hydrogen - bromine interaction. Figure 13 shows the MEPS for the eight water system.

For the eight water case the number of stationary points on the potential energy surface will be very large. It is only possible to ensure that the most favorable geometric arrangements have been found by a systematic sampling of the phase space. This would require use of molecular dynamics (MD), Monte Carlo (MC), or a genetic algorithm (GA) methods. These methods are presently being interfaced with the EFP method.

IV. Timings

The EFP method was to developed to model solvent effects accurately and cheaply. We have demonstrated above the accuracy of the method. In order to demonstrate how inexpensive the EFP method is in comparison to corresponding all *ab initio* calculations we present timings in Table 4.

The EFP method scales linearly with the number of water molecules; timings for the all *ab initio* calculations increase much more rapidly. For the eight water case the time required for an all *ab initio* energy + gradient calculation is 14 times that required for the EFP method. Even more impressive is the fact that the time for the all *ab initio* calculation for the eight water system is 26 times that required for the zero water case, while the EFP time only increases by a factor of two.

The last two columns in Table 4 show the increase in wall clock time required which results from each addition of two water molecules to the calculation. These times do not continuously increase down the columns, with the increase in the number of water molecules, as the number of SCF cycles required is not consistent between these calculations. For the all *ab initio* calculations the number of SCF cycles required varies between 10 and 14; for the EFP calculations the variation is between 10 and 12 SCF cycles. Comparison of the *ab initio* and EFP Δ Wall Clock times clearly demonstrates how inexpensive the addition of water molecules in the EFP method is relative to all *ab initio* calculations.

V. Conclusions

We have tested the recently developed effective fragment potential (EFP) method, for modelling solvent effects, on the ammonia plus methyl bromide Menshutkin reaction. The method was shown to reproduce the all *ab initio* geometries and energetics for the reaction with two solvating water molecules very accurately. Comparison of EFP energetics with all *ab initio* single point energies at the EFP geometries for four, six, and eight solvating waters also shows good agreement. Timings presented show the EFP method to be an inexpensive way to model solvation effects very accurately.

Calculations on the gas phase Menshutkin reaction confirm previous findings that an exothermic ion-pair product with the bromine anion hydrogen-bonded to an amine hydrogen exists ($\Delta E = -4.7$ kcal/mol for RHF) but the reaction is kinetically highly unfavorable with a barrier of 34.0 kcal/mol at the RHF/DZVP level. Dynamic correlation introduced through MP2 was found to have only a small effect on the gas phase potential energy surface.

With the addition of two water molecules the barrier is reduced to 22.5 kcal/mol and the

exothermicity is increased to -19.4 kcal/mol. For the four water the case the lowest energy surface produces a barrier of 17.5 kcal/mol and a ion-pair product which is exothermic by 30.10 kcal/mol. For six waters the corresponding figures are 16.2 kcal/mol and 28.9 kcal/mol. Finally for eight solvating water molecules the barrier is 20.3 kcal/mol and the ion-pair product is exothermic by 31.4 kcal/mol. All the ion-pair products in these solvated systems contain the bromine anion - amine hydrogen interaction seen in the gas phase.

For the four, six, and eight water systems studied it is clear that there will be many more possible geometric arrangements than those actually considered. In order to ensure that the most favorable geometric arrangements have been found for these systems (and systems with additional waters) it will be necessary to systematically sample the phase space with, for example, molecular dynamics or Monte Carlo methods.

References

1.   Karelson, M.; Tamm, T., Zerner, M. C. *J. Phys. Chem.* **1993**, 97. 11901.

2.   (a) Miertus, S.; Scrocco, E.; Tomasi, J. *Chem. Phys.* **1981**, 55, 117. (b) Tomasi, J.;
     Persico, M. *Chem. Rev.* **1994**, 94, 2027. (c) Cammi, R.; Tomasi, J. *J. Comput. Chem.*
     1995, 16, 1449.

3.   Schmidt, M. W.; Windus, T. L.; Gordon, M. S. *J. Am. Chem. Soc.* **1995**, 117, 7480.

4.   (a) Stefanovich, E. V.; Truong, T. N. *Chem. Phys. Lett.* **1995**, 244, 65. (b) Davidson,
     M. M.; Hillier, I. H.; Vincent, M. A. *Chem. Phys. Lett.* **1995**, 246, 536. (c) Wiberg.
     K. B.; Rablen, P. R.; Rush, D. J.; Keith, T. A. *J. Am. Chem. Soc.* **1995**, 117, 4261.

5.   Jensen, J. H.; Gordon, M. S. *J. Am. Chem. Soc.* **1995**, 117, 8159.

6.   (a) Gao, J. *Acc. Chem. Res.* **1996**, 29, 298. (b) Luzhkov, V.; Warshel, A. *J.*
     Comput. Chem. **1992**, 13, 199. (c) Field, M. J.; Bash, P. A.; Karplus, M. *J. Comput.*
     Chem. **1990**, 11, 700.

7.   Jensen, J. H.; Day, P. N.; Gordon, M. S.; Basch, H.; Cohen, D.; Garmer, D. R.;
     Krauss, M.; Stevens, W. J. in *Modeling the Hydrogen Bond*, edited by Douglas A.
     Smith, ACS Symposium Series 569, **1994**, p. 139.

8.   Day, P. N.; Jensen, J. H.; Gordon, M. S.; Webb, S. P.; Stevens, W. J.; Krauss, M.;
     Garmer, D. R.; Basch, H.; Cohen, D. *J. Chem . Phys.* **1996**, 105, 1969.

9.   Chen, W.; Gordon, M. S. *J. Chem . Phys.* **1996**, 105, 11081.

10. Krauss, M.; Webb, S. P. *J. Chem. Phys.* **1997**, 107, 5771.

11. Day, P. N.; Pachter, R. *J. Chem . Phys.* **1997**, 107, 22.

12. (a) Menshutkin, N. Z. *Phys. Chem.* **1890**, 5, 589. (b) Menshutkin, N. Z. *Phys. Chem.*
     1890, 6, 41.

13. McMurry, J. in *Organic Chemistry*, Brooks/Cole Publishing Company, 1984, p. 933.

14. Solà, M.; Lledós, A.; Duran, M.; Bertrán, J.; Abboud. J. M. *J. Am. Chem. Soc.* **1991**. 113, 2873.

15. Gao, J.; Xia, X. *J. Am. Chem. Soc.* **1993**, 115, 9667.

16. Jorgensen, W. L.; Chandrasekhar, J.; Madura, J. D.; Impey, R. W.; Klein. M. L. *J. Chem. Phys.* **1983**, 79, 926.

17. Maran, U.; Pakkanen, T. P.; Karelson, M. *J. Chem. Soc. Perkin. Trans.* **1994**, 2. 2445.

18. Maran, U.; Karelson, M.; Pakkanen, T. P. *J. Mol. Struc. (Theochem)* **1997**, 397. 263.

19. (a) Binkley, J.S.; Pople, J.A. *Int. J. Quantum Chem.* **1975**, 9, 229; (b) Krishnan, R; Pople, J.A. *Int. J. Quantum Chem.* **1978**, 14, 91.

20. Dunning, T. H.; Hay, P. J. Chapter 1 in *Methods of Electronic Structure Theory* H.F. Schaefer III, Ed. Plenum Press, New York, 1977, pp 1-27.

21. Binning, R. C.; Curtiss, L. A. *J. Comput. Chem.* **1990**, 11. 1206.

22. Schmidt, M.W.; Baldridge, K.K.; Boatz, J.A.; Jenson, J.H.; Koseki. S.; Matsunaga, N.; Gordon, M.S.; Ngugen, K.A.; Su, S.; Windus, T.L.; Elbert, S.T.; Montgomery. J.; Dupuis, M. *J. Comp. Chem.* **1993**, 14, 1347.

Table 1. Calculated energies (in kcal/mol) relative to the ion-pair reactant for the Menshutkin reaction (R1) in the gas phase.

	RHF/DZVP[a]	MP2/DZVP[a]
Separated Reactants	1.8	2.7
Ion-Pair Reactant	0.0	0.0
Transition State (1)	34.0	33.0
Ion-Pair Product (1)	25.6	24.9
Transition State (2)	25.9	28.2
Ion-Pair Product (2)	- 4.7	-7.3
Separated Ion Products	101.2	106.6

[a] Geometry is optimized at this level of theory.

Table 2. RHF/DZVP Mulliken charges for stationary points on the potential energy surface of the Menshutkin (R3) in the gas phase.

	Mulliken Charges				
	NH$_3$		CH$_3$		Br
	N	H	C	H	
Separated Reactants	- 0.747	0.249	- 0.283	0.158	- 0.193
Ion-Pair Reactant	- 0.758	0.255	- 0.251	0.158	- 0.229
Transition State (1)	- 0.730	0.319	- 0.169	0.225	- 0.739
Ion-Pair Product (1)	- 0.524	0.352	- 0.272	0.219	- 0.918
Transition State (2)	- 0.512	0.357 (x2) 0.348	- 0.251	0.191 (x2) 0.248	- 0.928
Ion-Pair Product (2)	- 0.441	0.328 (x2) 0.307	- 0.253	0.186 (x2) 0.138	- 0.780
Separated Ion Products	- 0.478	0.375	- 0.248	0.201	- 1.000

Table 3. Calculated barriers and exothermicities of the MEnshutkin (R3) with 0 - 8 solvating water molecules.

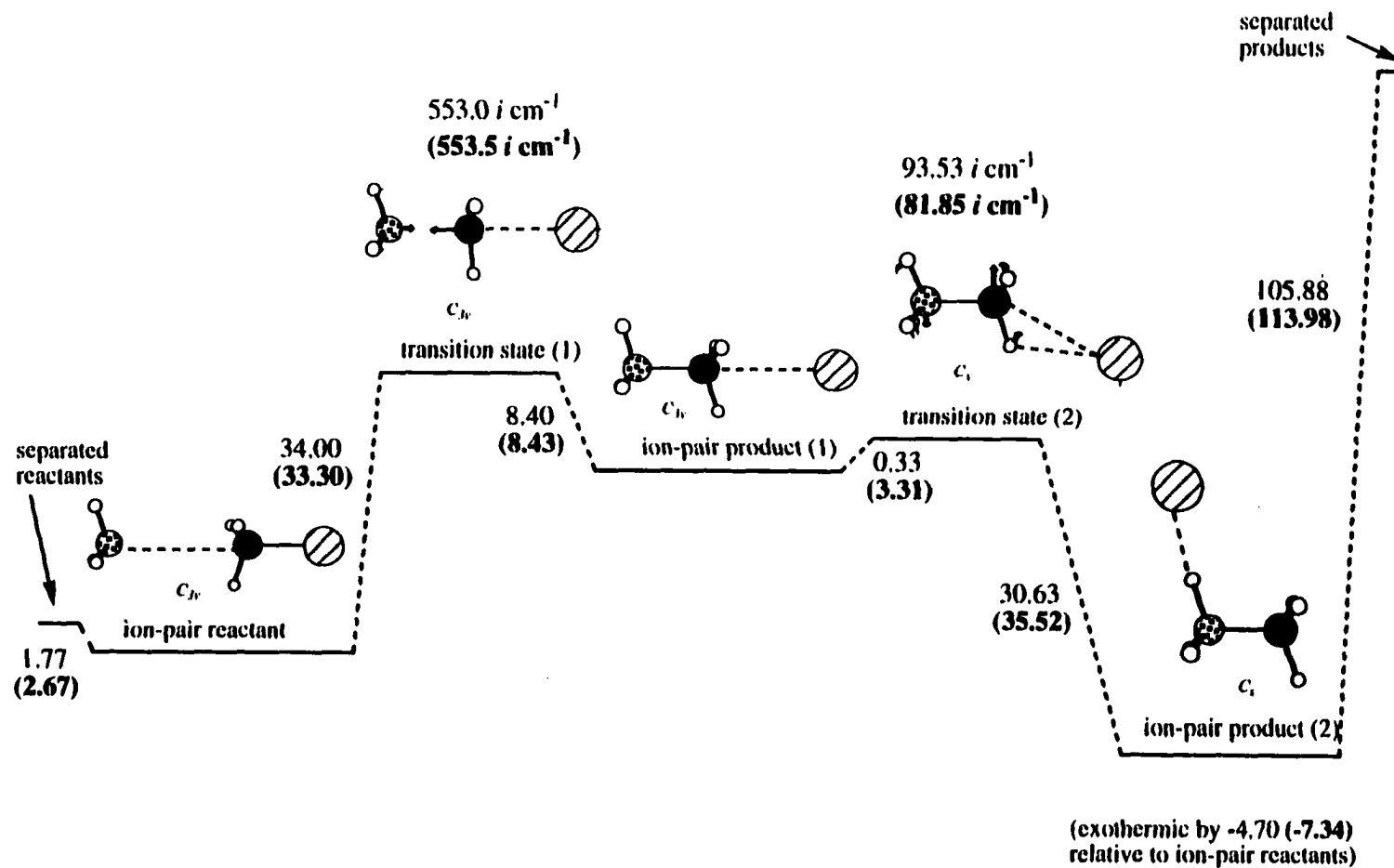| # Waters			Relative Energy / Kcal/mol	
			EFP	*Ab Initio*
0		I-P Reac.	-	0.0
		T.S.	-	34.0
		I-P Prod.	-	- 4.7
2		I-P Reac.	0.0	0.0
		T.S.	22.5	22.2
		I-P Prod.	- 19.4	- 19.2
4	Symmetric	I-P Reac.	0.0	0.0
		T.S.	13.7	14.3
		I-P Prod.	- 33.9	- 33.9
	Non-Symmetric	I-P Reac.	0.0	-
		T.S.	18.0	-
		I-P Prod.	- 26.2	-
6	Symmetric	I-P Reac.	0.0	0.0
		T.S.	22.2	20.3
		I-P Prod.	- 20.5	- 23.5
	Non-Symmetric	I-P Reac.	0.0	-
		T.S.	16.2	-
		I-P Prod.	- 28.9	-
8		I-P Reac.	0.0	-
		T.S.	20.3	-
		I-P Prod.	- 31.4	-

Table 4. All *ab initio* versus EFP method timings taken from calculations carried out on an IBM RS6000/350. Bracketed times are for direct SCF; others are for conventional SCF. All times are given in seconds.

| # Solvating H_2O's	# Basis Functions[a]	Energy				Energy + Gradient					
		CPU		Wall Clock		CPU		Wall Clock		Δ Wall Clock[c]	
		Ab	EFP	Ab	EFP	Ab	EFP	Ab	EFP	Ab	EFP
0 H_2O	94	266		596		556		889			
		(1416)		(1434)		(1706)		(1727)			
2 H_2O	144	1155	337	3141	817	2012	890	4006	1376	3117	487
		(4493)	(1546)	(4537)	(1561)	(5348)	(2099)	(5399)	(2118)	(3672)	(391)
4 H_2O	194	3334	366	9905	851	5182	1166	11768	1658	7762	282
		(15927)	(1603)	(16052)	(1619)	(17765)	(2400)	(17905)	(2422)	(12506)	(304)
6 H_2O	244	-	416	-	964	-	1493	-	2054	-	396
		(23008)	(1877)	(23205)	(1895)	(26460)	(2954)	(26684)	(2981)	(8779)	(559)
8 H_2O	294	-	430[b]	-	942[b]	-	1752	-	2275	-	221
		(39577)	(1764)[b]	(39918)	(1783)[b]	(44647)	(3082)	(45029)	(3134)	(18345)	(153)

[a] for EFP # basis functions always 94. [b] took 1 less SCF cycle than previous calculations. [c] time difference resulting from each addition of two water molecules.
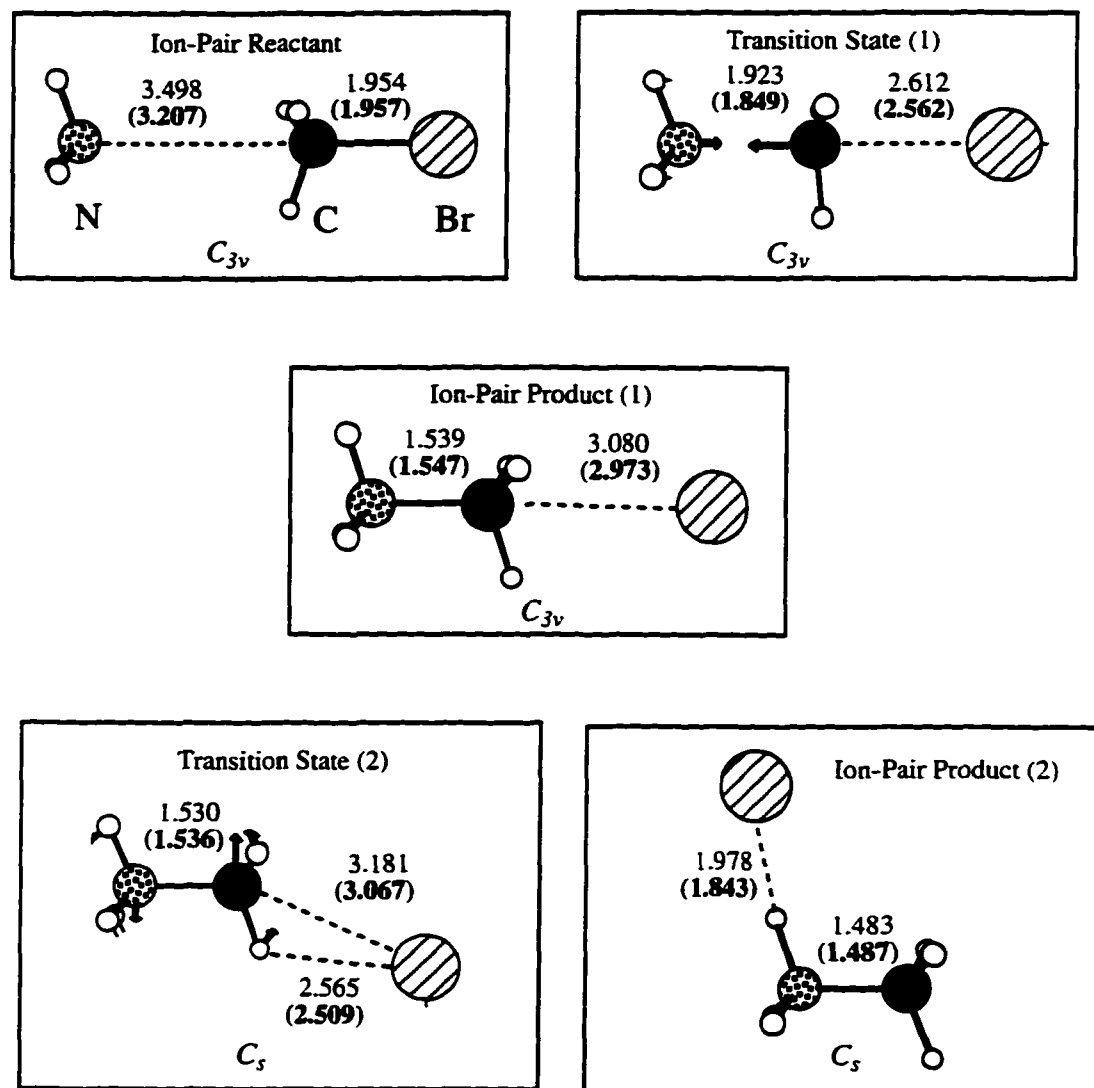
Figure 1. RHF/DZVP and MP2/DZVP optimized stationary point structures on the potential energy surface of the Menshutkin reaction (R3) in the gas phase. Bond lengths are in Angstroms. MP2 bond lengths are in bold type and brackets.

553.0 *i* cm⁻¹
(553.5 *i* cm⁻¹)

93.53 *i* cm⁻¹
(81.85 *i* cm⁻¹)

separated
products

105.88
(113.98)

c_{3v}

transition state (1)

8.40
(8.43)

c_{3v}

ion-pair product (1)

transition state (2)

c_s

34.00
(33.30)

separated
reactants

0.33
(3.31)

c_{3v}

30.63
(35.52)

ion-pair reactant

1.77
(2.67)

c_s

ion-pair product (2)

(exothermic by -4.70 **(-7.34)**
relative to ion-pair reactants)

Figure 2. The RHF/DZVP and MP2/DZVP potential energy surfaces of the Menshutkin reaction (R3)
in the gas phase. Energies are in kcal/mol. Harmonic vibrational frequencies are shown for transition states.
Diagram is not to scale. MP2/DZVP values are in bold type.
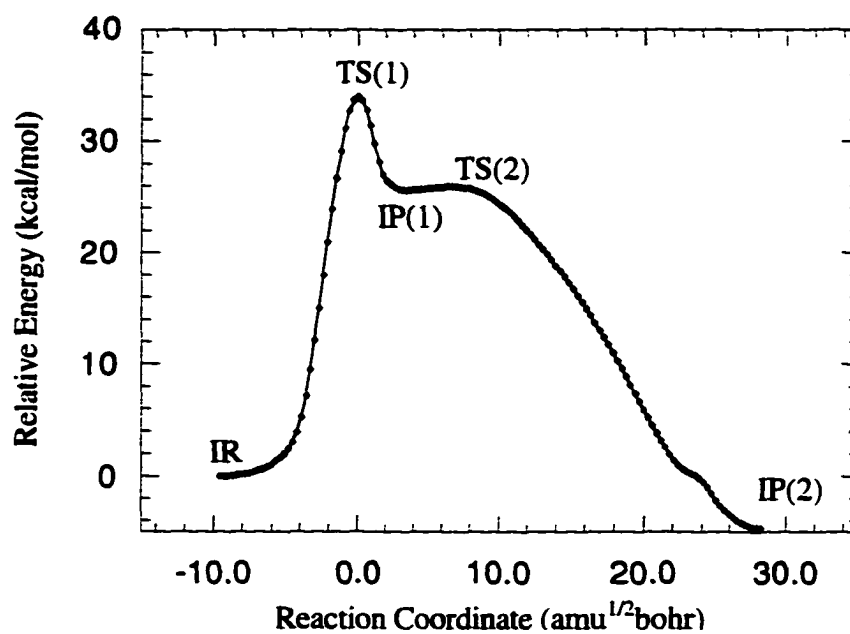
Figure 3. The minimum energy path for the gas phase Menshutkin reaction
(R3). Energy points are in kcal/mol and are relative to the ion-pair reactants.
IR = ion-pair reactants, TS(1) = first transition state,
IP(1) = first ion-pair product, TS(2) = second transition state,
IP(2) = second ion-pair product: see Figure 2.

( ) = fragment
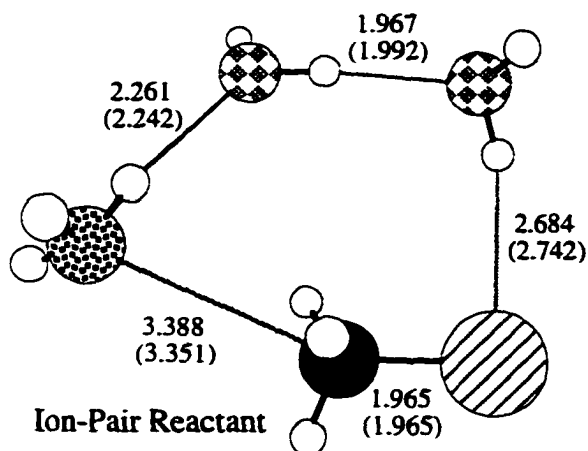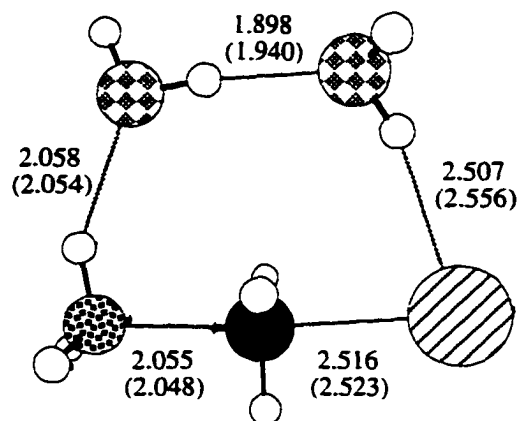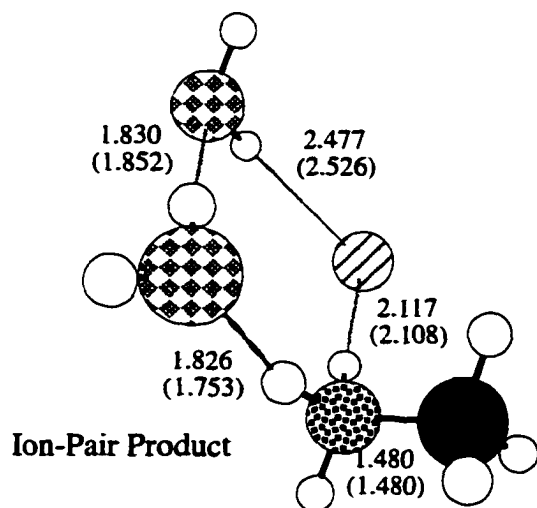
Figure 4. RHF/DZVP all *ab initio* structures and Mulliken charges for the Menshutkin reaction (R3) with two water molecules and the corresponding structures and charges with two EFP waters. Bond lengths are in Angstroms. Brackets indicate EFP method.
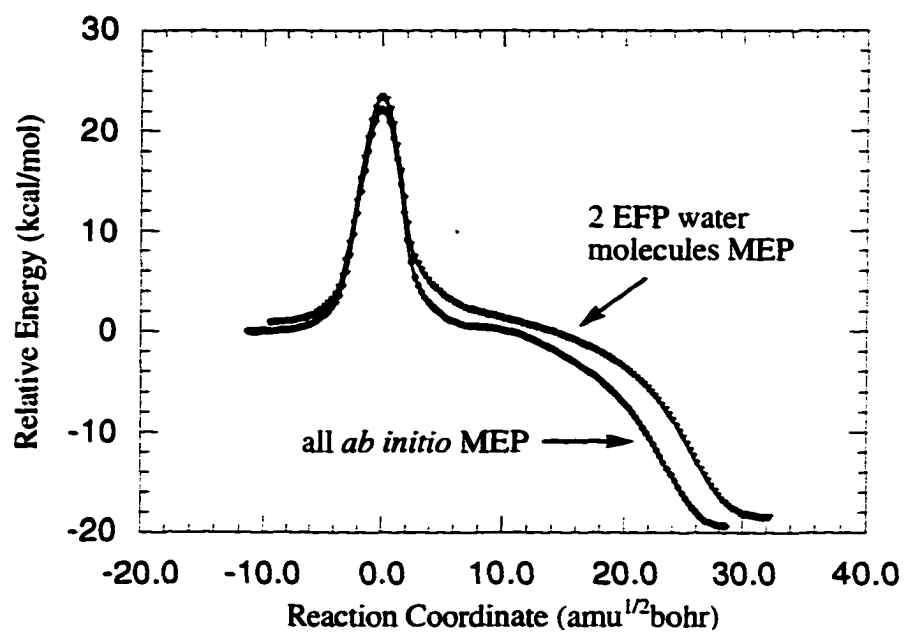
Figure 5. Minimum energy paths (MEPs) for the Menshutkin reaction (R3) with two water molecules. The bottom curve was calculated all *ab initio*; the top curve was calculated with two EFP water molecules.

3.124 1.979

2.805

2.426

2.019

Ion-Pair Reactant

2.150 2.438

2.613

2.203 1.977

Transition State 499.6 i cm^{-1}

N-C bond 1.478

1.826

1.874

2.239
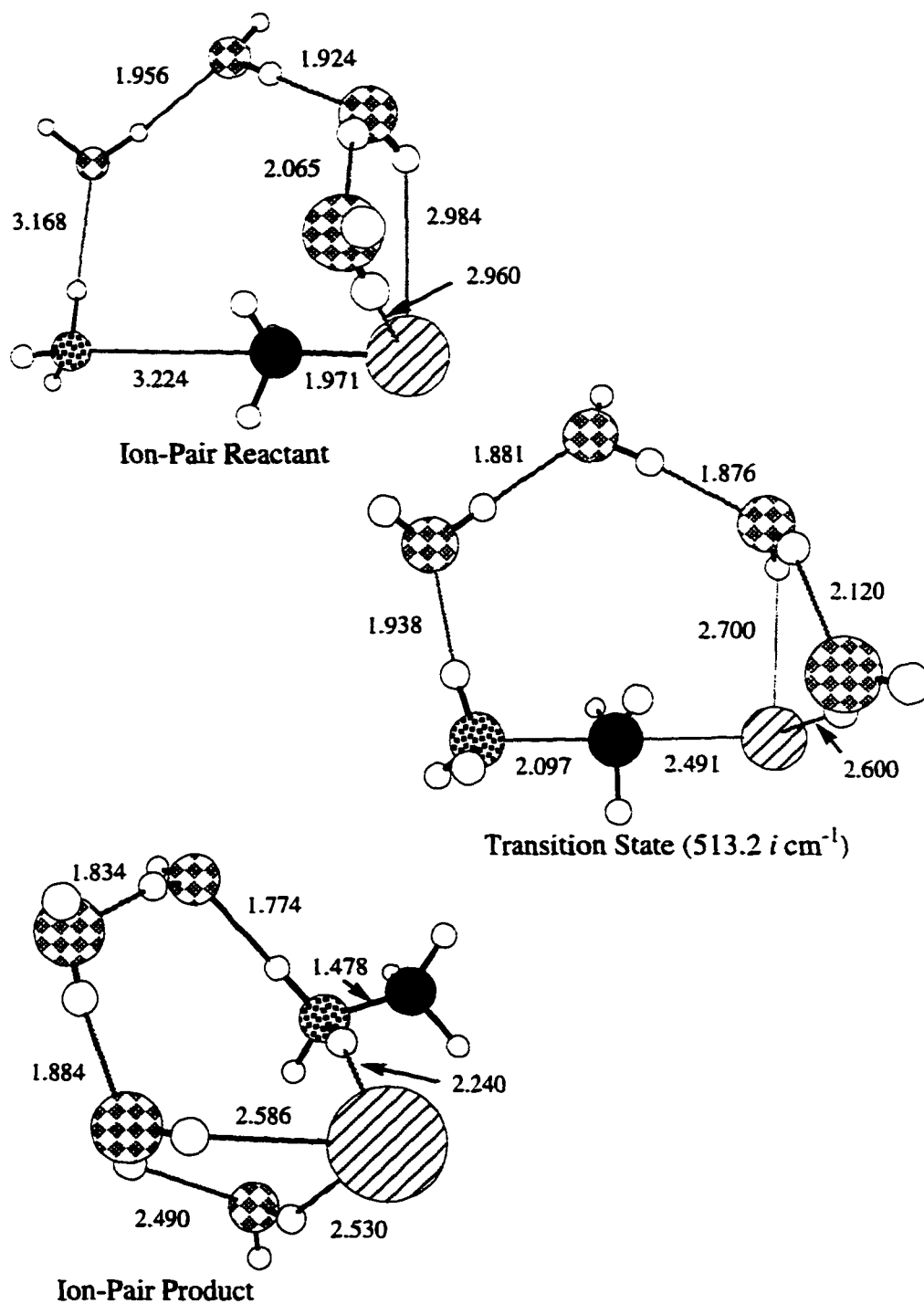
2.533

Ion-Pair Product
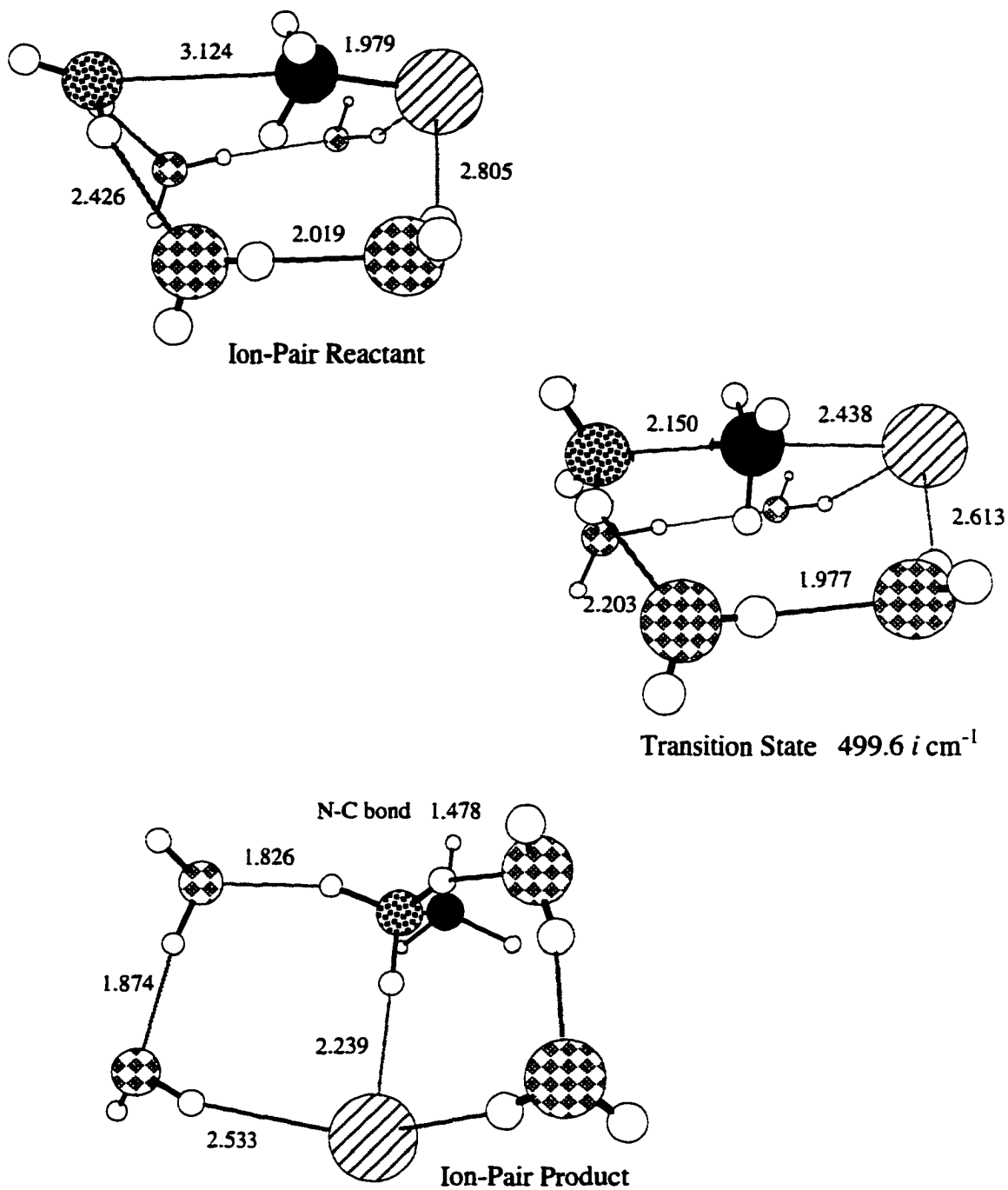
Figure 6. RHF/DZVP stationary point structures on the potential energy surface of the Menshutkin reaction (R3) with four EFP water molecules. Bond lengths are in Angstroms; only selected symmetry unique bond lengths are shown.
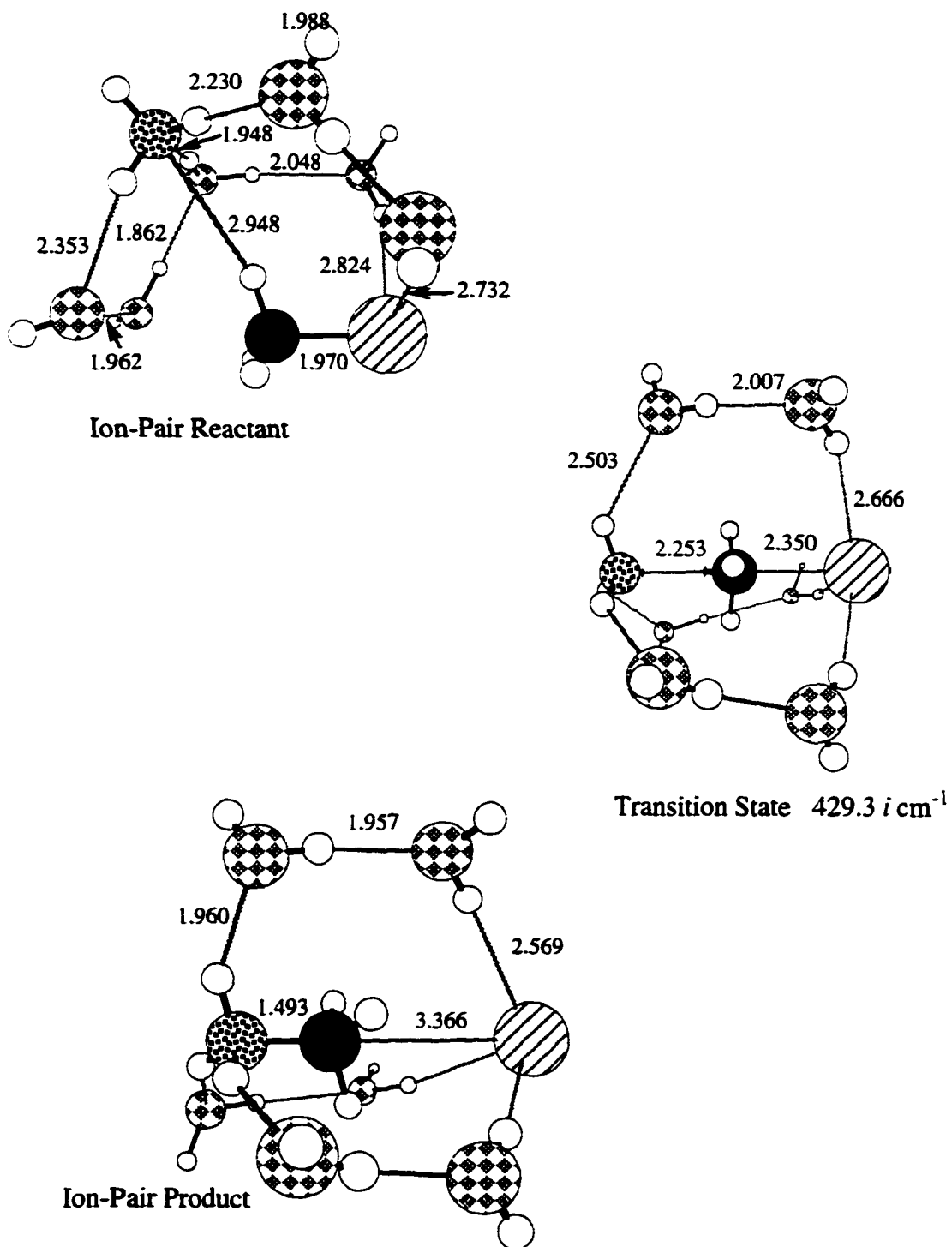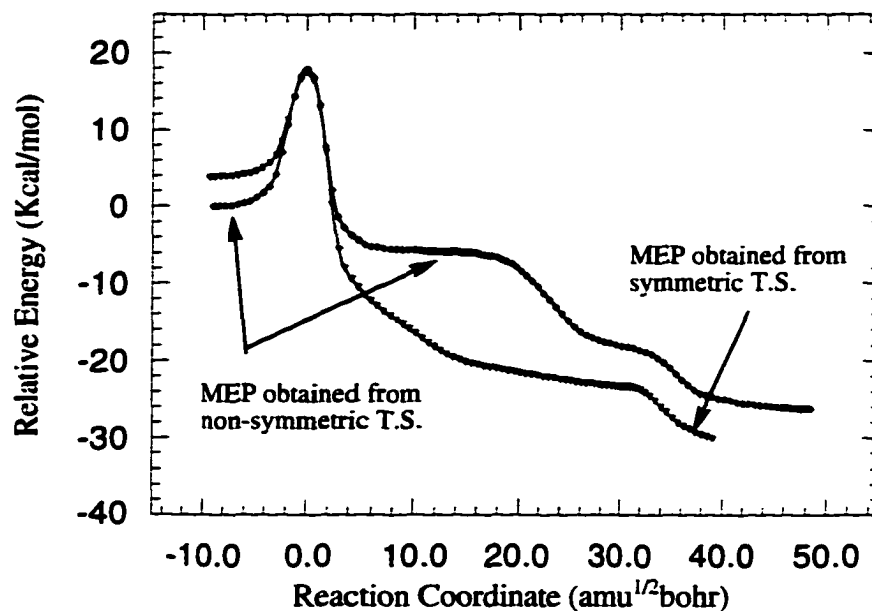
Figure 7. RHF/DZVP stationary point structures (symmetric T.S. and product) on the potential energy surface of the Menshutkin reaction (R3) with six EFP water molecules. Bond lengths are in Angstroms; only selected symmetry unique bond lengths are shown.

1.956   1.924

2.065

3.168   2.984

2.960

3.224   1.971

Ion-Pair Reactant

1.881   1.876

2.120

1.938   2.700

2.097   2.491   2.600

Transition State ($513.2\,i\,\text{cm}^{-1}$)

1.834

1.774

1.478

1.884

2.240
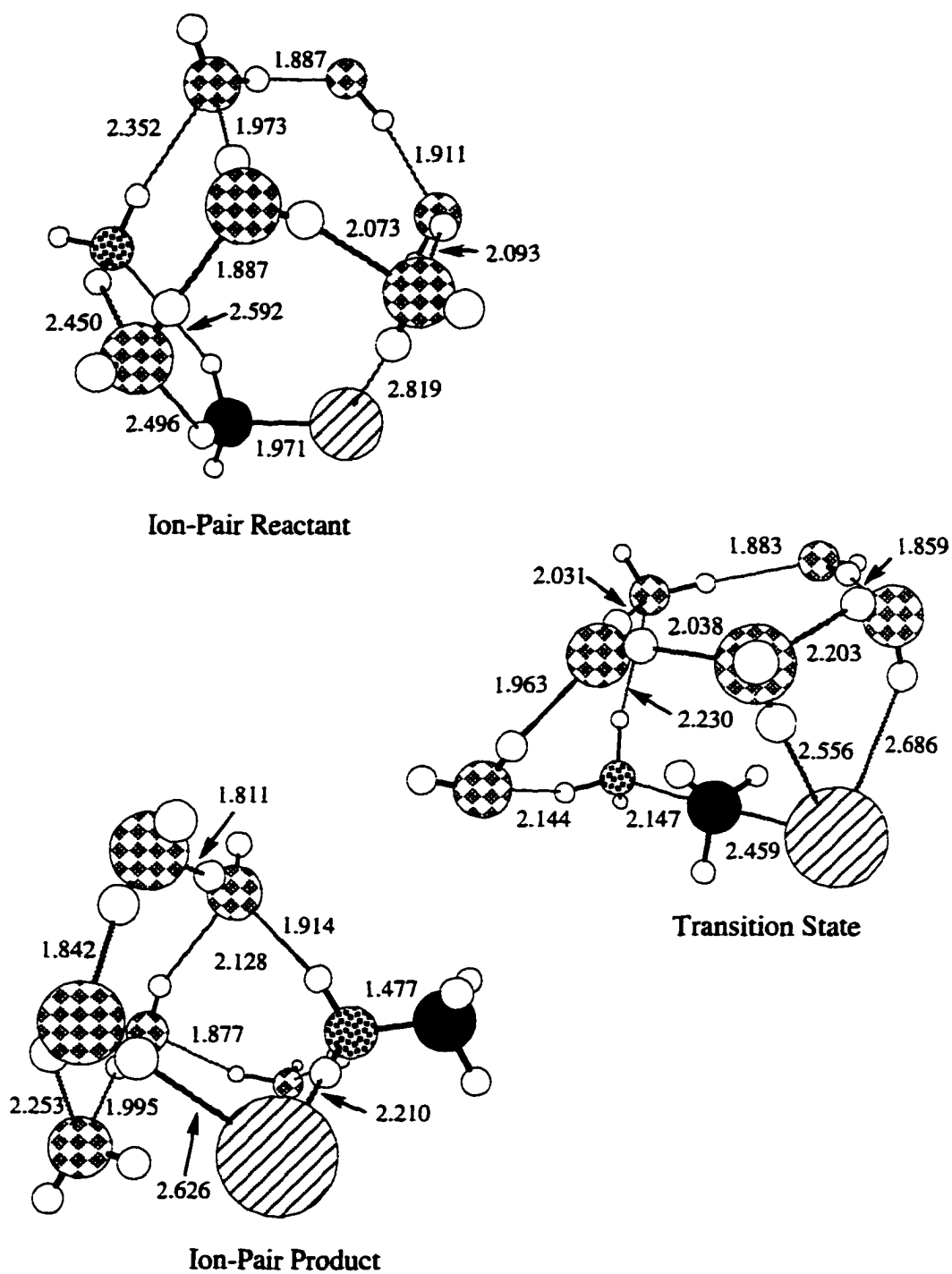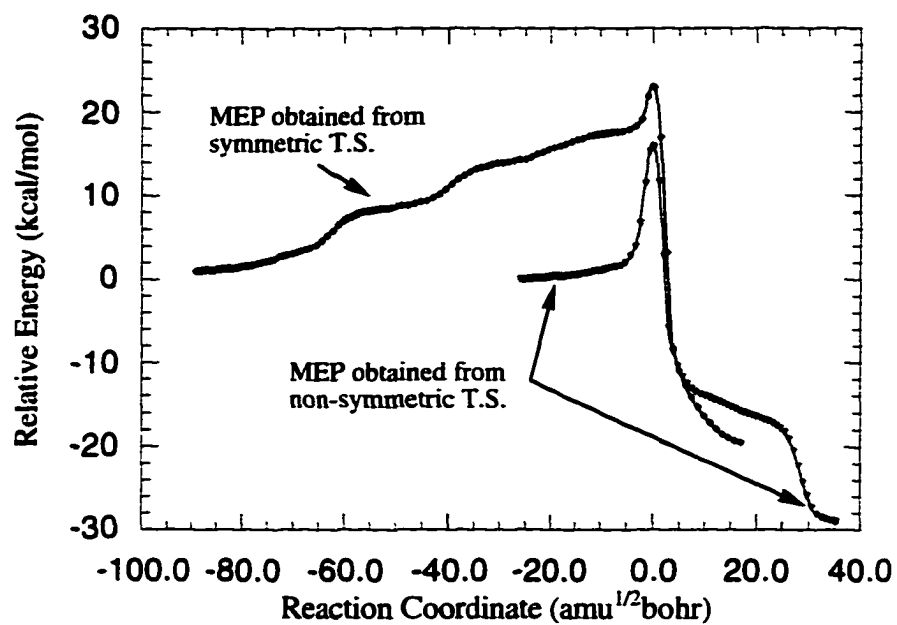
2.586

2.490   2.530

Ion-Pair Product

Figure 8. RHF/DZVP non-symmetric stationary point structures on the potential energy surface of the Menshutkin reaction (R3) with four EFP water molecules. Bond lengths are in Angstroms.
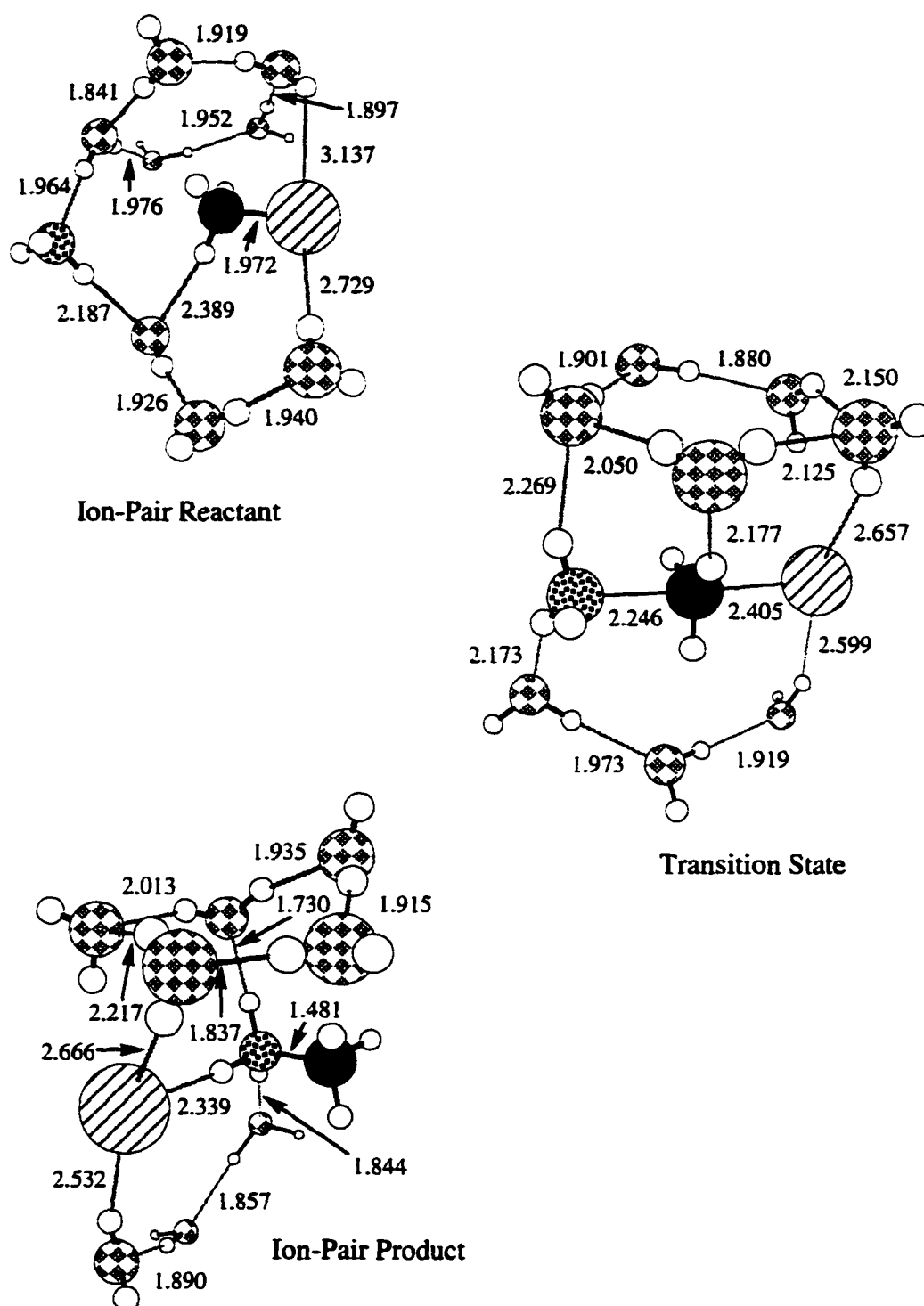
Figure 9. Minimum energy paths (MEPs) for the Menshutkin reaction (R3) with four EFP water molecules. One MEP was obtained from a symmetric transition state as the starting point; the other was obtained from a non-symmetric transition state as the starting point. Energy points are relative to the lowest energy ion-pair reactant (obtained from non-symmetric transition state).

Figure 10. RHF/DZVP non-symmetric stationary point structures on the potential energy surface of the Menshutkin reaction (R3) with six EFP water molecules. Bond lengths are in Angstroms.

Figure 11. Minimum energy paths (MEP's) for the Menshutkin reaction (R3) with six EFP water molecules. One MEP was obtained from a symmetric transition state as the starting point; the other was obtained from a non-symmetric transition state as the strting point. Energy points are relative to the lowest energy ion-pair reactant (obtained from non-symmetric transition state).

Figure 12. RHF/DZVP stationary point structures on the potential energy surface of the Menshutkin reaction (R3) with eight EFP water molecules. Bond lengths are in Angstroms.
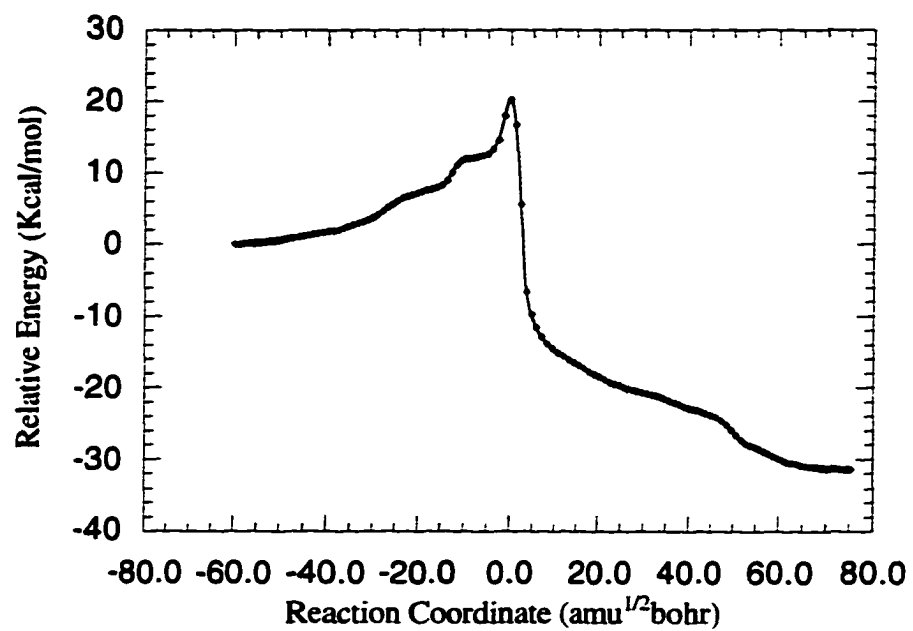
Figure 13. Minimum energy path (MEP) for the Menshutkin reaction (R3) with eight EFP water molecules. Energy points are relative to the ion-pair reactant.

CHAPTER 9. CONCLUSIONS

a) Specific Conclusions from Research Projects Presented.

Analytic Derivatives. The results of the derivation of the closed shell frozen-core MP2 analytic gradient expressions in Chapter 2 have been used to implement the method in the electronic structure code GAMESS. The complex nature of the effect of the frozen-core approximation on summation ranges and terms in these expressions demonstrates the necessity for such a derivation. This is especially true considering no such derivation exists in the literature. Now implemented, the method may be used in a wide range of applications. It is the method of choice for including the effects of dynamic electron correlation in the determination of molecular structure for closed shell systems. Once stationary points are found the analytic gradient allows their characterization, and also the calculation of harmonic frequencies, by numeric evaluation of the closed shell frozen-core MP2 energy second derivative. This is done by displacements of the nuclei along the x, y, and z axes and calculation of the energy gradient after each displacement.

The effective fragment potential (EFP) method models solvent effects by the addition of one-electron terms to the *ab initio* Hamiltonian. One of these terms accounts for polarization of the EFP solvent by the *ab initio* solute. Subsequent repolarization of the solute by induced dipoles in the EFP solvent requires that an iterative self-consistent procedure be carried out. Part of the work in Chapter 7 consists of folding these iterations into the SCF iterations themselves, resulting in a factor of two speed up over calculations done using the original method. The localized orbital dipole polarizabilities which are used to include these polarization effects were originally calculated using a numerical finite difference method. An analytic method for calculating these tensors is derived in Chapter 7. The analytic method has several advantages over the numeric finite-field method. The numeric method is tedious and cumbersome for systems with more than a few atoms and is not easily automated. Also, the

235

analytic method produces more symmetric and more transferable localized orbital dipole polarizabilities.

Transition Metal Chemistry. Titanium is an early first row transition metal. It contains the same number of valence electrons as carbon; their respective electron configurations are $4s^23d^2$ and $2s^22p^2$. However, Chapter 3 demonstrates the very different behavior of these two elements. TiH_4 is found to dimerize with no barrier forming double and triple hydrogen bridged dimers which are exothermic by up to ~ 46 kcal/mol. This is a result of the electron deficiency of titanium; that is, in an analogous manner to boron in diborane, dimerization occurs because of titanium's desire to fill its d-shell. The very flat surface between Ti_2H_8 isomers seen in Chapter 3 demonstrates that the two titanium centers allow the positions of the hydrogens to change with little or no energy penalty. Calculated vibrational frequencies suggest that it is possible that Ti_2H_8 isomers may have been observed in matrix isolation experiments.

If one removes two hydrogens from Ti_2H_8 to give the molecule Ti_2H_6 (Chapter 4), which has two electrons available for bonding, a Ti-Ti bond does *not* form in any of the five isomers found. In the D_{2h} isomer it was shown that this is due to unfavorable repulsive interactions between the Ti-Ti bond (if it were to form) and the Ti-H-Ti bridges. In fact, the most stable isomers of Ti_2H_6 contain unpaired electrons with small isotropic singlet-triplet energy gaps of the order of 0.3 - 1.5 kcal/mol. Calculated vibrational frequencies for the isomers of Ti_2H_6 suggest that these dimers may also have been observed experimentally.

The D_{2h} Ti_2H_6 isomer serves as a good model for many di-titanium (III) bridged compounds. The singlet - triplet energy gap in this model compound was examined in more detail in Chapter 5 with the inclusion of effects due to spin-orbit coupling. This is the first time that *ab initio* techniques have been used to calculate and identify spin-orbit coupling interactions in these types of di-metal systems. According to the calculations, the splitting of the triplet $M_s = 0$ and $M_s = \pm 1$ components is due almost entirely to the angular momentum operator

perpendicular to the Ti-H-Ti bridge, thereby explaining why experimentalists have been able to estimate the Ti-Ti separation accurately in similar compounds without taking spin-orbit coupling into account.

The introduction of halides into simple titanium systems (Chapter 6) has a large effect. The exothermicity of the TiX_4 (X = F, Cl, Br) dimers is much reduced over the hydride counterpart. Within the halide series the fluoride dimer is twice as strongly bound as the chlorine and bromine dimers. This is consistent with non-monotonic melting and boiling point trends seen in the titanium tetrahalides. The structures of the dimer minima: bridging bonds in the fluoride and weakly interacting tetrahedral units in the chloride and bromide are consistent with available experimental structural details of the titanium halides in the gas and solid phase. Transition states representing paths to halide exchange offer an explanation of unexpected line widths seen in NMR experiments on $TiCl_4$.

Solvation Studies. In Chapter 8 the effective fragment potential (EFP) method is shown to accurately and cheaply reproduce all *ab initio* calculations on the Menshutkin reaction between ammonia and methyl bromide with two, four, six, and eight solvating waters. The effect of solvating waters on the gas phase energy surface is found to be a reduction in barrier height from ion-pair reactants to transition state and an increase in exothermicity of ion-pair products.

b) General Conclusions. Work in the areas of energy derivative theory, transition metal chemistry, and solvation effects has been presented in this dissertation. This work represents a basis for further research and advancement in each of these three areas.

The derivation of the closed shell frozen-core MP2 analytic gradient is presented in a clear, methodical manner. Enough detail is included to demonstrate the techniques and special considerations required when dealing with derivatives of molecular orbital based perturbative methods which include frozen cores. It is expected, then, that this work will facilitate the

inclusion of the frozen-core approximation in the analytic gradient of the multiconfigurational quasidegenerate perturbation (MCQDPT) method, which is currently being implemented in GAMESS by collaborators.

The levels of *ab initio* theory required to describe certain simple titanium systems have been established. This knowledge may applied, in future studies, to more complex and experimentally accessible titanium systems for which the simple molecules serve as models.

The application of the EFP method, for modelling solvation effects, to the Menshutkin reaction between ammonia and methyl bromide represents conformation of the method's accuracy and efficiency. The success of the method clears the way for further development such as phase space sampling through, for example, molecular dynamics, and extension of the model to include correlation and dispersion effects.

Finally, to date, *ab initio* investigation of even the most simple aqueous transition metal chemistry is untouched territory. With the *combination* of the three areas of research, on which work was presented in this dissertation, will come exciting projects such as the investigation of molecular structure, electronic structure, and magnetic properties of di-transition metal complexes in solution.